ACS OMEGA

Article

Cite This: ACS Omega 2018, 3, 15743−15753

http://pubs.acs.org/journal/acsodf

Occupancy Dependency of Maxwell−Stefan Diffusivities in Ordered Crystalline Microporous Materials

Rajamani Krishna*

Van't Hoff Institute for Molecular Sciences, University of Amsterdam, Science Park 904, 1098 XH Amsterdam, The Netherlands

Supporting Information

ABSTRACT: Molecular dynamics simulation data for a variety of binary guest mixtures (H_2/CO_2, Ne/CO_2, CH_4/CO_2, CO_2/N_2, H_2/CH_4, H_2/Ar, CH_4/Ar, Ar/Kr, Ne/Ar, CH_4/C_2H_6, CH_4/C_3H_8, $C_2H_6C_3H_8$, CH_4/nC_4H_{10}, and CH_4/nC_5H_{11}) in zeolites (MFI, BEA, ISV, FAU (all-silica), NaY, NaX, LTA, CHA, DDR) and metal−organic frameworks (MOFs) (IRMOF-1, CuBTC, MgMOF-74) show that the Maxwell−Stefan (M−S) diffusivities, $Đ_1$, $Đ_2$, $Đ_{12}$, are strongly dependent on the molar loadings. The main aim of this article is to develop a fundamental basis for describing the loading dependence of M−S diffusivities. Using the ideal adsorbed solution theory, a thermodynamically rigorous definition of the occupancy, θ, is derived; this serves as a convenient proxy for the spreading pressure, π, and provides the correct metric to describe the loading dependence of diffusivities. Configurational-bias Monte Carlo simulations of the unary adsorption isotherms are used for the calculation of the spreading pressure, π, and occupancy, θ. The M−S diffusivity, $Đ_i$, of either constituent in binary mixtures has the same value as that for unary diffusion, provided the comparison is made at the same θ. Furthermore, compared at the same value of θ, the M−S diffusivity $Đ_i$ of any component in a mixture does not depend on it partner species. The $Đ_i$ versus θ dependence is amenable to simple interpretation using lattice-models. The degree of correlations, defined by the ratio $Đ_1/Đ_{12}$, that characterizes mixture diffusion shows a linear increase with occupancy θ, implying that correlations become increasingly important as pore saturation conditions are approached.

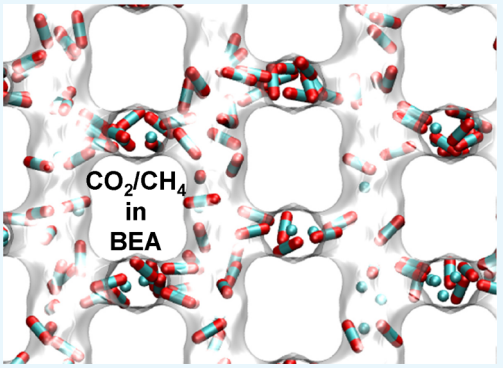

1. INTRODUCTION

Ordered crystalline microporous materials such as zeolites (alumino-silicates), metal−organic frameworks (MOFs), and zeolitic imidazolate frameworks have wide applications as catalysts, adsorbents, and as perm-selective layers in membrane separations.[1−8] The design and development of catalytic and separation processes requires reliable and accurate models to describe intracrystalline diffusion of mixtures of guest molecules.[3,7,9] Intracrystalline diffusion of reactants and products invariably exert a strong influence on the conversion and selectivity of catalyzed reactions.[10−12] For mixture separations in a fixed-bed adsorber, intraparticle diffusion limitations cause distended breakthrough characteristics and usually lead to diminished separation effectiveness.[13,14] Diffusional effects may become strong enough to over-ride the influence of mixture adsorption equilibrium and become the prime driver in fixed-bed separations.[14−18] The selectivities in membrane separations are governed by a combination of mixture adsorption equilibrium and mixture diffusion characteristics.[4,19−21]

It is widely recognized that the most convenient and practical approach to modeling n-component mixture diffusion is to adopt the Maxwell−Stefan (M−S) formulation that relates the intracrystalline molar fluxes N_i to the chemical potential gradients[6,7,9]

$$-\rho\frac{q_i}{RT}\frac{\mathrm{d}\mu_i}{\mathrm{d}z}=\sum_{\substack{j=1\\ j\neq i}}^{n}\frac{x_jN_i-x_iN_j}{Đ_{ij}}+\frac{N_i}{Đ_i};\qquad i=1,2,\ldots,n \tag{1}$$

where R is the gas constant (=8.314 J mol^{-1} K^{-1}), ρ represents the framework density of the microporous crystalline material, and the component loadings q_i are defined in terms of moles per kg of framework. The x_i in eq 1 are the component mole fractions of the adsorbed phase within the micropores

$$x_i=q_i/q_t;\qquad q_t=q_1+q_2+\ldots+q_n;\qquad i=1,2,\ldots,n \tag{2}$$

The $Đ_i$ characterize species i−wall interactions in the broadest sense. The $Đ_{ij}$ are exchange coefficients representing interaction between components i with component j. At the molecular level, the $Đ_{ij}$ reflect how the facility for transport of species i correlates with that of species j. Conformity with the Onsager reciprocal relations demands the symmetry constraint

Received: September 20, 2018
Accepted: November 6, 2018
Published: November 19, 2018

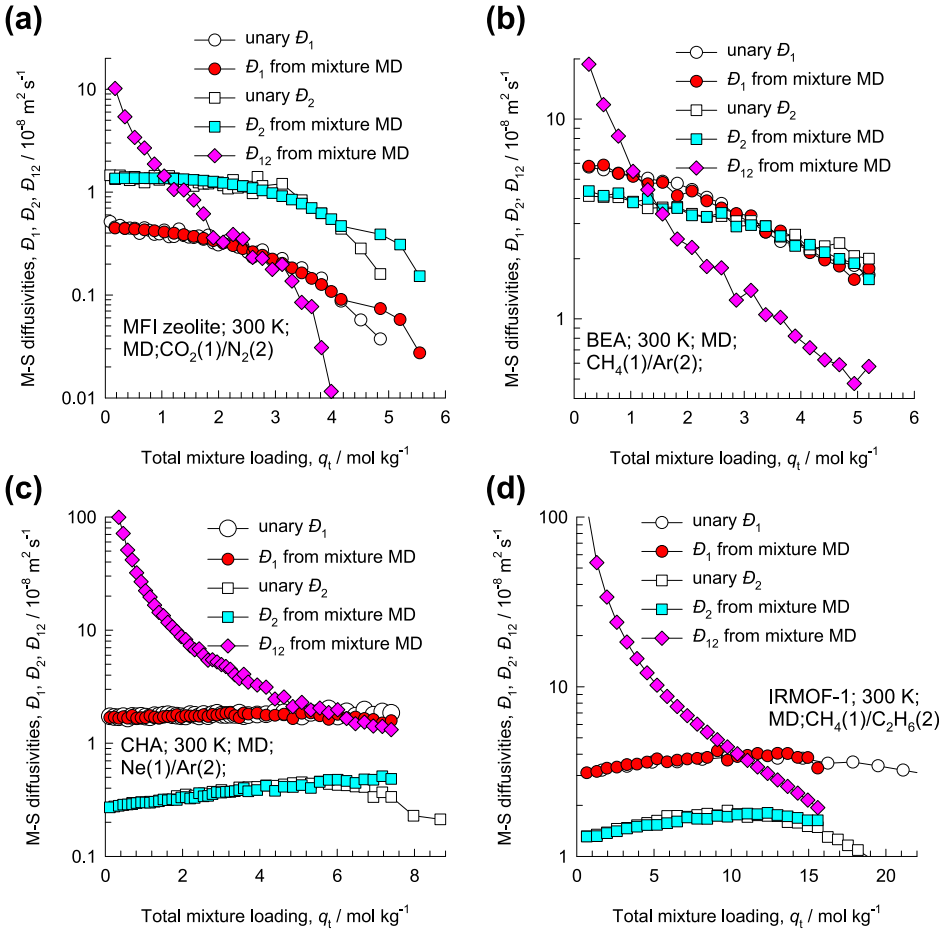

Figure 1. M−S diffusivities $Đ_1$, $Đ_2$, and $Đ_{12}$, backed out from MD-simulated values of Λ_{ij}, for equimolar ($q_1 = q_2$) binary mixtures: (a) $CO_2(1)/N_2(2)$ in MFI, (b) $CH_4(1)/Ar(2)$ in BEA, (c) $Ne(1)/Ar(2)$ in CHA, and (d) $CH_4(1)/C_2H_6(2)$ in IRMOF-1. The x-axis is the total mixture loading $q_t = q_1 + q_2$. Also plotted are the MD simulation data for the corresponding unary diffusivities.

$$Đ_{ij} = Đ_{ji} \tag{3}$$

Specifically, for a binary mixture, that is $n = 2$, the M−S eq 1 can be re-written to evaluate the fluxes N_i explicitly by defining a matrix $[\Lambda]$

$$N_i = -\rho \sum_{j=1}^{n} \Lambda_{ij} \frac{q_j}{RT} \frac{d\mu_j}{dz}; \qquad i = 1, 2, \ldots, n \tag{4}$$

Combining eq 1 with 4 we derive the following explicit expression for calculation of the elements of the 2 × 2 dimensional square matrix $[\Lambda]$

$$[\Lambda] = \begin{bmatrix} \frac{1}{Đ_1} + \frac{x_2}{Đ_{12}} & -\frac{x_1}{Đ_{12}} \\ -\frac{x_2}{Đ_{12}} & \frac{1}{Đ_2} + \frac{x_1}{Đ_{12}} \end{bmatrix}^{-1} = \frac{1}{1 + \frac{x_1 Đ_2}{Đ_{12}} + \frac{x_2 Đ_1}{Đ_{12}}} \begin{bmatrix} Đ_1\left(1 + \frac{x_1 Đ_2}{Đ_{12}}\right) & \frac{x_1 Đ_1 Đ_2}{Đ_{12}} \\ \frac{x_2 Đ_1 Đ_2}{Đ_{12}} & Đ_2\left(1 + \frac{x_2 Đ_1}{Đ_{12}}\right) \end{bmatrix} \tag{5}$$

The ratios $Đ_1/Đ_{12}$, and $Đ_2/Đ_{12}$ quantify the degrees of correlation. The magnitude of $Đ_1$, relative to that of $Đ_{12}$, determines the extent to which the flux of species 1 is influenced by the chemical potential gradient of species 2. The larger the degree of correlation, $Đ_1/Đ_{12}$, the stronger is the influence of diffusional "coupling". Generally speaking, the more-strongly-adsorbed-tardier partner species will have the effect of slowing down the less-strongly-adsorbed-more-mobile partner in the mixture.

The elements of $[\Lambda]$ cannot be determined directly from experimental measurements. However, Λ_{ij} are directly accessible from molecular dynamics (MD) simulations[22] by monitoring the individual molecular displacements

$$\Lambda_{ij} = \frac{1}{2} \lim_{\Delta t \to \infty} \frac{1}{n_j} \frac{1}{\Delta t} \left\langle \left(\sum_{l=1}^{n_i} (\mathbf{r}_{l,i}(t + \Delta t) - \mathbf{r}_{l,i}(t)) \right) \times \left(\sum_{k=1}^{n_j} (\mathbf{r}_{k,j}(t + \Delta t) - \mathbf{r}_{k,j}(t)) \right) \right\rangle \tag{6}$$

In this expression, n_i and n_j represent the number of molecules of species i and j, respectively, and $\mathbf{r}_{l,i}(t)$ is the position of molecule l of species i at any time t. The three M−S diffusivities $Đ_1$, $Đ_2$, and $Đ_{12}$ can be backed out from the MD-simulated values of Λ_{ij} for the binary mixture; detailed procedures are provided in the Supporting Information

DOI: 10.1021/acsomega.8b02465
ACS Omega 2018, 3, 15743−15753

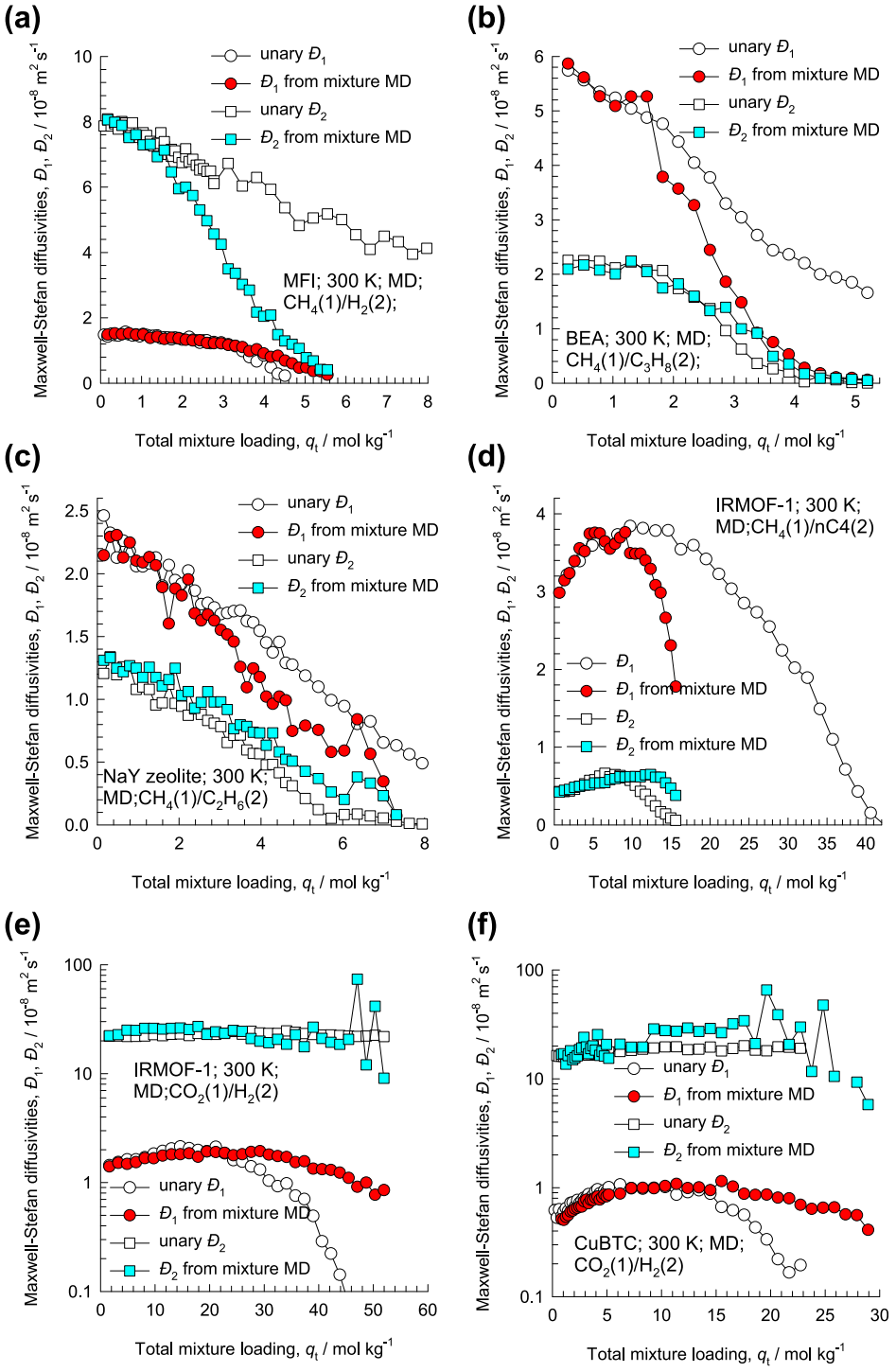

Figure 2. M−S diffusivities $Đ_1$ and $Đ_2$, backed out from MD-simulated values of $Λ_{ij}$, for equimolar ($q_1 = q_2$) binary mixtures: (a) $CH_4(1)/H_2(2)$ in MFI, (b) $CH_4(1)/C_3H_8(2)$ in BEA, (c) $CH_4(1)/C_2H_6(2)$ in NaY zeolite, (d) $CH_4(1)/nC_4H_{10}(2)$ in IRMOF-1, (e) $CO_2(1)/H_2(2)$ in IRMOF-1, and (f) $CO_2(1)/H_2(2)$ in CuBTC. The *x*-axis is the total mixture loading $q_t = q_1 + q_2$. Also plotted are the MD simulation data for the corresponding unary diffusivities.

accompanying this publication. As illustration, Figure 1 presents the M−S diffusivities for four different mixture/host combinations: CO_2/N_2 in MFI, CH_4/Ar in BEA, Ne/Ar in CHA, and CH_4/C_2H_6 in IRMOF-1. It is noteworthy that the M−S diffusivities are not constant but vary with the total mixture loading $q_t = q_1 + q_2$.

Formally speaking, the M−S eqs 1 and 4 serve only to define the M−S diffusivities $Đ_1$, $Đ_2$, and $Đ_{12}$; for practical applications, we need reliable procedures for estimation of these diffusivities. An important, persuasive advantage of the M−S formulation is that the M−S diffusivities $Đ_1$ and $Đ_2$ for mixture diffusion may be identified with the corresponding M−S diffusivities for unary diffusion that are more easily accessible from either experiments or MD simulations.[23] To test this hypothesis, the MD-simulated values of the unary diffusivities are also plotted in Figure 1. For the four sets,

DOI: 10.1021/acsomega.8b02465
ACS Omega 2018, 3, 15743−15753

there is reasonably good agreement between the unary diffusivities and the corresponding values in the mixture.

For binary mixtures of guest constituents that have significantly large differences in saturation capacities, the agreement between the M−S diffusivities in the mixture is not as good as portrayed in Figure 1, especially as pore saturation conditions are approached. This is evidenced by the data presented in Figure 2 for CH_4/H_2 in MFI, CH_4/C_3H_8 in BEA, CH_4/C_2H_6 in NaY zeolite, CH_4/nC_4H_{10} in IRMOF-1, CO_2/H_2 in IRMOF-1, and CO_2/H_2 in CuBTC. The departures between two sets of data on the M−S diffusivities $Đ_1$ and $Đ_2$ plotted in Figure 2 stem from the fact that the comparisons on the basis of total molar loadings are not based on a sound fundamental footing, as we shall demonstrate in this article.

This article has fourfold objectives. First, using the ideal adsorbed solution theory (IAST) of Myers and Prausnitz,[24] we develop arguments to demonstrate that comparisons of the diffusivities in the mixture with the constituent unary diffusivities need to be based on equality of spreading pressures, and not the total molar loadings. Second, we derive an expression for the occupancy, θ, as a function of the spreading pressure; the derived θ serves as a convenient and practical proxy for the spreading pressures, and is the appropriate parameter to be used as x-axes in Figures 1 and 2. The third objective is to show that unary M−S diffusivities, $Đ_1$ and $Đ_2$, when compared at the same occupancy θ are in good agreement with those determined from the MD simulations for binary mixtures, not just for the data in Figures 1 and 2 but for a wide variety of guest mixtures (H_2/CO_2, Ne/CO_2, CH_4/CO_2, CO_2/N_2, H_2/CH_4, H_2/Ar, CH_4/Ar, Ar/Kr, Ne/Ar, CH_4/C_2H_6, CH_4/C_3H_8, $C_2H_6C_3H_8$, CH_4/nC_4H_{10}, and CH_4/nC_5H_{11}) in zeolites (MFI, BEA, ISV, FAU (all-silica), NaY, NaX, LTA, CHA, DDR) and MOFs (IRMOF-1, CuBTC, MgMOF-74). The fourth objective is to show that degrees of correlations, $Đ_1/Đ_{12}$, and $Đ_2/Đ_{12}$, are linearly dependent on the occupancy θ.

The Supporting Information accompanying this publication provides (a) structural details for zeolites and MOFs considered and analyzed in this article, (b) configurational-bias Monte Carlo (CBMC) simulation methodology,[23,25,26] (c) MD simulation methodology,[23] (d) CBMC simulation data of the unary adsorption isotherms, along with dual-Langmuir−Freundlich data fits, (e) detailed derivation of the IAST calculation procedures for the spreading pressure, and its proxy θ, using the unary adsorption isotherms determined from CBMC simulations, (f) MD simulation data sets for unary and binary mixture diffusion for each mixture/host combination (a total of 70 data sets), and (g) procedures for estimation of the degrees of correlation for mixture diffusion.

2. THERMODYNAMICS OF MIXTURE ADSORPTION

The thermodynamics of mixture adsorption has an important bearing on the diffusion characteristics within microporous crystalline host materials because the guest constituent molecules exist entirely in the adsorbed phase. The Gibbs adsorption equation[3] in differential form is[27,28]

$$A\, d\pi = \sum_{i=1}^{n} q_i\, d\mu_i \tag{7}$$

In eq 7, A represents the surface area per kg of framework, q_i is the molar loading, μ_i is the molar chemical potential, and π is the spreading pressure.

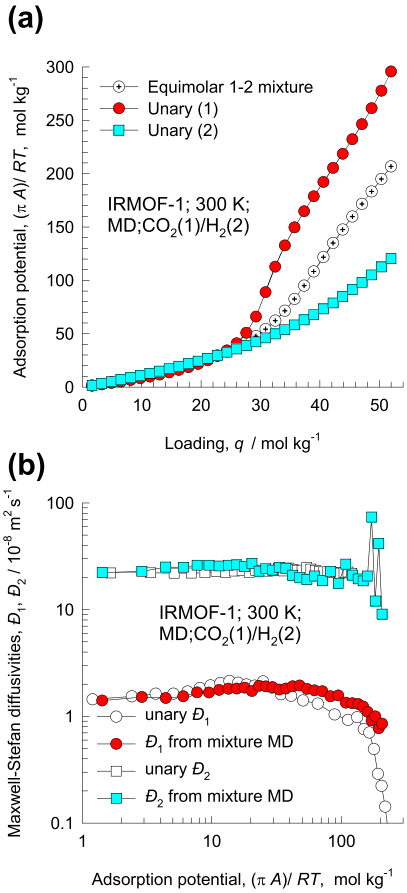

Figure 3. (a) Adsorption potential plotted as a function of the molar loading for equimolar ($q_1 = q_2$) binary $CO_2(1)/H_2(2)$ mixtures in IRMOF-1 at 300 K. (b) Comparison of the unary M−S diffusivities $Đ_1$ and $Đ_2$ with those backed out from mixture MD simulations, plotted as a function of the adsorption potential.

At phase equilibrium, equating the component chemical potentials, μ_i, in the adsorbed phase and in the bulk fluid phase mixture, we write

$$d\mu_i = RT\, d\ln f_i \tag{8}$$

Briefly, the basic equation of IAST of Myers and Prausnitz[24] is the analogue of Raoult's law for vapor−liquid equilibrium, that is

$$f_i = P_i^0 x_i; \qquad i = 1, 2, \ldots, n \tag{9}$$

where x_i is the mole fraction in the adsorbed phase defined by eq 2, and P_i^0 is the pressure for sorption of every component i, which yields the same spreading pressure, π, for each of the pure components, as that for the mixture

$$\frac{\pi A}{RT} = \int_0^{P_1^0} \frac{q_1^0(f)}{f}\, df = \int_0^{P_2^0} \frac{q_2^0(f)}{f}\, df = \int_0^{P_3^0} \frac{q_3^0(f)}{f}\, df = \ldots \tag{10}$$

where $q_i^0(f)$ is the pure component adsorption isotherm. The units of $\frac{\pi A}{RT}$, also called the adsorption potential,[29] are mol kg^{-1}. Eq 10 suggests that the fundamentally correct procedure for comparing the unary M−S diffusivities and those representing the mixture diffusion characteristics must be

DOI: 10.1021/acsomega.8b02465
ACS Omega 2018, 3, 15743−15753

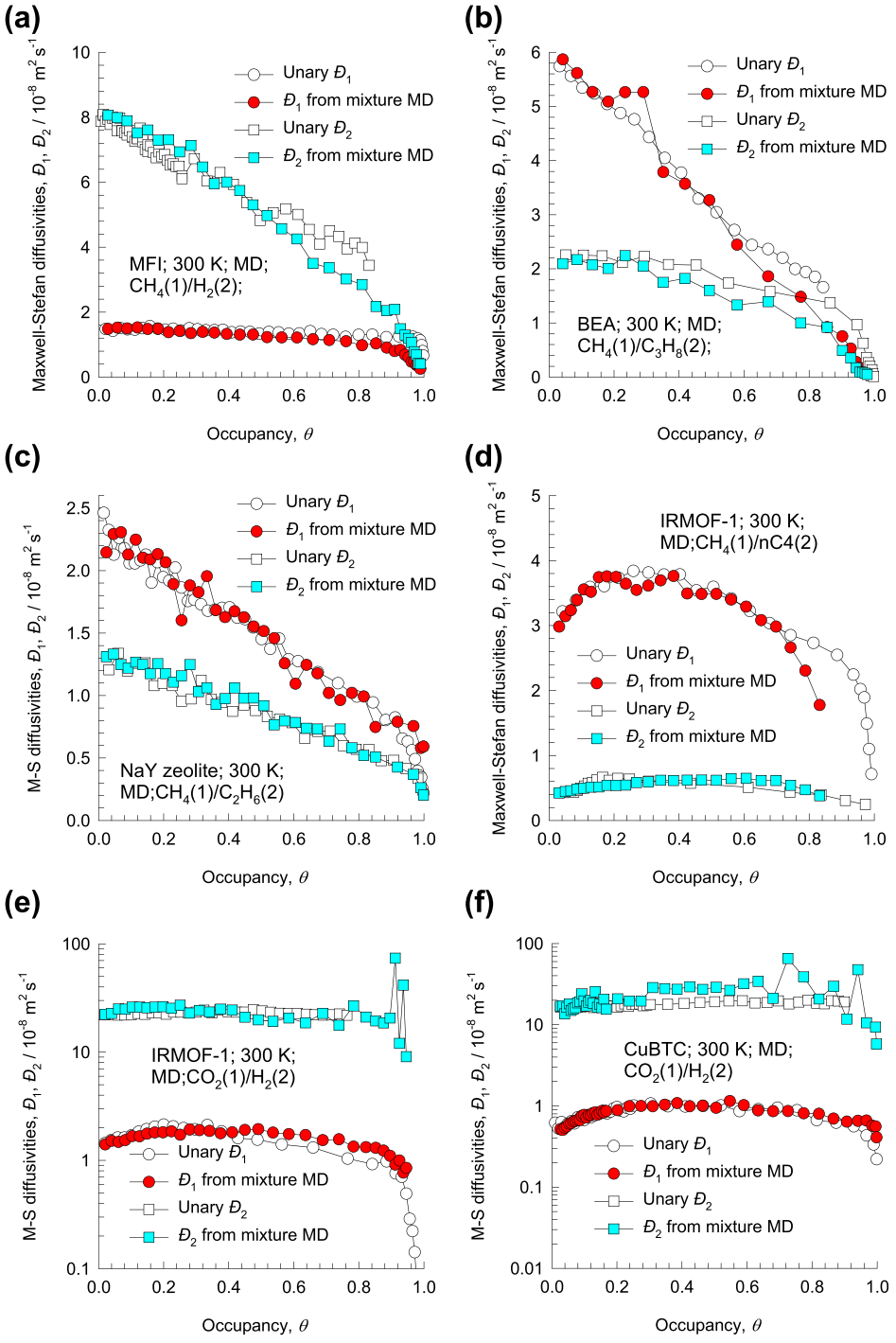

Figure 4. M−S diffusivities $Đ_1$ and $Đ_2$ backed out from MD-simulated values of Λ_{ij}, for equimolar ($q_1 = q_2$) binary mixtures: (a) $CH_4(1)/H_2(2)$ in MFI, (b) $CH_4(1)/C_3H_8(2)$ in BEA, (c) $CH_4(1)/C_2H_6(2)$ in NaY zeolite, (d) $CH_4(1)/nC_4H_{10}(2)$ in IRMOF-1, (e) $CO_2(1)/H_2(2)$ in IRMOF-1, and (f) $CO_2(1)/H_2(2)$ in CuBTC. The x-axis is the occupancy θ defined by eq 15.

done on the basis of equal adsorption potentials, that is a proxy for the spreading pressure.

For the simplest scenario in which the binary mixture is made up of components, whose unary isotherms are described by the 1-site Langmuir isotherm, with equal saturation capacities

$$q_i^0(f) = q_{sat}\frac{b_i f}{1 + b_i f}; \qquad i = 1, 2 \tag{11}$$

we derive the following expression for the mixture occupancy (detailed derivations are provided in the Supporting Information)

$$\theta_{Langmuir} = \theta_1 + \theta_2 = \frac{q_1}{q_{sat}} + \frac{q_2}{q_{sat}} = 1 - \exp\left(-\frac{\pi A}{q_{sat}RT}\right) = \frac{b_1 f_1 + b_2 f_2}{1 + b_1 f_1 + b_2 f_2} \tag{12}$$

DOI: 10.1021/acsomega.8b02465
ACS Omega 2018, 3, 15743−15753

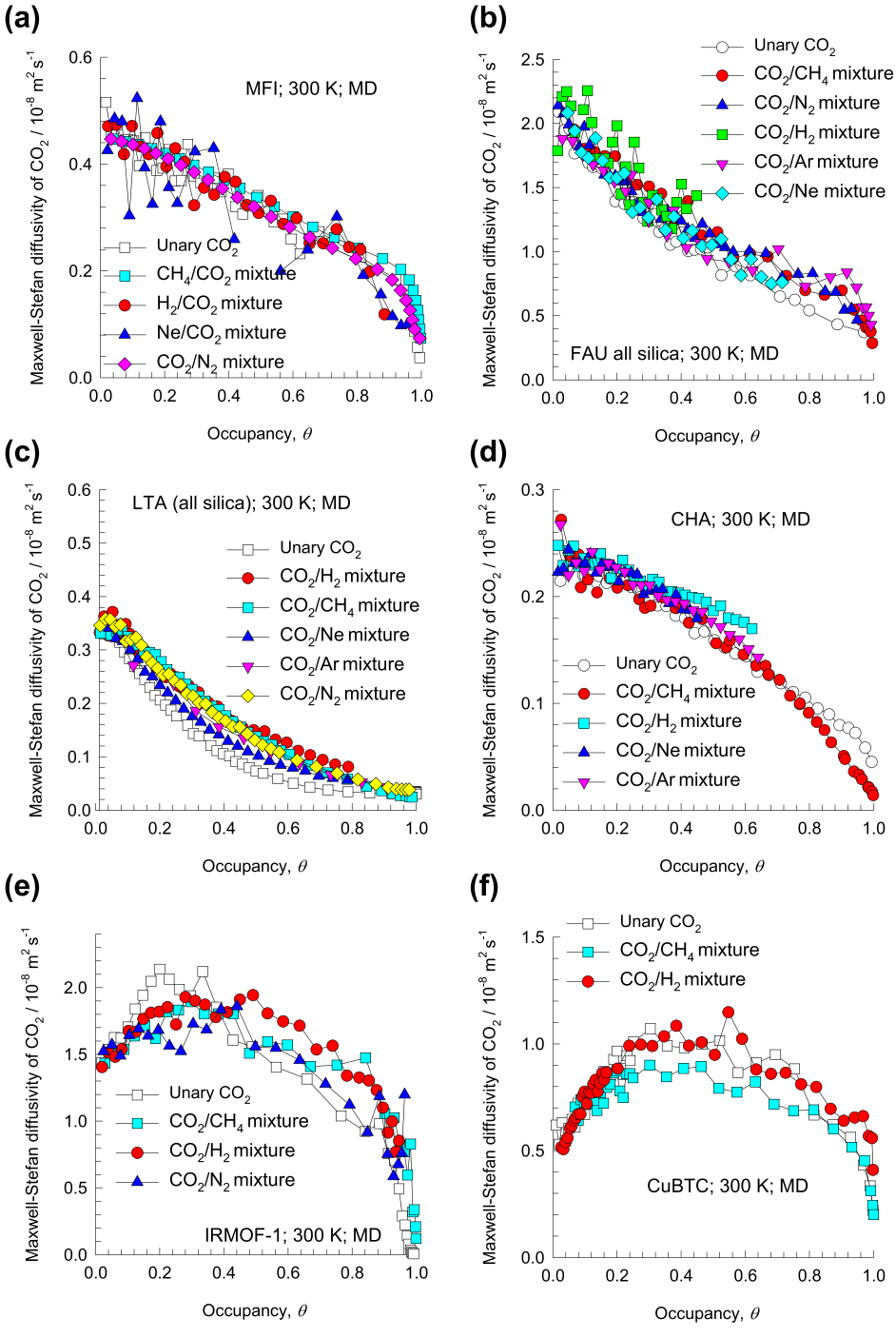

Figure 5. M−S diffusivity, $Đ_i$, of CO_2-determined MD simulation data for diffusion of a variety of equimolar ($q_1 = q_2$) binary mixtures of CO_2 and different partner species in (a) MFI, (b) FAU (all silica), (c) LTA, (d) CHA, (e) IRMOF-1, and (f) CuBTC. The x-axes represent the fractional θ defined by eq 15. Also shown in open symbols are the MD simulations of $Đ_i$ for unary CO_2 diffusion.

For each of the guest/host combinations investigated in this study, CBMC simulations[23,25,26,30] of the unary adsorption isotherms were performed in order to determine the unary isotherms. In every case, the unary isotherm characteristics required use of the more general dual-Langmuir−Freundlich model to describe the unary isotherms

$$q^0(f) = q_{A,sat}\frac{b_A f^{\nu A}}{1 + b_A f^{\nu A}} + q_{B,sat}\frac{b_B f^{\nu B}}{1 + b_B f^{\nu B}}; \qquad i = 1, 2 \tag{13}$$

The dual-site Langmuir−Freundlich model fit parameters for every guest/host combination is tabulated in the Supporting Information accompanying this publication. Analytic integration of eq 10, in conjunction with eq 13, yields

$$\frac{\pi A}{RT} = \int_{f=0}^{P_i^0}\frac{q^0(f)}{f}\,df = \frac{q_{A,sat}}{\nu_A}\ln(1 + b_A(P_i^0)^{\nu_A}) + \frac{q_{B,sat}}{\nu_B}\ln(1 + b_B(P_i^0)^{\nu_B}) \tag{14}$$

DOI: 10.1021/acsomega.8b02465
ACS Omega 2018, 3, 15743−15753

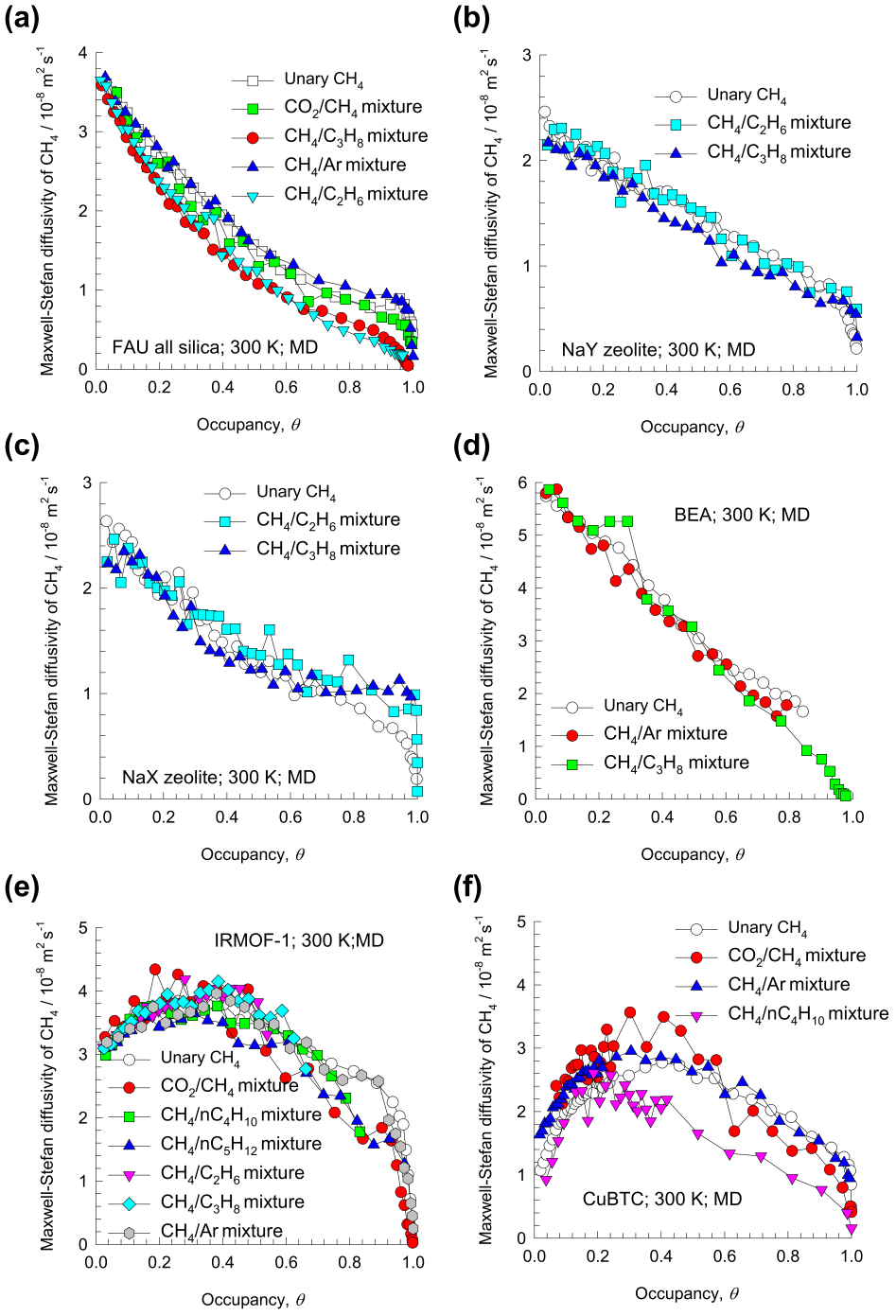

Figure 6. M−S diffusivity, $Đ_i$, of CH_4-determined MD simulation data for diffusion of a variety of equimolar ($q_1 = q_2$) binary mixtures of CH_4 and different partner species in (a) FAU (all silica), (b) NaY (48 Al), (c) NaX (86 Al), (d) BEA, (e) IRMOF-1, and (f) CuBTC. The x-axes represent the fractional θ defined by eq 15. Also shown in open symbols are the MD simulations of $Đ_i$ for unary CH_4 diffusion.

As illustration, Figure 3a presents IAST calculations of the adsorption potential plotted as a function of the molar loading for equimolar ($q_1 = q_2$) binary $CO_2(1)/H_2(2)$ mixtures in IRMOF-1 at 300 K. For molar loadings lower than 25 mol kg^{-1}, the value of $\frac{\pi A}{RT}$ is the same for each component as for the mixture. However, for molar loadings >25 mol kg^{-1}, the equality in the spreading pressures as demanded by eq 10 can only be achieved at different molar loadings of the unary components and the mixture. Indeed, if the MD data for the M−S diffusivities are plotted as a function of $\frac{\pi A}{RT}$, the two sets of M−S diffusivities are in good agreement with each other; see Figure 3b. Comparison of Figure 2e and 3b underscores the need for a proper thermodynamic comparison yardstick for diffusivities.

From Figure 3a, it is to be noted that the adsorption potential $\frac{\pi A}{RT}$ increases exponentially with the molar loading as the pores become increasingly saturated. Consequently, it is much more convenient in practice to compare the diffusivities on the basis of occupancy, θ, defined by the following generalization of eq 12

DOI: 10.1021/acsomega.8b02465
ACS Omega 2018, 3, 15743−15753

$$\theta \equiv 1 - \exp\left(-\frac{\pi A}{q_{\text{sat,mix}} RT}\right);$$
$$q_{\text{sat,mix}} = \frac{x_1}{q_{1,\text{A,sat}} + q_{1,\text{B,sat}}} + \frac{x_2}{q_{2,\text{A,sat}} + q_{2,\text{B,sat}}} \quad (15)$$

Eq 15 degenerates to eq 12 for the 1-site Langmuir isotherm; the occupancy θ is to be viewed as a convenient, and practical, proxy for the spreading pressure, π.

3. M−S DIFFUSIVITIES AS A FUNCTION OF OCCUPANCY

The same set of MD simulation data in Figure 2 are plotted in Figure 4 with the occupancy θ as x-axes. In each of the six guest/host combinations, there is much closer agreement between the unary diffusivities and those characterizing mixture diffusion. Comparisons analogous to those presented in Figure 4 are presented in the Supporting Information for 70 different mixture/host combinations. The same conclusions drawn from Figure 4 hold in most, but not all, of these cases. There are two scenarios in which the M−S diffusivity in the mixture deviates to a significant extent from the corresponding unary M−S diffusivity. For water/methanol and water/ethanol diffusion in MFI and FAU zeolites, the M−S diffusivities of either guest molecule in the mixture are significantly lower than the corresponding unary diffusivity because of the molecular clustering caused by hydrogen bonding.[31] Similar departures between unary M−S diffusivities and those characterizing mixture diffusion may also be expected for highly polar guest molecules such CHN, CH_2N_2, CH_2O, and C_2H_4O. For diffusion of CO_2-bearing mixtures in cage-type zeolites such as LTA, DDR, and ERI, CO_2 gets preferentially, and strongly, adsorbed at the narrow windows of these zeolites, hindering the diffusion of partner molecules. As a consequence, the M−S diffusivity of the partner molecule falls significantly below the corresponding value of the unary M−S diffusivity. Detailed analysis and explanation of the hindering effects caused by segregated adsorption effects are provided in earlier works.[32−34]

A further, not fully appreciated, advantage of the M−S formulation is that the M−S diffusivity of any species in a mixture is also not influenced by the choice of the partner molecules. To illustrate this, Figure 5 provides data on the M−S diffusivity of CO_2, $Đ_i$, determined from MD simulation data for diffusion of a variety of binary mixtures of CO_2 and different partner species in six different host materials (MFI, FAU, LTA, CHA, IRMOF-1, CuBTC). For any host material, we note that the diffusivity of CO_2 in a binary mixture is practically independent of the partner species. Furthermore, when compared at the same occupancy, θ, the values of $Đ_i$ are nearly the same in the mixture as those determined for unary diffusion, indicated by the open symbols in Figure 5. Similar conclusions hold for the M−S diffusivity of CH_4 in binary mixtures containing different partner species, in six different host materials (FAU, NaY, NaX, BEA, IRMOF-1, CuBTC); see Figure 6.

Figure 7 presents the data on the M−S diffusivity, $Đ_i$, of Ar determined from MD simulations for diffusion of a variety of binary mixtures of Ar and different partner species in MFI, FAU, and IRMOF-1. The M−S diffusivity of Ar is the same whether it diffuses on its own or in the presence of any other partner molecule.

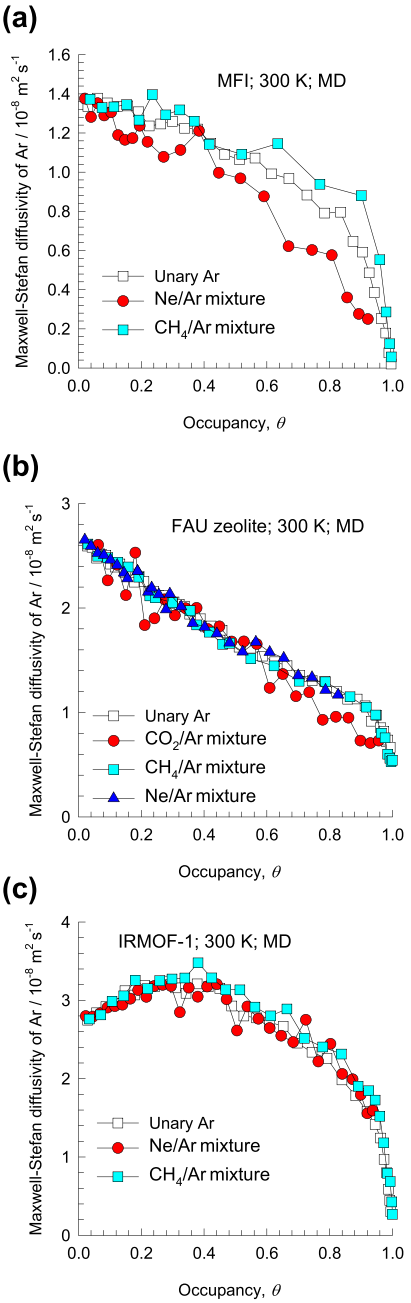

Figure 7. M−S diffusivity, $Đ_i$, of Ar-determined MD simulation data for diffusion of a variety of equimolar ($q_1 = q_2$) binary mixtures of Ar and different partner species in (a) MFI, (b) FAU-Si, and (c) IRMOF-1. The x-axes represent the fractional θ defined by eq 15. Also shown in open symbols are the MD simulations of $Đ_i$ for unary Ar diffusion.

Use of the generalized definition of occupancy θ (determined using eq 15) as a comparison metric also allows a simpler description of the occupancy dependence of the M−S diffusivities; for example, the M−S diffusivity of CO_2 in MFI, FAU, and CHA (see Figure 5a,b,d), CH_4 in FAU, NaY, NaX, and BEA zeolites (see Figure 6a−d), and Ar in FAU (see Figure 7b) conform reasonably well with a simple lattice model in which the hopping frequency of molecular jumps is proportional to the number of unoccupied sites.

$$Đ_i = Đ_i(0)(1 - \theta) \quad (16)$$

DOI: 10.1021/acsomega.8b02465
ACS Omega 2018, 3, 15743−15753

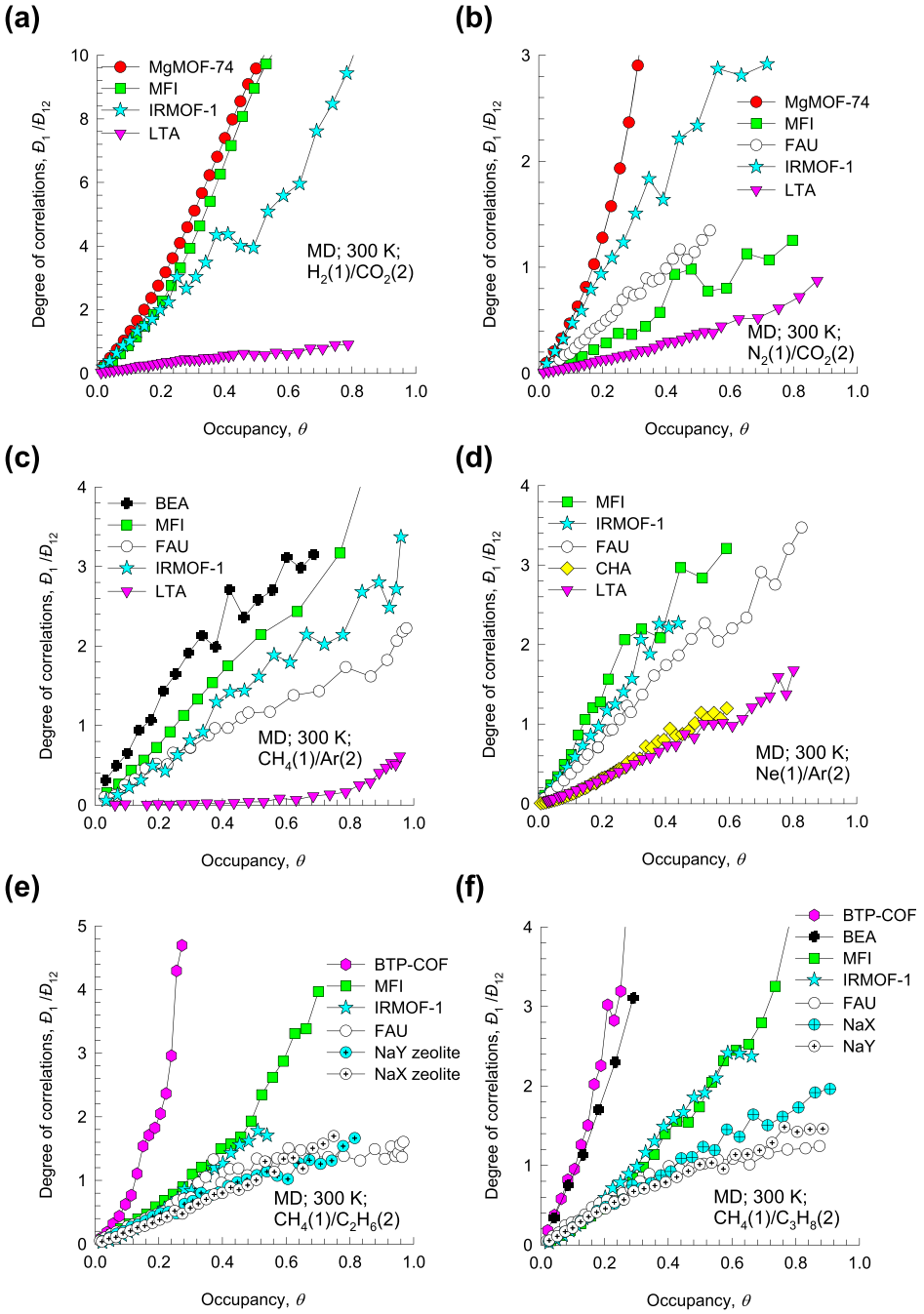

Figure 8. MD simulation data for the degree of correlations, $Đ_1/Đ_{12}$, for diffusion of equimolar ($q_1 = q_2$) binary mixtures (a) H_2/CO_2, (b) N_2/CO_2, (c) CH_4/Ar, (d) Ne/Ar, (e) CH_4/C_2H_6, and (f) CH_4/C_3H_8 at 300 K in a variety of host materials. The *x*-axes represent the fractional θ defined by eq 15. Procedures for estimation of the degrees of correlation are discussed in Chapter 10 of the Supporting Information.

The success of the simple model in these cases is directly ascribable to the fact that the occupancy defined by eq 15 takes proper account of all of the isotherm characteristics, such as inflections, that influence diffusivities.

For the other guest/host combinations, the $Đ_i$ versus θ dependences are more complicated and require models such as that of Reed and Ehrlich[35] that account for molecule–molecule interactions.[36−38]

4. DEGREE OF CORRELATIONS

Figure 8 shows MD simulation data for the degree of correlations, $Đ_1/Đ_{12}$, for diffusion of equimolar binary mixtures H_2/CO_2, N_2/CO_2, CH_4/Ar, Ne/Ar, CH_4/C_2H_6, and CH_4/C_3H_8 in a variety of host materials. For any guest/host combination, $Đ_1/Đ_{12}$ is seen to increase linearly as the pore occupancy increases; correlation effects are enhanced as the micropores become increasingly occupied. The degree of correlations is weakest in cage-type structures such as CHA, DDR, ERI, and LTA that have narrow eight-ring windows in the 3.6−4.2 Å size range. In such structures, the windows allow the intercage hopping of only one molecule at any given instant of time; consequently, the jumps are practically uncorrelated.[39] On the other hand, correlations are strongest in one-dimensional channel structures (e.g., BTP-COF, MgMOF-74, NiMOF-74), intersecting channels (e.g., MFI,

DOI: 10.1021/acsomega.8b02465
ACS Omega 2018, 3, 15743−15753

BEA, ISV), and "open" structures (e.g., IRMOF-1, CuBTC, FAU, NaY, NaX) consisting of large cages separated by wide windows.[39] Procedures for estimation of the degree of correlations are provided in the Supporting Information.

5. CONCLUSIONS

Using the IAST theory of Myers and Prausnitz,[24] a thermodynamically rigorous definition of the occupancy, θ, has been derived (see eq 15), which is a convenient proxy for the spreading pressure, π. The M−S diffusivity $Đ_i$ of any component in the mixture has the same value as that for unary diffusion if the comparison is made at the same θ. Compared at the same value of θ, the M−S diffusivity $Đ_i$ of any component in a mixture does not depend on it partner species. The $Đ_i$ versus θ dependence is amenable to simple interpretation using lattice-models such as that of Reed and Ehrlich.[35−38] The degree of correlations, $Đ_1/Đ_{12}$, exhibits a simple linear dependence on the occupancy θ, implying that correlations become increasingly important as pore saturation conditions are approached.

■ ASSOCIATED CONTENT

Supporting Information

The Supporting Information is available free of charge on the ACS Publications website at DOI: 10.1021/acsomega.8b02465.

structural details for zeolites and MOFs considered and analyzed in this article, CBMC simulation methodology,[23,25,26] MD simulation methodology,[23] CBMC simulation data of the unary adsorption isotherms, along with dual-Langmuir−Freundlich data fits, detailed derivation of the IAST calculation procedures for the spreading pressure, and its proxy θ, using the unary adsorption isotherms determined from CBMC simulations, MD simulation data sets for unary and binary mixture diffusion for each mixture/host combination (a total of 70 data sets), and procedures for estimation of the degrees of correlation for mixture diffusion (PDF)

■ AUTHOR INFORMATION

Corresponding Author

*E-mail: r.krishna@contact.uva.nl.

ORCID

Rajamani Krishna: 0000-0002-4784-8530

Notes

The author declares no competing financial interest.

■ ACKNOWLEDGMENTS

The generous assistance of Dr. Jasper van Baten, Amster-CHEM, in performing the CBMC and MD simulations is gratefully acknowledged.

■ NOMENCLATURE

Latin Alphabet

A surface area per kg of framework, $m^2\ kg^{-1}$
b_A dual-Langmuir−Freundlich constant for species i at adsorption site A, $Pa^{-\nu_i}$
b_B dual-Langmuir−Freundlich constant for species i at adsorption site B, $Pa^{-\nu_i}$
$Đ_i$ M−S diffusivity for molecule−wall interaction, $m^2\ s^{-1}$
$Đ_i(0)$ M−S diffusivity at zero-loading, $m^2\ s^{-1}$
$Đ_{12}$ M−S exchange coefficient for binary mixture, $m^2\ s^{-1}$
f_i partial fugacity of species i, Pa
f_t total fugacity of bulk fluid mixture, Pa
n number of species in the mixture, dimensionless
N_i molar flux of species i with respect to framework, mol $m^{-2}\ s^{-1}$
P_i^0 sorption pressure, Pa
q_i component molar loading of species i, mol kg^{-1}
$q_{i,sat}$ molar loading of species i at saturation, mol kg^{-1}
q_t total molar loading in mixture, mol kg^{-1}
R gas constant, 8.314 J $mol^{-1}\ K^{-1}$
T absolute temperature, K
x_i mole fraction of species i in adsorbed phase, dimensionless
z distance coordinate, m

Greek Alphabet

$[\Lambda]$ matrix of M−S diffusivities, $m^2\ s^{-1}$
μ_i molar chemical potential of component i, J mol^{-1}
π spreading pressure, N m^{-1}
θ_i fractional occupancy of component i, dimensionless
ν exponent in dual-Langmuir−Freundlich isotherm, dimensionless
ρ framework density, kg m^{-3}

Subscripts

1 referring to component 1
2 referring to component 2
i referring to component i
t referring to total mixture
sat referring to saturation conditions

■ REFERENCES

(1) Kärger, J.; Ruthven, D. M.; Theodorou, D. N. *Diffusion in Nanoporous Materials*; Wiley-VCH: Weinheim, 2012.
(2) Keil, F. J.; Krishna, R.; Coppens, M.-O. Modeling of diffusion in zeolites. *Rev. Chem. Eng.* **2000**, *16*, 71−197.
(3) Ruthven, D. M. *Principles of Adsorption and Adsorption Processes*; John Wiley: New York, 1984.
(4) Caro, J.; Noack, M. Zeolite membranes - Recent Developments and Progress. *Microporous Mesoporous Mater.* **2008**, *115*, 215−233.
(5) Caro, J. Are MOF membranes better in gas separation than those made of zeolites? *Curr. Opin. Chem. Eng.* **2011**, *1*, 77−83.
(6) Krishna, R. The Maxwell-Stefan Description of Mixture Diffusion in Nanoporous Crystalline Materials. *Microporous Mesoporous Mater.* **2014**, *185*, 30−50.
(7) Krishna, R. Describing the Diffusion of Guest Molecules inside Porous Structures. *J. Phys. Chem. C* **2009**, *113*, 19756−19781.
(8) Krishna, R. Methodologies for Screening and Selection of Crystalline Microporous Materials in Mixture Separations. *Sep. Purif. Technol.* **2018**, *194*, 281−300.
(9) Krishna, R. Diffusion in Porous Crystalline Materials. *Chem. Soc. Rev.* **2012**, *41*, 3099−3118.
(10) Hansen, N.; Krishna, R.; van Baten, J. M.; Bell, A. T.; Keil, F. J. Analysis of Diffusion Limitation in the Alkylation of Benzene over H-ZSM-5 by Combining Quantum Chemical Calculations, Molecular Simulations, and a Continuum Approach. *J. Phys. Chem. C* **2009**, *113*, 235−246.
(11) Hansen, N.; Krishna, R.; van Baten, J. M.; Bell, A. T.; Keil, F. J. Reactor simulation of benzene ethylation and ethane dehydrogenation catalyzed by ZSM-5: A multiscale approach. *Chem. Eng. Sci.* **2010**, *65*, 2472−2480.
(12) Krishna, R.; Baur, R.; van Baten, J. M. Highlighting Diffusional Coupling Effects in Zeolite Catalyzed Reactions by Combining the Maxwell-Stefan and Langmuir-Hinshelwood Formulations. *React. Chem. Eng.* **2017**, *2*, 324−336.

DOI: 10.1021/acsomega.8b02465
ACS Omega 2018, 3, 15743−15753

(13) Krishna, R. Methodologies for Evaluation of Metal-Organic Frameworks in Separation Applications. *RSC Adv.* **2015**, *5*, 52269−52295.
(14) Ruthven, D. M.; Farooq, S.; Knaebel, K. S. *Pressure Swing Adsorption*; VCH Publishers: New York, 1994.
(15) Yang, R. T. *Gas Separation by Adsorption Processes*; Butterworth: Boston, 1987.
(16) Yang, R. T. *Adsorbents: Fundamentals and Applications*; John Wiley & Sons, Inc.: Hoboken, New Jersey, 2003.
(17) Krishna, R. Tracing the Origins of Transient Overshoots for Binary Mixture Diffusion in Microporous Crystalline Materials. *Phys. Chem. Chem. Phys.* **2016**, *18*, 15482−15495.
(18) Krishna, R. A Maxwell-Stefan-Glueckauf Description of Transient Mixture Uptake in Microporous Adsorbents. *Sep. Purif. Technol.* **2018**, *191*, 392−399.
(19) Krishna, R. Using the Maxwell-Stefan formulation for highlighting the influence of interspecies (1−2) friction on binary mixture permeation across microporous and polymeric membranes. *J. Membr. Sci.* **2017**, *540*, 261−276.
(20) Bux, H.; Chmelik, C.; Krishna, R.; Caro, J. Ethene/Ethane Separation by the MOF Membrane ZIF-8: Molecular Correlation of Permeation, Adsorption, Diffusion. *J. Membr. Sci.* **2011**, *369*, 284−289.
(21) Bux, H.; Chmelik, C.; van Baten, J. M.; Krishna, R.; Caro, J. Novel MOF-Membrane for Molecular Sieving Predicted by IR-Diffusion Studies and Molecular Modeling. *Adv. Mater.* **2010**, *22*, 4741−4743.
(22) Krishna, R.; van Baten, J. M. Describing Mixture Diffusion in Microporous Materials under Conditions of Pore Saturation. *J. Phys. Chem. C* **2010**, *114*, 11557−11563.
(23) Frenkel, D.; Smit, B. *Understanding Molecular Simulations: From Algorithms to Applications*, 2nd ed.; Academic Press: San Diego, 2002.
(24) Myers, A. L.; Prausnitz, J. M. Thermodynamics of mixed-gas adsorption. *AIChE J.* **1965**, *11*, 121−127.
(25) Vlugt, T. J. H.; Krishna, R.; Smit, B. Molecular Simulations of Adsorption Isotherms for Linear and Branched Alkanes and Their Mixtures in Silicalite. *J. Phys. Chem. B* **1999**, *103*, 1102−1118.
(26) Dubbeldam, D.; Calero, S.; Vlugt, T. J. H.; Krishna, R.; Maesen, T. L. M.; Smit, B. United Atom Force Field for Alkanes in Nanoporous Materials. *J. Phys. Chem. B* **2004**, *108*, 12301−12313.
(27) Krishna, R.; van Baten, J. M.; Baur, R. Highlighting the origins and consequences of thermodynamic non-idealities in mixture separations using zeolites and metal-organic frameworks. *Microporous Mesoporous Mater.* **2018**, *267*, 274−292.
(28) Krishna, R.; van Baten, J. M. Investigating the Non-idealities in Adsorption of CO_2-bearing Mixtures in Cation-exchanged Zeolites. *Sep. Purif. Technol.* **2018**, *206*, 208−217.
(29) Siperstein, F. R.; Myers, A. L. Mixed-Gas Adsorption. *AIChE J.* **2001**, *47*, 1141−1159.
(30) García-Pérez, E.; Parra, J. B.; Ania, C. O.; García-Sánchez, A.; van Baten, J. M.; Krishna, R.; Dubbeldam, D.; Calero, S. A computational study of CO_2, N_2 and CH_4 adsorption in zeolites. *Adsorption* **2007**, *13*, 469−476.
(31) Krishna, R.; van Baten, J. M. Hydrogen Bonding Effects in Adsorption of Water−Alcohol Mixtures in Zeolites and the Consequences for the Characteristics of the Maxwell−Stefan Diffusivities. *Langmuir* **2010**, *26*, 10854−10867.
(32) Krishna, R.; van Baten, J. M. Segregation effects in adsorption of CO_2 containing mixtures and their consequences for separation selectivities in cage-type zeolites. *Sep. Purif. Technol.* **2008**, *61*, 414−423.
(33) Krishna, R.; van Baten, J. M. Onsager coefficients for binary mixture diffusion in nanopores. *Chem. Eng. Sci.* **2008**, *63*, 3120−3140.
(34) Krishna, R.; van Baten, J. M. Influence of segregated adsorption on mixture diffusion in DDR zeolite. *Chem. Phys. Lett.* **2007**, *446*, 344−349.
(35) Reed, D. A.; Ehrlich, G. Surface diffusion, atomic jump rates and thermodynamics. *Surf. Sci.* **1981**, *102*, 588−609.
(36) Krishna, R.; Paschek, D.; Baur, R. Modeling the occupancy dependence of diffusivities in zeolites. *Microporous Mesoporous Mater.* **2004**, *76*, 233−246.
(37) Krishna, R.; van Baten, J. M. A molecular dynamics investigation of a variety of influences of temperature on diffusion in zeolites. *Microporous Mesoporous Mater.* **2009**, *125*, 126−134.
(38) Krishna, R. The Maxwell-Stefan Description of Mixture Permeation across Nanoporous Graphene Membranes. *Chem. Eng. Res. Des.* **2018**, *133*, 316−325.
(39) Krishna, R.; van Baten, J. M. Investigating the Influence of Diffusional Coupling on Mixture Permeation across Porous Membranes. *J. Membr. Sci.* **2013**, *430*, 113−128.

DOI: 10.1021/acsomega.8b02465
ACS Omega 2018, 3, 15743−15753

The Occupancy Dependency of Maxwell-Stefan Diffusivities in Ordered Crystalline Micro-porous Materials

Rajamani Krishna*

Van 't Hoff Institute for Molecular Sciences

University of Amsterdam

Science Park 904

1098 XH Amsterdam, The Netherlands

email: r.krishna@contact.uva.nl

Table of Contents

1 Preamble

The Supporting Information accompanying our article *The Occupancy Dependency of Maxwell-Stefan Diffusivities in Ordered Crystalline Micro-porous Materials* provides (a) structural details for zeolites and MOFs considered and analyzed in this article, (b) Configurational-Bias Monte Carlo (CBMC) simulation methodology, (c) MD simulation methodology, (d) Configurational-Bias Monte Carlo (CBMC) simulation data of the unary adsorption isotherms, and dual-Langmuir-Freundlich data fits, (e) detailed derivation of the IAST calculation procedures for the spreading pressure, and its proxy θ, using the unary adsorption isotherms determined from CBMC simulations, (f) MD simulation data sets for unary and binary mixture diffusion for each mixture/host combination (a total of 70 data sets), and procedures for estimation of the degrees of correlation for mixture diffusion.

For ease of reading, the Supporting Information is written as a stand-alone document; as a consequence, there is some overlap of material with the main manuscript.

2 Structural details of microporous crystalline materials

A wide variety of ordered crystalline porous materials is used in several applications in separation applications.[1-4] These include zeolites (crystalline aluminosilicates), carbon nanotubes (CNTs), metal-organic frameworks (MOFs), zeolitic imidazolate frameworks (ZIFs), covalent organic frameworks (COFs), periodic mesoporous organosilicas organosilicas (PMOs), SBA-16, and MCM-41. The characteristic pore dimensions of these structures are either in the *micro*-porous (d_p < 2 nm), or *meso*-porous ranges (2 nm < d_p < 50 nm).

A number of different channel topologies and connectivities are encountered in zeolites, MOFs, COFs, and ZIFs; these can be divided into five broad classes;

1. One-dimensional (1D) channels (e.g. AFI, LTL, TON, MTW, Co-BDP, $Fe_2(BDP)_3$, MgMOF-74, NiMOF-74, Zn-MOF-74, MIL-47, MIL-53(Cr), BTP-COF); see Figure S2-1.
2. 1D channels with side pockets (e.g. MOR, FER); see Figure S2-2.
3. Intersecting channels (e.g. MFI, ISV, BEA, BOG, Zn(bdc)dabco, Co(bdc)dabco); see Figure S2-3
4. Cages separated by narrow windows (e.g. LTA (all-silica), LTA-4A, LTA-5A, CHA, DDR, ERI, TSC, ZIF-8); see Figure S2-4.
5. Cavities with large windows (e.g. FAU (all-silica), NaY, NaX, IRMOF-1, CuBTC, MOF-177); see Figure S2-5.

The crystallographic data are available on the zeolite atlas website of the International Zeolite Association (IZA).[5, 6] Further details on the structure, landscape, pore dimensions of a very wide variety of micro-porous materials are available in the published literature.[7-14] Table S2-1, Table S2-2, Table S2-3, and Table S2-4 provide some salient structural information on various zeolites and MOFs of interest.

Structural details of microporous crystalline materials

In comparison to traditionally used porous materials such as zeolites, MOFs and ZIFs offer significantly higher surface areas and porosities. This is underscored in the data presented in Figure S2-6 for surface areas, pore volumes, characteristic dimensions, and framework densities of some representative zeolites, MOFs and ZIFs. The commonly used Faujasite zeolite (FAU), for example, has a characteristic size (window aperture) of 7.4 Å, a pore volume of 0.33 cm^3/g, and a surface area of 980 m^2/g. MFI zeolite (also known as silicalite-1, and ZSM-5) has a channel dimension of 5.5 Å, pore volume of 0.165 $cm^3 g^{-1}$, and surface area of 490 $m^2 g^{-1}$. The accessible pore volumes of MOFs are commonly in the 0.5 – 2 cm^3/g range. Furthermore, significantly higher surface areas are available with MOFs; for example MOF-177 has an area of 4800 m^2/g. The pore dimensions of MOFs are also often significantly larger; MgMOF-74 has one-dimensional hexagonal-shaped channels of approximately 11 Å diameter. In the ensuing discussions, we use the terminology "open" structures to describe materials that have high pore volumes.

2.1 List of Tables for Structural details of microporous crystalline materials

Table S2-1. Salient structural information on zeolites.

Structure	Topology	Fractional pore volume, ϕ	Pore volume/ cm^3/g	Framework density/ kg/m^3
AFI	12-ring 1D channels of 7.3 Å size	0.274	0.159	1730
BEA	Intersecting channels of two sizes: 12-ring of 6.1 Å - 6.8 Å and 10-ring of 5.6 Å – 6.7 Å	0.408	0.271	1509
BOG	Intersecting channels: 12-ring 6.8 Å -7.4 Å and 10-ring of 5.6 Å - 5.8 Å	0.374	0.241	1996
CHA	316 $Å^3$ cages separated by 3.77 Å × 4.23 Å size windows	0.382	0.264	1444
DDR	277.8 $Å^3$ cages separated by 3.65 Å × 4.37 Å size windows	0.245	0.139	1760
ERI	408 $Å^3$ cages separated by 3.8 Å – 4.9 Å size windows	0.363	0.228	1595
FAU (all silica)	790 $Å^3$ cages separated by 7.4 Å size windows	0.439	0.328	1338
FER	10-ring 1D main channels of 4.2 Å -5.4 Å size, connected with 8-ring side pockets of 3.5 Å -4.8 Å size	0.283	0.160	1772
ISV	Intersecting channels of two sizes: 12-ring of 6.1 Å -6.5 Å and 12-ring of 5.9 Å - 6.6 Å	0.426	0.278	1533
ITQ-29	678 $Å^3$ cages separated by 4 Å × 4.22 Å size windows	0.405	0.283	1433
LTL	12-ring 1D channels of 7.1 Å size	0.277	0.170	1627
LTA (all silica)	743 $Å^3$ cages separated by 4.11 Å × 4.47 Å size windows	0.399	0.310	1285
LTA-4A	694 $Å^3$ cages separated by 4 Å × 4.58 Å size windows	0.38	0.25	1530
LTA-5A	702 $Å^3$ cages separated by 4 Å × 4.58 Å size windows	0.38	0.25	1508
MFI	10-ring intersecting channels of 5.4 Å – 5.5 Å and 5.4 Å – 5.6 Å size	0.297	0.165	1796
MOR	12-ring 1D main channels of 6.5 Å -7 Å size, connected with 8-ring side pockets of 2.6 Å -5.7 Å size	0.285	0.166	1715

MTW	12-ring 1D channels of 5.6 Å -6 Å size	0.215	0.111	1935
NaY	790 $Å^3$ cages separated by 7.4 Å size windows	0.41	0.303	1347
NaX	790 $Å^3$ cages separated by 7.4 Å size windows	0.40	0.280	1421
TON	10-ring 1D channels of 4.6 Å -5.7 Å size	0.190	0.097	1969

Table S2-2. Pore volumes, surface areas, and characteristic (Delaunary) dimenions for zeolites

Structure	**Pore volume** / $cm^3\ g^{-1}$	**Surface area** / $m^2\ g^{-1}$	**Delaunay diameter**/ Å
MFI	0.165	487.2	5.16
ISV	0.278	911.4	5.96
BEA	0.271	922.7	5.87
BOG	0.241	758.4	5.02
GME	0.265	717.6	7.09
LTL	0.170	520.6	7.26
MOR	0.166	416.7	7.47
FER	0.160	402.5	6.44
FAU (all silica)	0.328	1086	4.65
ITQ-12	0134	230	4.88
ITQ-29	0.283	773.3	5.69
LTA-Si	0.310	896	7.37
TSC	0.344	829	
CHA	0.264	757.5	3.98
ERI	0.228	635.3	4.10
DDR	0.139	350	4.02
AFX	0.246	674.5	3.77

Table S2-3. Salient structural information on MOFs, ZIFs, and COFs.

Structure	Topology	Fractional pore volume, ϕ	Pore volume/ cm^3/g	Framework density/ kg/m^3
CuBTC	Large cages are inter-connected by 9 Å windows of square cross-section. The large cages are also connected to tetrahedral-shaped pockets of ca. 6 Å size through triangular-shaped windows of 4.6 Å size	0.759	0.863	879
IRMOF-1	Two alternating, inter-connected, cavities of 10.9 Å and 14.3 Å with window size of 8 Å.	0.812	1.369	593
Zn(bdc)dabco	There exist two types of intersecting channels of about 7.5 Å × 7.5 Å along the x-axis and channels of 3.8 Å × 4.7 Å along y and z axes.	0.662	0.801	826
Co(bdc)dabco	There exist two types of intersecting channels of about 7.6 Å × 7.6 Å along the x-axis and channels of 3.7 Å × 5.1 Å along y and z axes.	0.648	0.796	814
MOF-177	Six diamond-shaped channels (upper) with diameter of 10.8 Å surround a pore containing eclipsed BTB^{3-} moieties.	0.840	1.968	427
Co(BDP)	1D square-shaped channels of 10 Å	0.67	0.927	721
MgMOF-74	1D hexagonal-shaped channels of 11 Å	0.708	0.782	905
NiMOF-74	1D hexagonal-shaped channels of 11 Å	0.695	0.582	1193
CoMOF-74	1D hexagonal-shaped channels of 11 Å	0.707	0.599	1180
ZnMOF-74	1D hexagonal-shaped channels of 11 Å	0.709	0.582	1219
FeMOF-74	1D hexagonal-shaped channels of 11 Å	0.705	0.626	1126
MIL-47	1D diamond-shaped channels of 8.5 Å	0.608	0.606	1004
MIL-53 (Cr)-lp	1D lozenge-shaped channels of 8.5 Å	0.539	0.518	1041
BTP-COF	1D hexagonal-shaped channels of 34 Å	0.752	1.79	420
COF-102	Cavity of size 8.9 Å	0.8	1.875	426
COF-103	Cavity of size 9.6 Å	0.82	2.040	400
COF-108	Two cavities, of sizes 15.2 Å and 29.6 Å	0.93	5.467	170
ZIF-7		0.277	0.223	1241
ZIF-8	1168 $Å^3$ cages separated by 3.26 Å size windows	0.476	0.515	924

Table S2-4. Pore volumes, surface areas, and characteristic (Delaunary) dimenions for MOFs, ZIFs, and BTP-COF.

Structure	**Pore volume** / $cm^3\ g^{-1}$	**Surface area** / $m^2\ g^{-1}$	**Delaunay diameter**/ Å
IRMOF1	1.369	3522.2	7.38
CuBTC	0.848	2097.0	6.23
MIL47	0.606	1472.8	8.03
MIL53(Cr)-lp	0.518	1280.5	7.40
CoFA	0.139		3.41
MnFA	0.190		3.66
Zn(tbip)	0.118		3.96
Zn(BDC)dabco	0.801	2022.5	8.32
Co(BDC)dabco	0.796		8.35
PCN-19	0.432		7.16
ZIF-68	0.439	1066.0	7.52
ZIF-7	0.223		3.26
ZIF-8	0.515	1164.7	3.26
PCN-6prime	3.228		14.62
MOF-177	1.968	4781.0	10.1
ZnMOF-74	0.582	1176.0	9.49
MgMOF-74	0.782	1640.0	10.66
NiMOF-74	0.582	1239.0	9.80
CoMOF-74	0.599	1274.0	9.52
FeMOF-74	0.626	1277.3	11.1
Co(BDP)	0.927	2148.8	10
BeBTB	1.908	4706	
CuBTT (blocked)	0.709	1564.6	9.99
BTP-COF	1.791		34.26
$Fe_2(BDP)_3$		1230	

2.2 List of Figures for Structural details of microporous crystalline materials

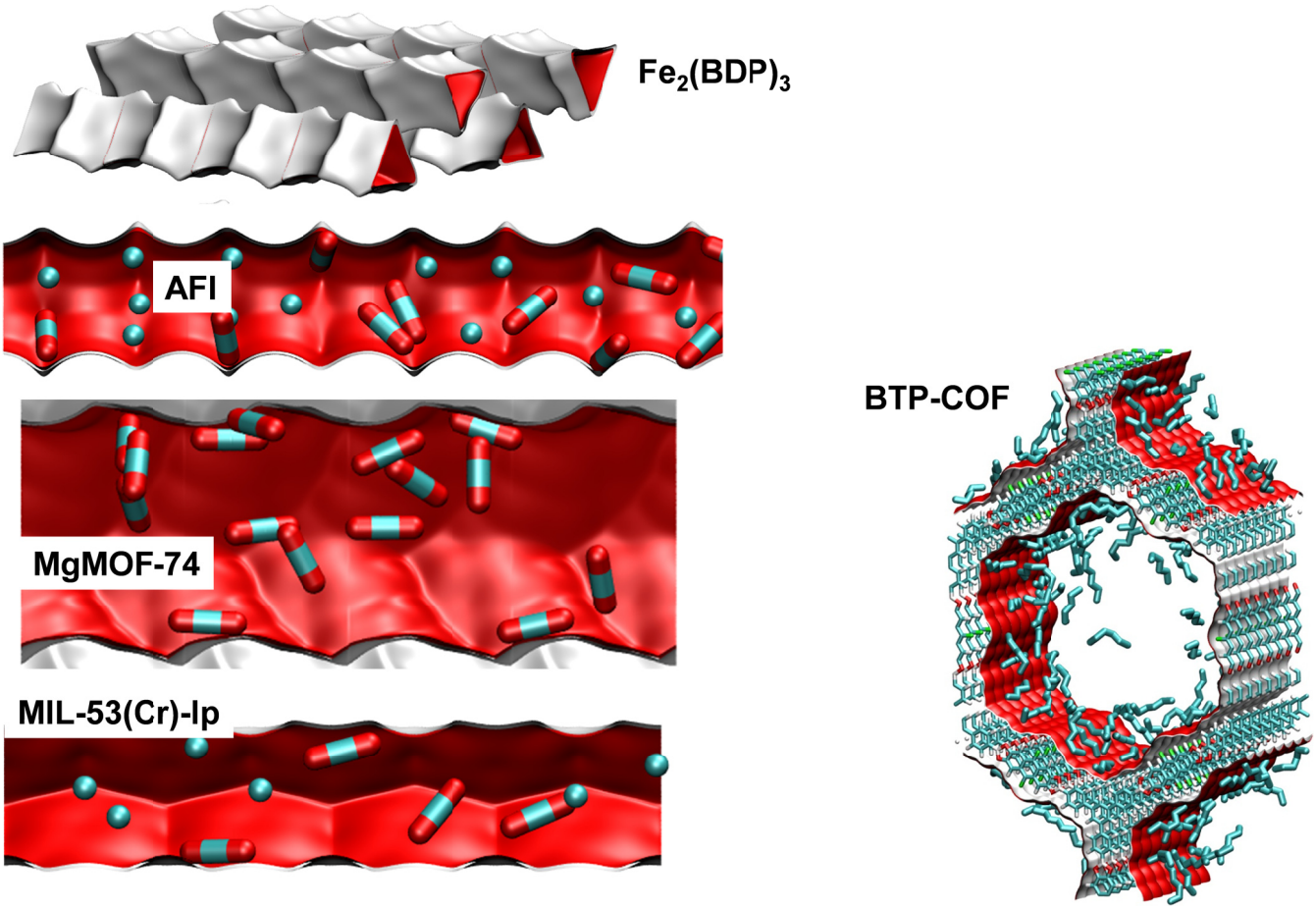

Figure S2-1. Examples of one-dimensional (1D) channel structures: AFI, MgMOF-74, and MIL-53(Cr)-lp, BTP-COF, and $Fe_2(BDP)_3$.

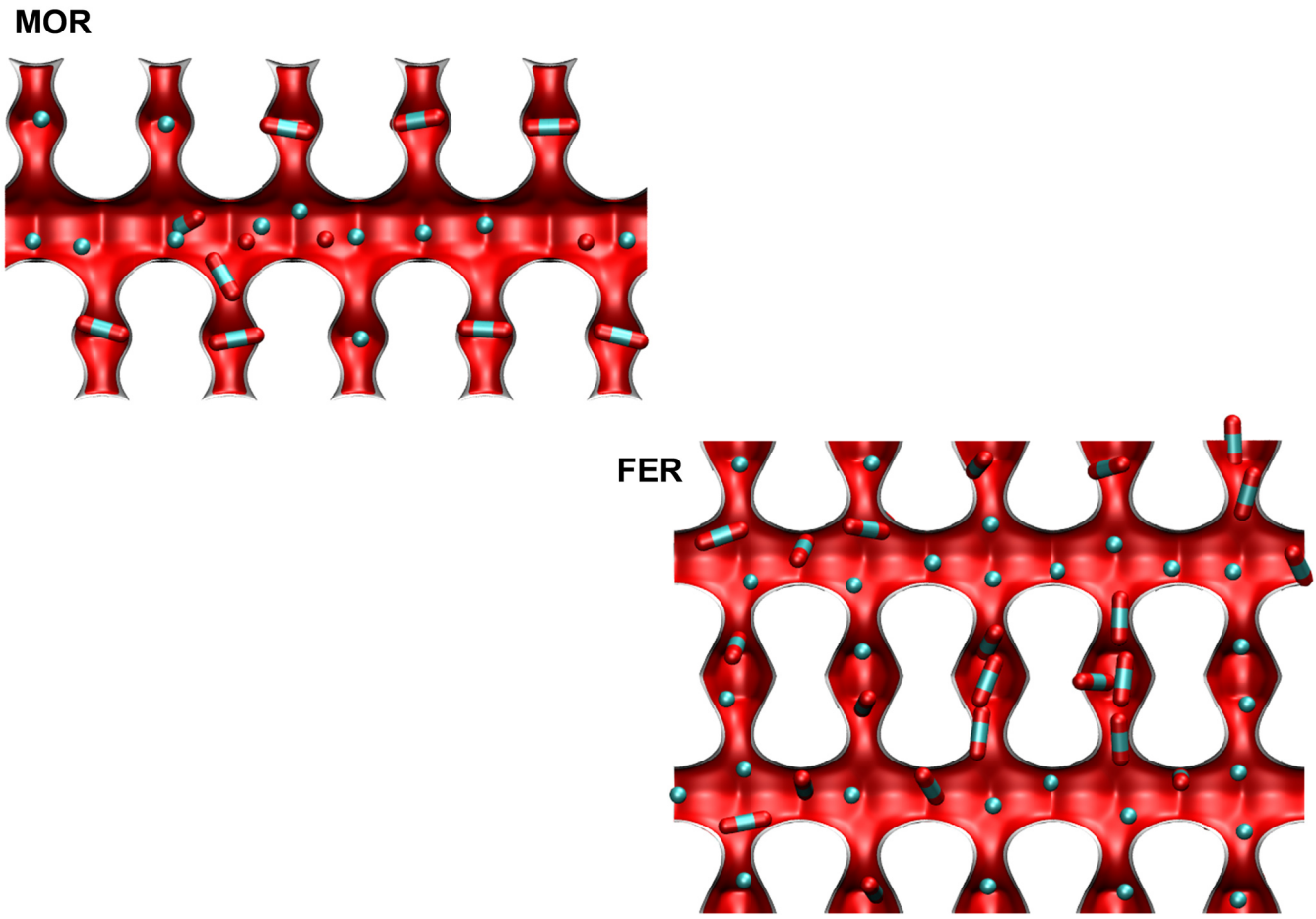

Figure S2-2. Examples of 1D channel structures with side pockets: MOR and FER.

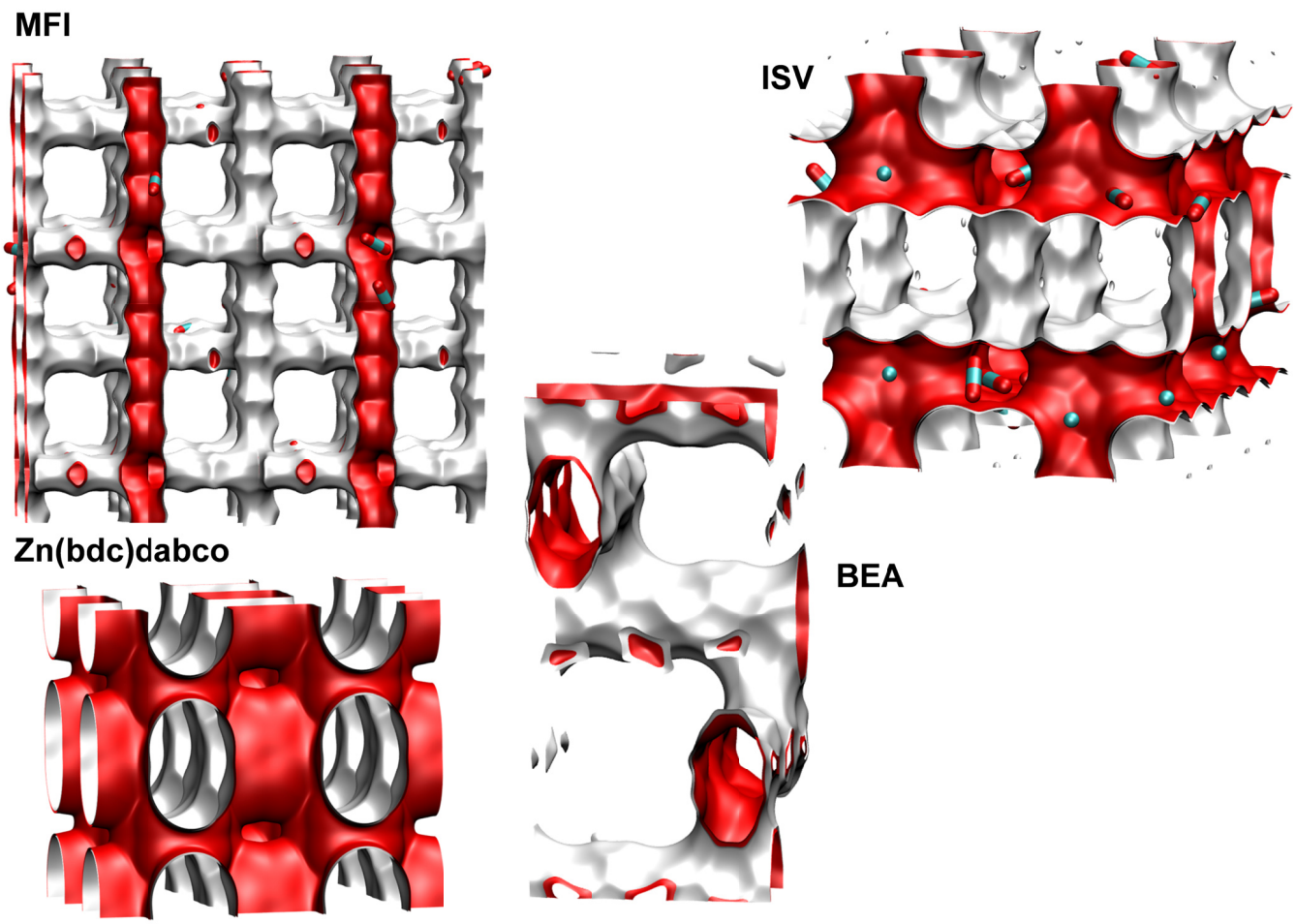

Figure S2-3. Examples of structures consisting of intersecting channels: MFI, ISV, BEA, and Zn(bdc)dabco.

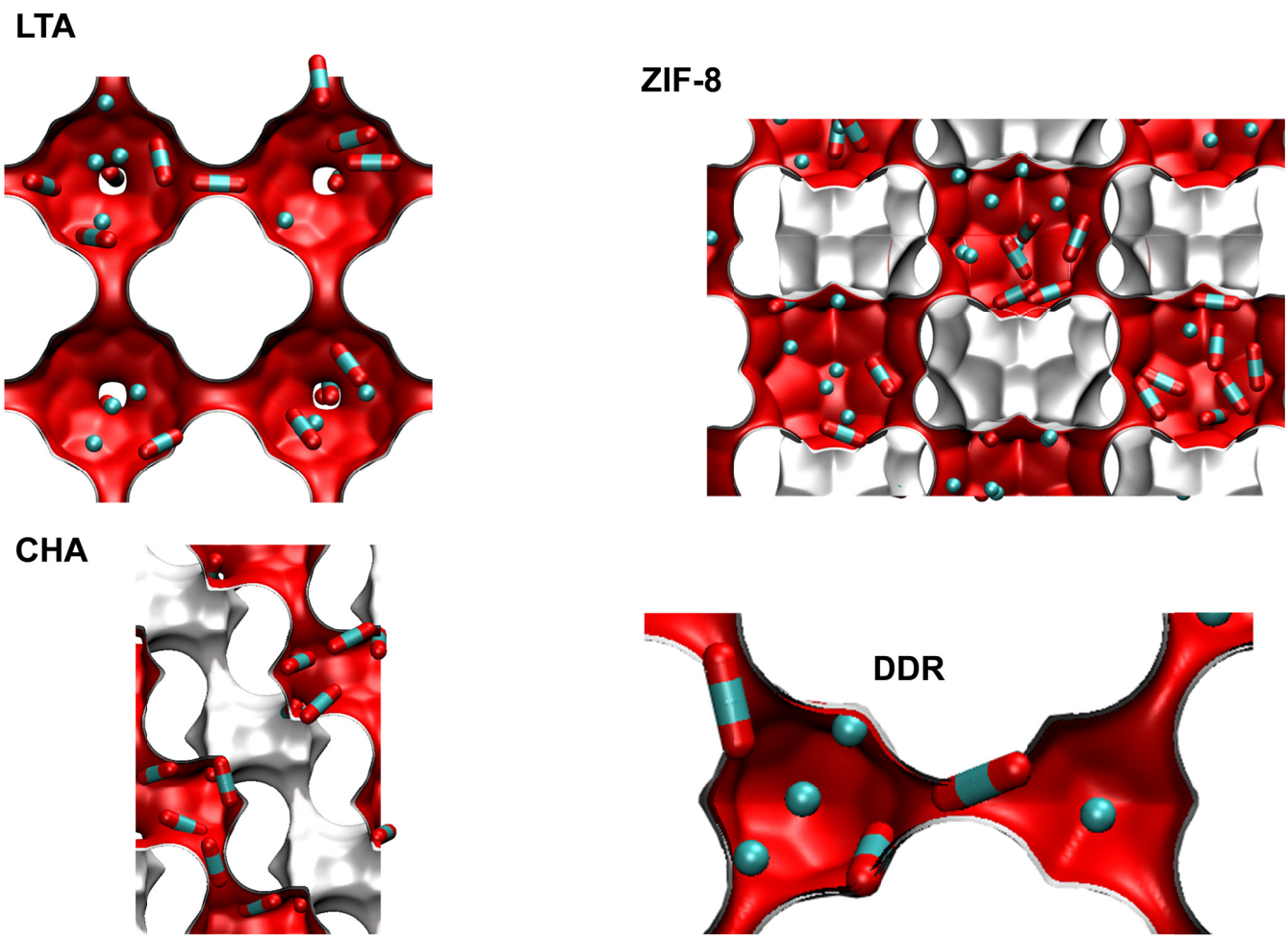

Figure S2-4. Structures consisting of cages separated by narrow windows: LTA, CHA, DDR, and ZIF-8.

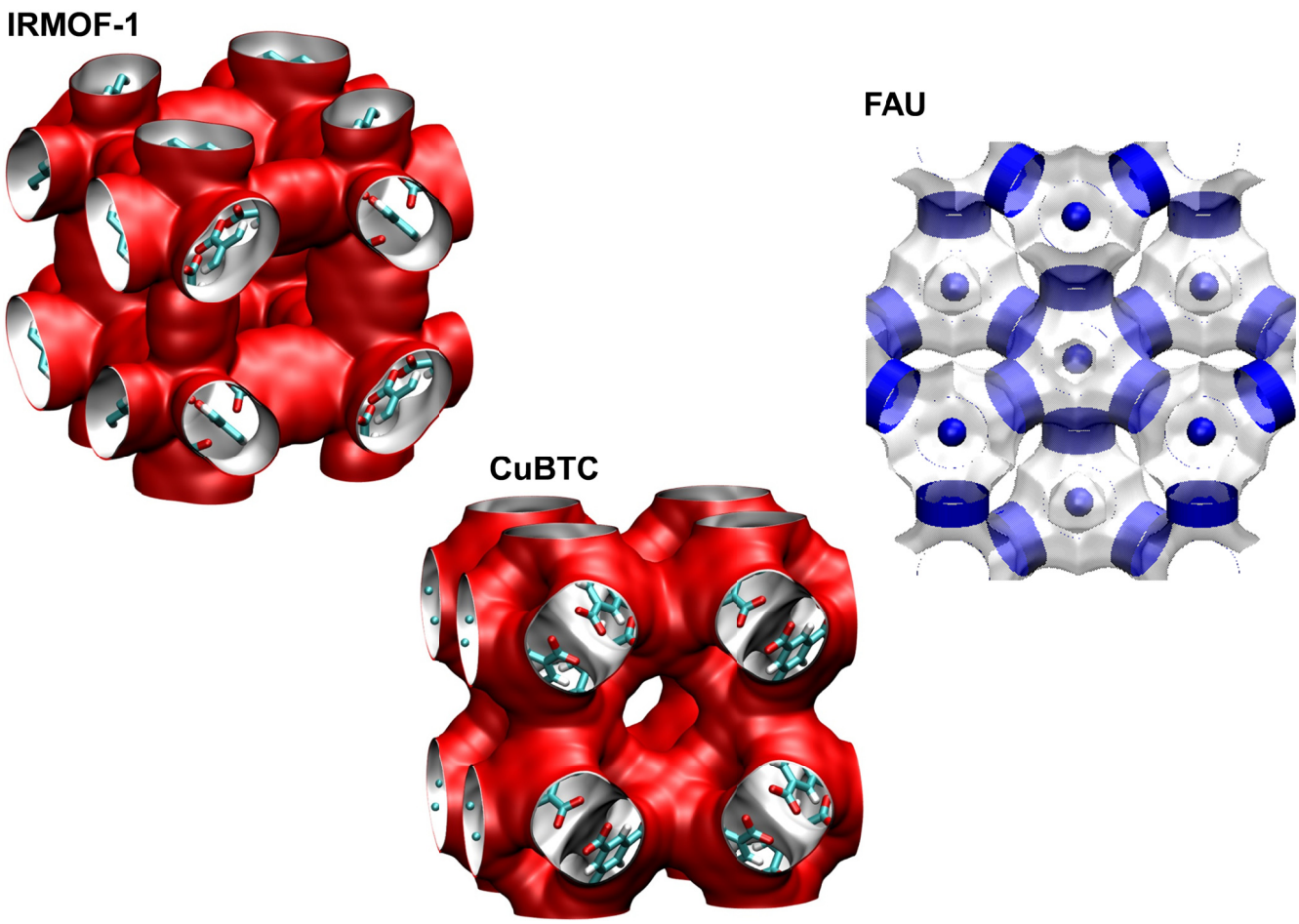

Figure S2-5. "Open" structures that consist of cages separated by large windows: IRMOF-1, CuBTC, and FAU.

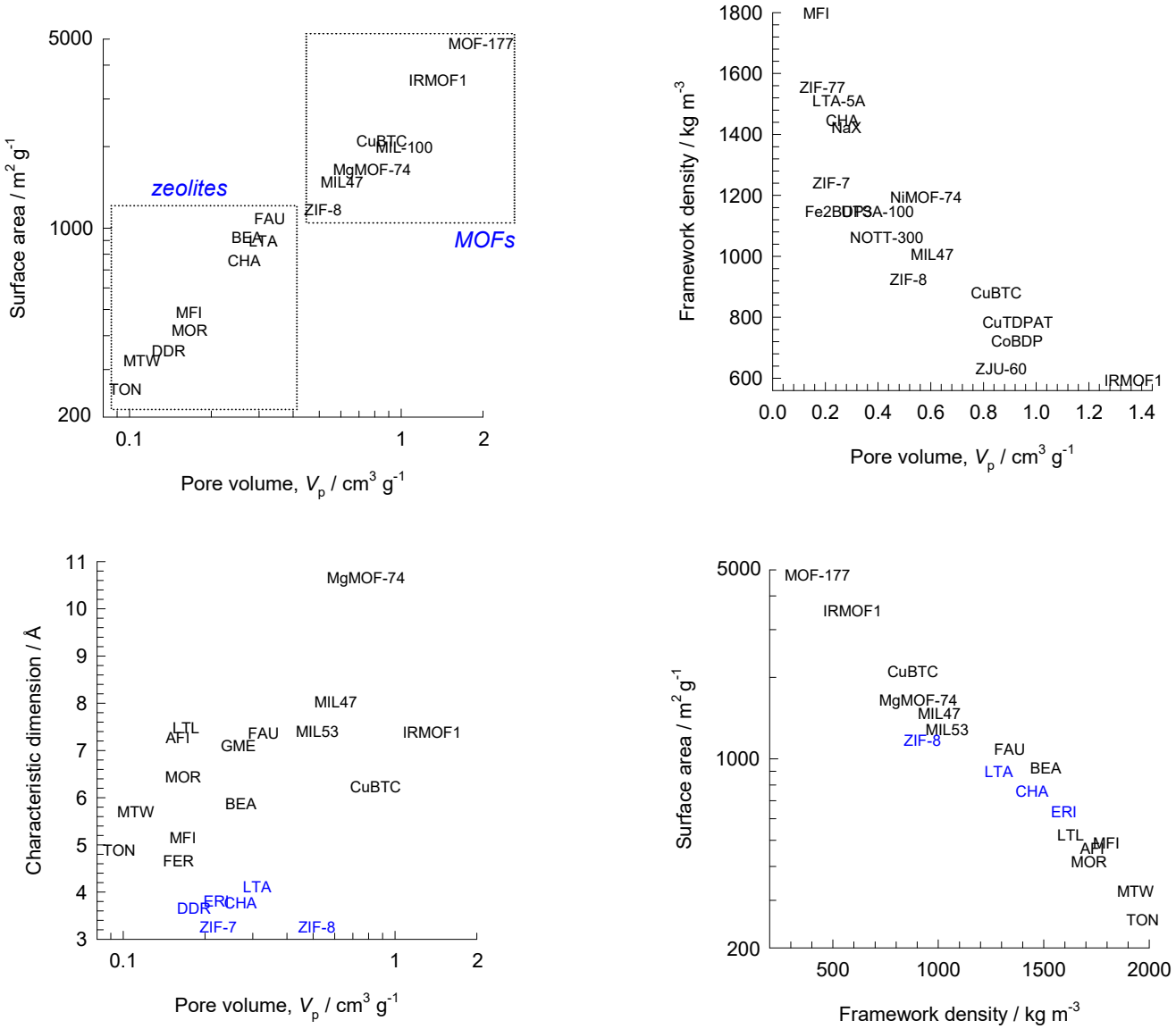

Figure S2-6. Comparison of surface area, pore volumes, framework densities, fractional pore volumes, and characteristic dimensions of some representative zeolites, MOFs and ZIFs.

3 Configurational-Bias Monte Carlo Simulation Methodology

The simulation methodologies and the force field information used are the same as detailed in the Supplementary Materials accompanying our earlier publications.[2, 3, 7, 9, 13, 15, 16] A short summary is provided hereunder.

3.1 Zeolites (all silica)

CH_4 molecules are described with a united atom model, in which each molecule is treated as a single interaction center.[17]The interaction between adsorbed molecules is described with Lennard-Jones terms. The Lennard-Jones parameters for CH_4-zeolite interactions are taken from Dubbeldam et al.[18]. The force fields for Ne and Ar are taken from the paper by Skoulidas and Sholl[19]. The force field for Kr is from Talu and Myers.[20] The Lennard-Jones parameters for CO_2-zeolite are essentially those of Makrodimitris et al.[21]; see also García-Pérez et al.[22] For simulations with linear alkanes with two or more C atoms, the beads in the chain are connected by harmonic bonding potentials. A harmonic cosine bending potential models the bond bending between three neighboring beads, a Ryckaert-Bellemans potential controls the torsion angle. The beads in a chain separated by more than three bonds interact with each other through a Lennard-Jones potential; see schematic in The force fields of Dubbeldam et al.[18] was used for the variety of potentials. The Lennard-Jones potentials are shifted and cut at 12 Å.

The zeolite frameworks were considered to be rigid in all the simulation results reported in the article.

3.2 Cation-exchanged zeolites

The following two cation-exchanged structures were investigated

NaX (106 Si, 86 Al, 86 Na^+, Si/Al=1.23)

NaY (144 Si, 48 Al, 48 Na^+, Si/Al=3)

The presence of cations reduces the accessible pore volume. The location of the cations are pictured in Figure S3-2, and Figure S3-3.

The force field information for the simulations with cations are taken from García-Sanchez et al.[23] In the MC simulations, the cations were allowed to move within the framework and both Lennard-Jones and Coulombic interactions are taken into consideration.

In the CBMC simulations both Lennard-Jones and Coulombic interactions are taken into consideration; see schematic sketch in Figure S3-4.

3.3 MOFs and ZIFs

For IRMOF-1 (= MOF 5 = $Zn_4O(BDC)_3$ with BDC^{2-} = 1-4 benzenedicarboxylate), we used the structural data published by Dubbeldam et al.[24, 25]

The structural information for CuBTC (= $Cu_3(BTC)_2$ with BTC = 1,3,5-benzenetricarboxylate) have been taken from Chui et al.[26] and Yang and Zhong.[27] The crystal structure of Chui et al. [26] includes axial oxygen atoms weakly bonded to the Cu atoms, which correspond to water ligands. Our simulations have been performed on the dry CuBTC with these oxygen atoms removed.

The structural information for Zn(bdc)dabco is from Bárcia et al.[28] and Lee et al.[29]

MIL-47 structural data was taken from Alaerts et al.,[30] Finsy et al., [31] and Barthelet et al.[32]

The structural data for MIL-53 (Cr) = $Cr(OH)(O_2C\text{-}C_6H_4\text{-}CO_2)$ was taken from Coombes et al. [33] (the simulations were carried out with the large-pore (-lp) structure).

The ZIF-8 = Zn(methylimidazole)$_2$ structure was constructed on the basis of the structural data from Banerjee et al.[34] The original structural data files (cif file) contain solvent molecules; these were removed and the solvent-free structures were considered.

The structural information on MgMOF-74 (= Mg_2(dobdc) = Mg\(dobdc) with dobdc = ($dobdc^{4-}$ = 1,4-dioxido-2,5-benzenedicarboxylate)), ZnMOF-74 (= Zn_2(dobdc) = Zn\(dobdc)), CoMOF-74 = (Co_2(dobdc) = Co\(dobdc)), NiMOF-74 = (Ni_2(dobdc) = Ni\(dobdc)), were obtained from a variety of references.[35-40]

The structural information on FeMOF-74 (= Fe_2(dobdc) = Fe\(dobdc) with dobdc = ($dobdc^{4-}$ = 1,4-dioxido-2,5-benzenedicarboxylate)) is from Bloch et al.[41]

The structural information for MOF-177 (= $Zn_4O(BTB)_2$ with (BTB^{3-} = 1,3,5-benzenetribenzoate)) is provided by Chae et al.[42]

The metal organic framework structures were considered to be rigid in the simulations. For the atoms in the host metal organic framework, the generic UFF[43] and DREIDING[44] force fields were used. The Lorentz-Berthelot mixing rules were applied for calculating σ and ε/k_B for guest-host interactions.

Simulations for CO_2 in CuBTC were carried out using the force field of Martín-Calvo et al.[45]

Simulations for CO_2 in IRMOF-1 were carried out using the force field of Walton et al.[46] and Dubbeldam et al.[25]

For CO_2 and N_2 adsorption in MOFs, the charges of the host framework need to be accounted for.

Our force field implementation for CO_2 in CuBTC correspond to those of Martín-Calvo et al.[45]

Our force field implementation for CO_2 in IRMOF-1 correspond to those of Walton et al.[46] and Dubbeldam et al.[25].

For MIL-47 (V) and MIL-53 (Cr) –lp simulations, the same CO_2-CO_2 interaction parameters were used as for zeolites and correspond to those of García-Pérez et al.[22] The charges on the host framework were taken from the works of Rosenbach et al.,[47] and Salles et al.[48]

For ZIF-8, the Lennard-Jones potentials for the framework atoms of ZIF-8 were taken from the combined works of Mayo et al.,[44] Yang and Zhong,[49] and Jorgensen et al.[50] as was reported in the computational study of Zhou et al.[51] The framework charges of ZIF-8 were estimated using the group-contribution procedure based on quantum mechanical calculations described in the paper by Xu and Zhong. [52]

The simulations for ZnMOF-74 and MgMOF-74 were carried out with the force field information provided by Yazaydin et al.[40]

3.4 Pore volume

The pore volume is determined using a simulation of a single helium molecule at the reference temperature T [53-55]

$$V_{pore} = \frac{1}{m} \int_0^{V_{pore}} \exp\left(- \frac{U(\mathbf{r})}{k_B T} \right) d\mathbf{r} \tag{3-1}$$

where U is the interaction energy between a single helium atom and the framework, and m is the mass of the framework. The pore volume can be readily computed from Monte Carlo sampling using Widom particle insertion.[56] Basically, the average Boltzmann factor associated with the random insertion of a probe molecule is computed. This value is averaged over all generated trial positions. In equation (3-1) the integration is over the entire mass of the sample and yields the value of the accessible pore volume per unit mass of the framework; the units of V_{pore} are m^3/kg, or in more commonly used units mL/(g framework). The volume fraction, ϕ, is then given by $V_{\text{pore}}/V_{\text{total}}$ where V_{total} is the total volume of the unit cell. Usually, a reference temperature of 298.15 K is chosen in experiment for determination of the helium void volume; this value is also used in the simulations.

The force field for He-He interactions are taken from Table 1 of Talu and Myers.[57] For zeolites the He-O interaction parameters were also taken from this Table 1. We should mention here that the force field for He of Talu and Myers [57] is not the same as that in Skoulidas and Sholl;[19] in particular there are significant differences in the energy parameter ε/k_B. We had earlier used the Skoulidas force field to simulate diffusion of He in a variety of zeolites.[13] For determination of the pore volume fraction we have switched to the Talu and Myers force field parameters that has been tuned to represent experimental data on pore volumes in MFI.

For MOFs, the interaction between He and the atoms of the MOF structures were then determined using the Lorentz-Berthelot mixing rules. For determination of the pore volumes the Lennard-Jones parameters for interactions of the He probe atoms with cations are also considered

For determination of the accessible pore volumes of FAU, NaX, NaY, TSC, ITQ-29, LTA, LTA-5A and LTA-4A the sodalite cages were blocked and no He probe atoms could enter these cages. Only the supercage volumes are determined for these structures.

3.5 Surface areas

The surface area of various structures were determined using the method described by Düren et al.[58].

3.6 Characteristic dimensions (Delaunay diameters)

In many cases, the characteristic size of the channels or windows of microporous structures are referred to in the article. These data are obtained following the method of Delaunay triangulation, described in the work by Foster et al.[59] These values represent the maximum hard-sphere diameter that can pass through the structure. The values quoted are obtained by substracting the Lennard-Jones sigma parameter of the framework atom.

3.7 List of Figures for Configurational-Bias Monte Carlo Simulation Methodology

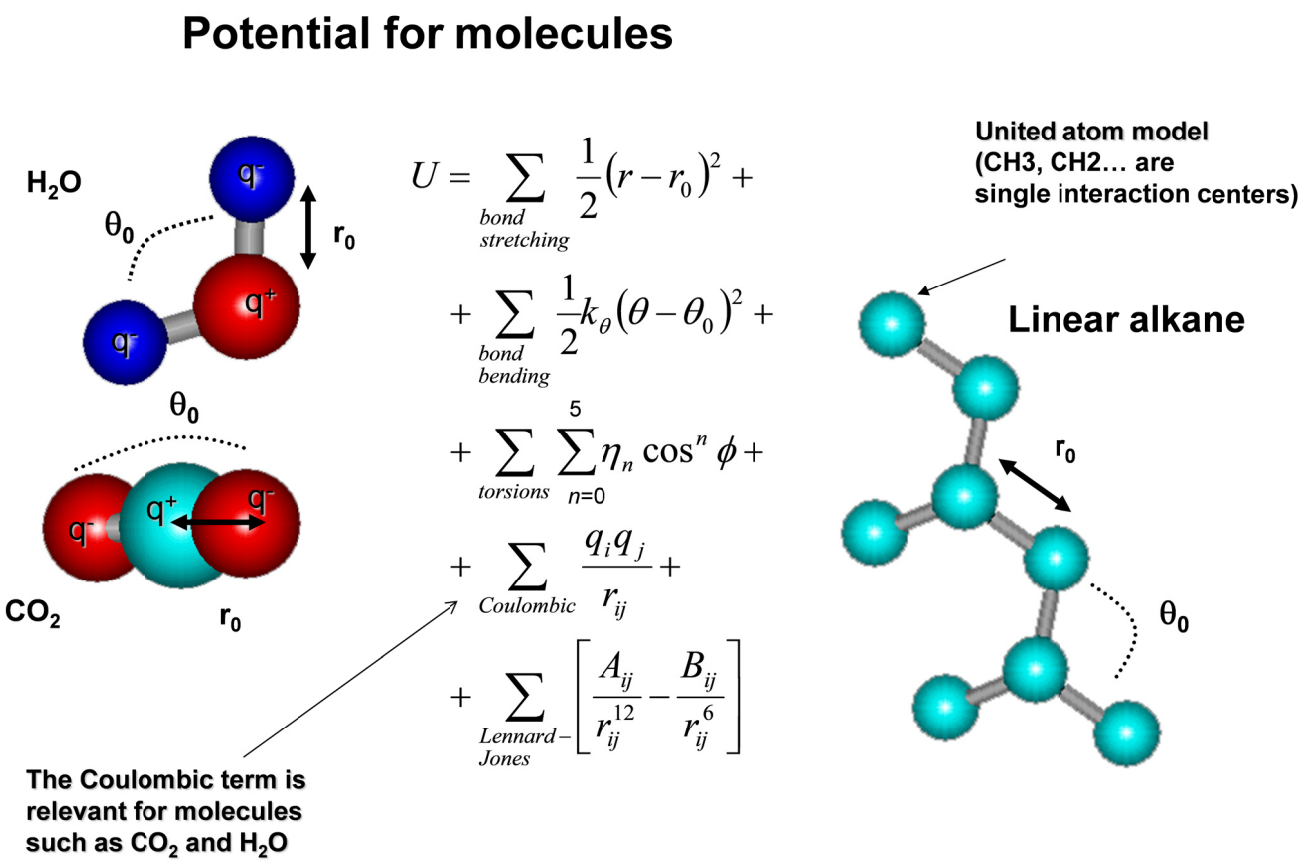

Figure S3-1. Potential for molecules.

NaX (106 Si, 86 Al, 86 Na+, Si/Al=1.23)

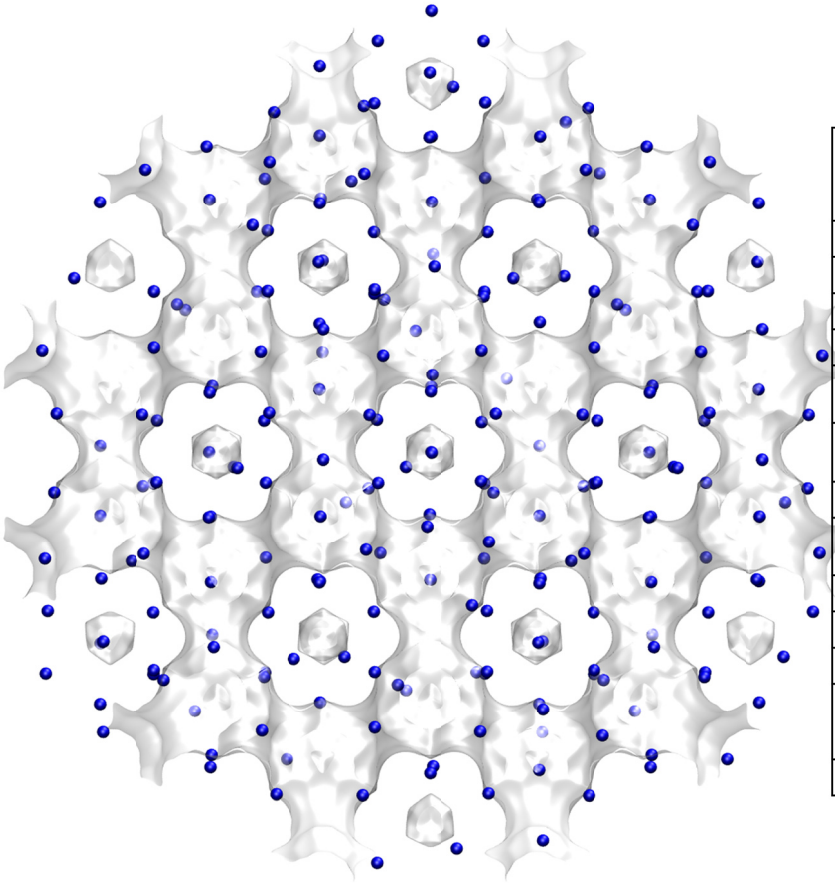

	FAU 86 Na/uc
a /Å	25.028
b /Å	25.028
c /Å	25.028
Cell volume / Å^3	15677.56
conversion factor for [mclec/uc] to [mol per kg Framework]	0.0745
conversion factor for [mclec/uc] to [kmol/m^3]	0.2658
ρ [kg/m3] (with cations)	1421.277
MW unit cell [g/mol(framework+cations)]	13418.42
ϕ, fractional pore volume	0.399
open space / Å^3/uc	6248.0
Pore volume / cm^3/g	0.280
Surface area /m^2/g	
DeLaunay diameter /Å	7.37

Figure S3-2. Location of cations for NaX zeolite (106 Si, 86 Al, 86 Na^+, Si/Al=1.23)

NaY (144 Si, 48 Al, 48 Na+, Si/Al=3)

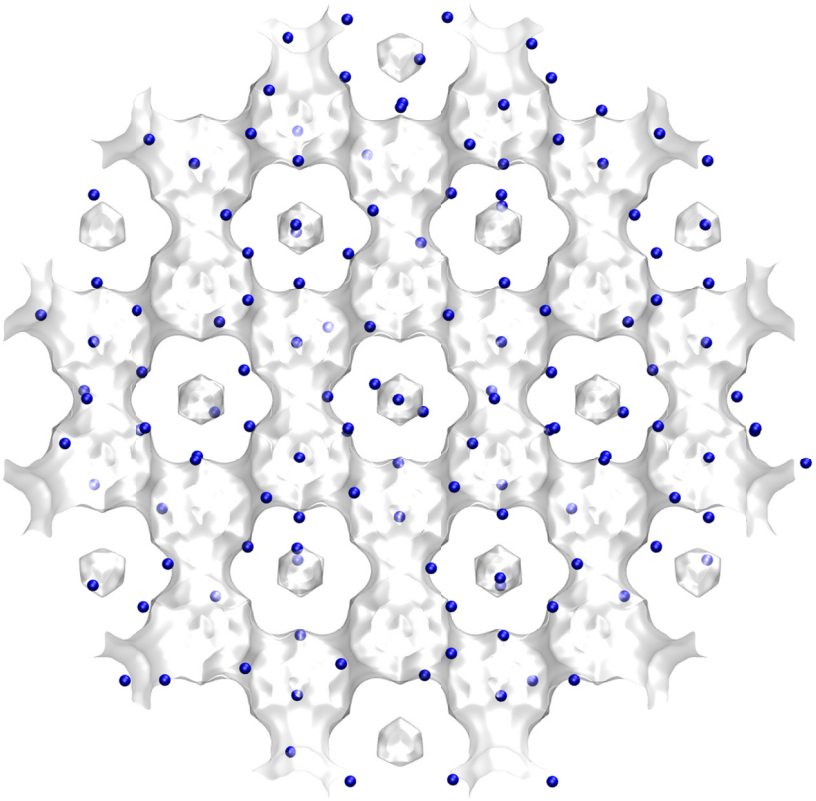

	FAU 48 Na/ucl
a /Å	25.028
b /Å	25.028
c /Å	25.028
Cell volume / Å^3	15677.56
conversion factor for [mclec/uc] to [mol per kg Framework]	0.0794
conversion factor for [mclec/uc] to [kmol/m^3]	0.2596
ρ [kg/m3] (with cations)	1333.19
MW unit cell [g/mol(framework+cations)]	12586.78
ϕ, fractional pore volume	0.408
open space / Å^3/uc	6396.6
Pore volume / cm^3/g	0.306
Surface area /m^2/g	
DeLaunay diameter /Å	7.37

Figure S3-3. Location of cations for NaY zeolite (144 Si, 48 Al, 48 Na^+, Si/Al=3)

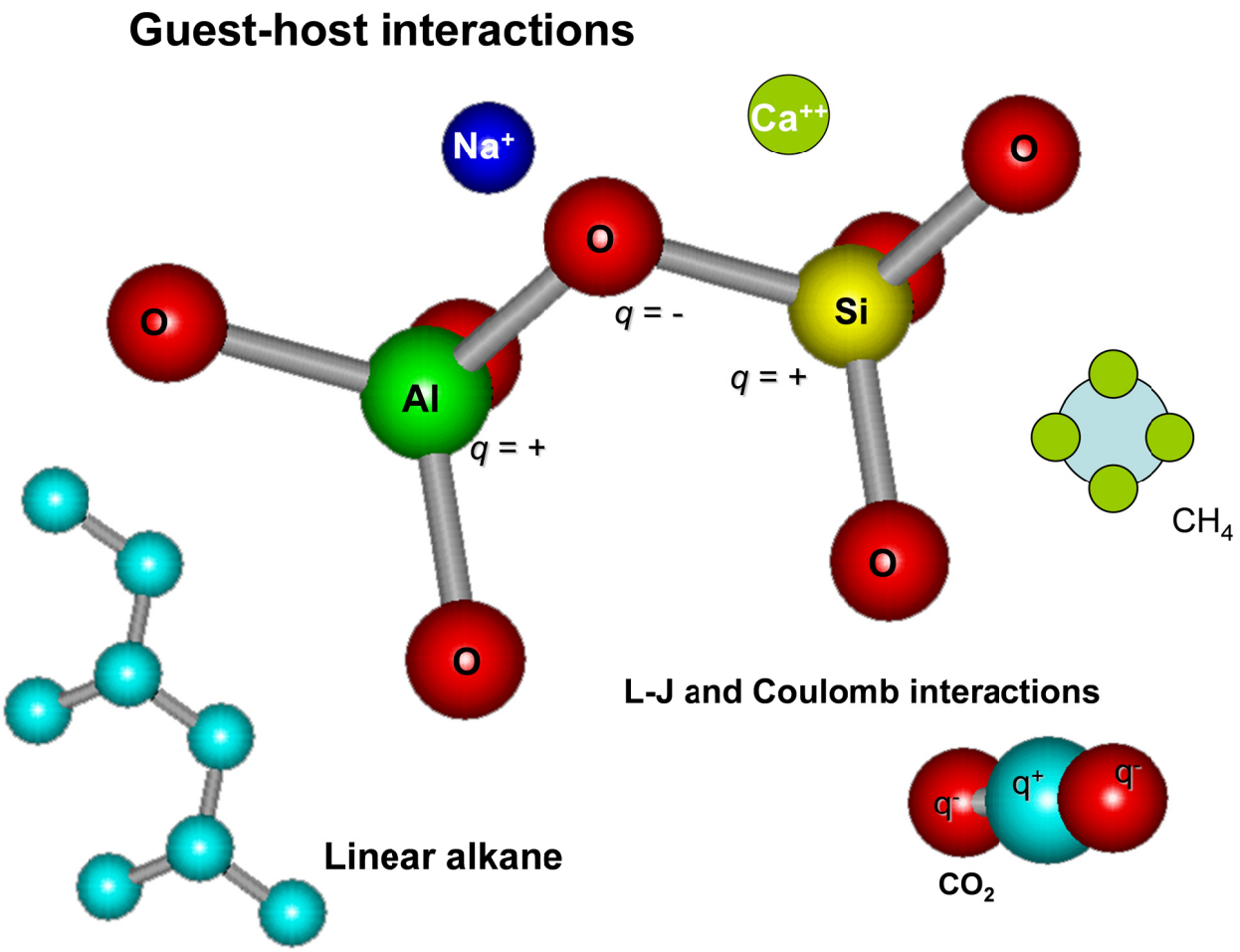

Figure S3-4. Guest-host interactions.

4 Molecular Dynamics (MD) Simulation Methodology

Diffusion is simulated using Newton's equations of motion until the system properties, on average, no longer change in time. The Verlet algorithm is used for time integration. A time step of 1 fs was used in all simulations. For each simulation, *initializing* CBMC moves are used to place the molecules in the domain, minimizing the energy. Next, follows an *equilibration* stage. These are essentially the same as the production cycles, only the statistics are not yet taken into account. This removes any initial large disturbances in the system that do not affect statistics on molecular displacements. After a fixed number of initialization and equilibrium steps, the MD simulation *production* cycles start. For every cycle, the statistics for determining the mean square displacements (MSDs) are updated. The MSDs are determined for time intervals ranging from 2 fs to 1 ns. In order to do this, an order-*N* algorithm, as detailed in Chapter 4 of Frenkel and Smit[56] is implemented. The Nosé-Hoover thermostat is applied to all the diffusing particles. In the MD simulations the cations were allowed to move within the framework and both Lennard-Jones and Coulombic interactions are taken into consideration; see schematic sketch in Figure S4-1.

For all the MD simulation results presented in this article, the DLPOLY code[60] was used along with the force field implementation as described in the previous section. DL_POLY is a molecular dynamics simulation package written by W. Smith, T.R. Forester and I.T. Todorov and has been obtained from CCLRCs Daresbury Laboratory via the website.[60]

The MD simulations were carried out for a variety of loadings within the various structures. All simulations were carried out on the LISA clusters of PCs equipped with Intel Xeon processors running at 3.4 GHz on the Linux operating system.[61] Each MD simulation, for a specified loading, was run for a time duration that is sufficiently long to obtain reliable statistics for determination of the diffusivities. In several cases the campaigns were replicated and the results averaged.

Molecular Dynamics (MD) Simulation Methodology

The unary Maxwell-Stefan diffusivities $Đ_i$ are obtained from MD simulations of molecular displacements using the formula in each of the coordinate direction

$$Đ_i = \frac{1}{2}\lim_{\Delta t\to\infty}\frac{1}{n_i}\frac{1}{\Delta t}\left\langle\left(\sum_{l=1}^{n_i}\left(\mathbf{r}_{l,i}(t+\Delta t)-\mathbf{r}_{l,i}(t)\right)\right)^2\right\rangle \tag{4-1}$$

In this expression n_i represents the number of molecules of species i, and $\mathbf{r}_{l,i}(t)$ is the position of molecule l of species i at any time t.

The unary self-diffusivities $D_{i,self}$ are computed from MD simulations by analyzing the mean square displacement of each species i for each coordinate direction

$$D_{i,self} = \frac{1}{2n_i}\lim_{\Delta t\to\infty}\frac{1}{\Delta t}\left\langle\left(\sum_{l=1}^{n_i}\left(\mathbf{r}_{l,i}(t+\Delta t)-\mathbf{r}_{l,i}(t)\right)^2\right)\right\rangle \tag{4-2}$$

For three-dimensional pore networks (e.g. MFI, BOG, FAU, NaX, NaY, BEA, LTA, TSC, ERI, LTA-5A, LTA-4A, CHA, ISV, IRMOF-1, CuBTC, ZIF-8, MOF-177, BeBTB, CuBTT) the arithmetic average of the diffusivities in the three coordinate directions were used in further analysis and reported. For one-dimensional pore structures (AFI, MTW, TON, LTL, MIL-47, MIL-53(Cr), MgMOF-74, ZnMOF-74, NiMOF-74, CoMOF-74, Co(BDP)) the diffusivities along the direction of diffusion are reported and analyzed. For DDR the reported diffusivities are the averages in x- and y- directions.

The elements of the Maxwell-Stefan matrix Λ_{ij} are accessible from MD simulations [9, 15, 62, 63] by monitoring the individual molecular displacements

$$\Lambda_{ij} = \frac{1}{2}\lim_{\Delta t\to\infty}\frac{1}{n_j}\frac{1}{\Delta t}\left\langle\left(\sum_{l=1}^{n_i}\left(\mathbf{r}_{l,i}(t+\Delta t)-\mathbf{r}_{l,i}(t)\right)\right)\bullet\left(\sum_{k=1}^{n_j}\left(\mathbf{r}_{k,j}(t+\Delta t)-\mathbf{r}_{k,j}(t)\right)\right)\right\rangle \tag{4-3}$$

In this expression n_i and n_j represent the number of molecules of species i and j respectively, and $\mathbf{r}_{l,i}(t)$ is the position of molecule l of species i at any time t. In this context we note a typographical error in equation (4-3) as printed in earlier publications[16, 64, 65] wherein the denominator in the right member had n_i instead of n_j. The simulation results presented in these publications are, however, correct as the proper formula given in equation (4-3) was used.

Compliance with the Onsager Reciprocal Relations demands

$$n_j \Lambda_{ij} = n_i \Lambda_{ji}; \quad i, j = 1, 2, ...n \tag{4-4}$$

4.1 List of Figures for Molecular Dynamics (MD) Simulation Methodology

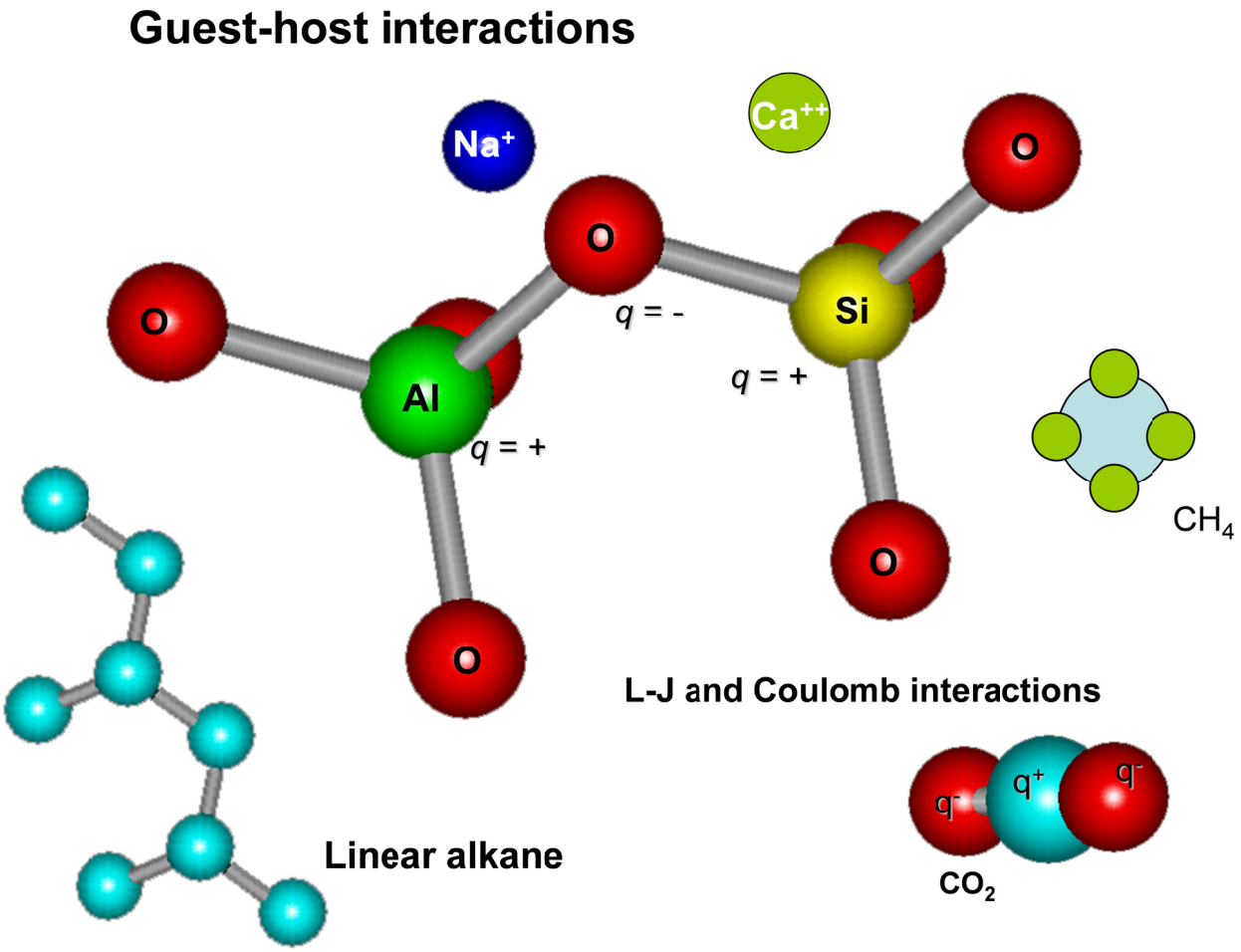

Figure S4-1. Guest-host interactions.

5 Thermodynamics of Mixture Adsorption in Micro-porous Materials

Within microporous crystalline materials, the guest molecules exist in the adsorbed phase, and the thermodynamics of mixture adsorption has an important bearing on the diffusion characteristics of guest molecules. For that reason, we provide below a brief summary of the Ideal Adsorbed Solution Theory (IAST) theory of Myers and Prausnitz.[66]

5.1 Brief outline of theory

The Gibbs adsorption equation[67] in differential form is

$$Ad\pi = \sum_{i=1}^{n} q_i d\mu_i \tag{5-1}$$

The quantity A is the surface area per kg of framework, with units of m^2 per kg of the framework of the crystalline material; q_i is the molar loading of component i in the adsorbed phase with units moles per kg of framework; μ_i is the molar chemical potential of component i. The spreading pressure π has the same units as surface tension, i.e. N m^{-1}.

The chemical potential of any component in the adsorbed phase, μ_i, equals that in the bulk fluid phase. If the partial fugacities in the bulk fluid phase are f_i, we have

$$d\mu_i = RTd \ln f_i \tag{5-2}$$

where R is the gas constant (= 8.314 J mol^{-1} K^{-1}).

Briefly, the basic equation of Ideal Adsorbed Solution Theory (IAST) theory of Myers and Prausnitz[66] is the analogue of Raoult's law for vapor-liquid equilibrium, i.e.

$$f_i = P_i^0 x_i; \quad i = 1,2,...n \tag{5-3}$$

where x_i is the mole fraction in the adsorbed phase

$$x_i = \frac{q_i}{q_1 + q_2 + ...q_n} \tag{5-4}$$

and P_i^0 is the pressure for sorption of every component *i*, which yields the same spreading pressure, π for each of the pure components, as that for the mixture:

$$\frac{\pi A}{RT} = \int_0^{P_1^0} \frac{q_1^0(f)}{f} df = \int_0^{P_2^0} \frac{q_2^0(f)}{f} df = \int_0^{P_3^0} \frac{q_3^0(f)}{f} df = ... \tag{5-5}$$

where $q_i^0(f)$ is the *pure* component adsorption isotherm. The units of $\frac{\pi A}{RT}$, also called the adsorption potential,[68] are mol kg^{-1}.

For all of the guest/host combinations considered in this article, the unary isotherms need to be described by the dual-Langmuir-Freundlich model

$$q^0(f) = q_{A,sat} \frac{b_A f^{\nu A}}{1 + b_A f^{\nu A}} + q_{B,sat} \frac{b_B f^{\nu B}}{1 + b_B f^{\nu B}} \tag{5-6}$$

Each of the integrals in Equation (5-5) can be evaluated analytically. For the dual-site Langmuir-Freundlich isotherm, for example, the integration yields for component *i*,

$$\begin{aligned} \frac{\pi A}{RT} &= \int_{f=0}^{P_i^0} \frac{q^0(f)}{f} df = \frac{q_{A,sat}}{\nu_A} \ln\left(1 + b_A \left(P_i^0\right)^{\nu_A}\right) + \frac{q_{B,sat}}{\nu_B} \ln\left(1 + b_B \left(P_i^0\right)^{\nu_B}\right); \\ \frac{\pi A}{RT} &= \int_{f=0}^{P_i^0} \frac{q^0(f)}{f} df = \frac{q_{A,sat}}{\nu_A} \ln\left(1 + b_A \left(\frac{f_i}{x_i}\right)^{\nu_A}\right) + \frac{q_{B,sat}}{\nu_B} \ln\left(1 + b_B \left(\frac{f_i}{x_i}\right)^{\nu_B}\right) \end{aligned} \tag{5-7}$$

The right hand side of equation (5-7) is a function of P_i^0. For multicomponent mixture adsorption, each of the equalities on the right hand side of Equation (5-5) must be satisfied. These constraints may be solved using a suitable equation solver, to yield the set of values of P_1^0, P_2^0, P_3^0,.. P_n^0, all of which satisfy Equation (5-5). The corresponding values of the integrals using these as upper limits of integration must yield the same value of $\frac{\pi A}{RT}$ for each component; this ensures that the obtained solution is the correct one.

The adsorbed phase mole fractions x_i are then determined from

$$x_i = \frac{f_i}{P_i^0}; \quad i = 1,2,...n \tag{5-8}$$

A key assumption of the IAST is that the enthalpies and surface areas of the adsorbed molecules do not change upon mixing. If the total mixture loading is q_t, the area covered by the adsorbed mixture is $\frac{A}{q_t}$ with units of m^2 (mol mixture)$^{-1}$. Therefore, the assumption of no surface area change due to mixture adsorption translates as $\frac{A}{q_t} = \frac{Ax_1}{q_1^0\left(P_1^0\right)} + \frac{Ax_2}{q_2^0\left(P_2^0\right)} + \cdots \frac{Ax_n}{q_n^0\left(P_n^0\right)}$; the total mixture loading is q_t is calculated from

$$q_t = q_1 + q_2 ... + q_n = \frac{1}{\frac{x_1}{q_1^0(P_1^0)} + \frac{x_2}{q_2^0(P_2^0)} + ... + \frac{x_n}{q_n^0(P_n^0)}} \tag{5-9}$$

in which $q_1^0(P_1^0)$, $q_2^0(P_2^0)$,… $q_n^0(P_n^0)$ are determined from the unary isotherm fits, using the sorption pressures for each component P_1^0, P_2^0, P_3^0,.. P_n^0 that are available from the solutions to equations Equations (5-5), and (5-7). The entire set of equations (5-3) to (5-9) need to be solved numerically to obtain the loadings, q_i of the individual components in the mixture.

For the interpretation of the MD simulations for binary mixture diffusion in microporous host materials, the IAST calculation procedure has to be performed differently because in the MD simulations, the molar loadings q_1, and q_2 in the mixture are specified, and the partial fugacities in the bulk fluid mixture are not known *a priori*. Also in this case, the equalities in equation (5-7) must be satisfied in conjunction with equation (5-9). The entire set of equations (5-3) to (5-9) need to be solved numerically to obtain the partial fugacities, f_i of the individual components in the mixture, that yield the same loadings as chosen in the MD simulations. In all of the calculations presented in this article, the set of equations were solved using the Given-Find solve block of MathCad 15.[69]

5.2 IAST model: 1-site Langmuir isotherms

The IAST procedure will be applied for binary mixture adsorption in which the unary isotherms are described by the 1-site Langmuir model in which the saturation capacities of components 1 and 2 are identical to each other, i.e. $q_{1,sat} = q_{2,sat} = q_{sat}$:

$$q^0(f) = q_{sat}\frac{bf}{1+bf}; \quad \theta = \frac{bf}{1+bf} \tag{5-10}$$

where we define the fractional *occupancy* of the adsorbate molecules, $\theta = q^0(f)/q_{sat}$. The superscript 0 is used to emphasize that $q^0(f)$ relates the *pure component* loading to the bulk fluid fugacity.

For unary adsorption, the adsorption potential for a 1-site Langmuir isotherm can be calculated analytically

$$\frac{\pi A}{RT} = q_{sat}\ln\left(1+bP^0\right) \tag{5-11}$$

The objective is to determine the molar loadings, q_1, and q_2, in the adsorbed phase.

Performing the integration of Equation (5-5) results in an expression relating the sorption pressures P_i^0 of the two species

$$\begin{aligned}&\frac{\pi A}{RT} = q_{sat}\ln\left(1+b_1P_1^0\right) = q_{sat}\ln\left(1+b_2P_2^0\right)\\ &b_1P_1^0 = b_2P_2^0 = \exp\left(\frac{\pi A}{q_{sat}RT}\right)-1\end{aligned} \tag{5-12}$$

The adsorbed phase mole fractions of component 1, and component 2 are given by equation (5-8)

$$x_1 = \frac{f_1}{P_1^0}; \quad x_2 = 1-x_1 = \frac{f_2}{P_2^0} \tag{5-13}$$

Combining equations (5-12), and (5-13):

$$\exp\left(\frac{\pi A}{q_{sat}RT}\right)-1 = b_1\frac{f_1}{x_1} = b_2\frac{f_2}{1-x_1} \tag{5-14}$$

The adsorbed phase mole fractions can be determined

$$\frac{x_1}{x_2}=\frac{q_1}{q_2}=\frac{b_1f_1}{b_2f_2};\quad x_1=\frac{q_1}{q_t}=\frac{b_1f_1}{b_1f_1+b_2f_2};\quad x_2=\frac{q_2}{q_t}=\frac{b_2f_2}{b_1f_1+b_2f_2} \tag{5-15}$$

Once x_1, and $x_2=1-x_1$ are determined, the sorption pressures can be calculated:

$$P_1^0=\frac{f_1}{x_1};\quad P_2^0=\frac{f_2}{x_2}=\frac{f_2}{1-x_1} \tag{5-16}$$

From equations (5-12), and (5-16) we get

$$\begin{aligned} b_iP_1^0&=\frac{b_1f_1}{x_1}=b_2P_2^0=\frac{b_2f_2}{x_2}=b_1f_1+b_2f_2\\ 1+b_iP_1^0&=1+b_2P_2^0=1+b_1f_1+b_2f_2 \end{aligned} \tag{5-17}$$

The total amount adsorbed, $q_t=q_1+q_2$ can be calculated from Equation (5-9)

$$q_t=q_1+q_2=q_{sat}\frac{b_1P_1^0}{1+b_1P_1^0}=q_{sat}\frac{b_2P_2^0}{1+b_2P_2^0}=q_{sat}\frac{b_1f_1+b_2f_2}{1+b_1f_1+b_2f_2} \tag{5-18}$$

Combining equations (5-15), and (5-18) we obtain the following explicit expressions for the component loadings, and fractional occupancies

$$\theta_1=\frac{q_1}{q_{sat}}=\frac{b_1f_1}{1+b_1f_1+b_2f_2};\quad \theta_2=\frac{q_2}{q_{sat}}=\frac{b_2f_2}{1+b_1f_1+b_2f_2} \tag{5-19}$$

Equation (5-19) is commonly referred to as the mixed-gas Langmuir model.

From equations (5-12), (5-18), and (5-19) we derive the following expression for the total occupancy of the mixture

$$\theta=\theta_1+\theta_2=\frac{q_t}{q_{sat}}=1-\exp\left(-\frac{\pi A}{q_{sat}RT}\right)=\frac{b_1f_1+b_2f_2}{1+b_1f_1+b_2f_2} \tag{5-20}$$

For *unary* adsorption of component *i*, say, $f_i = P_i^0$, the occupancy of component 1 is

$$\theta_i=1-\exp\left(-\frac{\pi A}{q_{i,sat}RT}\right)=\frac{b_if_i}{1+b_if_i};\quad \text{unary adsorption of species i} \tag{5-21}$$

From equations (5-20), and (5-21) we may also conclude the *occupancy* may be considered to be the appropriate *proxy* for the spreading pressure. The conclusion that we draw from the foregoing analysis is that the equalities of spreading pressures for unary adsorption of component 1, unary adsorption of

component 2, and binary 1-2 mixture adsorption also implies the corresponding equalities of the corresponding *occupancies* for unary adsorption of component 1, unary adsorption of component 2, and binary 1-2 mixture adsorption.

6 Phenomenological models for mixture diffusion

6.1 The Babbitt equation for unary diffusion in micropores

For describing the *unary* transport of bound moisture in wood, Babbitt[70, 71] suggested the use of the gradient of the spreading pressure $d\pi/dz$ as the thermodynamically correct driving force. The units of $d\pi/dz$ are N m^{-2}, and this represents the force acting per m^2 of material surface. The number of moles of adsorbate, species *i*, per m^2 of surface is $\frac{q_i}{A}$. Therefore the force per mole of adsorbate is $-\left(\frac{d\pi}{dz}\right)\Big/\left(\frac{q_i}{A}\right)=-\frac{d\mu_i}{dz}$. This force is balanced by friction between the mobile adsorbates and the surface of the material

$$-\left(\frac{d\pi}{dz}\right)\Big/\left(\frac{q_i}{A}\right)=-\frac{d\mu_i}{dz}=\frac{RT}{Đ_i}u_i \tag{6-1}$$

where u_i is the velocity of motion of the adsorbate with respect to the framework material. The quantity $\frac{RT}{Đ_i}$ in the right member of equation is interpreted as the "drag coefficient". The unary diffusivity $Đ_i$, with the units m^2 s^{-1}, is to be interpreted as an inverse drag coefficient between the adsorbate and the surface. If we define N_i as the number of moles of species *i* transported per m^2 of crystalline material per second

$$N_i \equiv \rho q_i u_i \tag{6-2}$$

where ρ is the framework density of the microporous crystalline material with units of kg m^{-3}, we obtain the flux relation

$$-\rho\frac{A}{RT}\frac{d\pi}{dz}=\frac{N_i}{Đ_i} \tag{6-3}$$

If the unary adsorption isotherm is described by the 1-site Langmuir isotherm, equation (5-10), the spreading pressure, or its proxy, the adsorption potential can be calculated using equation (5-11). A much more convenient proxy for the spreading pressure is the fractional occupancy, determined by equation (5-21) for a 1-site Langmuir isotherm. More generally, if the unary adsorption isotherm is described by the dual-Langmuir-Freundlich isotherm, equation (5-6), the fractional occupancy can be determined as follows

$$\begin{aligned}&\frac{\pi A}{RT}=\frac{q_{A,sat}}{\nu_A}\ln\left(1+b_A\left(f_i\right)^{\nu_A}\right)+\frac{q_{B,sat}}{\nu_B}\ln\left(1+b_B\left(f_i\right)^{\nu_B}\right);\quad q_{i,sat}=q_{A,sat}+q_{B,sat}\\&\theta_i=1-\exp\left(-\frac{\pi A}{q_{i,sat}RT}\right);\quad \text{unary adsorption of species i}\end{aligned}\tag{6-4}$$

Combining equations (6-1), and (6-3) we obtain

$$-\rho\frac{q_i}{RT}\frac{d\mu_i}{dz}=\frac{N_i}{Đ_i}\tag{6-5}$$

The Babbit equation (6-5) is a limiting case of the more general Maxwell-Stefan (M-S) formulation[7, 8, 72] for *n*-component diffusion, developed in the next section.

6.2 The Maxwell-Stefan (M-S) description of diffusion

Within micro-porous crystalline materials, such as zeolites, metal-organic frameworks (MOFs), and zeolitic imidazolate frameworks (ZIFs), the guest molecules exist in the adsorbed phase. The Maxwell-Stefan (M-S) equations for *n*-component diffusion in porous materials is applied in the following manner[7, 9, 62, 63, 73-76]

$$\begin{aligned}-\frac{d\mu_1}{dz}&=\frac{RT}{Đ_{12}}X_2\left(u_1-u_2\right)+\frac{RT}{Đ_{13}}X_3\left(u_1-u_3\right)+\ldots+\frac{RT}{Đ_{1m}}X_m\left(u_1-u_m\right)\\-\frac{d\mu_2}{dz}&=\frac{RT}{Đ_{21}}X_1\left(u_2-u_1\right)+\frac{RT}{Đ_{23}}X_3\left(u_2-u_3\right)+\ldots+\frac{RT}{Đ_{2m}}X_m\left(u_2-u_m\right)\\&\cdots\cdots\\-\frac{d\mu_n}{dz}&=\frac{RT}{Đ_{n1}}X_1\left(u_n-u_1\right)+\frac{RT}{Đ_{n2}}X_2\left(u_n-u_3\right)+\ldots+\frac{RT}{Đ_{nm}}X_m\left(u_n-u_m\right)\end{aligned}\tag{6-6}$$

The left members of equation (6-6) are the negative of the gradients of the chemical potentials, with the units N mol^{-1}; it represents the driving force acting per mole of species 1, 2, 3,..*n*. The u_i represents the velocity of motion of the adsorbate, defined in a reference frame with respect to the framework material. The subscript m refers to the porous material, that is regarded as the (*n*+1) th component in the mixture; the crystalline framework is considered to be stationary, i.e., $u_m = 0$. The term $RT/Đ_{im}$ is interpreted as the drag or friction coefficient between the guest species *i* and the pore wall. The term $RT/Đ_{ij}$ is interpreted as the friction coefficient for the *i-j* pair of guest molecules. The multiplier X_j in each of the right members represents a measure of the composition of component *j* in the mixture because we expect the friction to be dependent on the number of molecules of *j* relative to that of component *i*. Since the composition fraction X_m of the material is undefined, we re-define the M-S diffusivity for interaction of the penetrant (i.e. guest molecule) *i* with the pore wall as $Đ_i \equiv Đ_{im}/X_m$.

6.3 Unified M-S description of diffusion in porous materials

For a unified description of diffusion in porous materials, it is convenient to use as composition measures the mole fractions of the components in the adsorbed phase, $x_i = q_i / q_t$ where q_i is the molar loading of adsorbate, and q_t is the *total* mixture loading $q_t = \sum_{i=1}^{n} q_i$.

In terms of mole fractions, equations (6-6) are modified as follows

$$
\begin{aligned}
-\frac{d\mu_1}{dz} &= \frac{RT}{Đ_{12}} x_2(u_1 - u_2) + \frac{RT}{Đ_{13}} x_3(u_1 - u_3) + \ldots + \frac{RT}{Đ_1}(u_1) \\
-\frac{d\mu_2}{dz} &= \frac{RT}{Đ_{21}} x_1(u_2 - u_1) + \frac{RT}{Đ_{23}} x_3(u_2 - u_3) + \ldots + \frac{RT}{Đ_2}(u_2) \\
&\cdots\cdots \\
-\frac{d\mu_n}{dz} &= \frac{RT}{Đ_{n1}} x_1(u_n - u_1) + \frac{RT}{Đ_{n2}} x_2(u_n - u_3) + \ldots + \frac{RT}{Đ_n}(u_n)
\end{aligned}
\qquad (6\text{-}7)
$$

An important, persuasive, argument for the use of the M-S formulation for mixture diffusion is that the M-S diffusivity $Đ_i$ in mixtures can be estimated using information on the loading dependence of the

corresponding unary diffusivity values. Put another way, the M-S diffusivity $Đ_i$ can be estimated from experimental data on *unary* diffusion in the porous material.

The M-S diffusivity $Đ_{ij}$ has the units m^2 s^{-1} and the physical significance of an *inverse* drag coefficient. The magnitudes of the M-S diffusivities $Đ_{ij}$ do not depend on the choice of the mixture reference velocity because equation (6-6) is set up in terms of velocity differences. At the molecular level, the $Đ_{ij}$ reflect how the facility for transport of species *i correlates* with that of species *j*; they are also termed *exchange coefficients*.

For *meso*porous materials with pores in the 20 Å to 100 Å size range the values of the exchange coefficient $Đ_{12}$ are the nearly the same as the binary *fluid phase* M-S diffusivity, $Đ_{12,fl}$, over the entire range of pore concentrations.[7, 9, 62, 77, 78] For micro-porous materials, the exchange coefficient $Đ_{12}$ cannot be directly identified with the corresponding fluid phase diffusivity $Đ_{12,fl}$ because the molecule-molecule interactions are also significantly influenced by molecule-wall interactions.

The Maxwell-Stefan diffusion formulation (6-7) is consistent with the theory of irreversible thermodynamics. The Onsager Reciprocal Relations imply that the M-S pair diffusivities are symmetric

$$Đ_{ij} = Đ_{ji} \tag{6-8}$$

We define N_i as the number of moles of species *i* transported per m^2 of crystalline material per second

$$N_i \equiv \rho q_i u_i \tag{6-9}$$

where ρ is the framework density with units of kg m^{-3}. Multiplying both sides of equation (6-7) by ρq_i, the M-S equations for *n*-component diffusion in zeolites, MOFs, and ZIFs take the form [8, 77, 79]

$$-\rho \frac{q_i}{RT}\frac{d\mu_i}{dz} = \sum_{\substack{j=1 \\ j\neq i}}^{n} \frac{x_j N_i - x_i N_j}{Đ_{ij}} + \frac{N_i}{Đ_i}; \quad i = 1,2,..n \tag{6-10}$$

An entirely analogous manner of writing equation (6-10) is in terms of molar concentrations c_i, in the adsorbed phase, with units mol m^{-3}, based on the accessible pore volume, V_p (= m^3 pore volume per kg framework)

$$c_i = \frac{q_i}{V_p}; \quad c_t = \sum_{i=1}^{n} c_i = \frac{q_t}{V_p} \tag{6-11}$$

In terms of molar concentrations, the M-S description for intra-pore diffusion is

$$-\rho V_p \frac{c_i}{RT}\frac{d\mu_i}{dz} = \sum_{\substack{j=1 \\ j\neq i}}^{n}\left(\frac{x_j N_i - x_i N_j}{Đ_{ij}}\right) + \frac{N_i}{Đ_i}; \quad i = 1,2...n \tag{6-12}$$

The quantity $\rho V_p \equiv \varepsilon$ is the fractional pore volume,

$$\rho V_p = \left(\frac{\text{kg framework}}{\text{m}^3 \text{ framework}}\right)\left(\frac{\text{m}^3 \text{ pore volume}}{\text{kg framework}}\right) = \left(\frac{\text{m}^3 \text{ pore volume}}{\text{m}^3 \text{ framework}}\right) = \varepsilon \tag{6-13}$$

So, we re-write equation (6-12) in the form

$$-\varepsilon \frac{c_i}{RT}\frac{d\mu_i}{dz} = \sum_{\substack{j=1 \\ j\neq i}}^{n}\left(\frac{x_j N_i - x_i N_j}{Đ_{ij}}\right) + \frac{N_i}{Đ_i}; \quad i = 1,2...n \tag{6-14}$$

The formulation (6-14) has been employed to develop a unified theory of mixture diffusion in both micro-pores and meso-pores.[9, 15, 62, 76] The fluxes N_i in equations (6-10), and (6-14) are defined in terms of the moles transported per m^2 of the *total surface of crystalline material*. Alternatively, if we just focus on fluxes inside a single pore, it is convenient to define the fluxes N_i in terms of the moles transported per m^2 surface of the pore, then the factor $\rho V_p \equiv \varepsilon$ has to be omitted in the left member of equation (6-14).

6.4 Thermodynamic correction factors

At thermodynamic equilibrium, the chemical potential of component *i* in the bulk fluid mixture equals the chemical potential of that component in the adsorbed phase. For the bulk fluid phase mixture we have

$$\frac{1}{RT}\frac{d\mu_i}{dz} = \frac{d\ln f_i}{dz} = \frac{1}{f_i}\frac{df_i}{dz}; \qquad i = 1,2,..n \tag{6-15}$$

The chemical potential gradients $d\mu_i/dz$ can be related to the gradients of the molar loadings, q_i, by defining thermodynamic correction factors Γ_{ij}

$$\frac{q_i}{RT}\frac{d\mu_i}{dz}=\sum_{j=1}^{n}\Gamma_{ij}\frac{dq_j}{dz};\quad \frac{c_i}{RT}\frac{d\mu_i}{dz}=\sum_{j=1}^{n}\Gamma_{ij}\frac{dc_j}{dz};\qquad \Gamma_{ij}=\frac{q_i}{f_i}\frac{\partial f_i}{\partial q_j}=\frac{c_i}{p_i}\frac{\partial f_i}{\partial c_j};\qquad i,j=1,....n \tag{6-16}$$

The thermodynamic correction factors Γ_{ij} can be calculated by differentiation of the model describing mixture adsorption equilibrium. Generally speaking, the Ideal Adsorbed Solution Theory (IAST) of Myers and Prausnitz[66] is the preferred method for estimation of mixture adsorption equilibrium. In some special case, the mixed-gas Langmuir model

$$\frac{q_i}{q_{i,sat}}=\theta_i=\frac{b_i f_i}{1+\sum_{i=1}^{n}b_i f_i};\quad i=1,2,...n \tag{6-17}$$

may be of adequate accuracy. Analytic differentiation of equation (6-17) yields

$$\Gamma_{ij}=\delta_{ij}+\left(\frac{q_{i,sat}}{q_{j,sat}}\right)\left(\frac{\theta_i}{\theta_V}\right);\quad i,j=1,2\ldots n \tag{6-18}$$

where the fractional vacancy θ_V is defined as

$$\theta_V=1-\theta_t=1-\sum_{i=1}^{n}\theta_i \tag{6-19}$$

The elements of the matrix of thermodynamic factors Γ_{ij} can be calculated explicitly from information on the component loadings q_i in the adsorbed phase; this is the persuasive advantage of the use of the mixed-gas Langmuir model. By contrast, the IAST does not allow the calculation of Γ_{ij} explicitly from knowledge on the component loadings q_i in the adsorbed phase; a numerical procedure is required.

6.5 Explicit expression for the fluxes as function of loading gradients

By defining an n-dimensional square matrix $[B]$ with elements

$$B_{ii}=\frac{1}{Đ_i}+\sum_{\substack{j=1\\ j\neq i}}^{n}\frac{x_j}{Đ_{ij}};\qquad B_{ij}=-\frac{x_i}{Đ_{ij}};\quad i,j=1,2....n \tag{6-20}$$

we can recast equation (6-10), or equation (6-14), into the following form

$$-\rho\frac{q_i}{RT}\nabla\mu_i=-\varepsilon\frac{c_i}{RT}\frac{d\mu_i}{dz}=\sum_{j=1}^{n}B_{ij}N_j;\qquad i=1,2,..n \tag{6-21}$$

Equation (6-21) can be re-written in *n*-dimensional matrix notation as

$$(N) = -\rho\left[B\right]^{-1}\left[\Gamma\right]\frac{d\left(q\right)}{dz} = -\rho\left[\Lambda\right]\left[\Gamma\right]\frac{d\left(q\right)}{dz} = -\varepsilon\left[\Lambda\right]\left[\Gamma\right]\frac{d\left(c\right)}{dz} \tag{6-22}$$

We denote the inverse of $[B]$ as $\left[\Lambda\right]$:

$$[B]^{-1} \equiv \left[\Lambda\right] \tag{6-23}$$

The elements of $\left[\Lambda\right]$ cannot be determined from experimental measurements. However, Λ_{ij} are directly accessible from MD simulations [9, 15, 62, 63] by monitoring the individual molecular displacements

$$\Lambda_{ij} = \frac{1}{2}\lim_{\Delta t\to\infty}\frac{1}{n_j}\frac{1}{\Delta t}\left\langle\left(\sum_{l=1}^{n_i}\left(\mathbf{r}_{l,i}(t+\Delta t)-\mathbf{r}_{l,i}(t)\right)\right)\bullet\left(\sum_{k=1}^{n_j}\left(\mathbf{r}_{k,j}(t+\Delta t)-\mathbf{r}_{k,j}(t)\right)\right)\right\rangle \tag{6-24}$$

In this expression n_i and n_j represent the number of molecules of species *i* and *j* respectively, and $\mathbf{r}_{l,i}(t)$ is the position of molecule *l* of species *i* at any time *t*. In this context we note a typographical error in equation (6-24) as printed in earlier publications[16, 64, 65] wherein the denominator in the right member had n_i instead of n_j. The simulation results presented in these publications are, however, correct as the proper formula given in equation (6-24) was used.

Compliance with the Onsager Reciprocal Relations demands

$$n_j\Lambda_{ij} = n_i\Lambda_{ji};\quad i,j = 1,2,....n \tag{6-25}$$

7 Unary Diffusion in Microporous Materials

7.1 Unary self-diffusivity, $\mathcal{D}_{i,self}$, and M-S diffusivity, $Đ_i$

For unary diffusion, equation (6-14) simplifies to yield

$$-\varepsilon \frac{c_i}{RT}\frac{d\mu_i}{dz} = \frac{N_i}{Đ_i} \tag{7-1}$$

The pure component $Đ_i$ is obtained from MD simulations of molecular displacements using the formula in each of the coordinate direction

$$Đ_i = \frac{1}{2}\lim_{\Delta t\to\infty}\frac{1}{n_i}\frac{1}{\Delta t}\left\langle\left(\sum_{l=1}^{n_i}\left(\mathbf{r}_{l,i}(t+\Delta t)-\mathbf{r}_{l,i}(t)\right)\right)^2\right\rangle \tag{7-2}$$

In this expression n_i represents the number of molecules of species i, and $\mathbf{r}_{l,i}(t)$ is the position of molecule l of species i at any time t.

There is no experimental procedure for direct determination of the $Đ_i$. Transient uptake and chromatographic experiments yield the Fick diffusivity D_i, also termed "transport" diffusivity, that relates the flux N_i of species i to the gradient of the molar loadings, q_i, or pore concentration, c_i

$$N_i = -\rho D_i\frac{dq_i}{dz} = -\varepsilon D_i\frac{dc_i}{dz} \tag{7-3}$$

where ε is the fractional pore volume. The Fick diffusivity D_i are related to the M-S diffusivities by the thermodynamic factor Γ

$$D_i = Đ_i\Gamma;\quad \Gamma \equiv \frac{c_i}{f_i}\frac{\partial f_i}{\partial c_i} = \frac{q_i}{f_i}\frac{\partial f_i}{\partial q_i};\quad \text{unary diffusion} \tag{7-4}$$

The M-S diffusivity $Đ_i$ is often termed the "corrected" diffusivity because the formula (7-4) suggests that adsorption thermodynamic effects have been "factored out". The values of Γ can be determined by analytic differentiation of fits to the adsorption isotherms. For a proper understanding of the

concentration dependence of the diffusivities, we need the isotherm fits to be good representations over the entire range of concentrations, and not just in the Henry regime ($c_i \to 0; \quad q_i \to 0$).

The self-exchange diffusivity, $Đ_{ii}$, is defined by applying the M-S equations (6-14) to a binary mixture, that consists of identical species, tagged and un-tagged and assuming, furthermore, that we have equimolar diffusion $N_1 + N_2 = 0$. In this special case, the M-S equations (6-14) can be used to derive the following relation between the self-diffusivity, $D_{i,self}$, and the M-S diffusivity, $Đ_i$, for *unary* diffusion [62]

$$-\varepsilon \frac{c_1}{RT}\frac{d\mu_1}{dz} = \frac{(x_1 + x_2)N_1}{Đ_{11}} + \frac{N_1}{Đ_1} = \left(\frac{1}{Đ_{11}} + \frac{1}{Đ_1}\right)N_1 \tag{7-5}$$

Equation (7-4) defines the self-diffusivity within a pore for this special situation describing "tracer" diffusion

$$-\varepsilon \frac{c_i}{RT}\frac{d\mu_i}{dz} = \frac{N_i}{D_{i.self}} \tag{7-6}$$

and so we derive the expression

$$\frac{1}{D_{i,self}} = \frac{1}{Đ_i} + \frac{1}{Đ_{ii}} \tag{7-7}$$

The self-diffusivities $D_{i,self}$ are computed from MD simulations by analyzing the mean square displacement of each species i for each coordinate direction

$$D_{i,self} = \frac{1}{2n_i}\lim_{\Delta t\to\infty}\frac{1}{\Delta t}\left\langle\left(\sum_{l=1}^{n_i}\left(\mathbf{r}_{l,i}(t+\Delta t) - \mathbf{r}_{l,i}(t)\right)^2\right)\right\rangle \tag{7-8}$$

Equation (7-7) may used to determine the self-exchange diffusivities $Đ_{ii}$ from MD simulated $D_{i,self}$ and $Đ_i$ for unary diffusion. The self-exchange diffusivity, $Đ_{ii}$, quantifies the extent of correlations for unary diffusion. The $Đ_i$, reflecting *collective* motion of molecules (cf. equation (7-2)) is free from such correlation effects; it is for this reason that the $Đ_i$ are amenable to simpler interpretation, and modeling, than the $D_{i,self}$. The Fick diffusivity, determined from say uptake or chromatographic experiments,[1] is

directly influenced by adsorption thermodynamics and is therefore much more difficult to interpret from a fundamental viewpoint than the M-S $Đ_i$.

MD simulations of the unary self-diffusivities, $D_{i,self}$, and Maxwell-Stefan diffusivities, $Đ_i$, for a variety of guest molecules in a variety of host structures at 300 K were performed; these are reported in our earlier publications.[7, 9, 10, 13-16, 62, 63, 77, 80-83] The data are presented in the following set of Figures:

Figure S7-1: MFI zeolite

Figure S7-2: BEA, and ISV zeolite

Figure S7-3: all-silica FAU zeolite

Figure S7-4: NaY, and NaX zeolites

Figure S7-5: all-silica LTA zeolite

Figure S7-6: all-silica CHA zeolite

Figure S7-7: DDR, AFI, and MOR all-silica zeolites

Figure S7-8: IRMOF-1

Figure S7-9: CuBTC

Figure S7-10: MgMOF-74, and MOF-177

Figure S7-11: BTP-COF

Broadly speaking, for all guest/host combinations, both self-diffusivities, $D_{i,self}$, and Maxwell-Stefan diffusivities, $Đ_i$, are strongly dependent on the molar loadings. The diffusivities tend to decrease as the saturation loadings are approached. The loading dependence is often strongly influenced by the adsorption isotherms, and the spreading pressures. Configurational-Bias Monte Carlo (CBMC) simulations of the unary adsorption isotherms were also determined, and are plotted in the afore-listed Figures. These CBMC simulated isotherms were fitted with the dual-site Langmuir-Freundlich model; the fit parameters for each guest molecule (with sites A, and B) are tabulated for each host material as follows:

Table S7-1: MFI zeolite

Table S7-2: FAU all-silica zeolite

Table S7-3: NaY zeolite (48 Al)

Table S7-4: NaX zeolite (86 Al)

Table S7-5: LTA all-silica zeolite

Table S7-6: CHA all-silica zeolite

Table S7-7: DDR all-silica zeolite

Table S7-8: ISV zeolite

Table S7-9: BEA zeolite

Table S7-10, Table S7-11: IRMOF-1

Table S7-12: MgMOF-74

Table S7-13: CuBTC

Using the dual-site Langmuir-Freundlich isotherm fit parameters, the spreading pressures and occupancy can be determined using Equation (6-4). The diffusivities as function of the occupancy, θ, used as proxy for the spreading pressure, are also plotted in the afore-listed Figures. Generally, the diffusivities tend to reduce significantly, virtually to zero, as the occupancy approaches saturation conditions, $\theta \to 1$.

The simplest model to describe this loading dependence is

$$Đ_i = Đ_i(0)\left(1-\theta\right) = Đ_i(0)\theta_V \tag{7-9}$$

where $Đ_i(0)$ is the M-S diffusivity at "zero-loading", and $\theta_V = \left(1-\theta\right)$ is the fractional vacancy. Equation (7-9) is essentially based on a simple hopping model in which a molecule can jump from one adsorption site to an adjacent one, provided it is not already occupied. The loading dependence portrayed in equation (7-9) has been termed the "strong confinement" scenario by Krishna and Baur.[84]

For the specific case of a binary mixture, the hopping of molecules from one site to another on a 2D lattice is depicted in Figure S7-12. Using a simple lattice model, the M-S diffusivity in the limit of vanishingly small occupancies, $Đ_i(0) = \frac{1}{\zeta}\nu_i(0)\lambda^2$, where $\zeta = 4$ is the coordination number of the 2D

array of lattice sites, λ is the jump distance on the square lattice, and $\nu_i(0)$ is the jump frequency at vanishingly small occupancy.[85]

More generally, molecule-molecule interactions serve to influence the jump frequencies by a factor that depends on the energy of interaction, w. For repulsive interactions, $w > 0$, whereas for attractive interactions, $w < 0$. Using the quasi-chemical approach of Reed and Ehrlich[86] to quantify such interactions, the following expression is obtained for the loading dependence of the M-S diffusivities [85, 87, 88]

$$Đ_i = Đ_i(0)\left(\frac{1+\beta_i}{2\,(1-\theta_i)}\right)^{-\zeta}\left(1+\frac{(\beta_i-1+2\theta_i)\varphi}{2\,(1-\theta_i)}\right)^{\zeta-1} \tag{7-10}$$

In equation (7-10) the following dimensionless parameters are defined

$$\beta_i = \sqrt{1-4\,\theta_i(1-\theta_i)(1-1/\phi)}; \quad \phi = \exp(w/RT) \tag{7-11}$$

In the limiting case of negligible molecule-molecule interactions, $w = 0$, $\phi = 1$, $\beta_i = 1$ equation (7-10) degenerates to yield Equation (7-9).

A careful examination of the MD simulations of the diffusivities show that the assumption of loading-independent diffusivities, termed the "weak confinement" scenario by Krishna and Baur:[84]

$$Đ_i = Đ_i(0) \tag{7-12}$$

can only be applied for small guest molecules such as H_2, and Ne for occupancies below about 0.5.

For any guest molecule, the loading dependence is strongly influenced also by the pore topology and connectivity, and molecule-molecule interactions. To illustrate this, Figure S7-13 compares the dependence of the M-S diffusivity of CH_4 in a wide variety of host structures, as a function of (a) the pore concentration, c_i, (b) the adsorption potential, and (c, d) the fractional occupancy, determined using Equation (6-4). Broadly speaking, the $Đ_i$ versus θ dependence is amenable to easier interpretation and analysis.

Preferential location of molecules within the MFI structural framework can cause strong isotherm inflections. For example, branched alkanes, benzene, alkyl benzenes, and cyclohexane prefer to locate at the channel intersections of MFI zeolite due to extra "leg-room" and other configurational considerations.[89] There are only 4 intersection sites available per unit cell of MFI. This implies that to obtain loadings higher than $\Theta_i = 4$ molecules per unit cell, an extra "push" will be required to locate the molecules elsewhere within the channels; this leads to isotherm inflection; see Figure S7-14(a). Due to strong isotherm inflections, the $1/\Gamma$ exhibits a cusp-like inflection at a loading of $\Theta_i = 4$, when all the preferred adsorption sites are occupied; is demonstrated in the data on $1/\Gamma$ for iso-butane/MFI in Figure S7-14(b). In the range $0 < \Theta_i < 4$, $1/\Gamma$ decreases nearly linearly with Θ_i signifying the fact that the vacancy *decreases* almost linearly with loading. For $\Theta_i > 4$, $1/\Gamma$ increases with Θ_i because additional sites *within* the MFI channels are created to accommodate more than 4 molecules per unit cell, i.e. the number of available sites *increases* within this loading range. These additional sites must be accommodated within the channels, requiring the additional "push" that caused the inflection. The cusp-like dependence of $1/\Gamma$ on the loading Θ_i causes the Maxwell-Stefan diffusivity, measured by Chmelik et al.[90], to also exhibit a corresponding cusp-like dependence; see Figure S7-14(b). Plotted as a function of the adsorption potential $\pi A/RT$ or occupancy $\theta = 1 - \exp\left(-\frac{\pi A}{q_{sat} RT}\right)$ leads to a reduction in the sharpness of the "valley" in the M-S diffusivity; see Figure S7-14(c,d).

7.2 List of Tables for Unary Diffusion in Microporous Materials

Table S7-1. Dual-site Langmuir-Freundlich parameters for guest molecules in MFI at 300 K. To convert from molecules uc^{-1} to mol kg^{-1}, multiply by 0.173367.

	Site A			Site B		
	$\Theta_{A,sat}$ molecules uc^{-1}	b_A $Pa^{-\nu}$	ν_A dimensionless	$\Theta_{B,sat}$ molecules uc^{-1}	b_B $Pa^{-\nu}$	ν_B dimensionless
Ne	57	6.69E-11	1	42	1.70E-08	1
Ar	19	2.61E-07	1	15	6.75E-08	0.8
H2	30	3.57E-08	1	42	1.39E-09	1
N2	16	6.37E-07	1	16	3.82E-07	0.7
CO2	19	6.12E-06	1	11	1.73E-08	1
CH4	7	5.00E-09	1	16	3.10E-06	1
C2H6	3.3	4.08E-07	1	13	7.74E-05	1
C3H8	1.4	3.35E-04	0.67	10.7	6.34E-04	1.06
nC4H10	1.5	2.24E-03	0.57	8.7	9.75E-03	1.12
iso-C4H10	4	2.29E-02	1	6	2.87E-05	1
nC5H12	4	5.35E-02	1.537320948	4	2.28E-01	1
nC6H14	6.6	7.08E-01	0.83	1.4	1.66E+01	1.5

Table S7-2. Dual-site Langmuir-Freundlich parameters for guest molecules in FAU (all-silica) at 300 K. To convert from molecules uc^{-1} to mol kg^{-1}, multiply by 0.086683044.

	Site A			Site B		
	$\Theta_{A,sat}$ molecules uc^{-1}	b_A $Pa^{-\nu}$	ν_A dimensionless	$\Theta_{B,sat}$ molecules uc^{-1}	b_B $Pa^{-\nu}$	ν_B dimensionless
Ne	158	4.39E-11	1.00E+00	197	9.12E-09	1
Ar	40	1.00E-09	1.00E+00	100	6.12E-08	1
Kr	53	2.67E-07	0.7	100	2.12E-07	1
H2	85	2.75E-08	1.00E+00	67	1.03E-08	1
N2	60	1.53E-09	1.00E+00	75	1.32E-07	1
CO2	32	2.55E-13	2.20E+00	70	6.86E-07	1
CH4	56	2.78E-08	8.00E-01	60	2.90E-07	1
C2H6	60	2.87E-06	1.00E+00	40	1.00E-09	1
C3H8	40	1.34E-05	6.00E-01	15	1.72E-06	1.27
nC4H10	30	9.00E-07	1.70E+00	20	2.36E-04	0.56
nC5H12	25	4.69E-07	2.40E+00	197	7.26E-04	0.54

Table S7-3. Dual-site Langmuir-Freundlich parameters for guest molecules in NaY zeolite (all-silica) at 300 K. Per unit cell of NaY zeolite we have 144 Si, 48 Al, 48 Na+, with Si/Al=3. To convert from molecules uc^{-1} to mol kg^{-1}, multiply by 0.079448462.

	Site A			Site B		
	$\Theta_{A,sat}$ molecules uc^{-1}	b_A $Pa^{-\nu}$	ν_A dimensionless	$\Theta_{B,sat}$ molecules uc^{-1}	b_B $Pa^{-\nu}$	ν_B dimensionless
CO2	76	4.04E-05	1	24	2.71E-05	0.66
CH4	66	3.77E-07	1.09	58	3.01E-06	0.68
C2H6	18	6.76E-09	1.8	41	1.08E-05	1
C3H8	13	5.68E-09	2.48	35	1.20E-04	1

Table S7-4. Dual-site Langmuir-Freundlich parameters for guest molecules in NaX zeolite (all-silica) at 300 K. Per unit cell of NaX zeolite we have 106 Si, 86 Al, 86 Na^+ with Si/Al=1.23. To convert from molecules uc^{-1} to mol kg^{-1}, multiply by 0.074524437.

	Site A			Site B		
	$\Theta_{A,sat}$ molecules uc^{-1}	b_A $Pa^{-\nu}$	ν_A dimensionless	$\Theta_{B,sat}$ molecules uc^{-1}	b_B $Pa^{-\nu}$	ν_B dimensionless
CO2	28	1.57E-04	0.7	59	4.26E-04	1
CH4	73	2.25E-06	1	29	1.56E-08	1
C2H6	64	1.88E-05	1	20	7.63E-07	0.65
C3H8	42	8.25E-05	1.3	17	1.09E-03	0.46

Table S7-5. Dual-site Langmuir-Freundlich parameters for guest molecules in LTA (all-silica) at 300 K. To convert from molecules uc^{-1} to mol kg^{-1}, multiply by 0.086683044.

	Site A			Site B		
	$\Theta_{A,sat}$ molecules uc^{-1}	b_A $Pa^{-\nu}$	ν_A dimensionless	$\Theta_{B,sat}$ molecules uc^{-1}	b_B $Pa^{-\nu}$	ν_B dimensionless
Ne	176	4.57E-11	1	1.80E+02	1.20E-08	1
Ar	88	8.10E-08	1	60	1.57E-09	1
Kr	60	3.72E-07	0.77	60	1.55E-07	1.07
H2	88	2.55E-08	1	88	1.51E-08	1
N2	70	1.36E-07	1	60	5.03E-10	1
CO2	36	1.51E-05	0.54	85	2.06E-07	1.15
CH4	52	6.63E-08	0.82	65	3.77E-07	1

Table S7-6. Dual-site Langmuir-Freundlich parameters for guest molecules in CHA (all-silica) at 300 K. To convert from molecules uc^{-1} to mol kg^{-1}, multiply by 0.231154783.

	Site A			Site B		
	$\Theta_{A,sat}$ molecules uc^{-1}	b_A $Pa^{-\nu}$	ν_A dimensionless	$\Theta_{B,sat}$ molecules uc^{-1}	b_B $Pa^{-\nu}$	ν_B dimensionless
Ne	62	1.06E-08	1	53	4.73E-11	1
Ar	26	1.22E-07	1	14	4.62E-09	1
H2	63	2.58E-08	0.73	68	1.57E-08	1
N2	28	8.71E-08	0.6	32	4.87E-07	0.88
CO2	28	1.71E-06	1.1	12	8.74E-06	0.7
CH4	12	1.36E-06	1	24	4.59E-07	0.8

Table S7-7. Dual-site Langmuir-Freundlich parameters for guest molecules in DDR (all-silica) at 300 K. To convert from molecules uc^{-1} to mol kg^{-1}, multiply by 0.069346435.

	Site A			Site B		
	$\Theta_{A,sat}$ molecules uc^{-1}	b_A $Pa^{-\nu}$	ν_A dimensionless	$\Theta_{B,sat}$ molecules uc^{-1}	b_B $Pa^{-\nu}$	ν_B dimensionless
Ne	98	1.56E-08	1	90	6.79E-11	1
Ar	38	2.57E-07	1	40	2.09E-09	1

Table S7-8. Dual-site Langmuir-Freundlich parameters for guest molecules in ISV (all-silica) at 300 K. To convert from molecules uc^{-1} to mol kg^{-1}, multiply by 0.260049131.

	Site A			Site B		
	$\Theta_{A,sat}$ molecules uc^{-1}	b_A $Pa^{-\nu}$	ν_A dimensionless	$\Theta_{B,sat}$ molecules uc^{-1}	b_B $Pa^{-\nu}$	ν_B dimensionless
CH4	17	9.31E-07	1	21	1.93E-07	0.61
C2H6	16	1.46E-03	0.21	13	1.59E-05	1

Table S7-9. Dual-site Langmuir-Freundlich parameters for guest molecules in BEA (all-silica) at 300 K. To convert from molecules uc^{-1} to mol kg^{-1}, multiply by 0.260049131.

	Site A			Site B		
	$\Theta_{A,sat}$ molecules uc^{-1}	b_A $Pa^{-\nu}$	ν_A dimensionless	$\Theta_{B,sat}$ molecules uc^{-1}	b_B $Pa^{-\nu}$	ν_B dimensionless
Ar	15	1.58E-07	1	15	2.98E-08	1
CH4	17	2.12E-08	1	14	1.14E-06	1
C3H8	3.3	4.08E-07	1	13	7.74E-05	1

Table S7-10. Dual-site Langmuir-Freundlich parameters for guest molecules in IRMOF-1 at 300 K. To convert from molecules uc^{-1} to mol kg^{-1}, multiply by 0.162395981.

	Site A			Site B		
	$\Theta_{A,sat}$ molecules uc^{-1}	b_A $Pa^{-\nu}$	ν_A dimensionless	$\Theta_{B,sat}$ molecules uc^{-1}	b_B $Pa^{-\nu}$	ν_B dimensionless
Ne	342	1.31E-08	1	270	9.66E-11	1
Ar	236	5.56E-08	1	115	5.25E-08	0.75
H2	211	5.00E-10	1	303	1.44E-08	1
N2	160	6.82E-09	0.85	160	7.52E-08	1
CO2	200	1.01E-06	0.66	177	5.82E-10	1.5
CH4	60	1.69E-16	1.8	177	1.26E-07	1.03
C2H6	78	1.66E-06	1	54	2.32E-16	2.9
C3H8	60	1.86E-12	2.6	42	1.17E-05	1
nC4H10	32	6.66E-05	1	50	2.23E-27	7.5
nC5H12	19	4.69E-04	1	50	5.13E-29	10.7
nC6H14	12	3.35E-03	1	46	2.27E-36	19.7

Table S7-11. Dual-site Langmuir-Freundlich parameters for guest molecules in IRMOF-1 at 200 K. To convert from molecules uc^{-1} to mol kg^{-1}, multiply by 0.162395981.

	Site A			Site B		
	$\Theta_{A,sat}$ molecules uc^{-1}	b_A $Pa^{-\nu}$	ν_A dimensionless	$\Theta_{B,sat}$ molecules uc^{-1}	b_B $Pa^{-\nu}$	ν_B dimensionless
CO2	160	5.31E-58	13	68	1.61E-05	1
CH4	166	1.66E-07	1.2	74	6.62E-06	0.67

Table S7-12. Dual-site Langmuir-Freundlich parameters for guest molecules in MgMOF-74 at 300 K. To convert from molecules uc^{-1} to mol kg^{-1}, multiply by 0.457959224.

	Site A			Site B		
	$\Theta_{A,sat}$ molecules uc^{-1}	b_A $Pa^{-\nu}$	ν_A dimensionless	$\Theta_{B,sat}$ molecules uc^{-1}	b_B $Pa^{-\nu}$	ν_B dimensionless
H2	31	7.73E-09	1	31	3.05E-08	1
CO2	28	2.05E-05	1	12	3.03E-07	1
N2	25	2.93E-07	1	20	6.06E-09	1
CH4	32	6.24E-07	1	8	2.71E-17	2

Table S7-13. Dual-site Langmuir-Freundlich parameters for guest molecules in CuBTC at 300 K. To convert from molecules uc^{-1} to mol kg^{-1}, multiply by 0.103360722.

	Site A			Site B		
	$\Theta_{A,sat}$ molecules uc^{-1}	b_A $Pa^{-\nu}$	ν_A dimensionless	$\Theta_{B,sat}$ molecules uc^{-1}	b_B $Pa^{-\nu}$	ν_B dimensionless
Ne	300	8.45E-09	0.8	300	1.57E-08	1
Ar	202	2.51E-07	0.96	95	3.87E-08	0.76
H2	282	5.86E-09	0.78	346	1.25E-08	1
CO2	38	3.68E-06	0.71	167	1.97E-06	1
CH4	171	1.29E-06	0.91	58	4.87E-07	0.66
nC4H10	14	2.59E-19	6.3	69	2.23E-03	0.86

7.3 List of Figures for Unary Diffusion in Microporous Materials

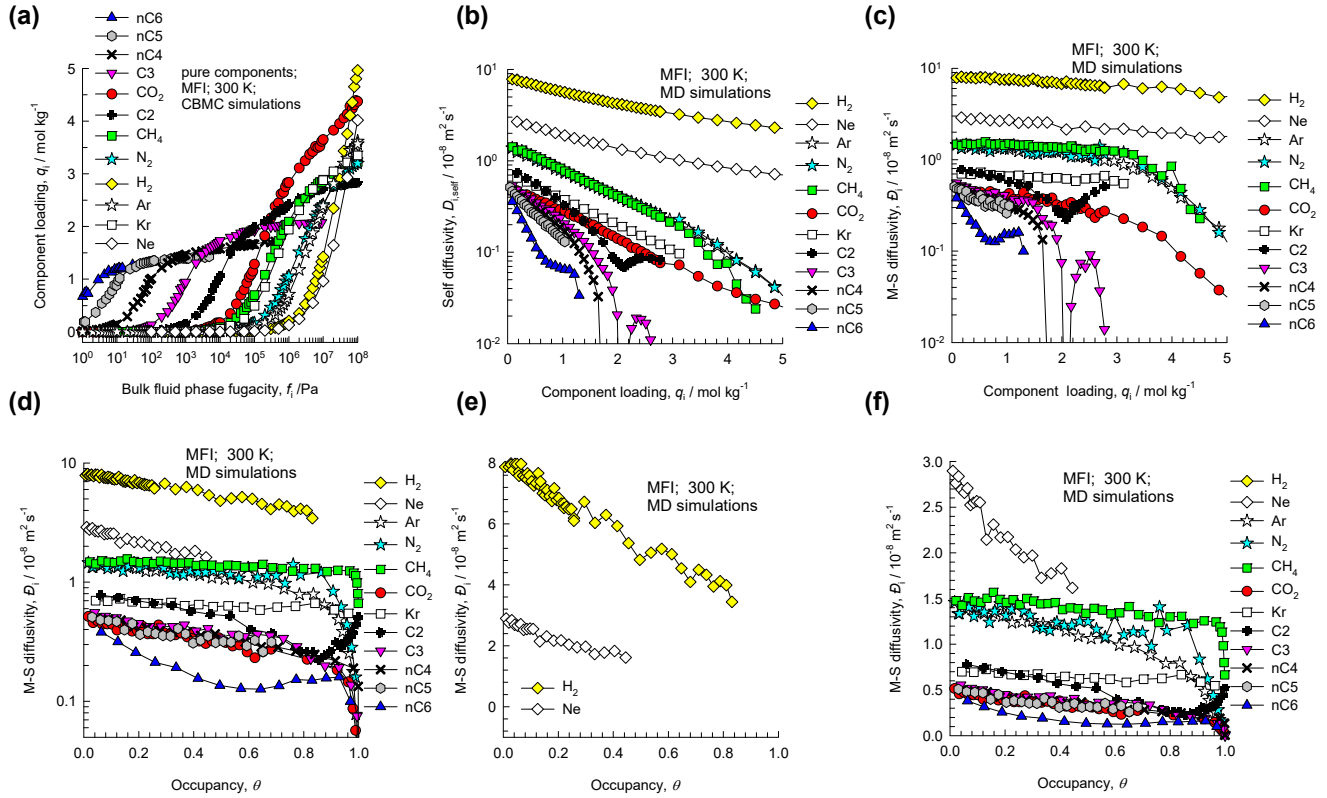

Figure S7-1. CBMC simulations of unary adsorption isotherms, along with MD simulations of unary self-diffusivities, $D_{i,self}$, and Maxwell-Stefan diffusivities, $Đ_i$, for a variety of guest molecules in MFI zeolite at 300 K. The M-S diffusivity data is plotted both as function of the molar loading, q_i, and the occupancy, determined from Equation (6-4), where the saturation capacity is determined from the unary isotherm fits.

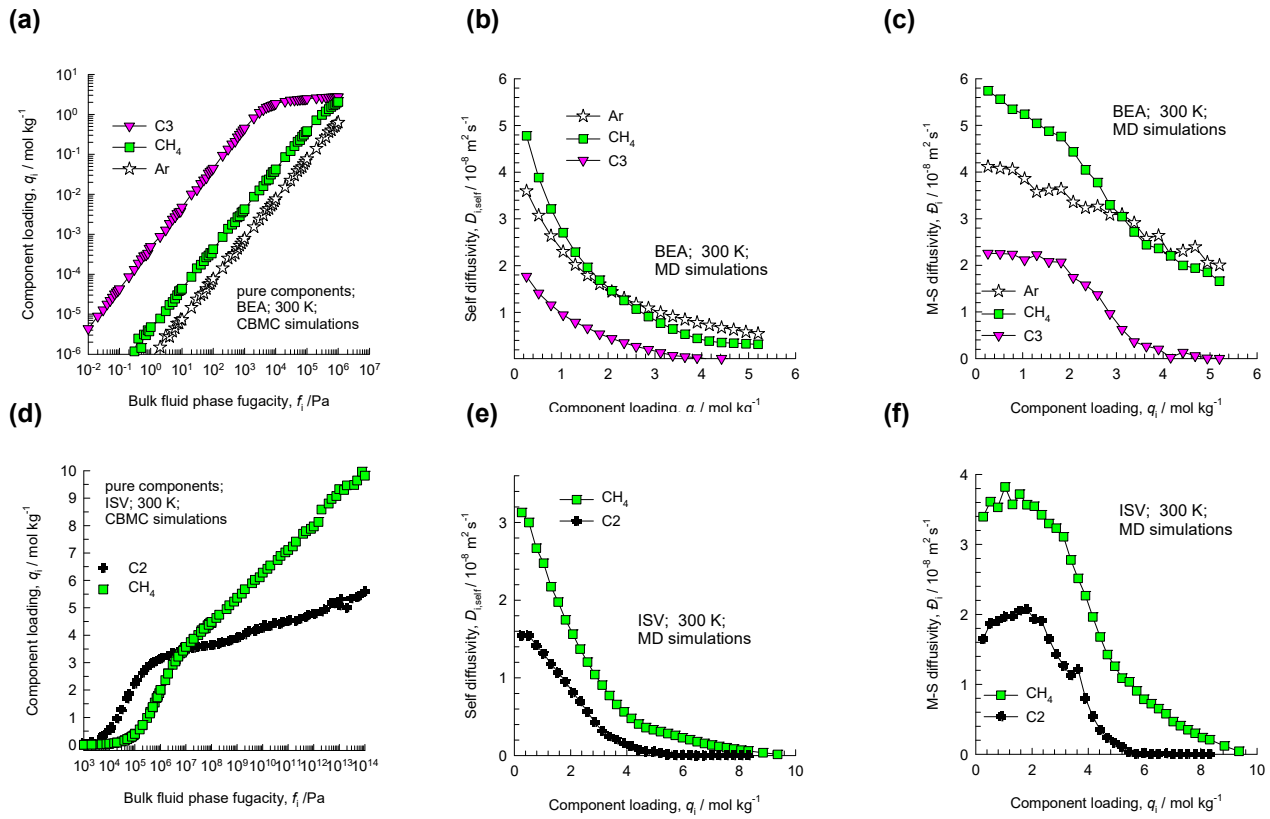

Figure S7-2. CBMC simulations of unary adsorption isotherms, along with MD simulations of unary self-diffusivities, $D_{i,self}$, and Maxwell-Stefan diffusivities, $Đ_i$, for a variety of guest molecules in BEA, and ISV all-silica zeolites at 300 K.

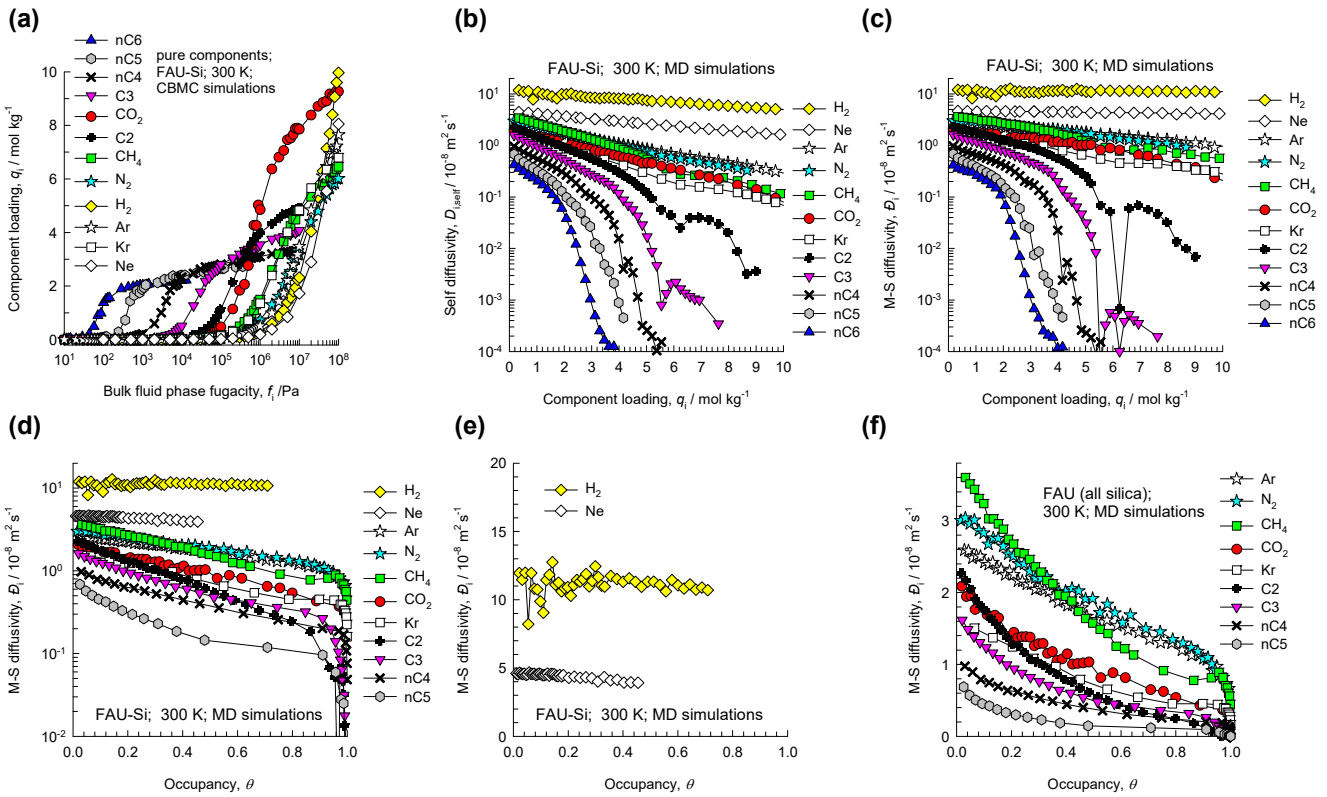

Figure S7-3. CBMC simulations of unary adsorption isotherms, along with MD simulations of unary self-diffusivities, $D_{i,self}$, and Maxwell-Stefan diffusivities, $Đ_i$, for a variety of guest molecules in FAU all-silica zeolite at 300 K. The M-S diffusivity data is plotted both as function of the molar loading, q_i, and the occupancy, determined from Equation (6-4), where the saturation capacity is determined from the unary isotherm fits.

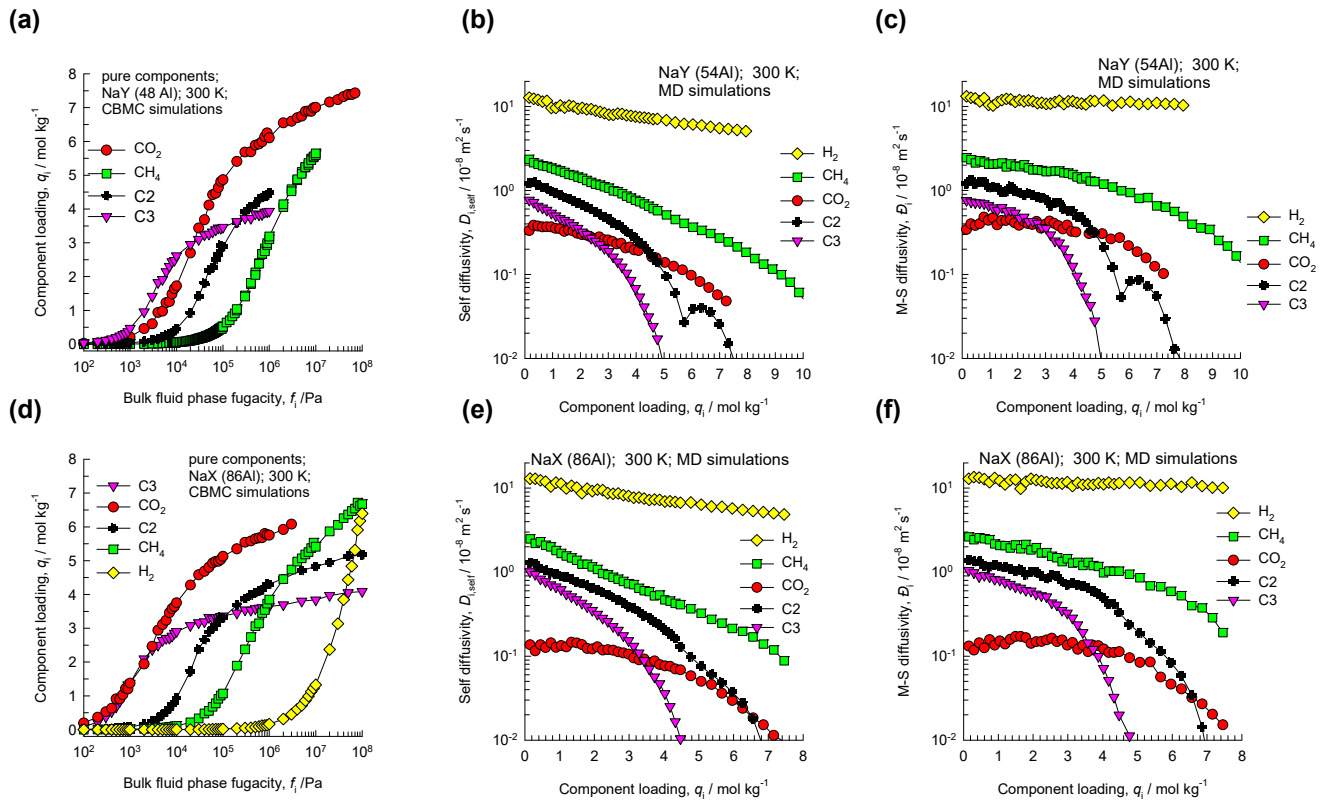

Figure S7-4. CBMC simulations of unary adsorption isotherms, along with MD simulations of unary self-diffusivities, $D_{i,self}$, and Maxwell-Stefan diffusivities, $Đ_i$, for a variety of guest molecules in NaY zeolite (48 Al per uc), and NaX zeolite (86 Al per uc) at 300 K.

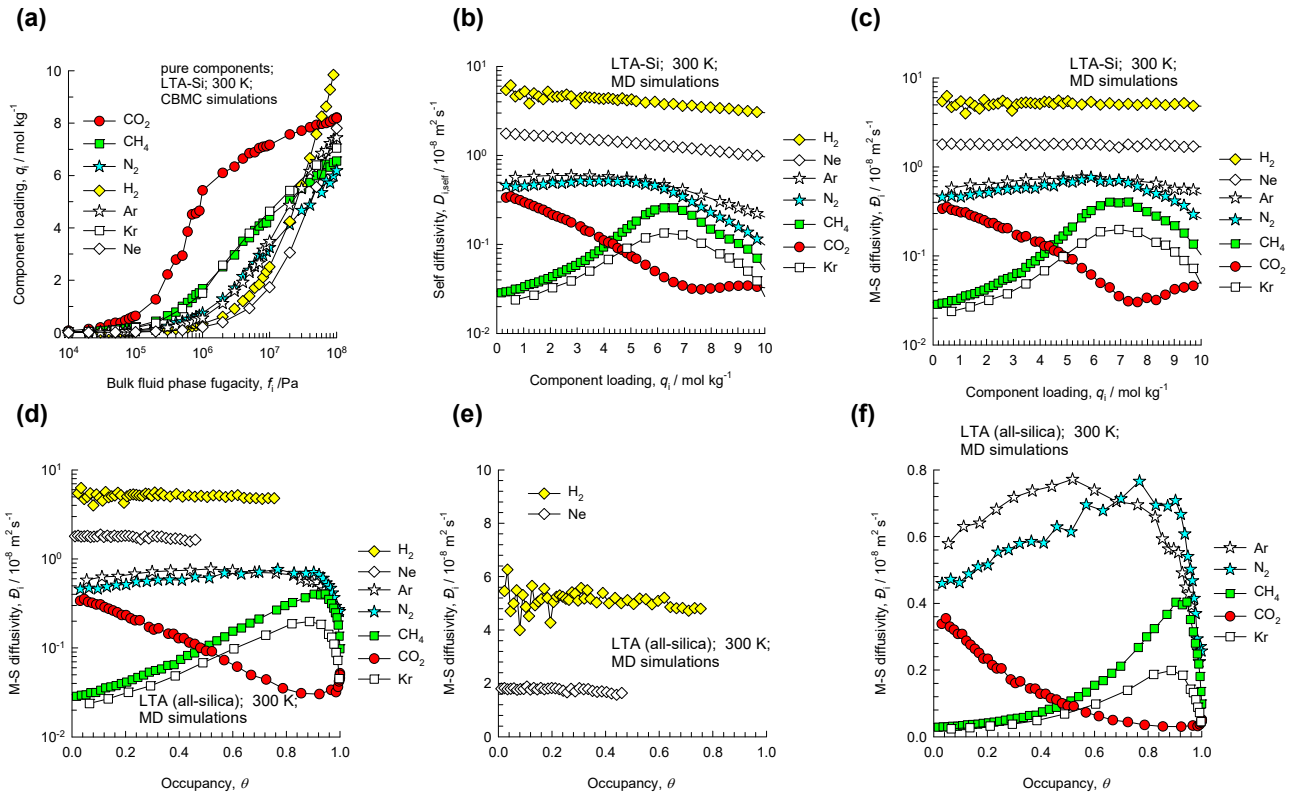

Figure S7-5. CBMC simulations of unary adsorption isotherms, along with MD simulations of unary self-diffusivities, $D_{i,self}$, and Maxwell-Stefan diffusivities, $Đ_i$, for a variety of guest molecules in LTA all-silica zeolite at 300 K. The M-S diffusivity data is plotted both as function of the molar loading, q_i, and the occupancy, determined from Equation (6-4), where the saturation capacity is determined from the unary isotherm fits.

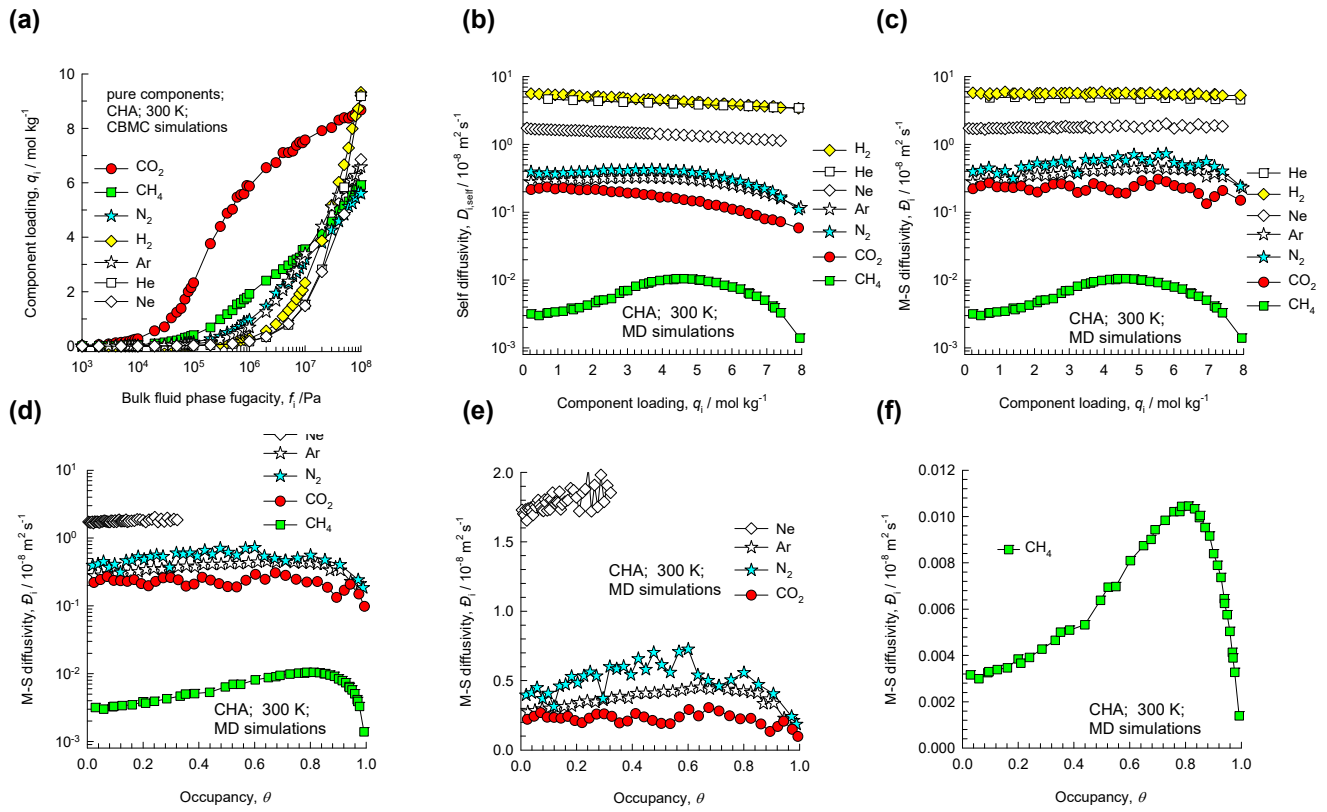

Figure S7-6. CBMC simulations of unary adsorption isotherms, along with MD simulations of unary self-diffusivities, $D_{i,self}$, and Maxwell-Stefan diffusivities, $Đ_i$, for a variety of guest molecules in CHA all-silica zeolite at 300 K. The M-S diffusivity data is plotted both as function of the molar loading, q_i, and the occupancy, determined from Equation (6-4), where the saturation capacity is determined from the unary isotherm fits.

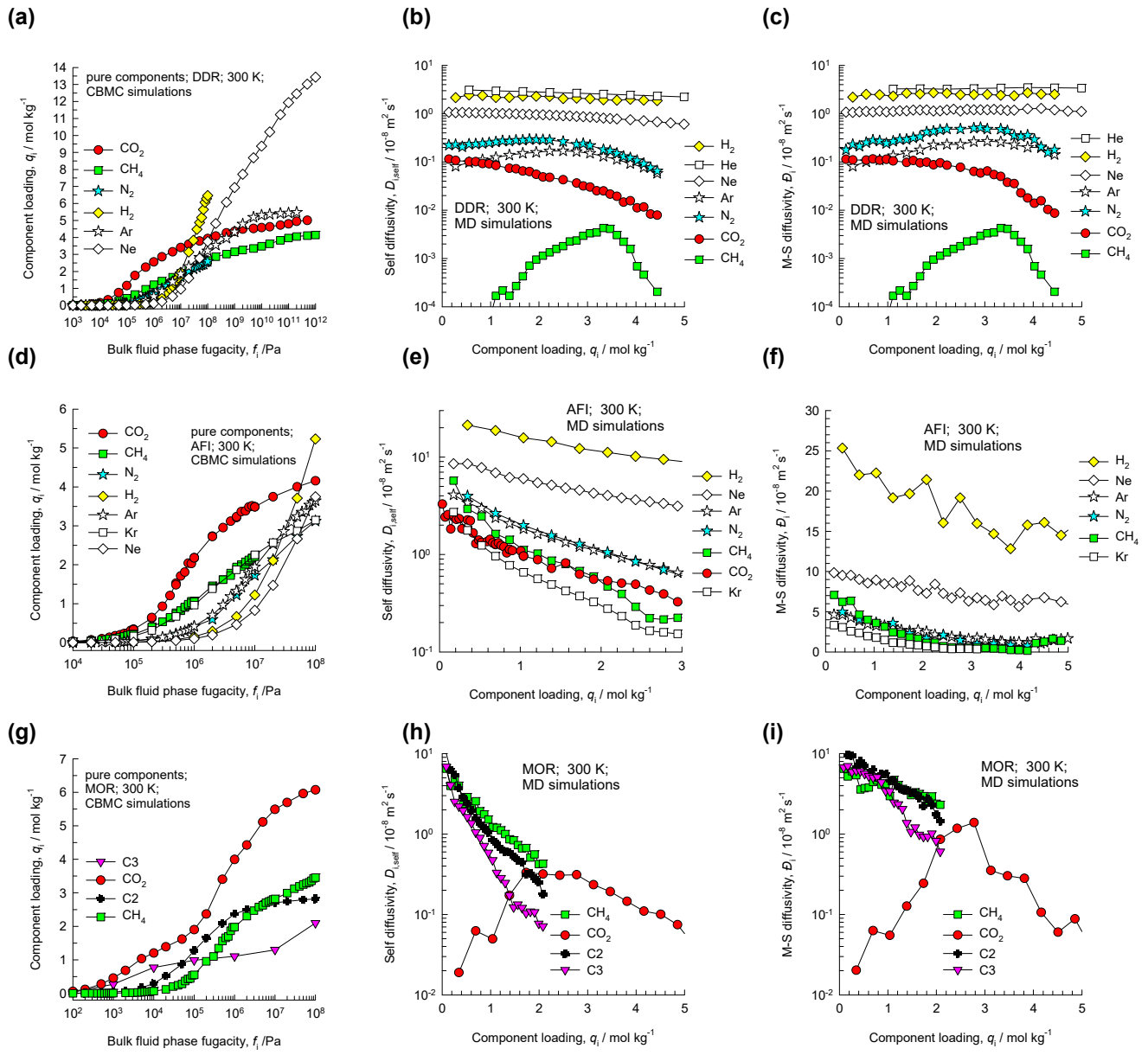

Figure S7-7. CBMC simulations of unary adsorption isotherms, along with MD simulations of unary self-diffusivities, $D_{i,self}$, and Maxwell-Stefan diffusivities, $Đ_i$, for a variety of guest molecules in DDR, AFI, and MOR zeolites at 300 K.

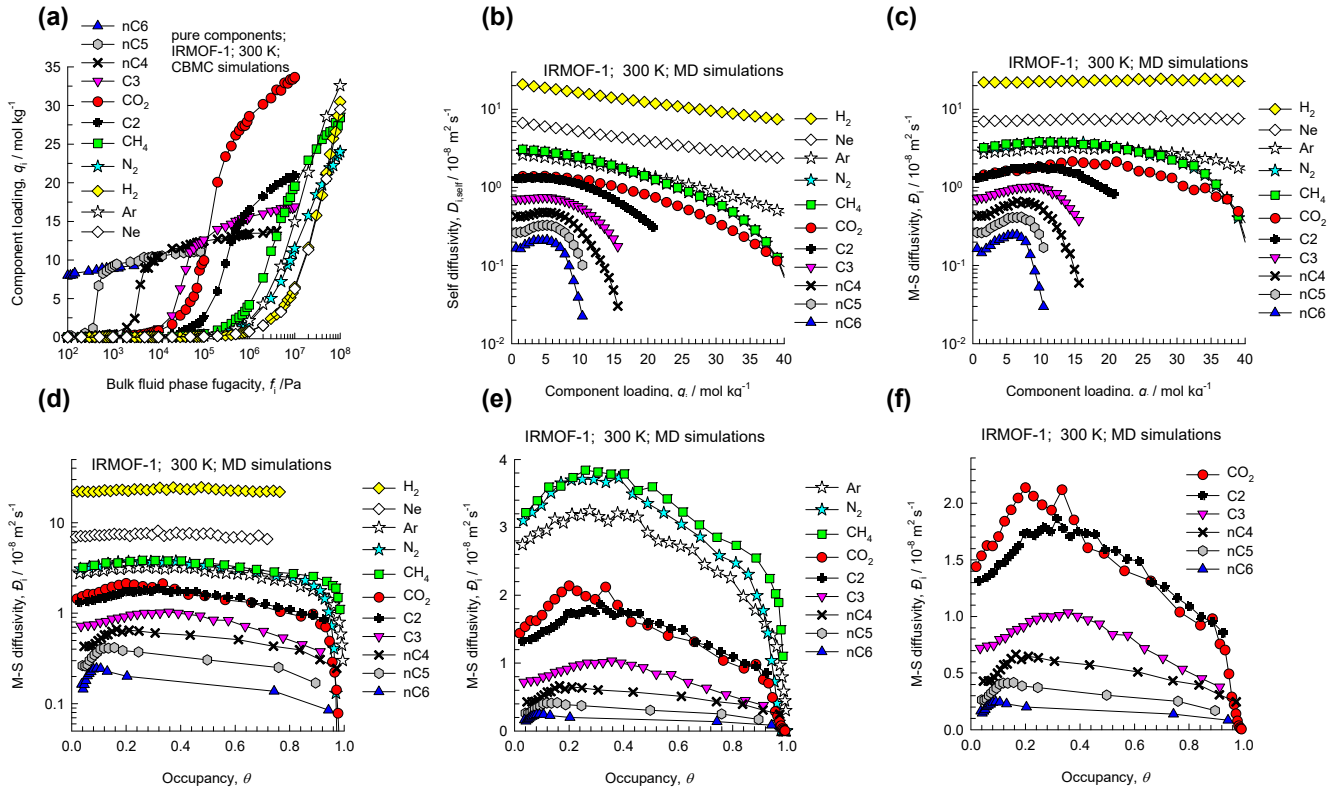

Figure S7-8. CBMC simulations of unary adsorption isotherms, along with MD simulations of unary self-diffusivities, $D_{i,self}$, and Maxwell-Stefan diffusivities, $Đ_i$, for a variety of guest molecules in IRMOF-1 at 300 K. The M-S diffusivity data is plotted both as function of the molar loading, q_i, and the occupancy, determined from Equation (6-4), where the saturation capacity is determined from the unary isotherm fits.

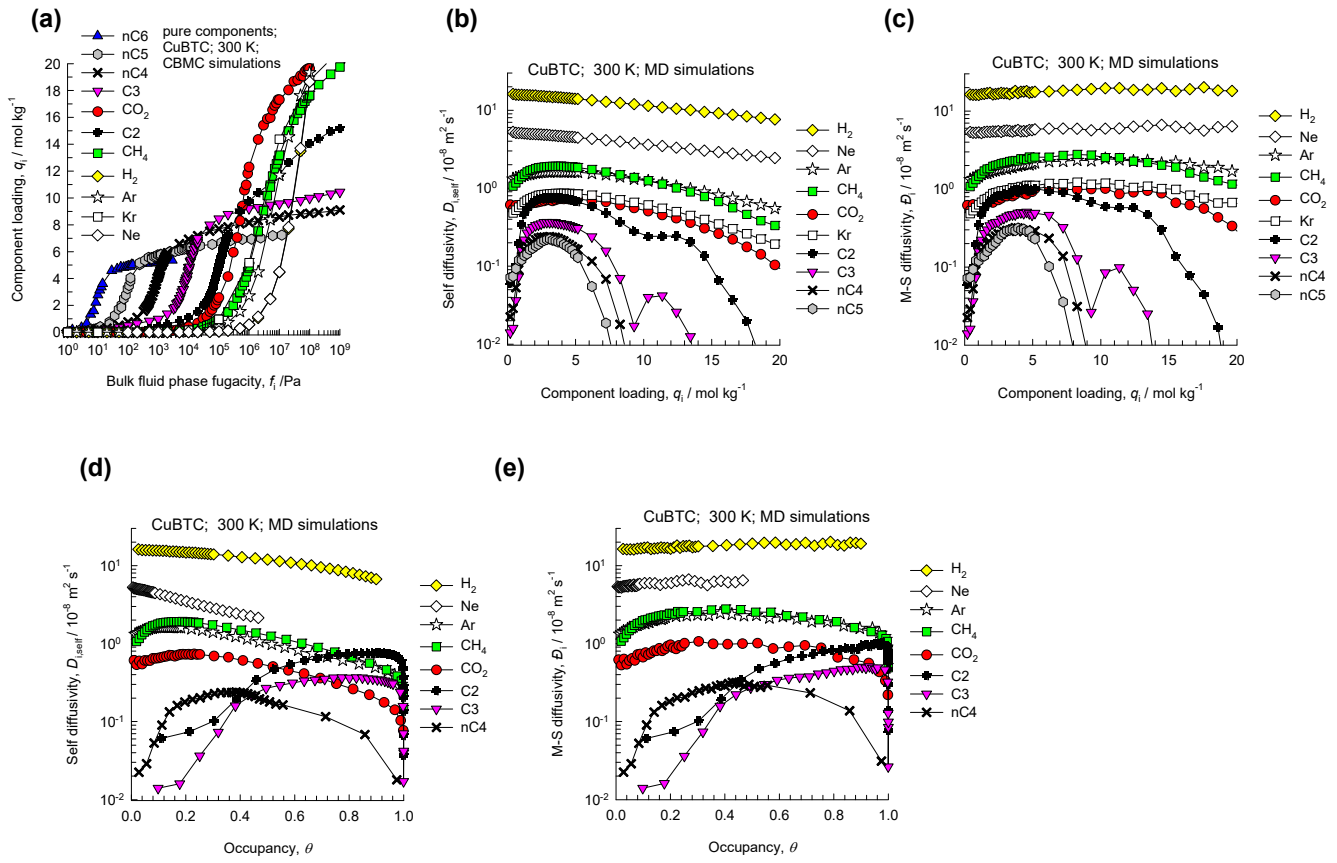

Figure S7-9. CBMC simulations of unary adsorption isotherms, along with MD simulations of unary self-diffusivities, $D_{i,self}$, and Maxwell-Stefan diffusivities, $Đ_i$, for a variety of guest molecules in CuBTC at 300 K.

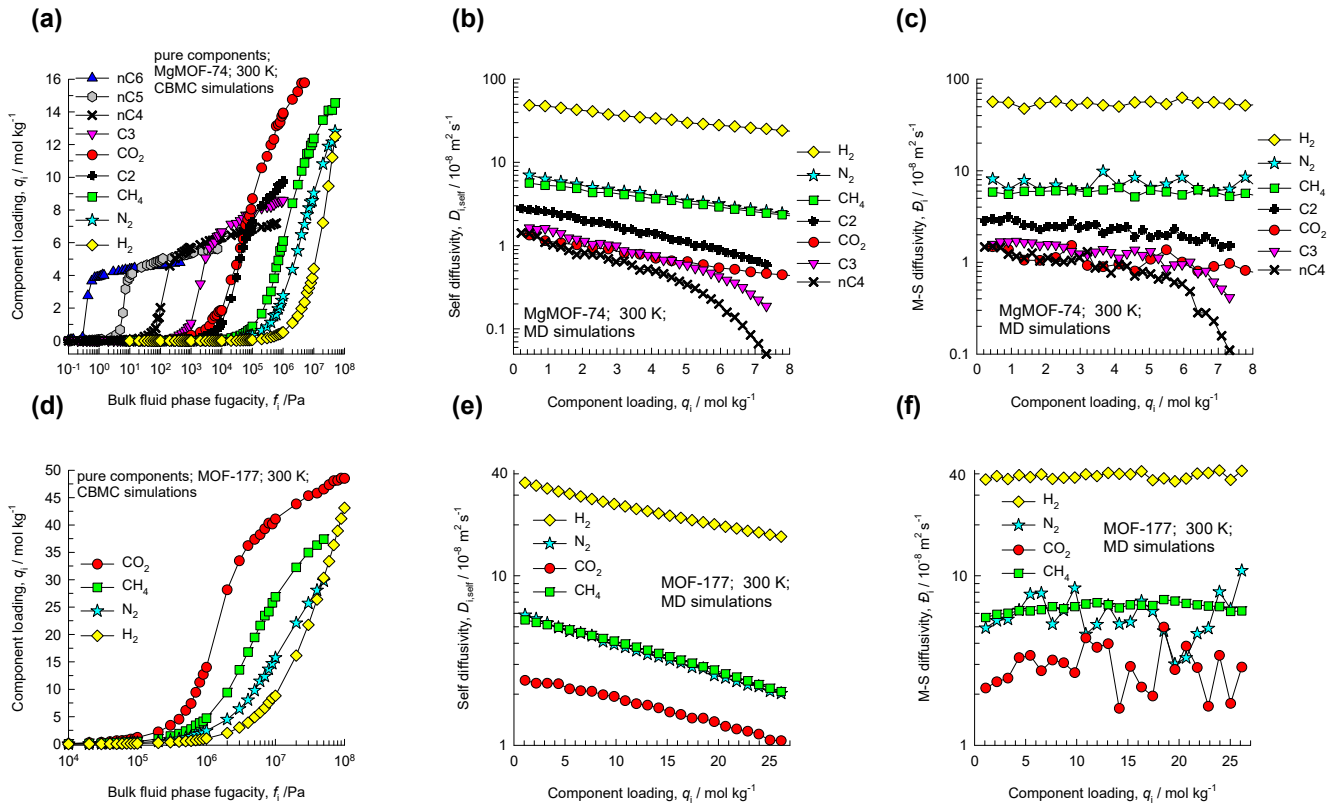

Figure S7-10. CBMC simulations of unary adsorption isotherms, along with MD simulations of unary self-diffusivities, $D_{i,self}$, and Maxwell-Stefan diffusivities, $Đ_i$, for a variety of guest molecules in MgMOF-74, and MOF-177 at 300 K.

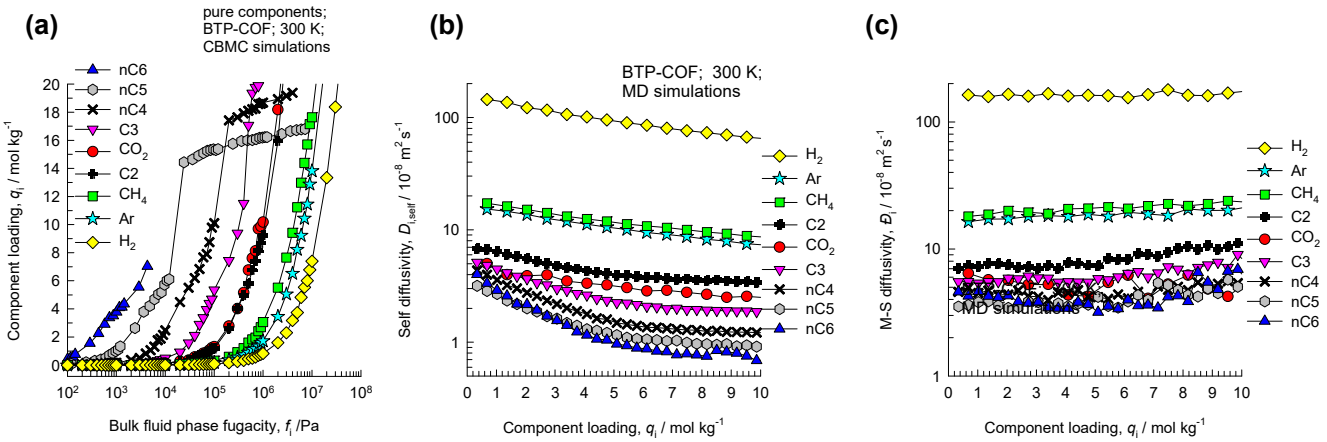

Figure S7-11. CBMC simulations of unary adsorption isotherms, along with MD simulations of unary self-diffusivities, $D_{i,self}$, and Maxwell-Stefan diffusivities, $Đ_i$, for a variety of guest molecules in BTP-COF at 300 K.

$$-\frac{d\mu_1}{dz} = -RT\frac{d\ln p_1}{dz} = \frac{RT}{Đ_{12}}\theta_2(u_1 - u_2) + \frac{RT}{Đ_{1V}}\theta_V(u_1 - u_V)$$

$$-\frac{d\mu_2}{dz} = -RT\frac{d\ln p_2}{dz} = \frac{RT}{Đ_{12}}\theta_1(u_2 - u_1) + \frac{RT}{Đ_{2V}}\theta_V(u_2 - u_V)$$

Fractional vacancy

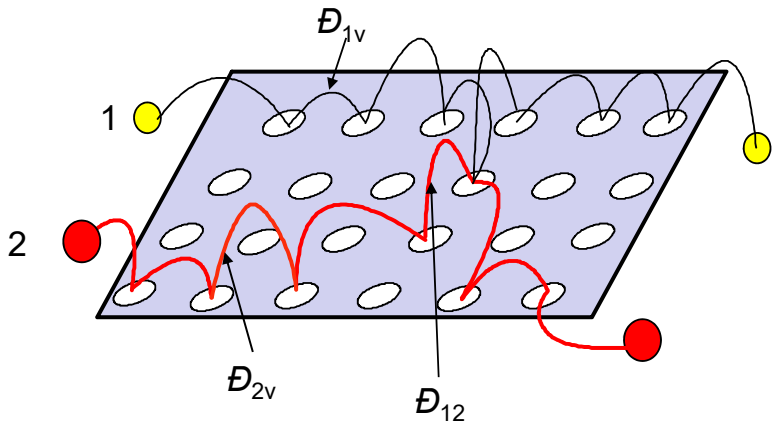

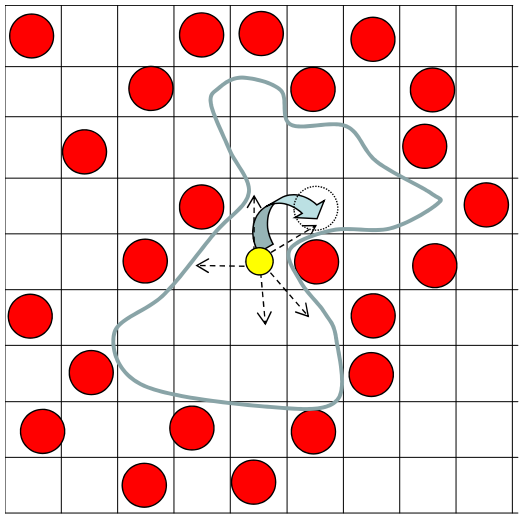

$$Đ_{iV} = \frac{1}{4}a^2\nu_i$$

Exchange coefficient quantifying correlations

Figure S7-12. The Maxwell- Stefan description of hopping of molecules on a 2D surface.

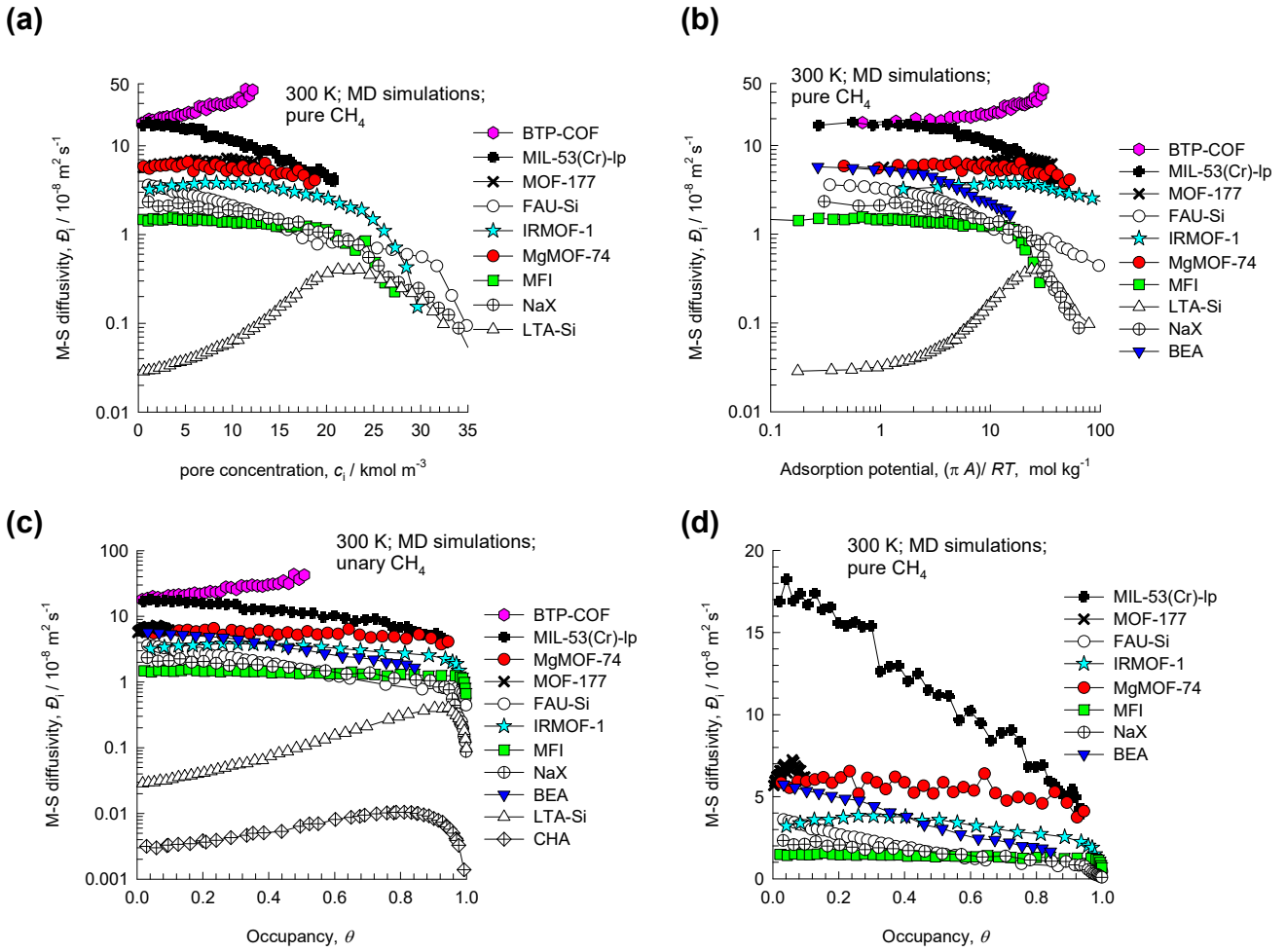

Figure S7-13. MD simulations of Maxwell-Stefan diffusivity, $Đ_i$, of CH_4 in a variety of host structures. as a function of the (a) pore concentrations c_i, (b) adsorption potential, (c, d) occupancies, determined from Equation (6-4), where the saturation capacity is determined from the unary isotherm fits.

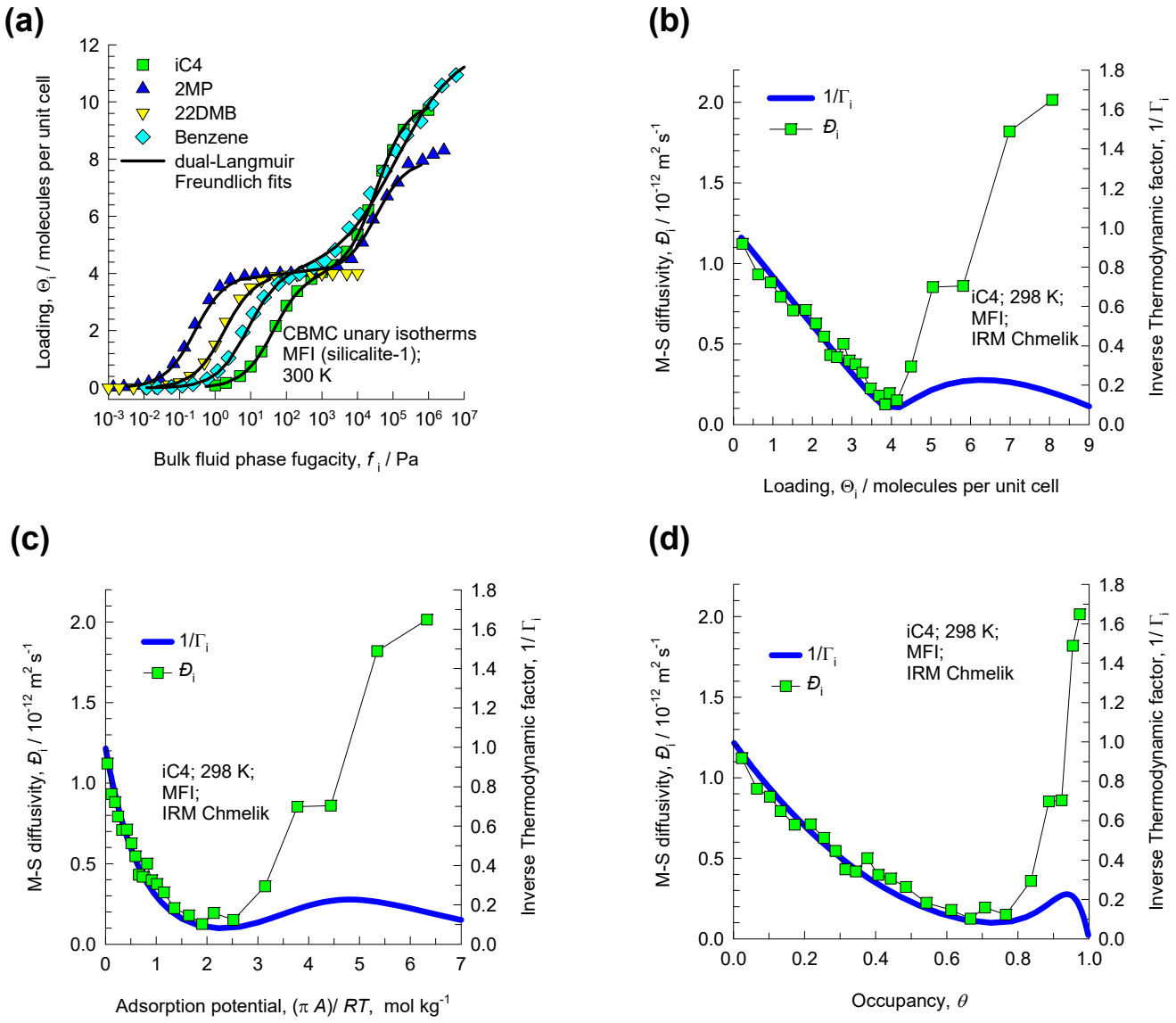

Figure S7-14. (a) CBMC simulations of unary adsorption isotherms for branched alkanes, and benzene in MFI zeolite at 300 K. (b, c, d) Experimental data[90] on the M-S diffusivity, $Đ_i$, of is-butane in MFI at 298 K as a function of (b) loading Θ_i, expressed in molecules uc^{-1}, (c) adsorption potential, (d) occupancy, determined from Equation (6-4), where the saturation capacity is determined from the unary isotherm fits.

8 Correlation Effects for Unary Diffusion in Microporous Materials

8.1 Unary self-exchange diffusivities, $Đ_{ii}$

MD simulations of the values of $D_{i,self}$, $Đ_i$, along with the $Đ_{ii}$ calculated using Equation (7-7), for CH_4 diffusion are shown in Figure S8-1 for six different host structures. At any pore concentration, $D_{i,self} \leq Đ_i$; this is because individual jumps of molecules are *correlated* due to re-visitation of sorption sites that have been recently vacated. The extent of correlations is captured by the self-exchange coefficient $Đ_{ii}$. For all structures, in the limit of low pore concentrations, $c_i \to 0$; $q_i \to 0$, molecule-molecule interactions are of negligible importance, and $Đ_{ii}$ is significantly higher than $D_{i,self}$ and $Đ_i$. Correlations become increasingly significant as the pore concentrations are increased, and this is evidenced by the observation that $Đ_{ii}$ decreases more sharply with increasing c_i, than the M-S diffusivity $Đ_i$. As pore saturation conditions are approached, the diffusion characteristics are dominated by correlation effects.[15, 91]

The relative importance of molecule-wall and molecule-molecule interactions is different for each structure. In meso-porous materials, the self-exchange coefficient $Đ_{ii}$ can be identified with the self-diffusivity in the *fluid* phase, $Đ_{ii,fl}$, over the entire range of pore concentrations.[62] This is demonstrated by the data for BTP-COF that has 1D hexagonal-shaped channels of 34 Å size; see Figure S8-1(f). For BTP-COF we note that $Đ_{ii} \approx Đ_{ii,fl}$ and the self-diffusivity is described by

$$\frac{1}{D_{i,self}} = \frac{1}{Đ_i} + \frac{1}{Đ_{ii,fl}} \tag{8-1}$$

over the entire range of concentrations; this conclusion is valid for all guest molecules in meso-porous channels.[62, 76, 82, 83] The expression (8-1), with the Knudsen prescription for $Đ_i$, was developed by Bosanquet in a classified report dated September 27, 1944, and this interpolation formula only became known when it was later cited by Pollard and Present;[92] see also Krishna and van Baten.[83]

Correlations are relatively weak for LTA-5A in which the diffusivities are largely dictated by hopping of molecules, one-at-a-time, across 4 Å × 4.58 Å size windows; this is evidenced by the fact that $D_{i,self} \approx$

$Đ_i$ for $c_i < 20$ kmol m^{-3}; see Figure S8-1(c). Correlations in LTA-5A become of importance only at higher pore concentrations; these conclusions are also valid for other cage-type structures such as CHA, DDR, ITQ-29, ERI, and ZIF-8.[11, 63] The constraining window regions offer significant free energy barriers for inter-cage hopping of molecules. An important consequence is that the free energy of the molecules within the cage increases with increasing cage occupancy. The net result is that there is a reduction in the free energy barrier for inter-cage hopping; this results in an increase in the M-S diffusivity with occupancy;[7-14] this is also evidenced in Figure S7-5, and Figure S7-6. The increase of $Đ_i$ with loading, or occupancy, is not monotonic because the cage capacity is limited and there are fewer intra-cage vacant sites to occupy. As the saturation loading is approached, progressively fewer vacant sites become available, $\theta_V \to 0$; the net result is a sharp reduction in the M-S diffusivity at pore saturation.

The self-exchange coefficients $Đ_{ii}$ were determined for several guest/host combinations from unary MD simulations.[11, 62] In each case the $Đ_{ii}$ is also a fraction, F, defined as

$$F \equiv Đ_{ii} / Đ_{ii,fl} \tag{8-2}$$

of the corresponding value of the fluid phase $Đ_{ii,fl}$; see data in Figure S8-2 for nine different guest/host combinations. For micro-porous materials, the values of $Đ_{ii}$ are lower than $Đ_{ii,fl}$ by a factor F; this factor is practically constant over the entire range of pore concentrations.[11, 62]

Generally speaking, the more "open" the structure, the closer is the value of F to unity. Conversely, for structures in which the structures are strongly confined, the fraction F is significantly below unity. The extent of lowering depends on pore size, pore topology and connectivity. In MFI zeolite, the factor $F \approx 0.1$. For MgMOF-74, NaX, and IRMOF-1, the factor F falls in the range 0.4 – 0.7. Figure S8-3 presents a plot of the F plotted against the pore volume of the porous host structures, V_p. The correlation is not perfect, suggesting that other aspects such as channel dimensions, and pore connectivity are also determinants of the exchange coefficient $Đ_{ii}$.

8.2 Degree of correlations for unary diffusion, $Đ_i/Đ_{ii}$

For the analysis of binary mixture diffusion, to be discussed in the subsequent chapter, it is convenient to define the degree of correlations for unary diffusion in microporous materials, as $\frac{Đ_i}{Đ_{ii}}$. In view Equation (7-7) we get

$$\frac{Đ_i}{Đ_{ii}} = \frac{Đ_i}{D_{i,self}} - 1 \tag{8-3}$$

Equation (8-3) shows that the degree of correlations can be determined from MD simulations of $D_{i,self}$ and $Đ_i$. The persuasive reason for defining the degree of correlations, $\frac{Đ_i}{Đ_{ii}}$, is that this metric portrays a practically linear dependence on the pore concentration, c_i, for any guest species in different host structures; as evidence see the plots in Figure S8-4 for nine different guest species in a variety of hosts. The degree of correlations are particular strong in mesoporous BTP-COF, in the intersecting channel structures of MFI, BEA zeolites, and "open" structures such as IRMOF-1, CuBTC, FAU, NaY, NaX. The degree of correlations are significantly low in cage-type structures such as LTA, CHA, DDR, ERI in which the cages are separated by narrow 8-ring windows. The degree of correlations are small because the molecules jump one-at-a-time across the window.

For any given host material, the degree of correlations, $\frac{Đ_i}{Đ_{ii}}$, for different guest molecules need to be compared at the same fractional occupancy, θ, determined from Equation (6-4). Figure S8-5 shows the data for $\frac{Đ_i}{Đ_{ii}}$, determined from MD simulations for a variety of guest molecules in (a) MFI, (b) all-silica FAU, (c) IRMOF-1, and (d) CuBTC. The relationship between $\frac{Đ_i}{Đ_{ii}}$ and is practically linear as a function of the fractional occupancy. The important advantage of the linear dependence of $\frac{Đ_i}{Đ_{ii}}$ on the occupancy θ is that the data can be simply extrapolated to saturation conditions: $\theta \to 1$. We will

exploit the linear dependence of $\frac{Đ_i}{Đ_{ii}}$ on θ for estimating the degrees of correlations for binary mixture diffusion in a later Chapter.

A further advantage of using the defining the degree of correlations $\frac{Đ_i}{Đ_{ii}}$ is that there is no need to further model the occupancy dependence of the exchange coefficient, $Đ_{ii}$, because this dependence has been related to that of the M-S diffusivity for which we need to use the appropriate models (e.g. Reed-Ehrlich) to quantify the occupancy dependence.

8.3 List of Figures for Correlation Effects for Unary Diffusion in Microporous Materials

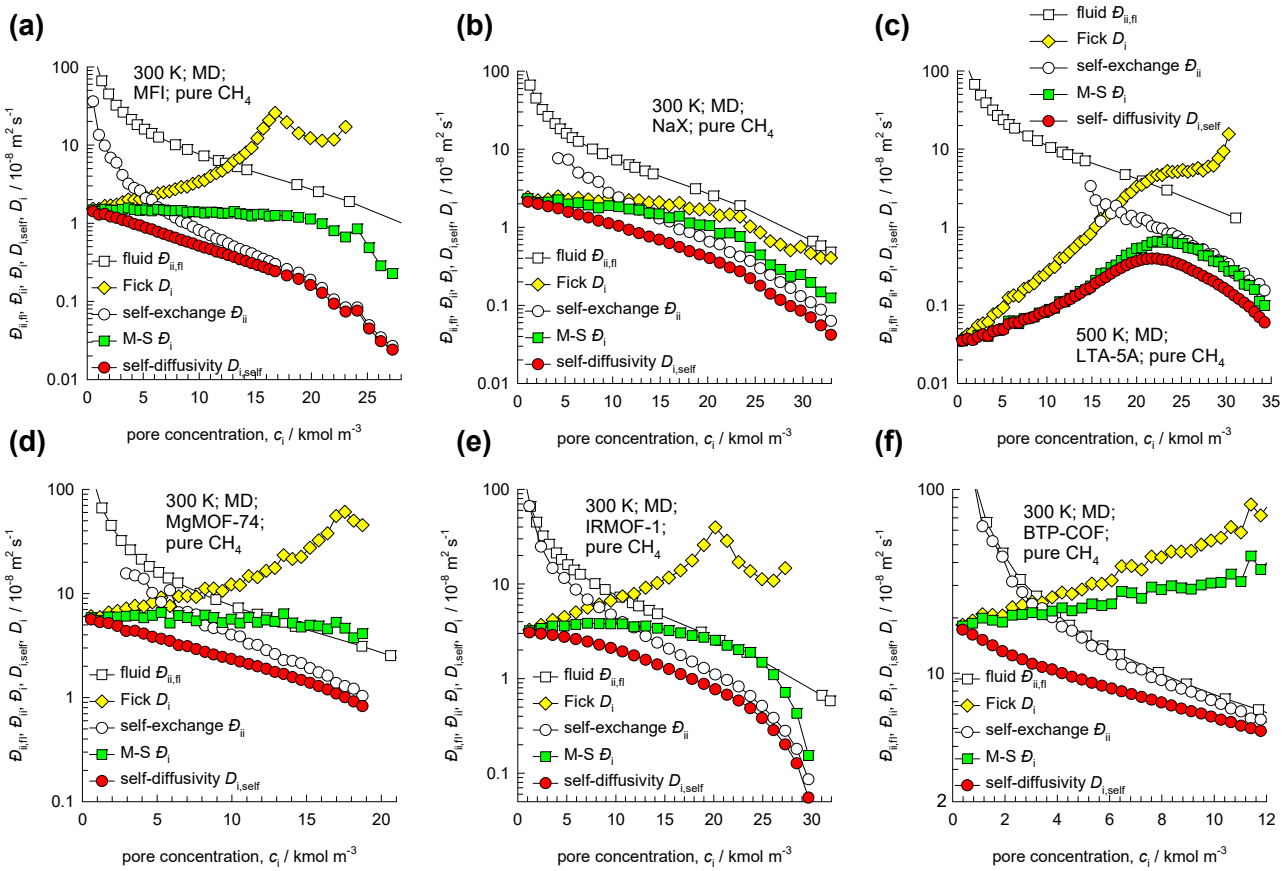

Figure S8-1. MD simulations of self-diffusivity $D_{i,self}$, Maxwell-Stefan diffusivity $Đ_i$, self-exchange coefficient $Đ_{ii}$, and Fick diffusivity D_i, for CH_4 in (a) MFI, (b) NaX, (c) LTA-5A, (d) MgMOF-74, (e) IRMOF-1, and (f) BTP-COF, as a function of the pore concentrations c_i. Also indicated by open square symbols are the values of the fluid phase self-diffusivities, $Đ_{ii,fl}$, determined from MD simulations using the same force field parameters. Note that the data for LTA-5A is at 500 K, whereas the rest of the data are for 300 K.

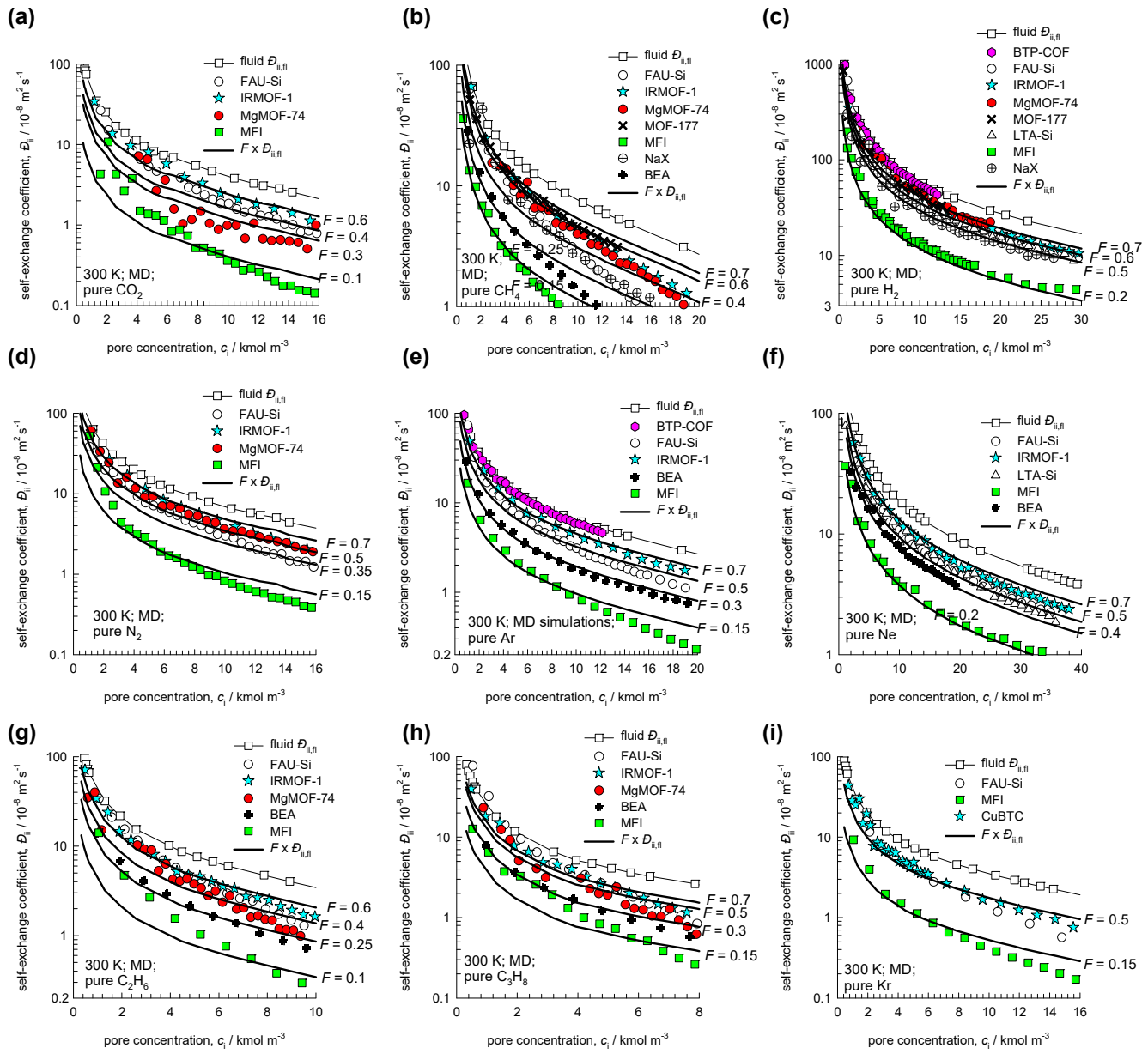

Figure S8-2. The self-exchange coefficients $Đ_{ii}$, for unary diffusion of (a) CO_2, (b) CH_4, (c) H_2, (d) N_2, (e) Ar, (f) Ne, (g) C_2H_6, (h) C_3H_8, and (i) Kr at 300 K in a variety of host materials as a function of the pore concentration, c_i. The $Đ_{ii,fl}$ for self-diffusivity in the *fluid phase*, obtained from independent MD simulations, are also presented in square symbols, along with continuous solid lines that represent the fraction F times $Đ_{ii,fl}$. The MD data are culled from our previous publications.[7, 10, 13, 14, 16, 62, 63, 77, 80-83]

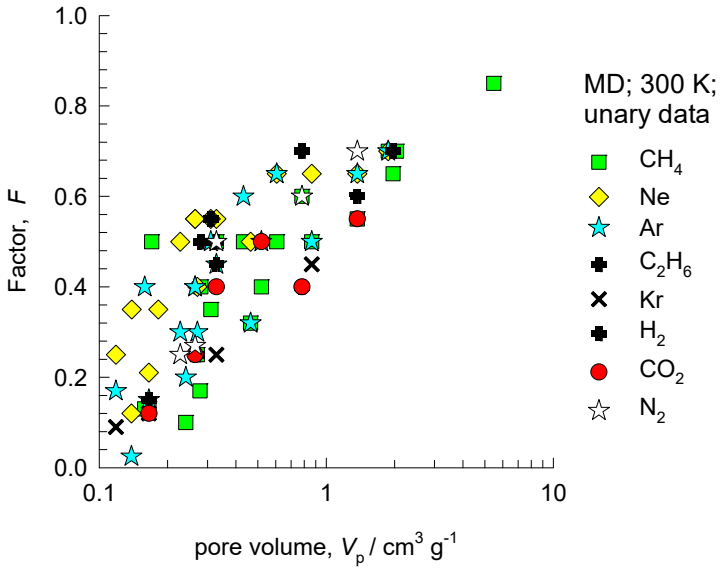

Figure S8-3. Fraction F determined from MD simulations of the self-exchange coefficient for unary diffusion, expressed as a function of the pore volume of the micro-porous host structures, V_p.

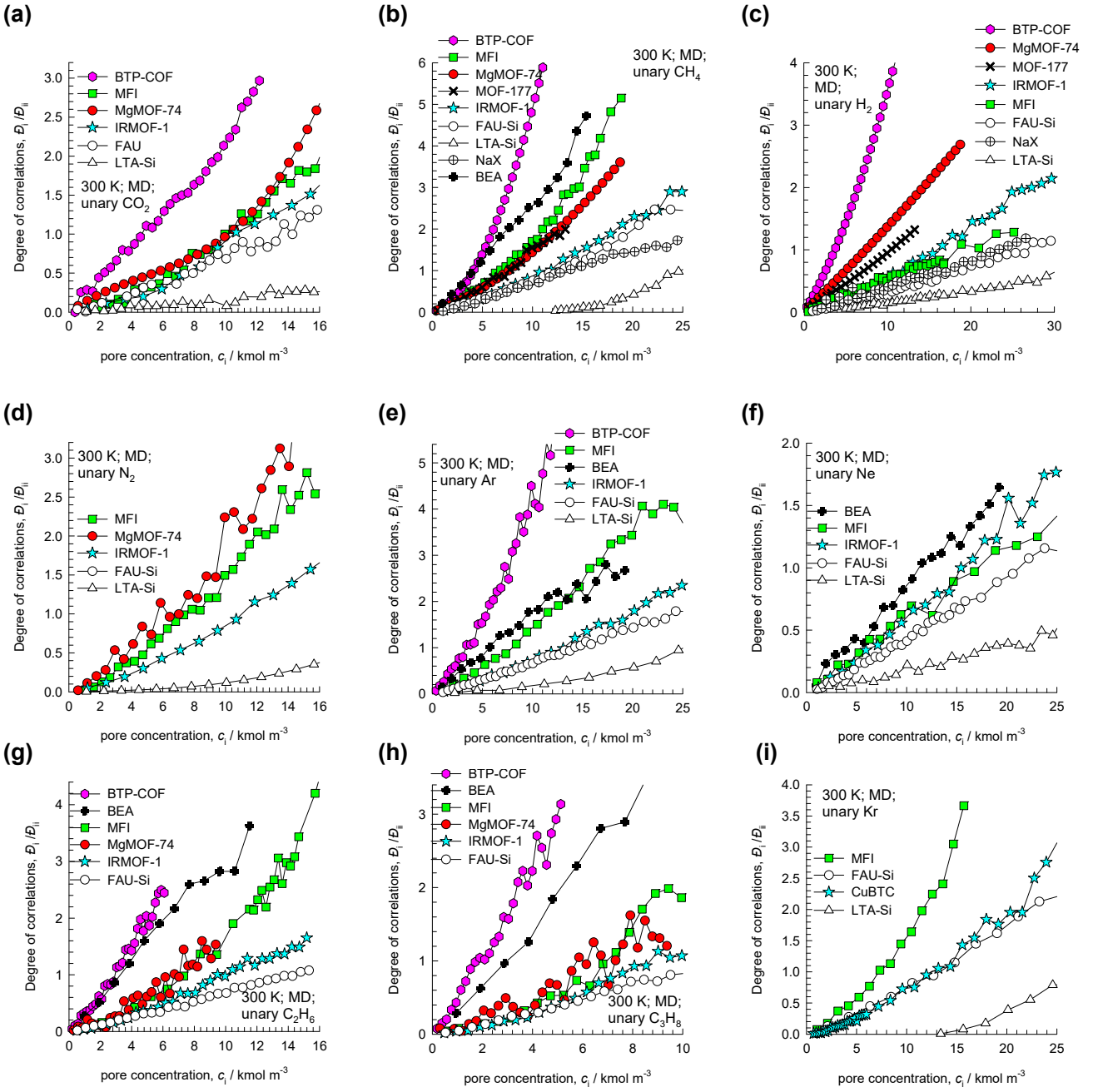

Figure S8-4. The degree of correlations, $Đ_i/Đ_{ii}$, for unary diffusion of (a) CO_2, (b) CH_4, (c) H_2, (d) N_2, (e) Ar, (f) Ne, (g) C_2H_6, (h) C_3H_8, and (i) Kr at 300 K in a variety of host materials as a function of the pore concentration, c_i. The MD data are culled from our previous publications.[7, 10, 13, 14, 16, 62, 63, 77, 80-83]

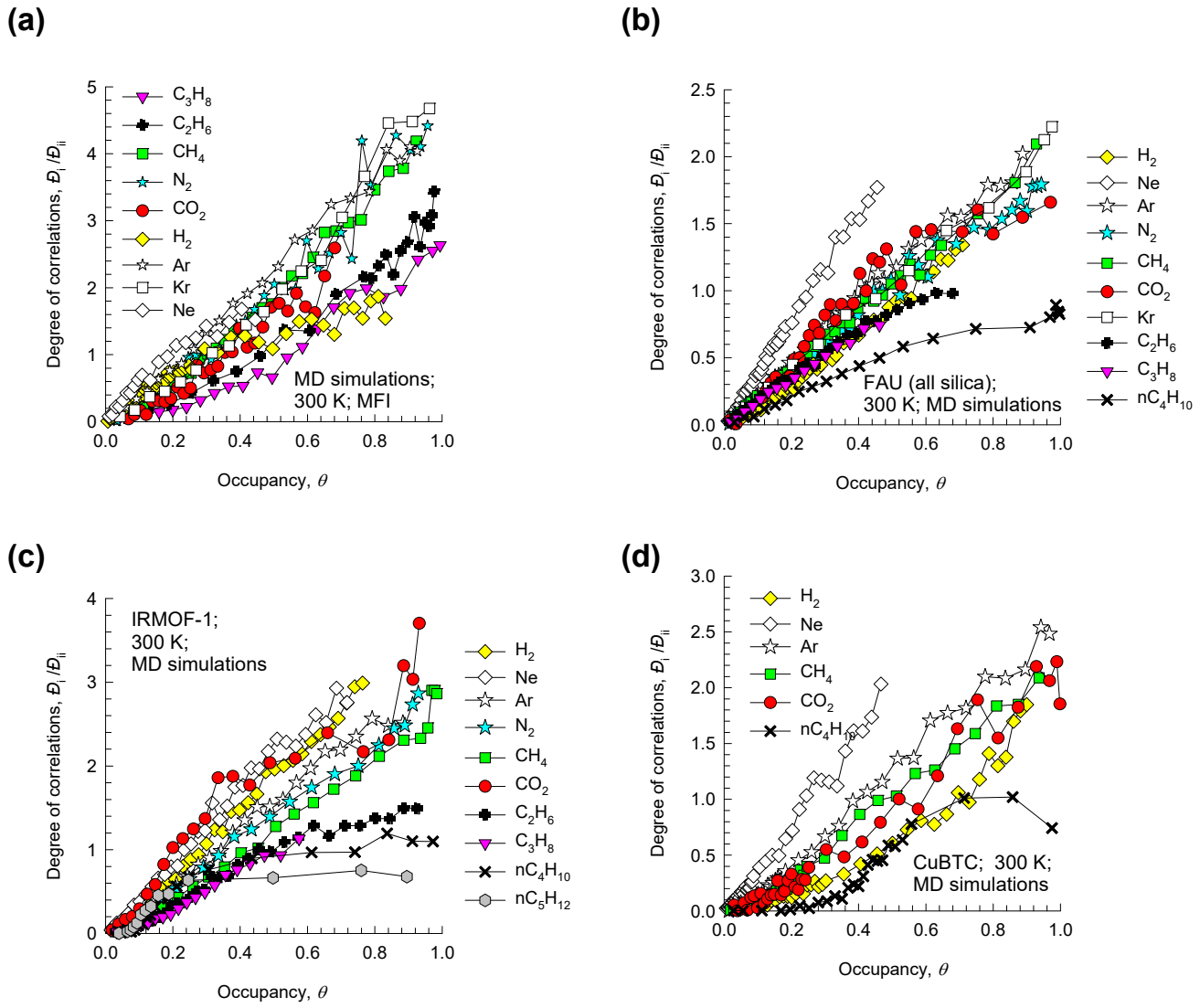

Figure S8-5. The degree of correlations, $Đ_i/Đ_{ii}$, for unary diffusion of a variety of guest molecules in (a) MFI, (b) all-silica FAU, (c) IRMOF-1, and (d) CuBTC as a function of the occupancy, determined from Equation (6-4), where the saturation capacity is determined from the unary isotherm fits.

9 Diffusion of Binary Mixtures in Microporous Materials

9.1 M-S formulation for binary mixture diffusion

For binary mixture diffusion inside microporous crystalline materials the Maxwell-Stefan equations (6-10) are written

$$\begin{aligned} -\rho\frac{q_1}{RT}\frac{d\mu_1}{dz} &= \frac{x_2N_1 - x_1N_2}{Đ_{12}} + \frac{N_1}{Đ_1} \\ -\rho\frac{q_2}{RT}\frac{d\mu_2}{dz} &= \frac{x_1N_2 - x_2N_1}{Đ_{12}} + \frac{N_2}{Đ_2} \end{aligned} \tag{9-1}$$

The first members on the right hand side of Equation (9-1) are required to quantify slowing-down effects that characterize binary mixture diffusion.[7, 9, 11] There is no experimental technique for direct determination of the exchange coefficients $Đ_{12}$, that quantify molecule-molecule interactions.

In two-dimensional matrix notation, equation (6-16) take the form

$$-\begin{pmatrix} \frac{q_1}{RT}\frac{d\mu_1}{dz} \\ \frac{q_2}{RT}\frac{d\mu_2}{dz} \end{pmatrix} = [\Gamma]\begin{pmatrix} \frac{dq_1}{dz} \\ \frac{dq_2}{dz} \end{pmatrix} \tag{9-2}$$

For the mixed-gas Langmuir model, equation (6-17), we can derive simple analytic expressions for the four elements of the matrix of thermodynamic factors:[84]

$$\begin{bmatrix} \Gamma_{11} & \Gamma_{12} \\ \Gamma_{21} & \Gamma_{22} \end{bmatrix} = \frac{1}{1-\theta_1-\theta_2}\begin{bmatrix} 1-\theta_2 & \frac{q_{1,sat}}{q_{2,sat}}\theta_1 \\ \frac{q_{2,sat}}{q_{1,sat}}\theta_2 & 1-\theta_1 \end{bmatrix} \tag{9-3}$$

where the fractional occupancies, θ_i, are defined by equation (6-17).

Let us define the square matrix [B]

$$[B]=\begin{bmatrix}\frac{1}{Đ_1}+\frac{x_2}{Đ_{12}} & -\frac{x_1}{Đ_{12}}\\ -\frac{x_2}{Đ_{12}} & \frac{1}{Đ_2}+\frac{x_1}{Đ_{12}}\end{bmatrix};\quad [B]^{-1}=\frac{1}{1+\frac{x_1Đ_2}{Đ_{12}}+\frac{x_2Đ_1}{Đ_{12}}}\begin{bmatrix}Đ_1\left(1+\frac{x_1Đ_2}{Đ_{12}}\right) & \frac{x_1Đ_1Đ_2}{Đ_{12}}\\ \frac{x_2Đ_1Đ_2}{Đ_{12}} & Đ_2\left(1+\frac{x_2Đ_1}{Đ_{12}}\right)\end{bmatrix} \tag{9-4}$$

In proceeding further, it is convenient to define a 2×2 dimensional square matrix $[\Lambda]\equiv[B]^{-1}$:

$$[\Lambda]=\begin{bmatrix}\frac{1}{Đ_1}+\frac{x_2}{Đ_{12}} & -\frac{x_1}{Đ_{12}}\\ -\frac{x_2}{Đ_{12}} & \frac{1}{Đ_2}+\frac{x_1}{Đ_{12}}\end{bmatrix}^{-1}=\frac{1}{1+\frac{x_1Đ_2}{Đ_{12}}+\frac{x_2Đ_1}{Đ_{12}}}\begin{bmatrix}Đ_1\left(1+\frac{x_1Đ_2}{Đ_{12}}\right) & \frac{x_1Đ_1Đ_2}{Đ_{12}}\\ \frac{x_2Đ_1Đ_2}{Đ_{12}} & Đ_2\left(1+\frac{x_2Đ_1}{Đ_{12}}\right)\end{bmatrix} \tag{9-5}$$

Equation (9-1) can be re-cast into 2-dimensional matrix notation

$$(N)=-\rho[\Lambda][\Gamma]\frac{d(q)}{dz};$$

$$\begin{pmatrix}N_1\\ N_2\end{pmatrix}=-\frac{\rho}{1+\frac{x_1Đ_2}{Đ_{12}}+\frac{x_2Đ_1}{Đ_{12}}}\begin{bmatrix}Đ_1\left(1+\frac{x_1Đ_2}{Đ_{12}}\right) & \frac{x_1Đ_1Đ_2}{Đ_{12}}\\ \frac{x_2Đ_1Đ_2}{Đ_{12}} & Đ_2\left(1+\frac{x_2Đ_1}{Đ_{12}}\right)\end{bmatrix}\begin{bmatrix}\Gamma_{11} & \Gamma_{12}\\ \Gamma_{21} & \Gamma_{22}\end{bmatrix}\begin{pmatrix}\frac{dq_1}{dz}\\ \frac{dq_2}{dz}\end{pmatrix} \tag{9-6}$$

The elements of $[B]$ can be obtained by inverting the matrix $[\Lambda]$ determined using MD simulations using equation (6-24): $\begin{bmatrix}B_{11} & B_{12}\\ B_{21} & B_{22}\end{bmatrix}=\begin{bmatrix}\frac{1}{Đ_1}+\frac{x_2}{Đ_{12}} & -\frac{x_1}{Đ_{12}}\\ -\frac{x_2}{Đ_{12}} & \frac{1}{Đ_2}+\frac{x_1}{Đ_{12}}\end{bmatrix}=[\Lambda]^{-1}$. The three M-S diffusivities can be backed-out from the four elements $\begin{bmatrix}B_{11} & B_{12}\\ B_{21} & B_{22}\end{bmatrix}$ using;

$$Đ_{12}=-\frac{x_2}{B_{21}};\quad Đ_1=\frac{1}{B_{11}-\frac{x_2}{Đ_{12}}};\quad Đ_2=\frac{1}{B_{22}-\frac{x_1}{Đ_{12}}} \tag{9-7}$$

For a wide variety of guest/host combinations we used MD simulations to determine the four elements $\Lambda_{11},\Lambda_{12},\Lambda_{21},\Lambda_{22}$ for binary mixtures for a range of total mixture loadings, q_t= q_1+q_2, using equation (6-24). These simulations are reported in our earlier publications.[7, 9, 10, 13-16, 62, 63, 77, 80-83] In most, but not

all cases, the MD simulations are for equimolar (q_1=q_2; c_1=c_2) binary mixtures. A representative selection of the MD simulated data are presented in the following Figures:

Figure S9-1: Ne(1)/Ar(2) mixtures in MFI zeolite

Figure S9-2: CH_4(1)/H_2(2) mixtures in MFI zeolite

Figure S9-3: H_2(1)/Ar(2) mixtures in MFI zeolite

Figure S9-4: CH_4(1)/Ar(2) mixtures in MFI zeolite

Figure S9-5: C_2H_6(1)/C_3H_8(2) mixtures in MFI zeolite

Figure S9-6: equimolar (q_1=q_2) binary CH_4(1)/C_2H_6(2) mixtures in MFI zeolite

Figure S9-7: 25/75 (q_1/q_2=25/75) binary CH_4(1)/C_2H_6(2) mixtures in MFI zeolite

Figure S9-8: 75/25 (q_1/q_2=75/25) binary CH_4(1)/C_2H_4(2) mixtures in MFI zeolite

Figure S9-9: CH_4(1)/C_3H_8(2) mixtures in MFI zeolite

Figure S9-10: CO_2(1)/N_2(2) mixtures in MFI zeolite

Figure S9-11: CO_2(1)/H_2(2) mixtures in MFI zeolite

Figure S9-12: CH_4(1)/CO_2(2) mixtures in MFI zeolite

Figure S9-13: CO_2(1)/Ne(2) mixtures in MFI zeolite

Figure S9-14: Ne(1)/Ar(2) mixtures in FAU all-silica zeolite

Figure S9-15: CO_2(1)/CH_4(2) mixtures in FAU all-silica zeolite

Figure S9-16: CO_2(1)/N_2(2) mixtures in FAU all-silica zeolite

Figure S9-17: CO_2(1)/Ar(2) mixtures in FAU all-silica zeolite

Figure S9-18: CO_2(1)/Ne(2) mixtures in FAU all-silica zeolite

Figure S9-19: CO_2(1)/H_2(2) mixtures in FAU all-silica zeolite

Figure S9-20: CH_4(1)/H_2(2) mixtures in FAU all-silica zeolite

Figure S9-21: CH_4(1)/Ar(2) mixtures in FAU all-silica zeolite

Figure S9-22: CH_4(1)/C_2H_6(2) mixtures in FAU all-silica zeolite

Figure S9-23: CH_4(1)/C_3H_8(2) mixtures in FAU all-silica zeolite

Figure S9-24: CH_4(1)/CO_2(2) mixtures in NaY zeolite (48 Al)

Also plotted in Figure S9-1 to Figure S9-71 are the MD simulated data for unary M-S diffusivities, $Đ_1, Đ_2$. The backed-out M-S diffusivities $Đ_1, Đ_2, Đ_{12}$ from MD simulated values $\Lambda_{11}, \Lambda_{12}, \Lambda_{21}, \Lambda_{22}$ using equation (9-7) are also presented in the Figures listed above. The diffusivity data for binary mixtures are compared with the M-S diffusivities $Đ_1, Đ_2, Đ_{12}$ in two different ways: (a) the unary diffusivities have

the same loadings as for the total mixture loading $q_t = q_1 + q_2$, (b) the data are compared at the same occupancy, θ.

For unary diffusion, the occupancy θ is determined from equation (6-4); the spreading pressures and saturation capacity values are determined from Configurational-Bias Monte Carlo (CBMC) simulations of the unary adsorption isotherms that are fitted with the dual-site Langmuir-Freundlich model. For binary mixture diffusion, the spreading pressures are determined by applying the IAST model; in this case the saturation capacity to be used in equation (6-4) is calculated from the saturation capacities of the constituent guests

$$q_{sat,mix} = \frac{1}{\frac{1}{q_{1,sat}} + \frac{1}{q_{1,sat}}}; \quad q_{1,sat} = q_{1,A,sat} + q_{1,B,sat}; \quad q_{2,sat} = q_{2,A,sat} + q_{2,B,sat} \tag{9-8}$$

The required dual-site Langmuir-Freundlich model fit parameters for each guest molecule (with sites A, and B) are tabulated for each host material:

Table S7-1: MFI zeolite

Table S7-2: FAU all-silica zeolite

Table S7-3: NaY zeolite (48 Al)

Table S7-4: NaX zeolite (86 Al)

Table S7-5: LTA all-silica zeolite

Table S7-6: CHA all-silica zeolite

Table S7-7: DDR all-silica zeolite

Table S7-8: ISV zeolite

Table S7-9: BEA zeolite

Table S7-10, Table S7-11: IRMOF-1

Table S7-12: MgMOF-74

Table S7-13: CuBTC

The occupancy for binary mixtures θ is calculated from

$$\theta = 1 - \exp\left(-\frac{\pi A}{q_{sat,mix} RT}\right) \tag{9-9}$$

In equation (9-9), the $q_{sat,mix}$ is calculated using equation (9-8). It is easy to verify that equation (9-9), degenerates to equation (5-20),for the scenario in which each of the constituents of the binary mixture follows 1-site Langmuir isotherm behavior, with equal saturation capacities.

A careful examination of presented MD data in Figure S9-1 to Figure S9-63 reveal a number of common characteristic features.

In the limit of vanishingly small loadings, or occupancies:

$$q_t \to 0; \quad \theta \to 0; \quad \Lambda_{11} \to Đ_1; \Lambda_{22} \to Đ_2; \Lambda_{12} \to 0; \Lambda_{21} \to 0 \tag{9-10}$$

With increasing mixture loadings, the diagonal elements $\Lambda_{11}, \Lambda_{22}$ are lowered below the corresponding values of the unary M-S diffusivities $Đ_1, Đ_2$.

$$q_t > 0; \quad \theta > 0; \quad \Lambda_{11} < Đ_1; \Lambda_{22} < Đ_2 \tag{9-11}$$

The extent of lowering, caused by correlation effects, is higher for the more mobile partner species. For the tardier species, the extent of lowering is significantly smaller.

As the total pore concentration approaches saturation, *all* diffusivities appear to converge to the same diffusivity values:

$$q_t \to q_{sat,mix}; \quad \theta \to 1; \quad \Lambda_{11} \approx Đ_1 \approx \Lambda_{22} \approx Đ_2 \approx \Lambda_{12} \approx \Lambda_{21} \tag{9-12}$$

The rationalization of Equation (9-12) is provided in a subsequent section entitled Correlations dominant scenario.

For MD data presented in Figure S9-1 to Figure S9-63, the M-S diffusivities $Đ_1, Đ_2$ that are backed-out for mixture simulatons using equation (9-7) are in reasonably good agreement with the corresponding values of the *unary* M-S diffusivities $Đ_1, Đ_2$, though this agreement is not perfect in some cases due to the fact that (a) the backing-out process involves inversion of the matrix $[\Lambda]$; consequently the $Đ_1, Đ_2$ are also dependent on the off-diagonal elements $\Lambda_{12}, \Lambda_{21}$, and (b) the mixture simulations are

subject to larger errors for the off-diagonal elements, $\Lambda_{12}, \Lambda_{21}$. The agreement of the unary diffusivities $Đ_1, Đ_2$ with the values characterizing the mixture, underscores the persuasive advantage of the use of the Maxwell-Stefan equations to describing diffusion in microporous crystalline materials.

The M-S diffusivity of any species in a mixture is also not influenced by the choice of the partner molecules. To illustrate this, Figure S9-72 provides data on the M-S diffusivity of CO_2, $Đ_i$, determined MD simulation data for diffusion of a variety of equimolar ($c_1 = c_2$) binary mixtures of CO_2 and different partner species in seven different host materials (MFI, FAU, LTA, CHA, IRMOF-1, CuBTC, MgMOF-74). For any host material, we note that the diffusivity of CO_2 in a binary mixture is practically independent of the partner species. Furthermore, when compared at the same occupancy, θ, the values of $Đ_i$ are nearly the same in the mixture as those determined for *unary* diffusion, indicated by the open symbols in Figure S9-72.

Similar conclusions hold for the diffusivity of CH_4 in binary mixtures, containing different partner species, in nine different host materials (MFI, FAU, NaY, NaX, LTA, CHA, BEA, IRMOF-1, CuBTC); see Figure S9-73. The M-S diffusivity of CH_4 is the same whether it diffuses on its own, or in the presence of *any other* partner molecule.

Figure S9-74 presents the data on the Maxwell-Stefan diffusivity, $Đ_i$, of Ar determined from MD simulations for diffusion of a variety of equimolar ($q_1 = q_2$) binary mixtures of Ar and different partner species in (a) MFI, (b) FAU-Si, and (c) IRMOF-1. The M-S diffusivity of Ar is the same whether it diffuses on its own, or in the presence of *any other* partner molecule.

Figure S9-75 presents the data on the Maxwell-Stefan diffusivity, $Đ_i$, of C_2H_6 determined MD simulation data for diffusion of three binary mixtures of C_2H_6 in MFI at 300 K. The M-S diffusivity of C_2H_6 is the same whether it diffuses on its own, or in the presence of *any other* partner molecule.

There are two scenarios in which the M-S diffusivity in the mixture deviates to a significantly extent from the corresponding unary M-S diffusivity; these are discussed hereunder.

For water/methanol and water/ethanol diffusion in MFI and FAU zeolites (see Figure S9-64, Figure S9-65, and Figure S9-66), the M-S diffusivities of either guest molecule in the mixture is significantly lower than the corresponding unary diffusivity due the molecular clustering caused by hydrogen bonding.[93] Detailed discussions on molecular clustering influences will be taken up in a later section.

For diffusion of CO_2-bearing mixtures in cage-type zeolites such as LTA, DDR, and ERI, CO_2 gets preferentially, and strongly, adsorbed at the narrow windows of these zeolites, hindering the diffusion of partner molecules. As a consequence, the Maxwell-Stefan diffusivity of the partner molecule falls significantly below the corresponding value of the unary M-S diffusivity. Evidence of such hindering influences are evident in

Figure S9-67: $CO_2(1)/H_2(2)$ mixtures in LTA all-silica zeolite

Figure S9-68: $CO_2(1)/N_2(2)$ mixtures in LTA all-silica zeolite

Figure S9-69: $CH_4(1)/CO_2(2)$ mixtures in LTA all-silica zeolite

Figure S9-70: $CO_2(1)$/Ne(2) mixtures in LTA all-silica zeolite

Figure S9-71: $CO_2(1)$/Ar(2) mixtures in LTA all-silica zeolite

Detailed analysis and explanation of the hindering effects caused by segregated adsorption effects are provided in our earlier works.[63, 94, 95]

The preferentially location of CO_2 also manifests for CHA zeolite, [63, 94, 95] but the extent of diffusion hindering of partner molecules is negligibly small; see the MD simulated data in

Figure S9-38: $CO_2(1)/CH_4(2)$ mixtures in CHA all-silica zeolite

Figure S9-39: $CO_2(1)/H_2(2)$ mixtures in CHA all-silica zeolite

Figure S9-40: $CO_2(1)$/Ne(2) mixtures in CHA all-silica zeolite

Figure S9-41: $CO_2(1)$/Ar(2) mixtures in CHA all-silica zeolite

9.2 Self-diffusivity in *n*-component mixtures

Equation (7-7) can be extended to *n*-component mixtures by considering the mixture to be made of tagged and un-tagged species *i*, in the company of other partner molecules[96]

$$\frac{1}{D_{i,self}} = \frac{1}{Đ_i} + \frac{x_i}{Đ_{ii}} + \sum_{\substack{j=1 \\ j\neq i}}^{n} \frac{x_j}{Đ_{ij}}; \quad i = 1,2,...n \tag{9-13}$$

The self-diffusivity $D_{i,self}$ within is dictated by (a) species i - wall, (b) species i – species i, and (c) species i – species j interactions. Specifically, for a binary mixture of species 1, and 2, we have

$$\frac{1}{D_{1,self}} = \frac{1}{Đ_1} + \frac{x_2}{Đ_{12}} + \frac{x_1}{Đ_{11}}; \quad \frac{1}{D_{2,self}} = \frac{1}{Đ_2} + \frac{x_1}{Đ_{12}} + \frac{x_2}{Đ_{22}} \tag{9-14}$$

In view of equation (9-4), we may relate the self-diffusivities to the diagonal elements of the matrix

$$[B] = \begin{bmatrix} \frac{1}{Đ_1} + \frac{x_2}{Đ_{12}} & -\frac{x_1}{Đ_{12}} \\ -\frac{x_2}{Đ_{12}} & \frac{1}{Đ_2} + \frac{x_1}{Đ_{12}} \end{bmatrix} :$$

$$\frac{1}{D_{1,self}} = B_{11} + \frac{x_1}{Đ_{11}}; \quad \frac{1}{D_{2,self}} = B_{22} + \frac{x_2}{Đ_{22}} \tag{9-15}$$

Equation (9-15) implies that the self-diffusivities experience correlation effects to a stronger extent than the elements of the matrices $[B] = \begin{bmatrix} \frac{1}{Đ_1} + \frac{x_2}{Đ_{12}} & -\frac{x_1}{Đ_{12}} \\ -\frac{x_2}{Đ_{12}} & \frac{1}{Đ_2} + \frac{x_1}{Đ_{12}} \end{bmatrix}$ and

$[\Lambda] = \frac{1}{1 + \frac{x_1 Đ_2}{Đ_{12}} + \frac{x_2 Đ_1}{Đ_{12}}} \begin{bmatrix} Đ_1\left(1 + \frac{x_1 Đ_2}{Đ_{12}}\right) & \frac{x_1 Đ_1 Đ_2}{Đ_{12}} \\ \frac{x_2 Đ_1 Đ_2}{Đ_{12}} & Đ_2\left(1 + \frac{x_2 Đ_1}{Đ_{12}}\right) \end{bmatrix}$ that characterize binary mixture diffusion.

9.3 Degree of correlations

In order to appreciate the relative importance of correlations on the calculations of the fluxes for binary mixture diffusion, we define the *degrees of correlation*, $Đ_1/Đ_{12}$, and $Đ_2/Đ_{12}$; the values can be determined from those backed-out from mixture MD simulations, and plotted in Figure S9-1 to Figure S9-71. The magnitude of $Đ_1$, relative to that of $Đ_{12}$, determines the extent to which the flux of species 1 is influenced by the chemical potential gradient of species 2. The larger the degree of correlation,

$Đ_1/Đ_{12}$, the stronger is the influence of coupling. Generally speaking, the more-strongly-adsorbed-tardier partner species will have the effect of slowing down the less-strongly-adsorbed-more-mobile partner in the mixture.

Figure S9-76 shows MD simulation data for the degree of correlations, $Đ_1/Đ_{12}$, for diffusion of equimolar ($q_1 = q_2$) binary mixtures (a) CO_2/CH_4, (b) H_2/CO_2, (c) N_2/CO_2, (d) Ne/CO_2, (e) CH_4/Ar (f) H_2/CH_4, (g) Ne/Ar, (h) CH_4/C_2H_6, and (i) CH_4/C_3H_8 at 300 K in a variety of host materials. The *x*- axes represent the fractional occupancy θ. For any guest/host combination, $Đ_1/Đ_{12}$ is seen to increase as the pore occupancy increases; this implies that correlation effects are expected to be stronger for high occupancies.

The degree of correlations is weakest in cage-type structures such as CHA, DDR and LTA; the reason is that the molecules jump one-at-a-time across the narrow windows separating adjacent cages; CO_2 molecules jump length-wise across the windows. At the other end of the spectrum, correlations are strongest in one-dimensional (1D) channel structures (e.g. BTP-COF, MgMOF-74, NiMOF-74), intersecting channels (e.g. MFI), and "open" structures (e.g. IRMOF-1, FAU, NaY, NaX) consisting of large cages separated by wide windows.

9.4 Negligible correlations scenario for M-S diffusivities

For values of $Đ_1/Đ_{12} \to 0$, and $Đ_2/Đ_{12} \to 0$, the contribution of the first right member of M-S Equation (9-1) can be ignored and correlations can be considered to be of negligible importance; we derive

$$\frac{Đ_1}{Đ_{12}} \to 0; \quad \frac{Đ_2}{Đ_{12}} \to 0; \quad \begin{bmatrix} \Lambda_{11} & \Lambda_{12} \\ \Lambda_{21} & \Lambda_{22} \end{bmatrix} \to \begin{bmatrix} Đ_1 & 0 \\ 0 & Đ_2 \end{bmatrix} \tag{9-16}$$

As validation of equation (9-16), Figure S9-30 to Figure S9-42 present MD simulations of the elements of the matrix $\Lambda_{11}, \Lambda_{12}, \Lambda_{22}$ for equimolar binary mixtures in LTA, CHA, and DDR zeolites. We note that the values of the off-diagonal elements $\Lambda_{12} = \Lambda_{21}$ are about 1 – 3 orders of magnitude lower than

the corresponding values of the diagonal elements $\Lambda_{11}, \Lambda_{22}$. The diagonal elements are practically the same as the unary M-S diffusivities $Đ_1$, and $Đ_2$; this is consistent with equation (9-16).

When correlation effects are negligible, the diffusional coupling effects are solely traceable to mixture adsorption thermodynamics, embodied in the matrix $[\Gamma]$.

9.5 Correlations dominant scenario for M-S diffusivities

For the case in which correlation effects are dominant $\frac{Đ_1}{Đ_{12}} >> 1; \quad \frac{Đ_2}{Đ_{12}} >> 1; \quad \text{correlations dominant}$.

This also implies that $\frac{x_1 Đ_2 + x_2 Đ_1}{Đ_{12}} >> 1$ because the sum of the adsorbed phase mole fractions add to unity, i.e. $x_1+x_2 = 1$. Therefore, the term $1 + \frac{x_1 Đ_2}{Đ_{12}} + \frac{x_2 Đ_1}{Đ_{12}}$ in equation (9-5) can be simplified as $1 + \frac{x_1 Đ_2 + x_2 Đ_1}{Đ_{12}} \to \frac{x_1 Đ_2 + x_2 Đ_1}{Đ_{12}}$, and the matrix $[\Lambda]$ reduces to

$$[\Lambda] = \frac{1}{\frac{x_1 Đ_2 + x_2 Đ_1}{Đ_{12}}} \begin{bmatrix} Đ_1\left(1 + \frac{x_1 Đ_2}{Đ_{12}}\right) & Đ_1 \frac{x_1 Đ_2}{Đ_{12}} \\ Đ_2 \frac{x_2 Đ_1}{Đ_{12}} & Đ_2\left(1 + \frac{x_2 Đ_1}{Đ_{12}}\right) \end{bmatrix} \tag{9-17}$$

The expressions for Λ_{12} and Λ_{21} can be further simplified

$$\begin{aligned} \Lambda_{12} &= \frac{Đ_1\left(\frac{x_1 Đ_2}{Đ_{12}}\right)}{\frac{x_1 Đ_2}{Đ_{12}} + \frac{x_2 Đ_1}{Đ_{12}}} = \frac{Đ_1}{1 + \frac{x_2}{x_1}\frac{Đ_1}{Đ_2}} = \frac{x_1}{\frac{x_1}{Đ_1} + \frac{x_2}{Đ_2}}; \\ \Lambda_{21} &= \frac{Đ_2\left(\frac{x_2 Đ_1}{Đ_{12}}\right)}{\frac{x_1 Đ_2}{Đ_{12}} + \frac{x_2 Đ_1}{Đ_{12}}} = \frac{Đ_2}{1 + \frac{x_1}{x_2}\frac{Đ_2}{Đ_1}} = \frac{x_2}{\frac{x_1}{Đ_1} + \frac{x_2}{Đ_2}} \end{aligned} \tag{9-18}$$

The expressions for Λ_{11} and Λ_{22} for the correlations dominant scenario must be derived with more care. The diagonal elements must degenerate to the corresponding pure component $Đ_i$ values at either ends of the composition range, i.e.

$$\Lambda_{11} \to Đ_1; \quad x_1 \to 1; \quad x_2 \to 0 \tag{9-19}$$

and,

$$\Lambda_{22} \to Đ_2; \quad x_2 \to 1; \quad x_1 \to 0 \tag{9-20}$$

Equations (9-19), and (9-20) must be satisfied for *any* degree of correlations, not just in the Correlations Dominant scenario. Consider Λ_{11}. For equation (9-17) to satisfy equation (9-19) for $\frac{Đ_1}{Đ_{12}} >> 1; \quad \frac{Đ_2}{Đ_{12}} >> 1$ we must *also* satisfy the conditions

$$\frac{x_1 Đ_2}{Đ_{12}} >> 1; \quad \frac{x_2 Đ_1}{Đ_{12}} >> 1 \tag{9-21}$$

because, otherwise, (9-19) will be violated. Invoking equation (9-21) we obtain from equation (9-17)

$$\Lambda_{11} = \frac{Đ_1}{1+\frac{x_2}{x_1}\frac{Đ_1}{Đ_2}} = \frac{x_1}{\frac{x_1}{Đ_1}+\frac{x_2}{Đ_2}}; \quad \Lambda_{22} = \frac{Đ_2}{1+\frac{x_1}{x_2}\frac{Đ_2}{Đ_1}} = \frac{x_2}{\frac{x_1}{Đ_1}+\frac{x_2}{Đ_2}} \tag{9-22}$$

The M-S diffusivity matrix $[\Lambda]$ for the correlations dominant scenario yields the remarkably simple result

$$[\Lambda] = \frac{1}{\frac{x_1}{Đ_1}+\frac{x_2}{Đ_2}}\begin{bmatrix} x_1 & x_1 \\ x_2 & x_2 \end{bmatrix} = \frac{1}{\frac{q_1}{Đ_1}+\frac{q_2}{Đ_2}}\begin{bmatrix} q_1 & q_1 \\ q_2 & q_2 \end{bmatrix} \tag{9-23}$$

Remarkably, in this scenario, $\Lambda_{11} = \Lambda_{12}$, and $\Lambda_{21} = \Lambda_{22}$. For equimolar mixtures, $x_1 = x_2$, all the four elements of $[\Lambda]$ are equal to one another.

The dominant correlations scenario is a good approximation under pore saturation conditions.[15] As validation, the MD simulated values of $\Lambda_{11}, \Lambda_{12}, \Lambda_{21}, \Lambda_{22}$ are compared with the calculations using the *unary* diffusivities, $Đ_1, Đ_2$ and equation (9-23) in:

Figure S9-1(b): Ne(1)/Ar(2) mixtures in MFI zeolite

Figure S9-2(b): CH_4(1)/H_2(2) mixtures in MFI zeolite

Figure S9-3(b): H_2(1)/Ar(2) mixtures in MFI zeolite

Figure S9-5(b): $C_2H_6(1)/C_3H_8(2)$ mixtures in MFI zeolite

Figure S9-43(b): $CH_4(1)/C_2H_6(2)$ mixtures in ISV zeolite

Figure S9-44(b): $CH_4(1)/C_3H_8(2)$ mixtures in BEA zeolite

All three zeolites: MFI, BEA, ISV have intersecting channel topologies, and in all three cases we note that the elements $\Lambda_{11}, \Lambda_{12}, \Lambda_{22}$ converge to the same diffusivity value at increasing mixture loadings; the continuous solid lines are the calculations of $\Lambda_{11}, \Lambda_{12}, \Lambda_{22}$ using equation (9-23). In this scenario, there is only one characteristic diffusivity in the mixture when the zeolite pores are saturated.

A more extensive and detailed validation of equation (9-23) at pore saturation conditions is provided in our earlier works.[15, 91]

9.6 Onsager formulation for diffusion in micropores

In the Onsager formulation, the fluxes are linearly related to the chemical potential gradients by defining a matrix of Onsager coefficients $[L]$

$$\begin{pmatrix} N_1 \\ N_2 \end{pmatrix} = -\frac{\rho}{RT} \begin{bmatrix} L_{11} & L_{12} \\ L_{21} & L_{22} \end{bmatrix} \begin{pmatrix} \frac{d\mu_1}{dz} \\ \frac{d\mu_2}{dz} \end{pmatrix}; \quad \text{Onsager formulation} \tag{9-24}$$

The Onsager Reciprocal Relations[63] prescribes the symmetry relation

$$L_{12} = L_{21} \tag{9-25}$$

The units of the elements of the Onsager matrix in microporous materials are mol kg^{-1} m^2 s^{-1}. The Onsager formulation suffers from the major disadvantage that the diagonal elements L_{11} and L_{22} cannot be identified with the corresponding values L_1, and L_2 for unary transport of species 1 and 2.[63] The inter-relationship between $[\Lambda]$ and $[L]$ is

$$[L] = [\Lambda] \begin{bmatrix} q_1 & 0 \\ 0 & q_2 \end{bmatrix} \tag{9-26}$$

In the correlations dominant scenario, the elements of the Onsager matrix $[L]=[\Lambda]\begin{bmatrix} q_1 & 0 \\ 0 & q_2 \end{bmatrix}$ can be determined by combining equations (9-23), and (9-24):

$$[L]=[\Lambda]\begin{bmatrix} q_1 & 0 \\ 0 & q_2 \end{bmatrix}=\frac{1}{\frac{q_1}{Đ_1}+\frac{q_2}{Đ_2}}\begin{bmatrix} q_1^2 & q_1q_2 \\ q_1q_2 & q_2^2 \end{bmatrix}; \quad \text{correlations dominant} \tag{9-27}$$

9.7 Influence of cluster formation due to hydrogen bonding

Exceptional circumstances prevail in cases of severe molecular segregation[63, 94] or cluster formation [93, 97-99]; in such situations, the coefficients $Đ_1$, and $Đ_2$ in the mixture are significantly different to those determined from unary experiments or simulations. For water/alcohol mixture diffusion, the diffusivity of each component is lowered due to molecular clusters being formed as a consequence of hydrogen bonding. This is illustrated in Figure S9-77 that present MD simulations of $Đ_1$, and $Đ_2$ for water/alcohol mixture diffusion in FAU, MFI, LTA, DDR, and CHA zeolites. In all cases, the diffusivity of water is reduced with increasing proportion of alcohol. Hydrogen bonding between water and alcohol molecule pairs serves to act as a "flexible leash" linking the motion of the more mobile (water) and tardier (alcohol) species. The net result is that the motion of water is retarded due to cluster formation. For MFI, the diffusivity of methanol is practically independent of composition, while that for water shows a dramatic decrease with increasing methanol concentration (cf. Figure S9-77(c)); this trend is the same as determined in the NMR experiments data of Caro et al.[100] For LTA, and DDR the $Đ_{i,self}$ of methanol decreases with increasing proportion of water; see Figure S9-77(d), and Figure S9-77(e). For CHA, the self-diffusivities for methanol show a decreasing trend for low water concentrations, till a minimum is reached; see Figure S9-77(f). A similar minimum in the alcohol self-diffusivity is observed for FAU zeolite; see Figure S9-77(a,b). The general conclusion to be drawn from the MD data in Figure S9-77(c) is that at either ends of the composition range, there is slowing down of either component, due to increasing proportion of its partner species.

Further detailed discussions on the influence of molecular clustering on the loading dependences of diffusivities are available in earlier works. [7, 12, 93, 97-99, 101-104]

9.8 List of Figures for Diffusion of Binary Mixtures in Microporous Materials

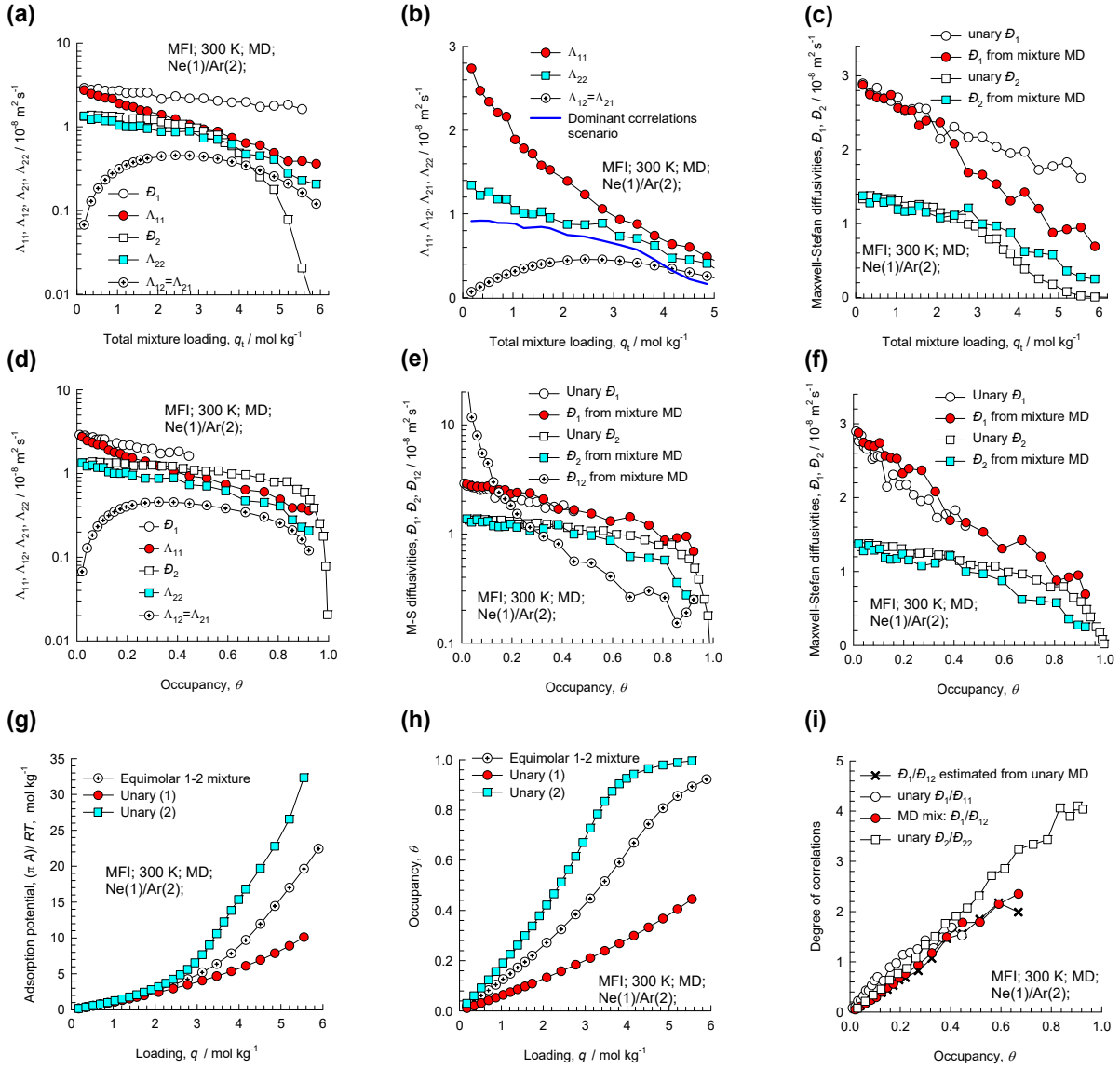

Figure S9-1. MD simulated values of $\Lambda_{11}, \Lambda_{12}, \Lambda_{22}$, along with the backed-out M-S diffusivities, $Đ_1, Đ_2, Đ_{12}$ for equimolar (q_1=q_2) binary Ne(1)/Ar(2) mixtures in MFI zeolite at 300 K plotted as a function of (a, b, c) the total mixture loading q_t= q_1+q_2, and (d, e, f) occupancy θ. (g, h) The adsorption potential, and the occupancy plotted as function of the molar loading. (i) degree of correlations.

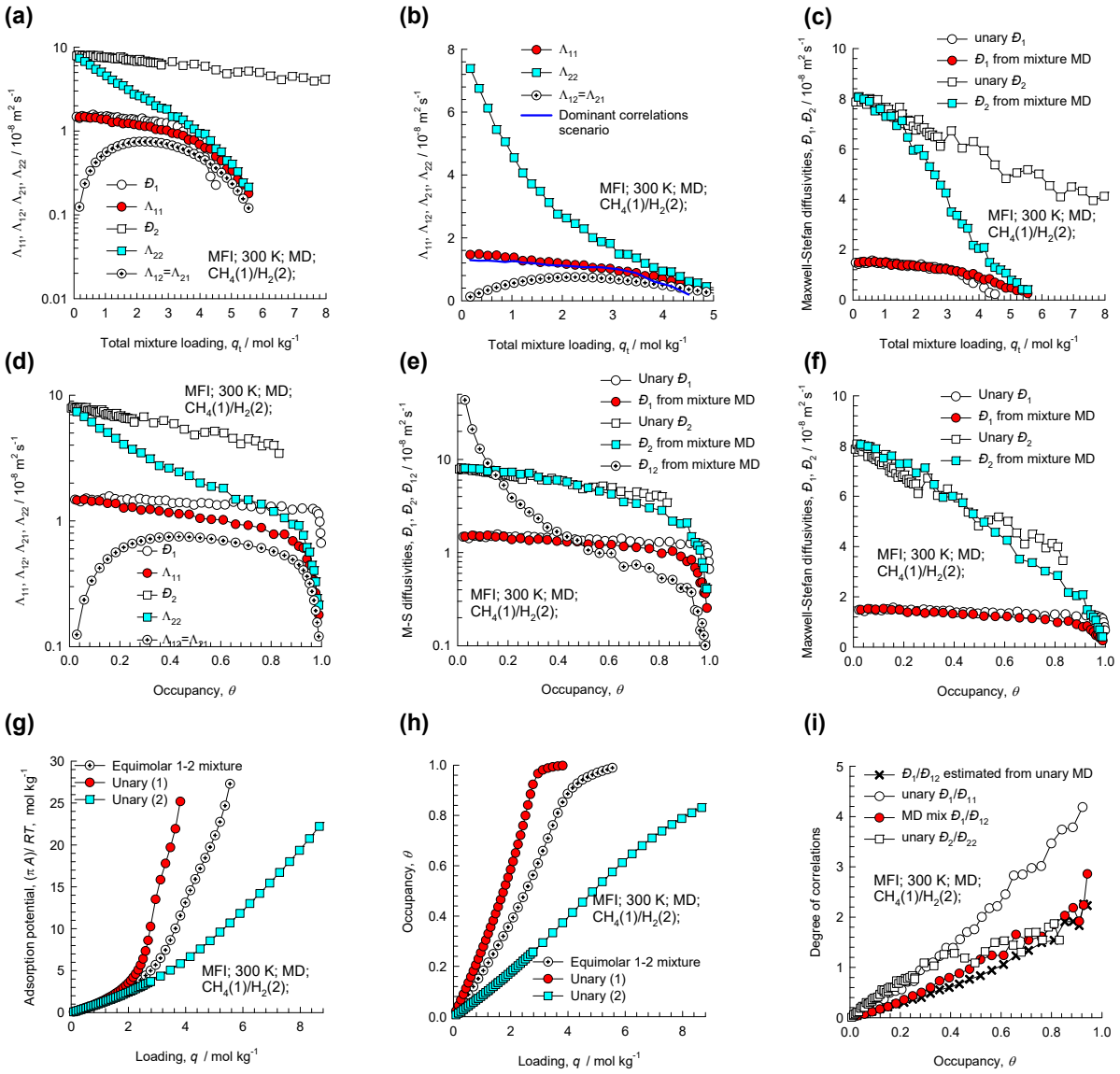

Figure S9-2. MD simulated values of $\Lambda_{11}, \Lambda_{12}, \Lambda_{22}$, along with the backed-out M-S diffusivities, $Đ_1, Đ_2, Đ_{12}$ for equimolar (q_1=q_2) binary $CH_4(1)/H_2(2)$ mixtures in MFI zeolite at 300 K plotted as a function of (a, b, c) the total mixture loading $q_t = q_1+q_2$, and (d, e, f) occupancy θ. (g, h) The adsorption potential, and the occupancy plotted as function of the molar loading. (i) degree of correlations.

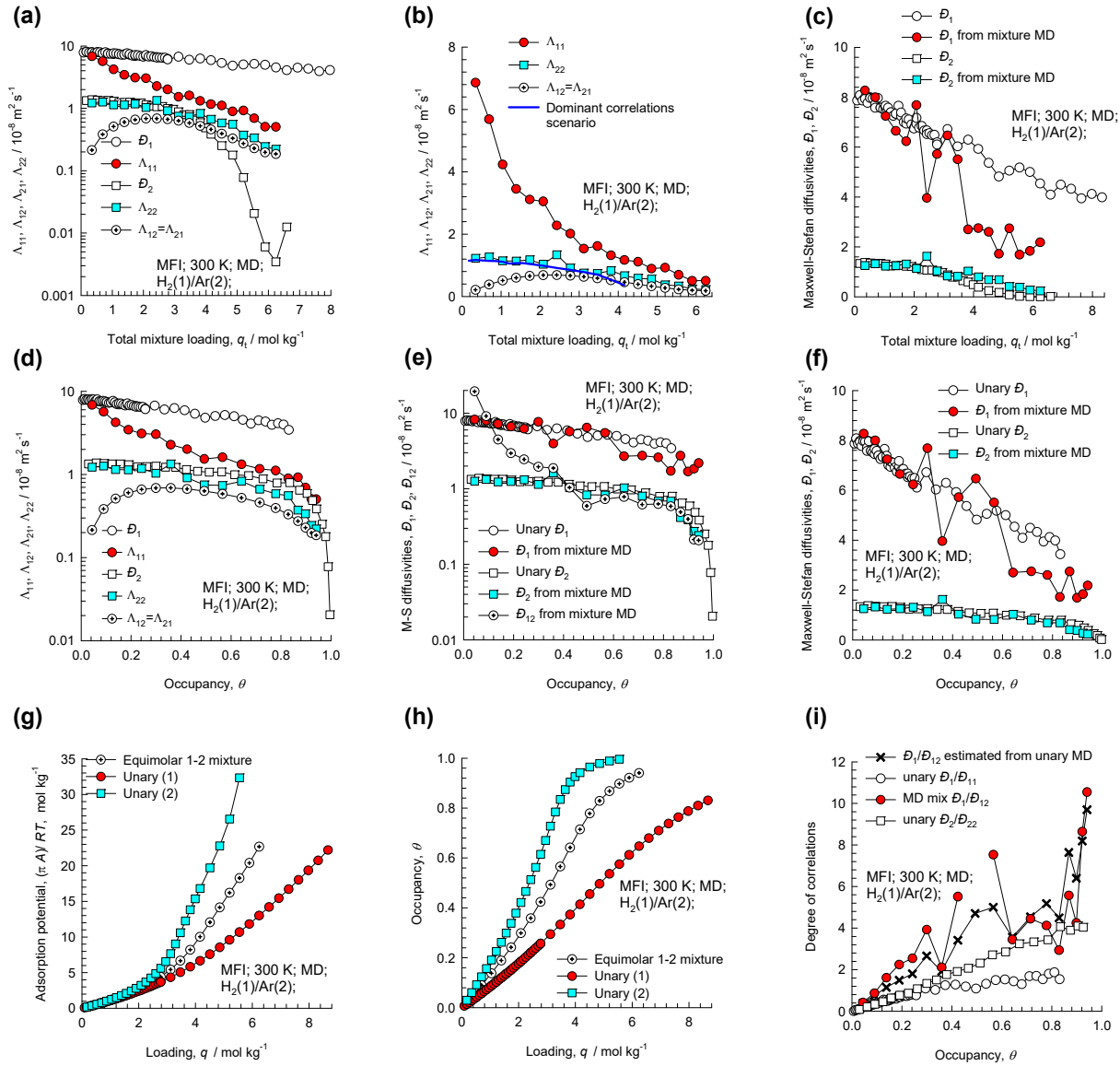

Figure S9-3. MD simulated values of $\Lambda_{11}, \Lambda_{12}, \Lambda_{22}$, along with the backed-out M-S diffusivities, $Đ_1, Đ_2, Đ_{12}$ for equimolar (q_1=q_2) binary H$_2$(1)/Ar(2) mixtures in MFI zeolite at 300 K plotted as a function of (a, b, c) the total mixture loading q_t= q_1+q_2, and (d, e, f) occupancy θ. (g, h) The adsorption potential, and the occupancy plotted as function of the molar loading. (i) degree of correlations.

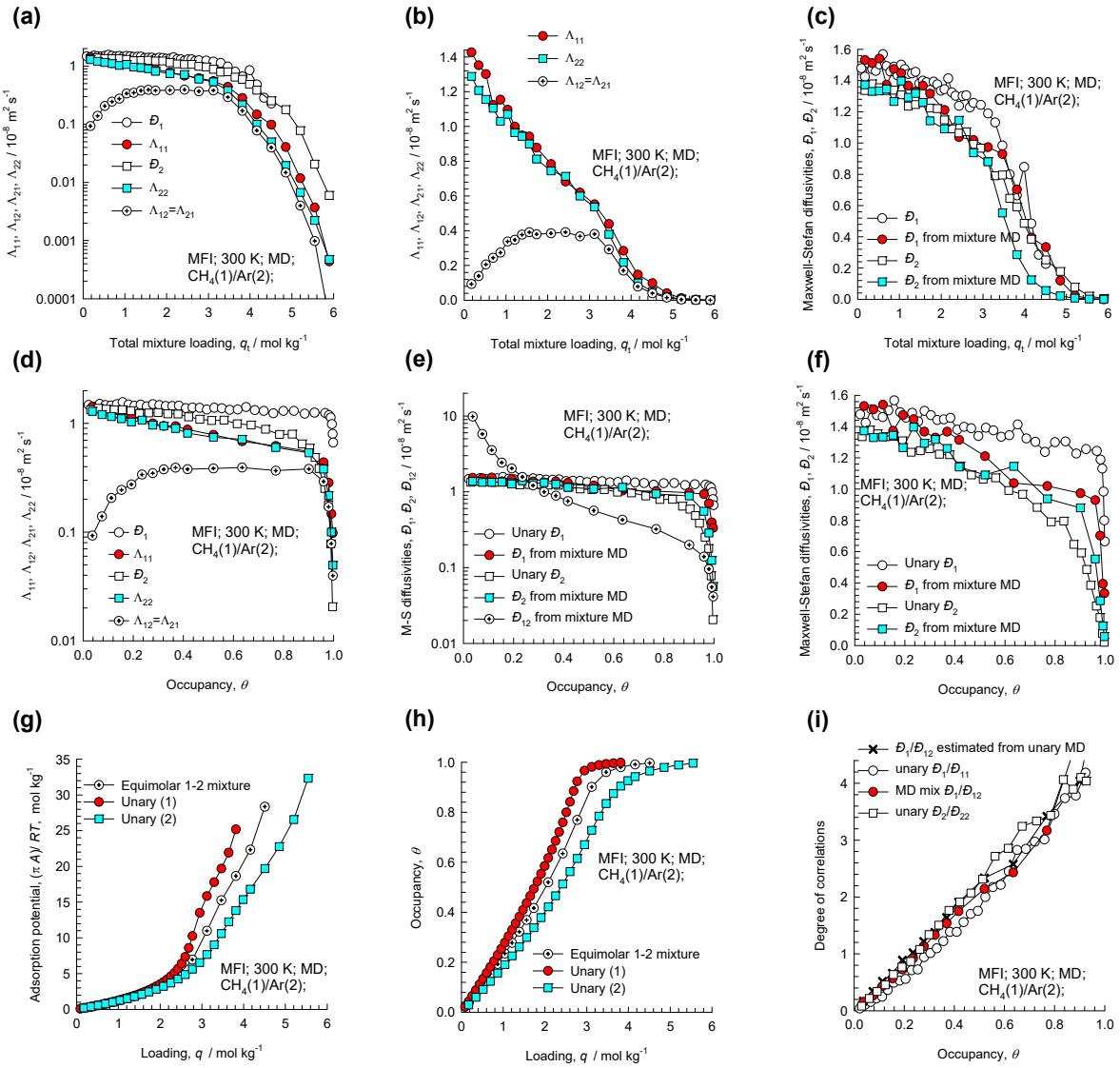

Figure S9-4. MD simulated values of $\Lambda_{11}, \Lambda_{12}, \Lambda_{22}$, along with the backed-out M-S diffusivities, $Đ_1, Đ_2, Đ_{12}$ for equimolar (q_1=q_2) binary CH4(1)/Ar(2) mixtures in MFI zeolite at 300 K plotted as a function of (a, b, c) the total mixture loading $q_t = q_1+q_2$, and (d, e, f) occupancy θ. (g, h) The adsorption potential, and the occupancy plotted as function of the molar loading. (i) degree of correlations.

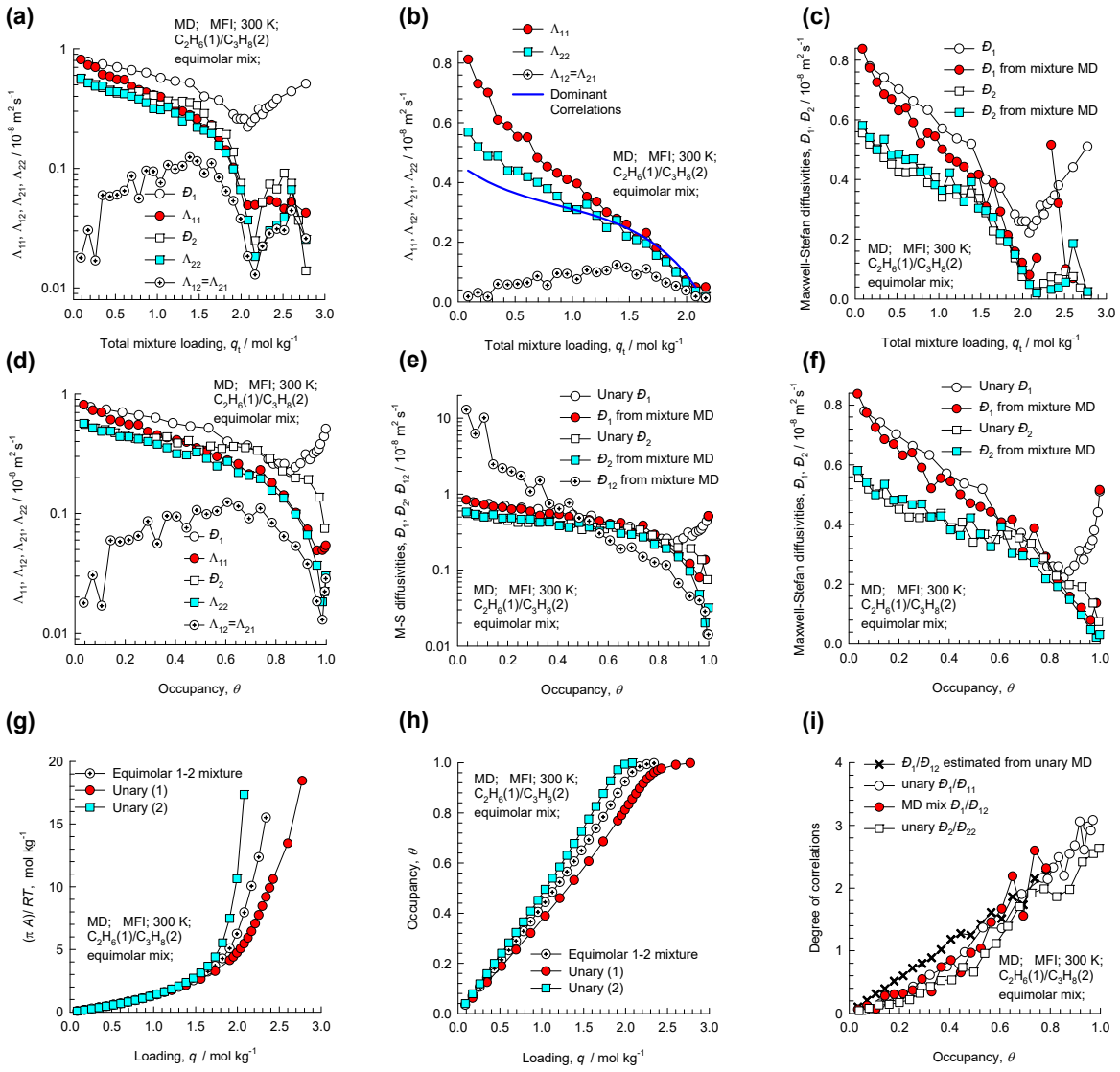

Figure S9-5. MD simulated values of $\Lambda_{11},\Lambda_{12},\Lambda_{22}$, along with the backed-out M-S diffusivities, $Đ_1,Đ_2,Đ_{12}$ for equimolar (q_1=q_2) binary $C_2H_6(1)/C_3H_8(2)$ mixtures in MFI zeolite at 300 K plotted as a function of (a, b, c) the total mixture loading q_t= q_1+q_2, and (d, e, f) occupancy θ. (g, h) The adsorption potential, and the occupancy plotted as function of the molar loading. (i) degree of correlations.

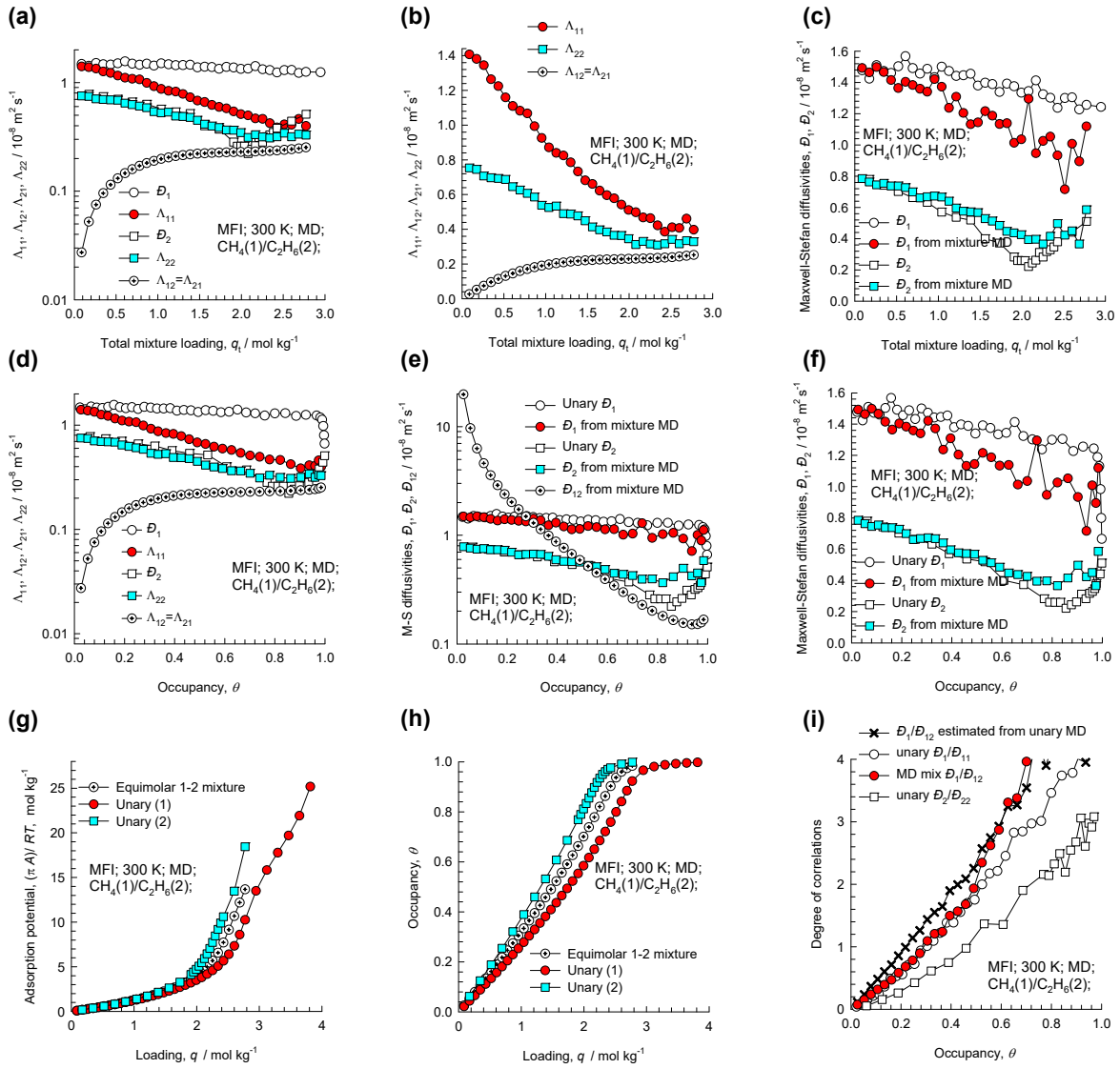

Figure S9-6. MD simulated values of $\Lambda_{11}, \Lambda_{12}, \Lambda_{22}$, along with the backed-out M-S diffusivities, $Đ_1, Đ_2, Đ_{12}$ for equimolar (q_1=q_2) binary $CH_4(1)/C_2H_6(2)$ mixtures in MFI zeolite at 300 K plotted as a function of (a, b, c) the total mixture loading $q_t = q_1+q_2$, and (d, e, f) occupancy θ. (g, h) The adsorption potential, and the occupancy plotted as function of the molar loading. (i) degree of correlations.

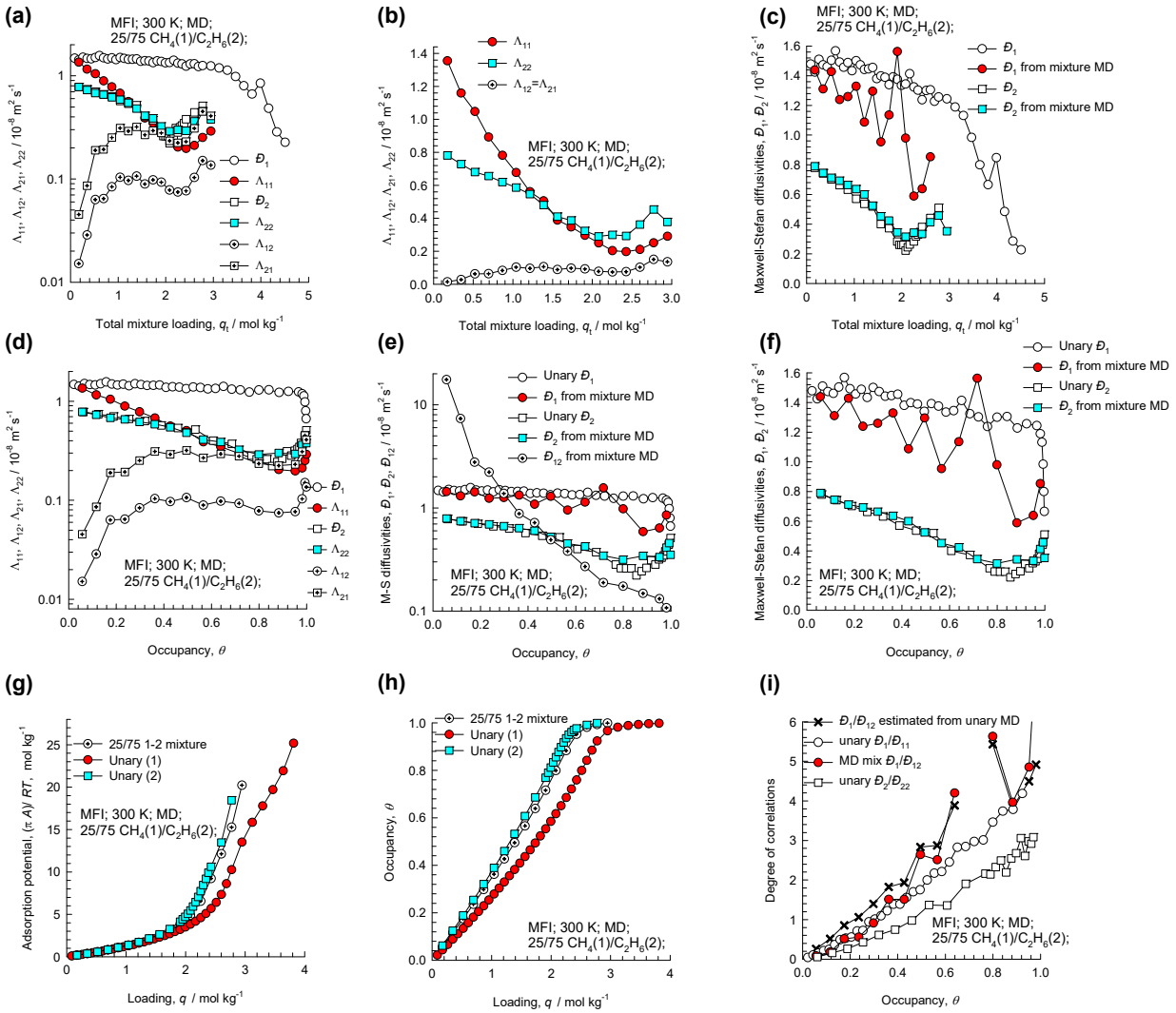

Figure S9-7. MD simulated values of $\Lambda_{11}, \Lambda_{12}, \Lambda_{22}$, along with the backed-out M-S diffusivities, $Đ_1, Đ_2, Đ_{12}$ for 25/75 (q_1/q_2=25/75) binary $CH_4(1)/C_2H_6(2)$ mixtures in MFI zeolite at 300 K plotted as a function of (a, b, c) the total mixture loading $q_t = q_1+q_2$, and (d, e, f) occupancy θ. (g, h) The adsorption potential, and the occupancy plotted as function of the molar loading. (i) degree of correlations.

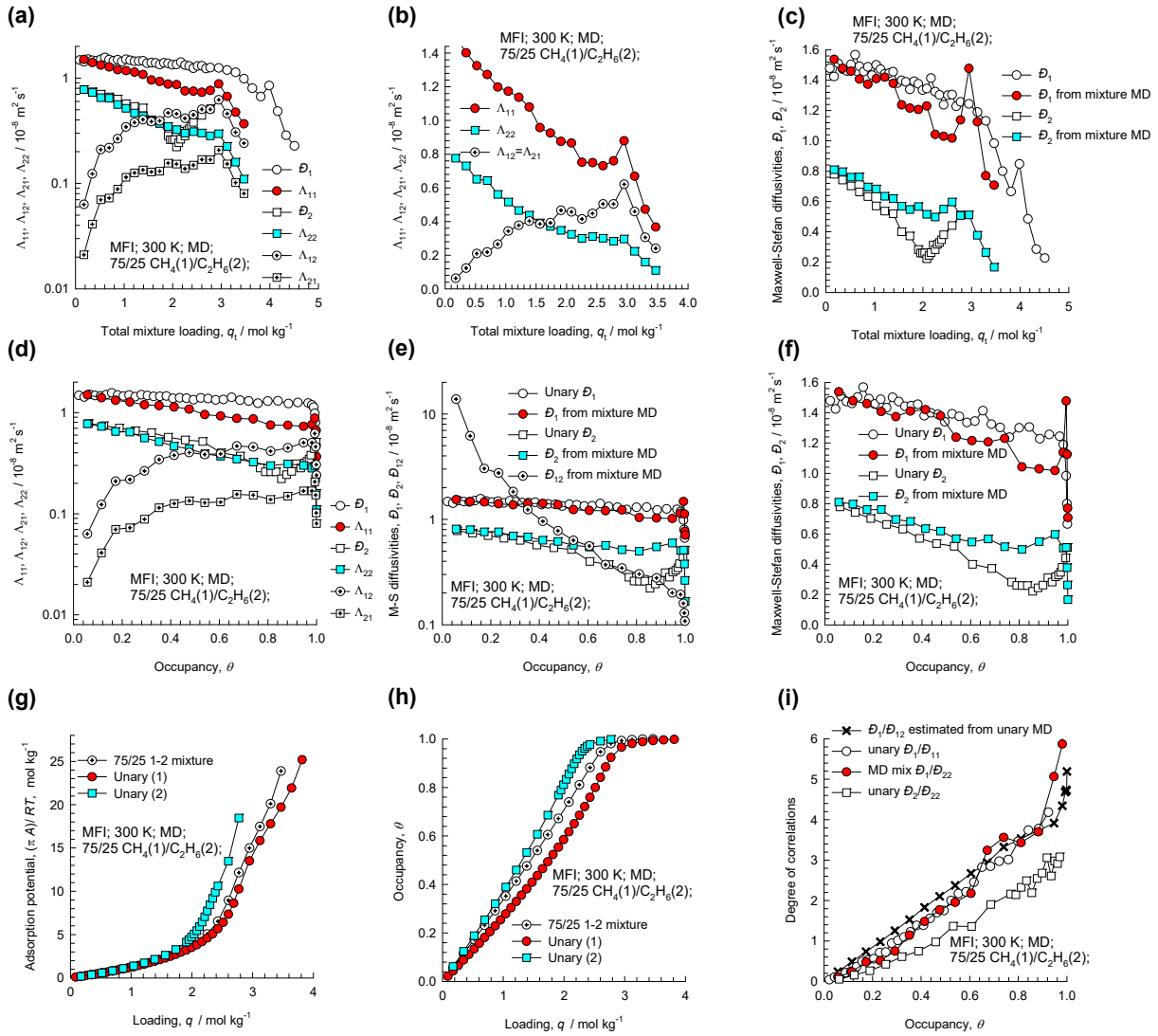

Figure S9-8. MD simulated values of $\Lambda_{11}, \Lambda_{12}, \Lambda_{22}$, along with the backed-out M-S diffusivities, $Đ_1, Đ_2, Đ_{12}$ for 75/25 (q_1/q_2=75/25) binary $CH_4(1)/C_2H_4(2)$ mixtures in MFI zeolite at 300 K plotted as a function of (a, b, c) the total mixture loading $q_t = q_1+q_2$, and (d, e, f) occupancy θ. (g, h) The adsorption potential, and the occupancy plotted as function of the molar loading. (i) degree of correlations.

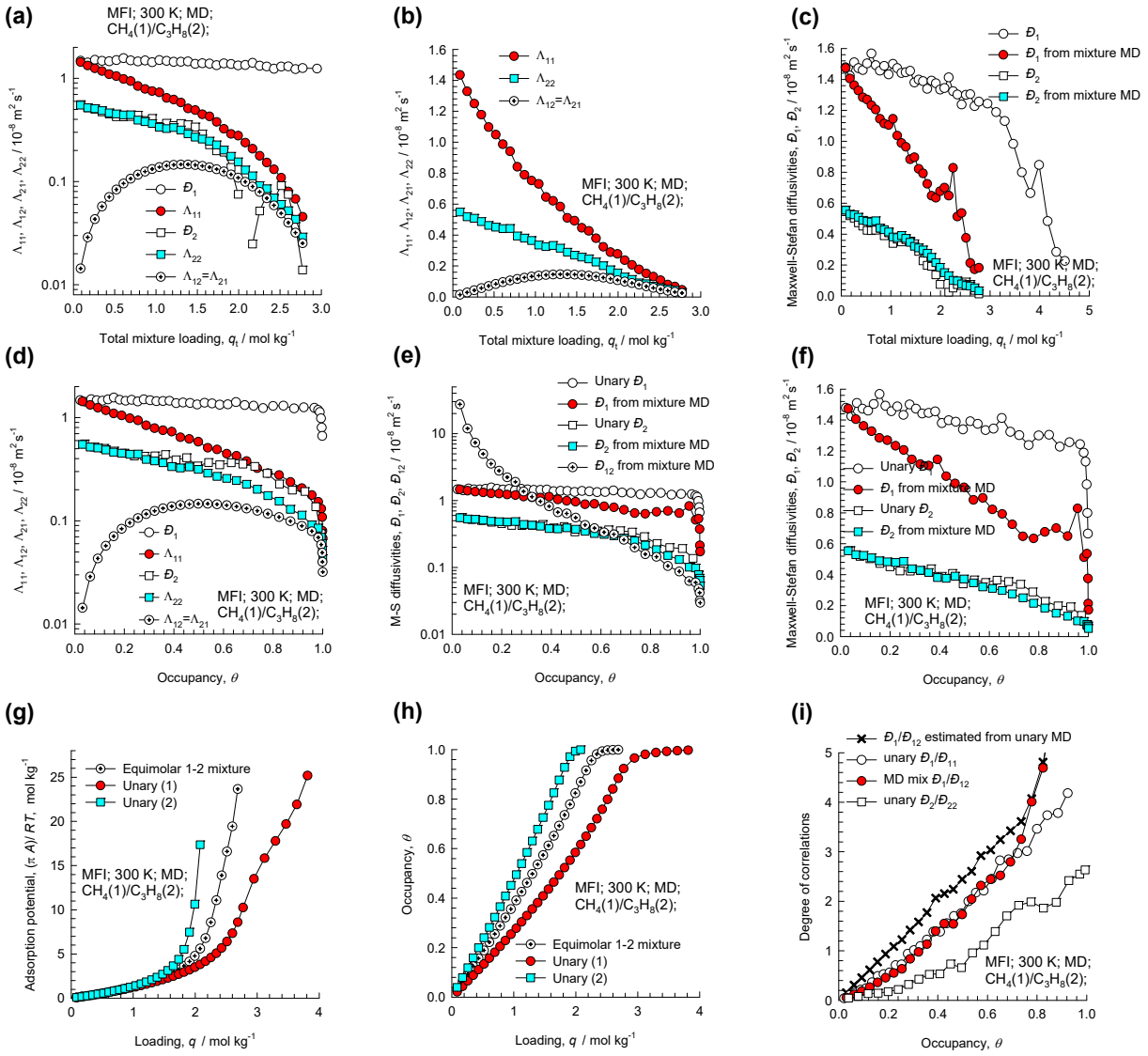

Figure S9-9. MD simulated values of $\Lambda_{11}, \Lambda_{12}, \Lambda_{22}$, along with the backed-out M-S diffusivities, $Đ_1, Đ_2, Đ_{12}$ for equimolar (q_1=q_2) binary $CH_4(1)/C_3H_8(2)$ mixtures in MFI zeolite at 300 K plotted as a function of (a, b, c) the total mixture loading q_t= q_1+q_2, and (d, e, f) occupancy θ. (g, h) The adsorption potential, and the occupancy plotted as function of the molar loading. (i) degree of correlations.

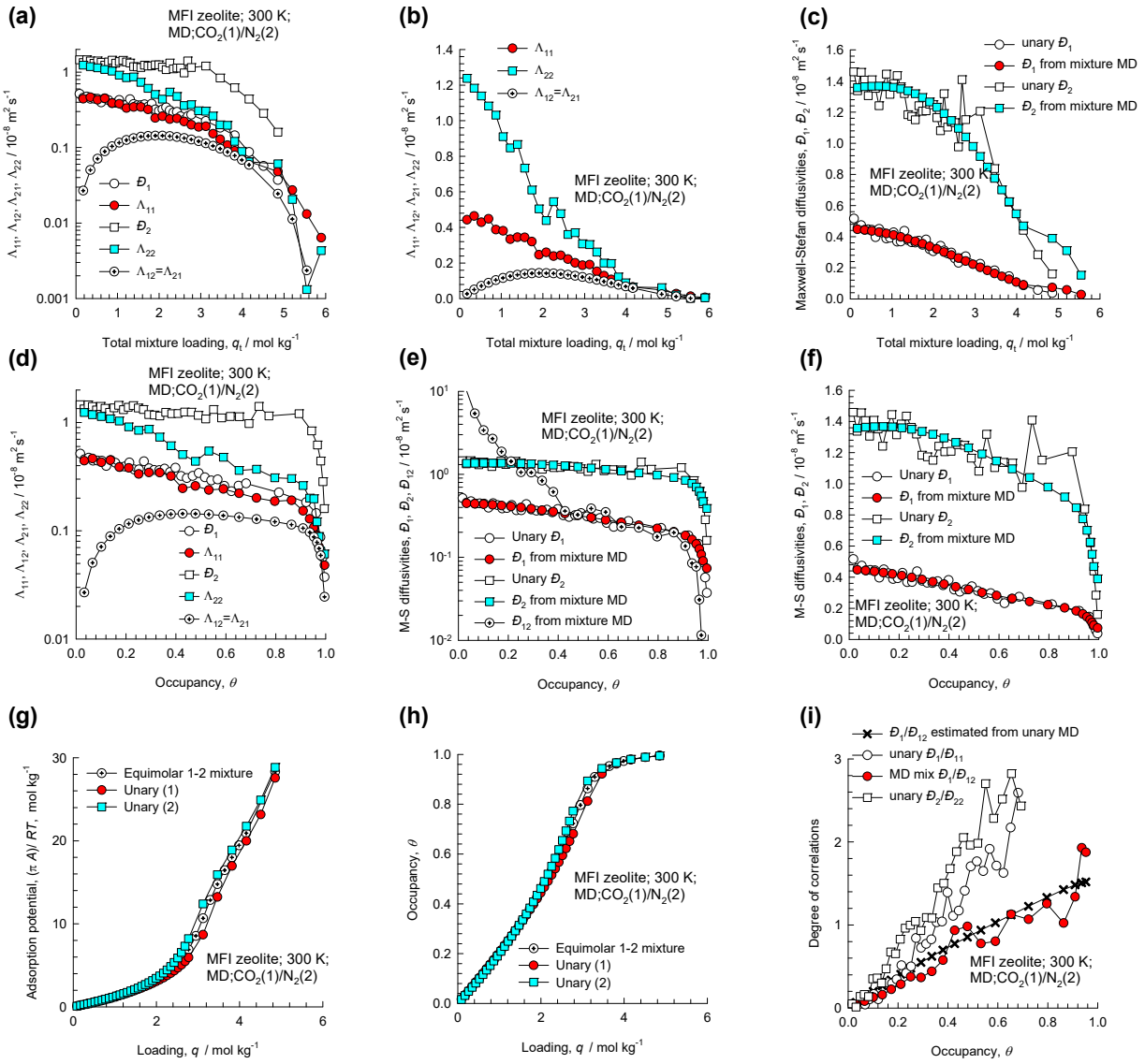

Figure S9-10. MD simulated values of $\Lambda_{11},\Lambda_{12},\Lambda_{22}$, along with the backed-out M-S diffusivities, $Đ_1,Đ_2,Đ_{12}$ for equimolar (q_1=q_2) binary $CO_2(1)/N_2(2)$ mixtures in MFI zeolite at 300 K plotted as a function of (a, b, c) the total mixture loading q_t= q_1+q_2, and (d, e, f) occupancy θ. (g, h) The adsorption potential, and the occupancy plotted as function of the molar loading. (i) degree of correlations.

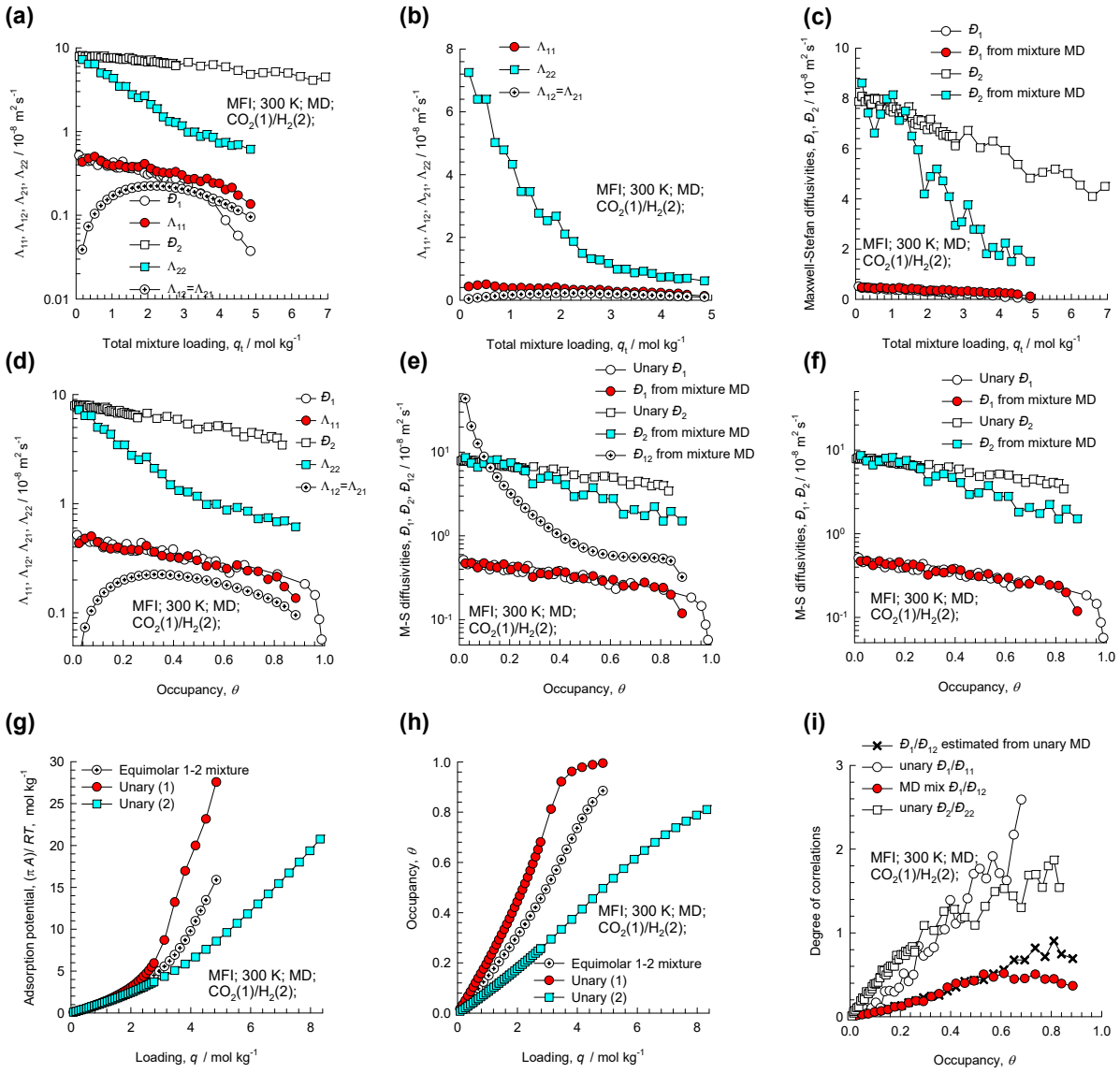

Figure S9-11. MD simulated values of $\Lambda_{11}, \Lambda_{12}, \Lambda_{22}$, along with the backed-out M-S diffusivities, $Đ_1, Đ_2, Đ_{12}$ for equimolar (q_1=q_2) binary CO_2(1)/H_2(2) mixtures in MFI zeolite at 300 K plotted as a function of (a, b, c) the total mixture loading q_t= q_1+q_2, and (d, e, f) occupancy θ. (g, h) The adsorption potential, and the occupancy plotted as function of the molar loading. (i) degree of correlations.

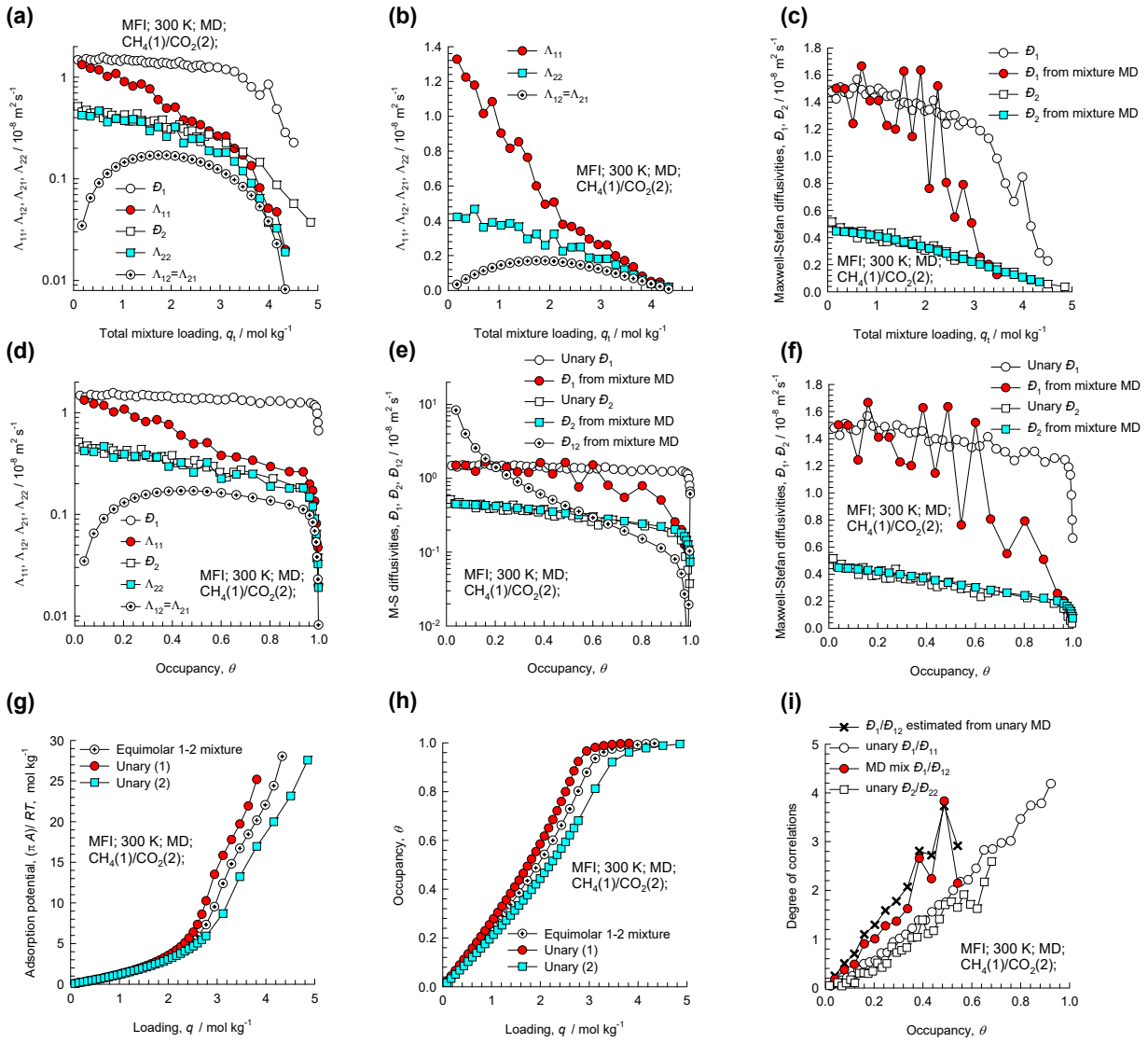

Figure S9-12. MD simulated values of $\Lambda_{11},\Lambda_{12},\Lambda_{22}$, along with the backed-out M-S diffusivities, $Đ_1,Đ_2,Đ_{12}$ for equimolar (q_1=q_2) binary $CH_4(1)/CO_2(2)$ mixtures in MFI zeolite at 300 K plotted as a function of (a, b, c) the total mixture loading q_t= q_1+q_2, and (d, e, f) occupancy θ. (g, h) The adsorption potential, and the occupancy plotted as function of the molar loading. (i) degree of correlations.

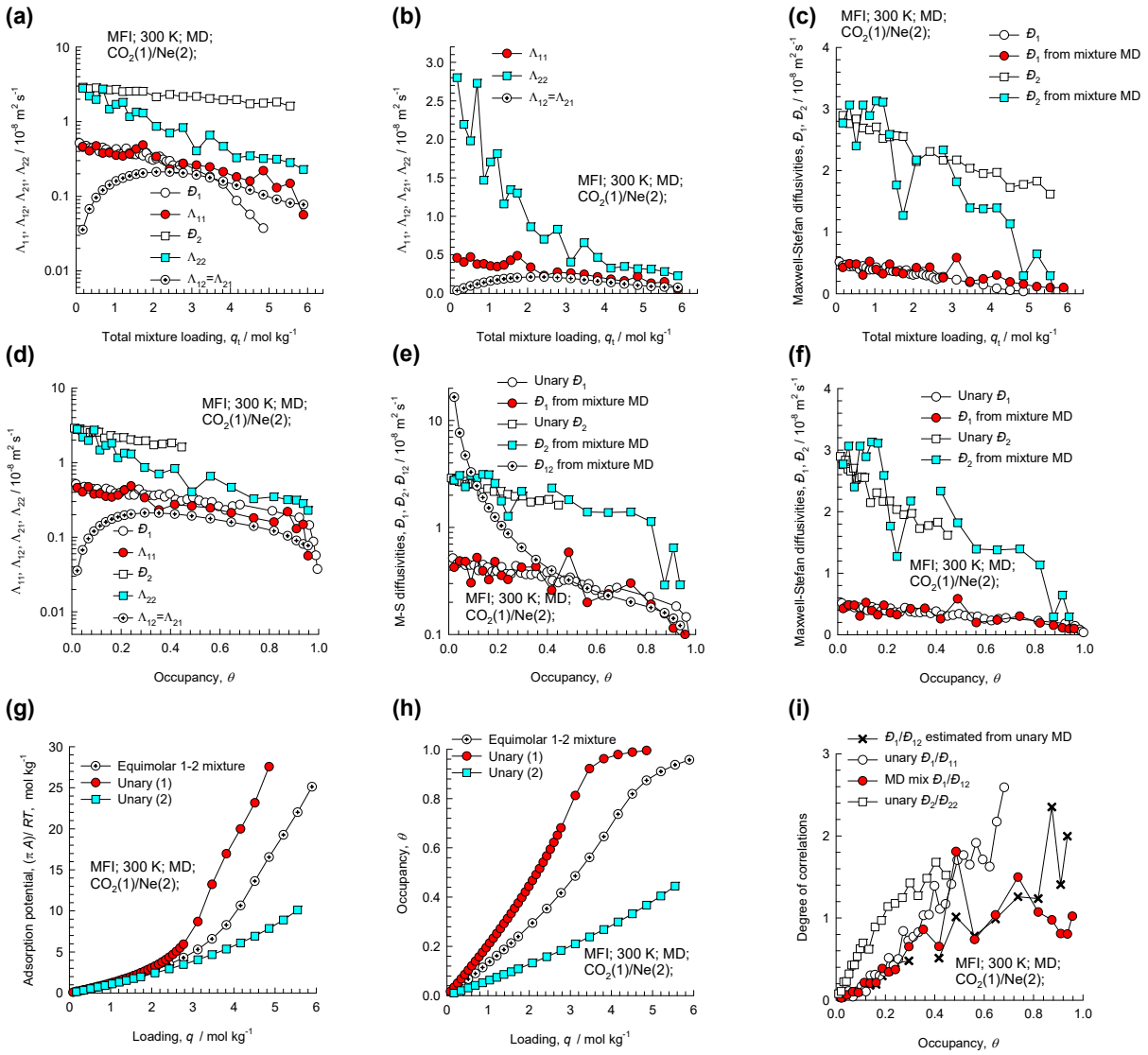

Figure S9-13. MD simulated values of $\Lambda_{11},\Lambda_{12},\Lambda_{22}$, along with the backed-out M-S diffusivities, $Đ_1,Đ_2,Đ_{12}$ for equimolar (q_1=q_2) binary CO$_2$(1)/Ne(2) mixtures in MFI zeolite at 300 K plotted as a function of (a, b, c) the total mixture loading q_t= q_1+q_2, and (d, e, f) occupancy θ. (g, h) The adsorption potential, and the occupancy plotted as function of the molar loading. (i) degree of correlations.

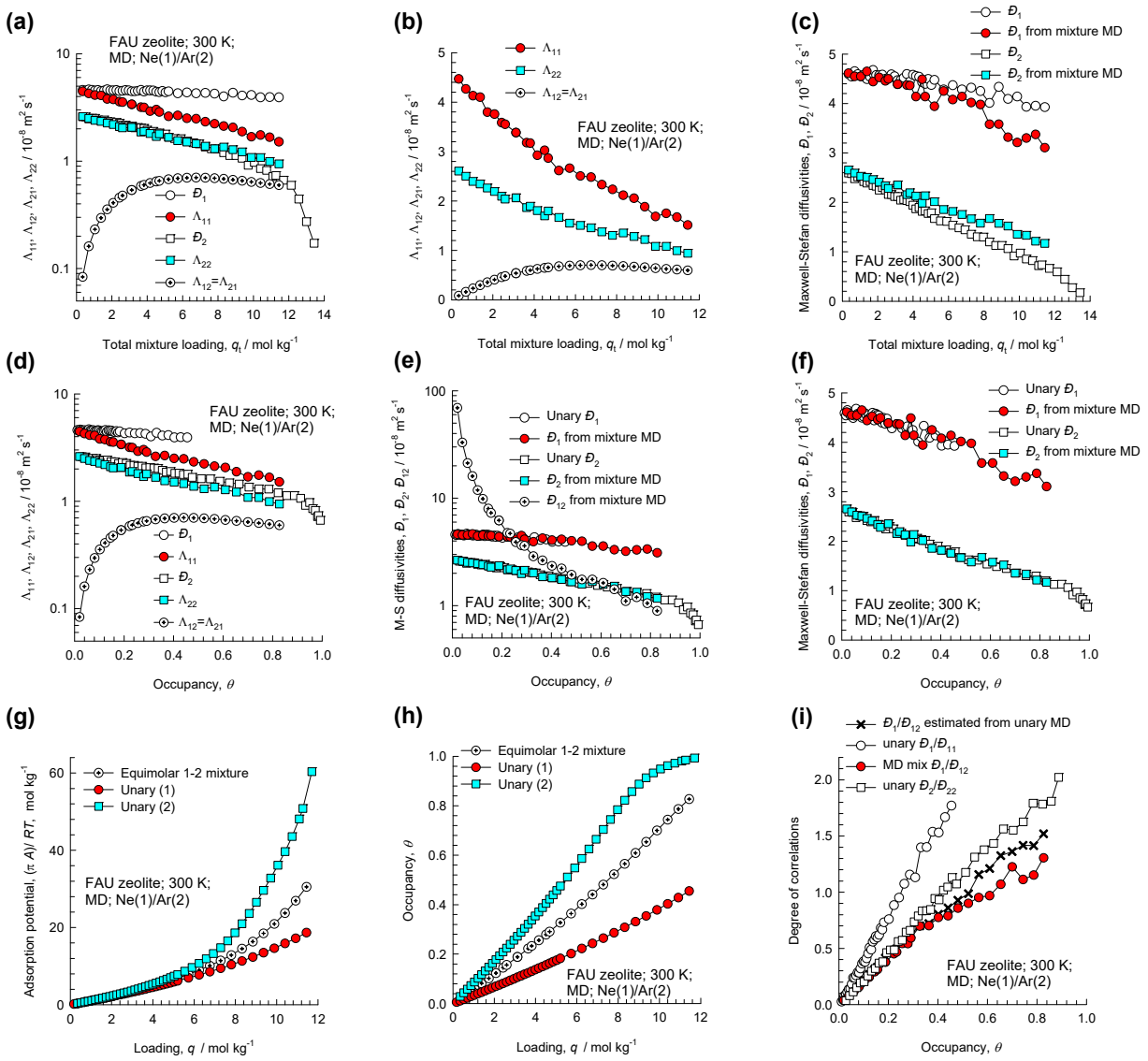

Figure S9-14. MD simulated values of $\Lambda_{11}, \Lambda_{12}, \Lambda_{22}$, along with the backed-out M-S diffusivities, $Đ_1, Đ_2, Đ_{12}$ for equimolar (q_1=q_2) binary Ne(1)/Ar(2) mixtures in FAU all-silica zeolite at 300 K plotted as a function of (a, b, c) the total mixture loading q_t= q_1+q_2, and (d, e, f) occupancy θ. (g, h) The adsorption potential, and the occupancy plotted as function of the molar loading. (i) degree of correlations.

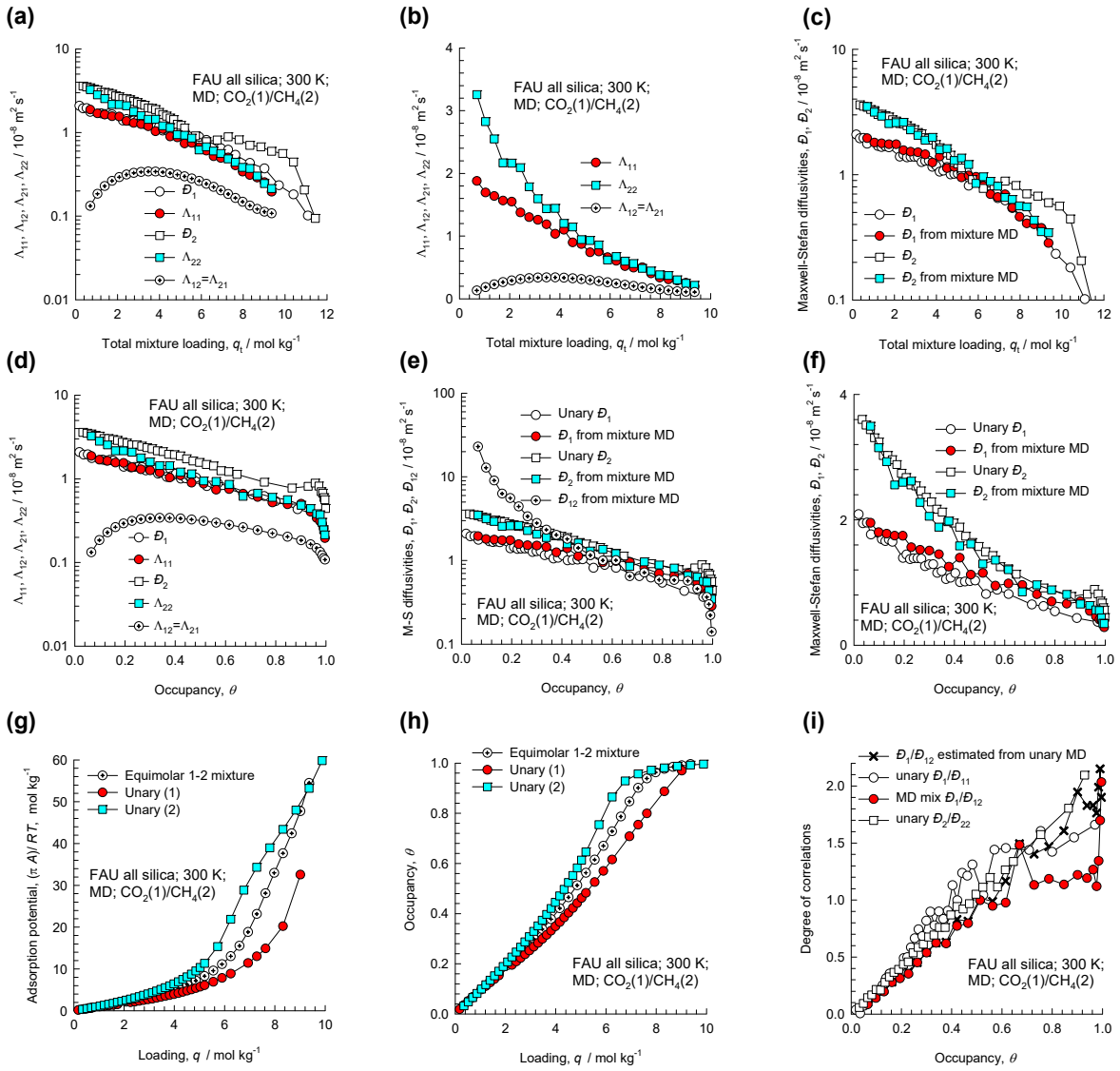

Figure S9-15. MD simulated values of $\Lambda_{11},\Lambda_{12},\Lambda_{22}$, along with the backed-out M-S diffusivities, $Đ_1,Đ_2,Đ_{12}$ for equimolar (q_1=q_2) binary CO_2(1)/CH_4(2) mixtures in FAU all-silica zeolite at 300 K plotted as a function of (a, b, c) the total mixture loading q_t= q_1+q_2, and (d, e, f) occupancy θ. (g, h) The adsorption potential, and the occupancy plotted as function of the molar loading. (i) degree of correlations.

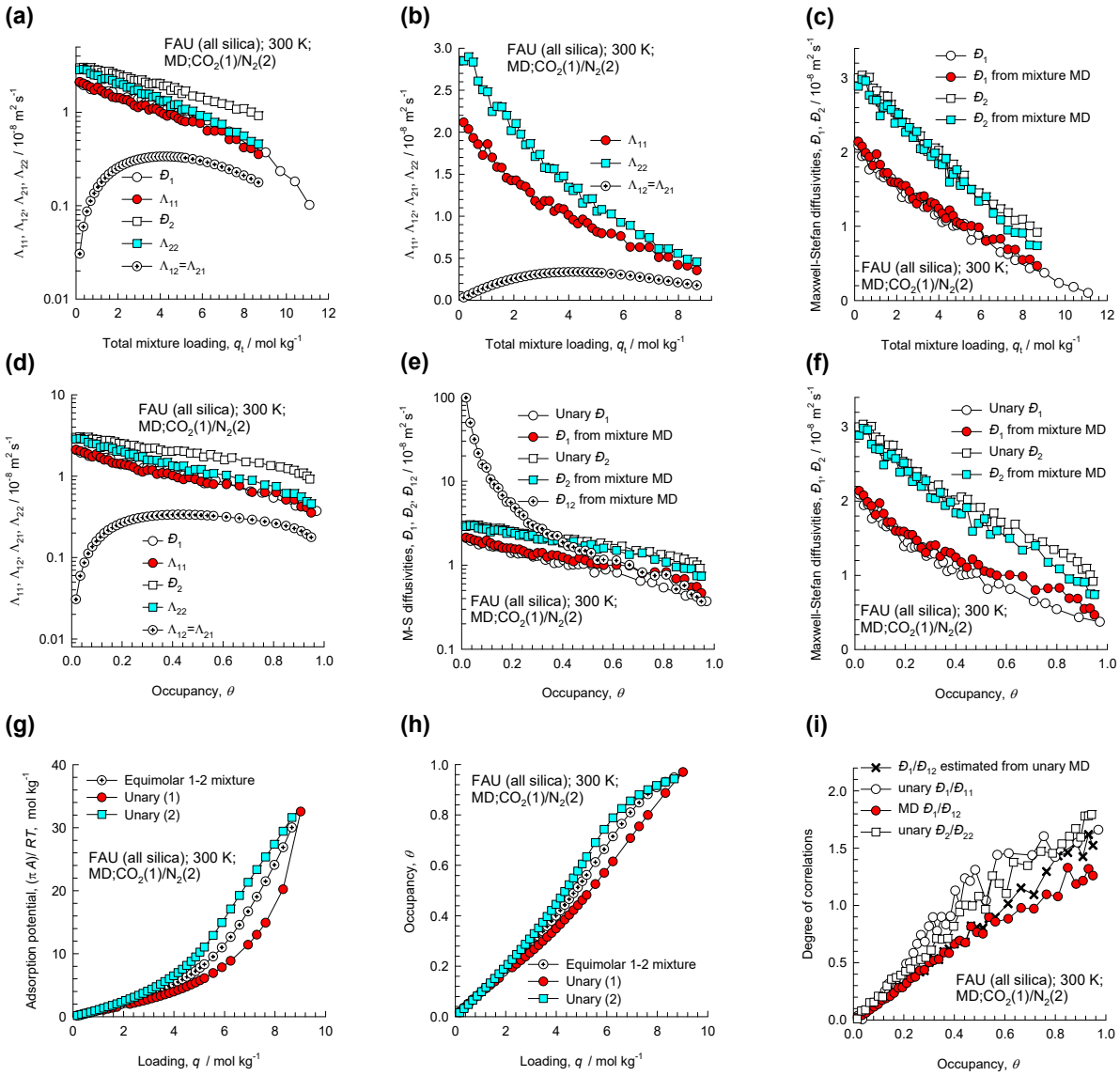

Figure S9-16. MD simulated values of $\Lambda_{11}, \Lambda_{12}, \Lambda_{22}$, along with the backed-out M-S diffusivities, $Đ_1, Đ_2, Đ_{12}$ for equimolar (q_1=q_2) binary CO_2(1)/N_2(2) mixtures in FAU all-silica zeolite at 300 K plotted as a function of (a, b, c) the total mixture loading q_t= q_1+q_2, and (d, e, f) occupancy θ. (g, h) The adsorption potential, and the occupancy plotted as function of the molar loading. (i) degree of correlations.

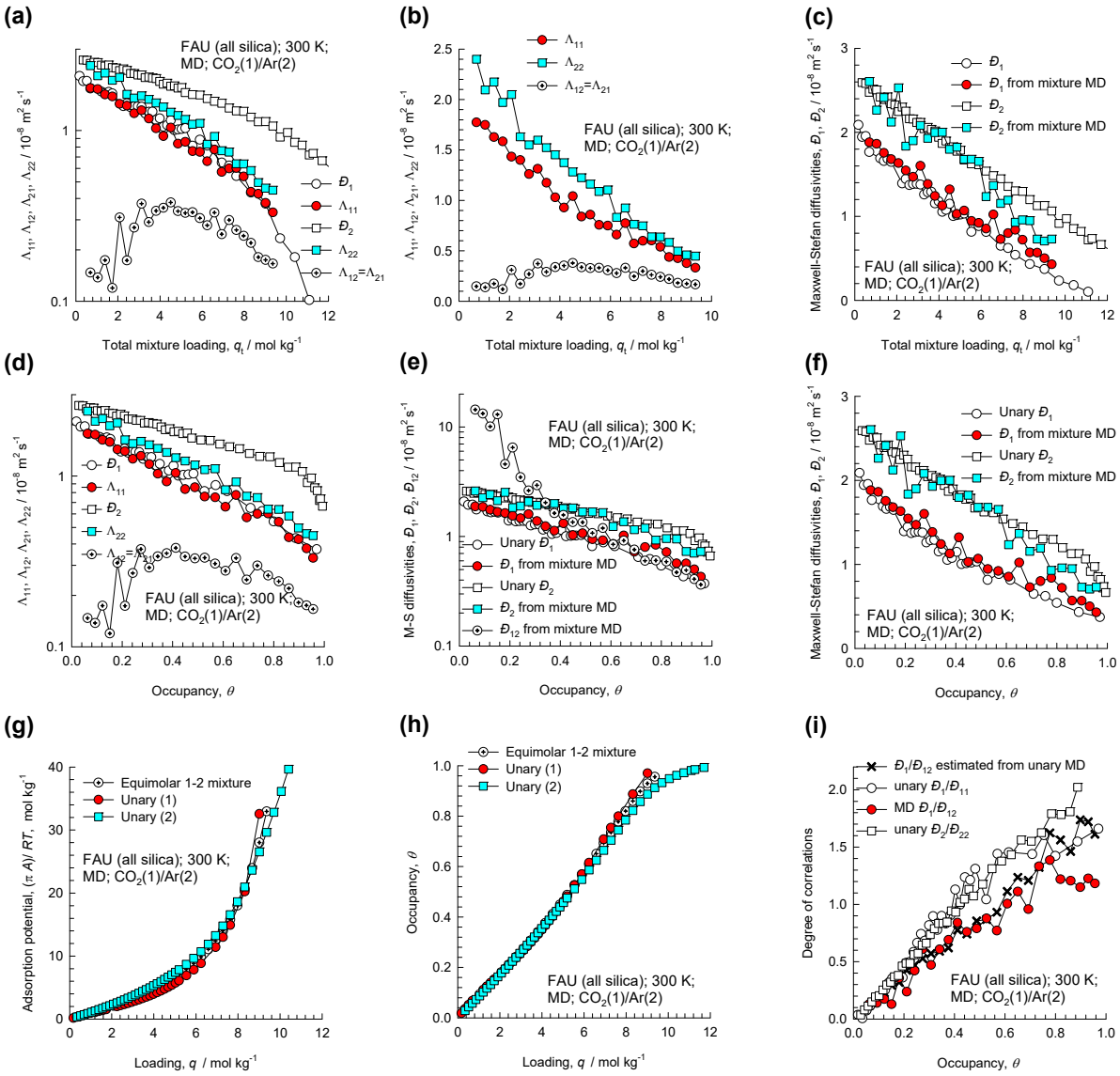

Figure S9-17. MD simulated values of $\Lambda_{11},\Lambda_{12},\Lambda_{22}$, along with the backed-out M-S diffusivities, $Đ_1,Đ_2,Đ_{12}$ for equimolar (q_1=q_2) binary CO_2(1)/Ar(2) mixtures in FAU all-silica zeolite at 300 K plotted as a function of (a, b, c) the total mixture loading q_t= q_1+q_2, and (d, e, f) occupancy θ. (g, h) The adsorption potential, and the occupancy plotted as function of the molar loading. (i) degree of correlations.

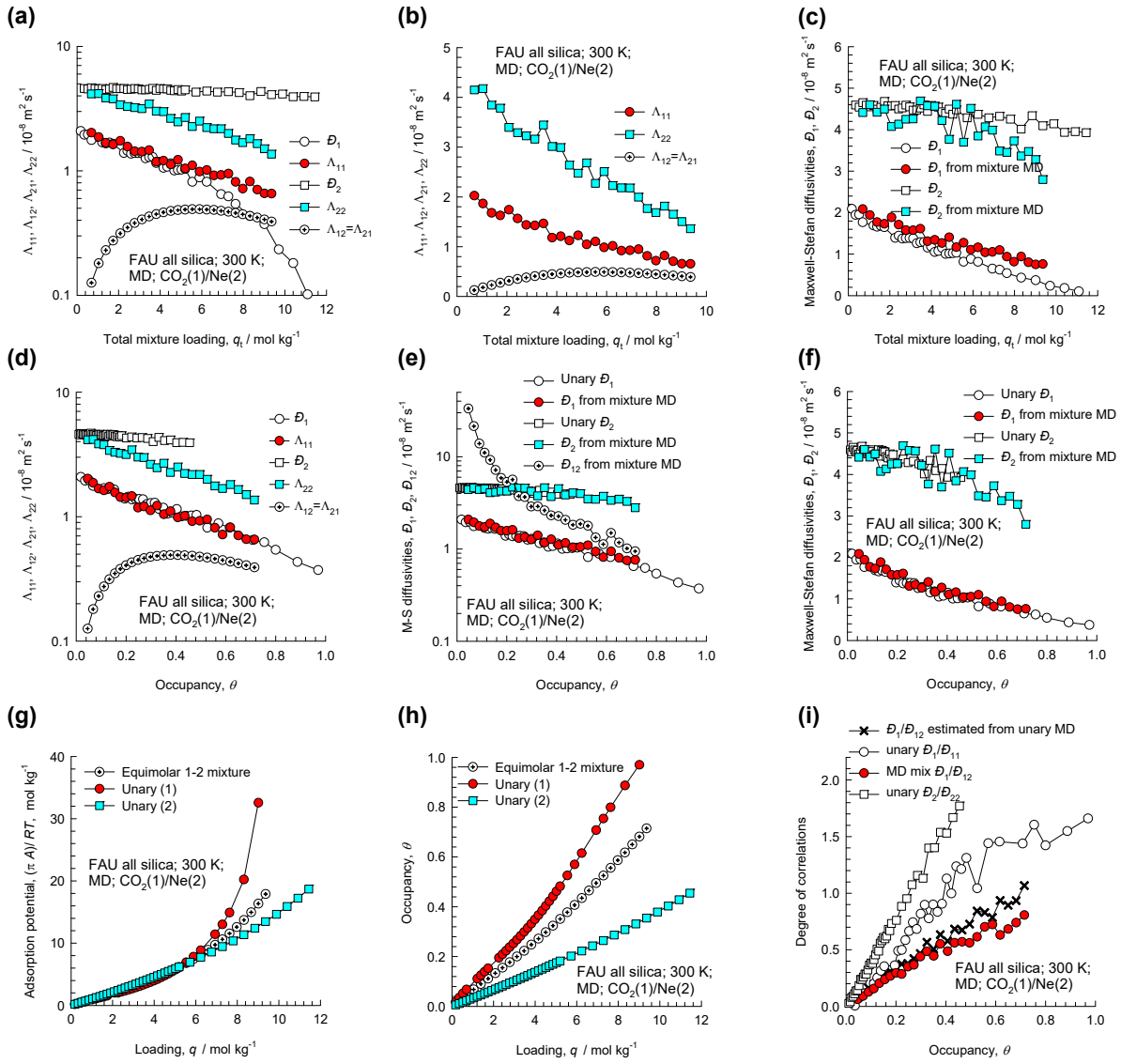

Figure S9-18. MD simulated values of $\Lambda_{11},\Lambda_{12},\Lambda_{22}$, along with the backed-out M-S diffusivities, $Đ_1,Đ_2,Đ_{12}$ for equimolar (q_1=q_2) binary CO_2(1)/Ne(2) mixtures in FAU all-silica zeolite at 300 K plotted as a function of (a, b, c) the total mixture loading q_t= q_1+q_2, and (d, e, f) occupancy θ. (g, h) The adsorption potential, and the occupancy plotted as function of the molar loading. (i) degree of correlations.

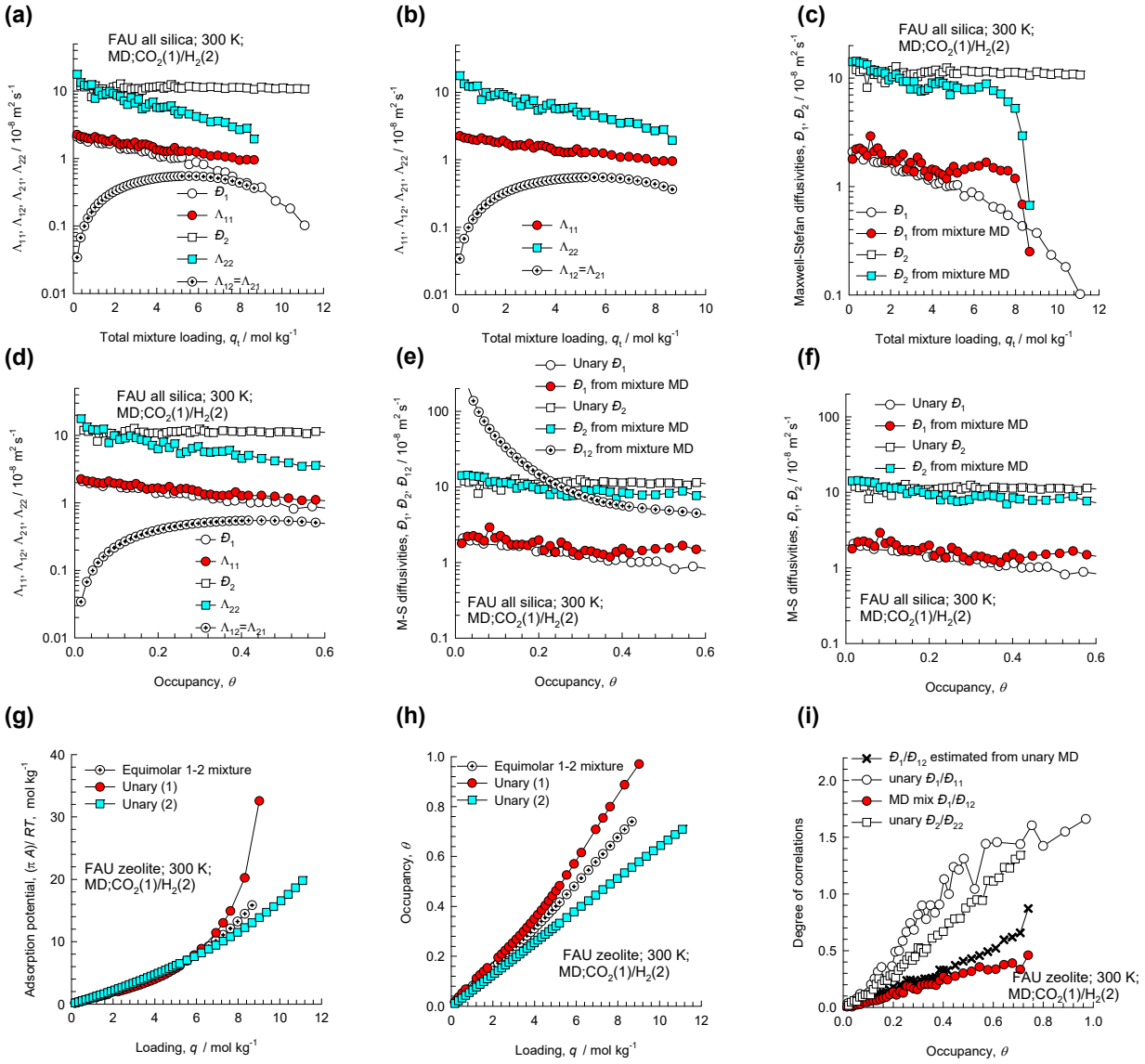

Figure S9-19. MD simulated values of $\Lambda_{11}, \Lambda_{12}, \Lambda_{22}$, along with the backed-out M-S diffusivities, $Đ_1, Đ_2, Đ_{12}$ for equimolar (q_1=q_2) binary CO_2(1)/H_2(2) mixtures in FAU all-silica zeolite at 300 K plotted as a function of (a, b, c) the total mixture loading q_t= q_1+q_2, and (d, e, f) occupancy θ. (g, h) The adsorption potential, and the occupancy plotted as function of the molar loading. (i) degree of correlations.

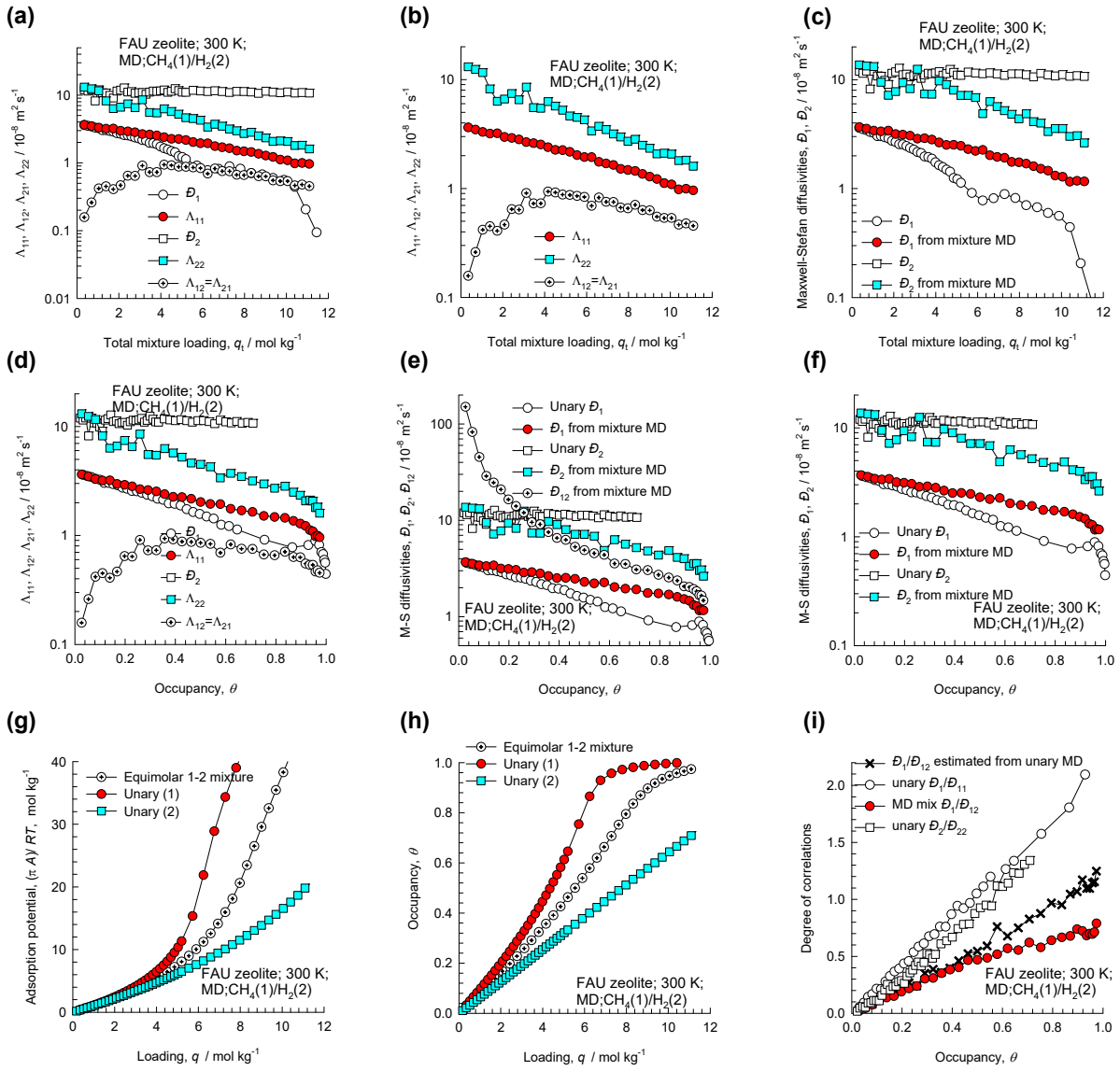

Figure S9-20. MD simulated values of $\Lambda_{11}, \Lambda_{12}, \Lambda_{22}$, along with the backed-out M-S diffusivities, $Đ_1, Đ_2, Đ_{12}$ for equimolar (q_1=q_2) binary $CH_4(1)/H_2(2)$ mixtures in FAU all-silica zeolite plotted as a function of (a, b, c) the total mixture loading $q_t = q_1+q_2$, and (d, e, f) occupancy θ. (g, h) The adsorption potential, and the occupancy plotted as function of the molar loading. (i) degree of correlations.

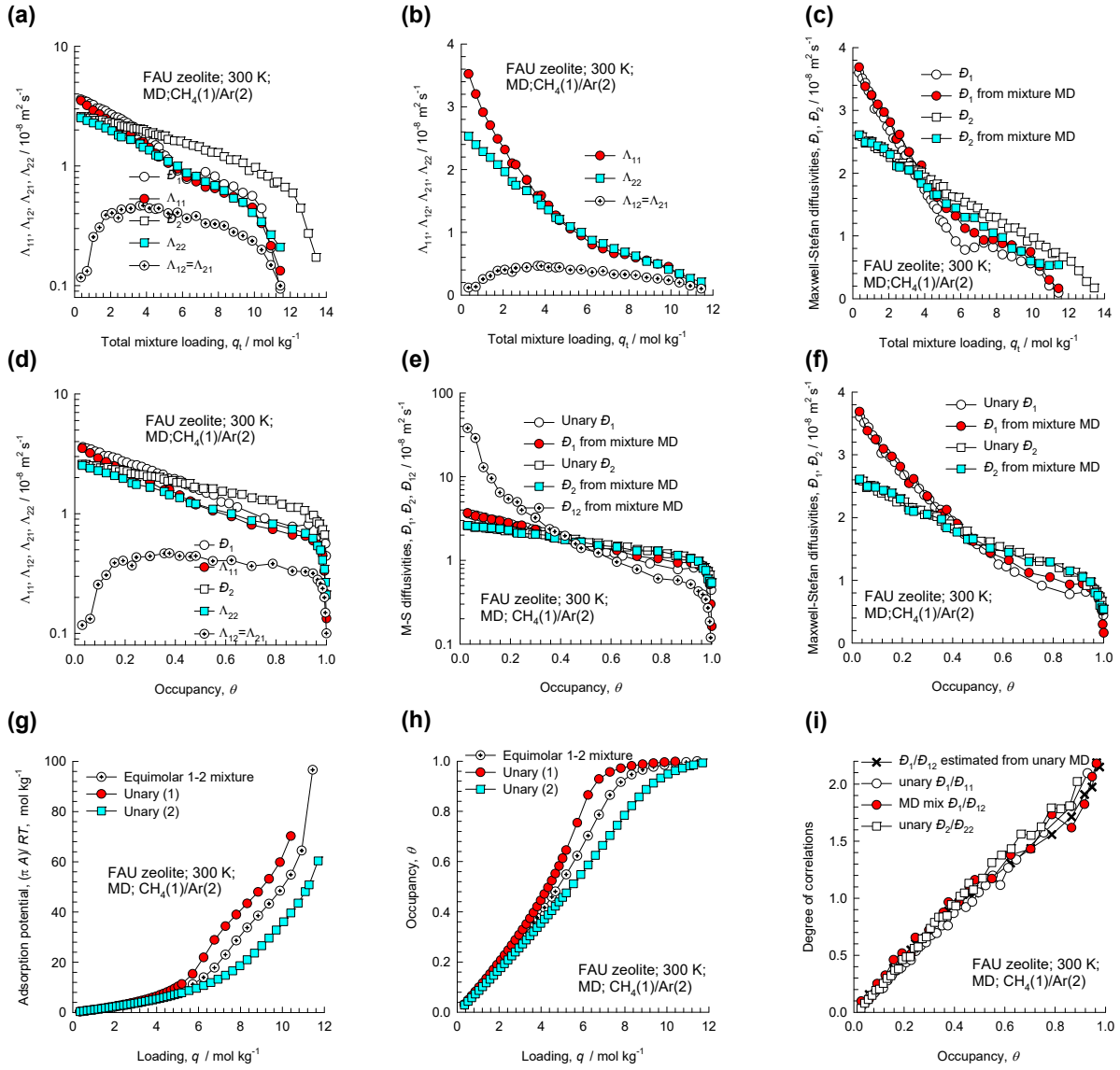

Figure S9-21. MD simulated values of $\Lambda_{11}, \Lambda_{12}, \Lambda_{22}$, along with the backed-out M-S diffusivities, $Đ_1, Đ_2, Đ_{12}$ for equimolar (q_1=q_2) binary CH4(1)/Ar(2) mixtures in FAU all-silica zeolite at 300 K plotted as a function of (a, b, c) the total mixture loading $q_t = q_1+q_2$, and (d, e, f) occupancy θ. (g, h) The adsorption potential, and the occupancy plotted as function of the molar loading. (i) degree of correlations.

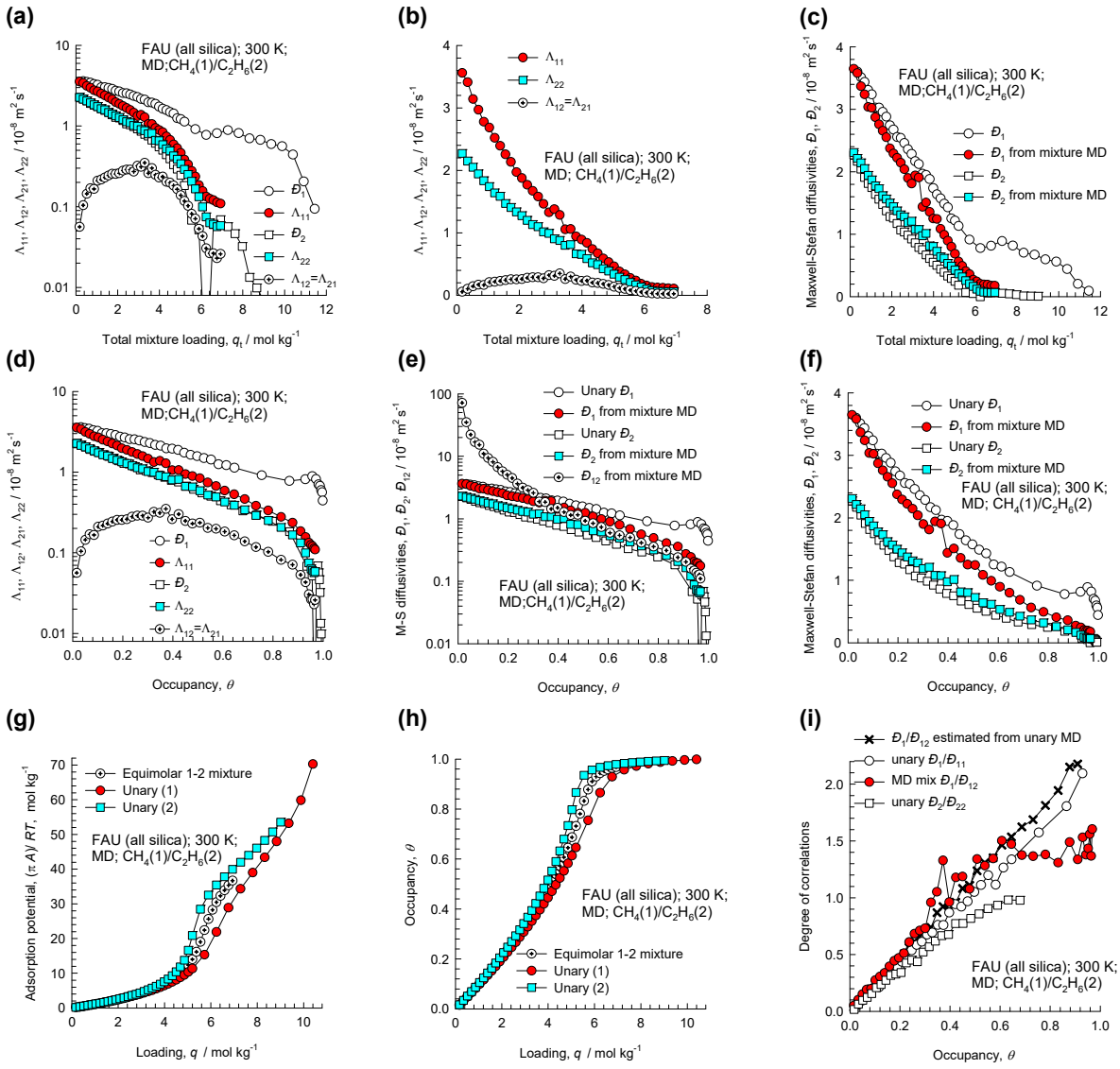

Figure S9-22. MD simulated values of $\Lambda_{11}, \Lambda_{12}, \Lambda_{22}$, along with the backed-out M-S diffusivities, $Đ_1, Đ_2, Đ_{12}$ for equimolar (q_1=q_2) binary $CH_4(1)/C_2H_6(2)$ mixtures in FAU all-silica zeolite at 300 K plotted as a function of (a, b, c) the total mixture loading $q_t = q_1+q_2$, and (d, e, f) occupancy θ. (g, h) The adsorption potential, and the occupancy plotted as function of the molar loading. (i) degree of correlations.

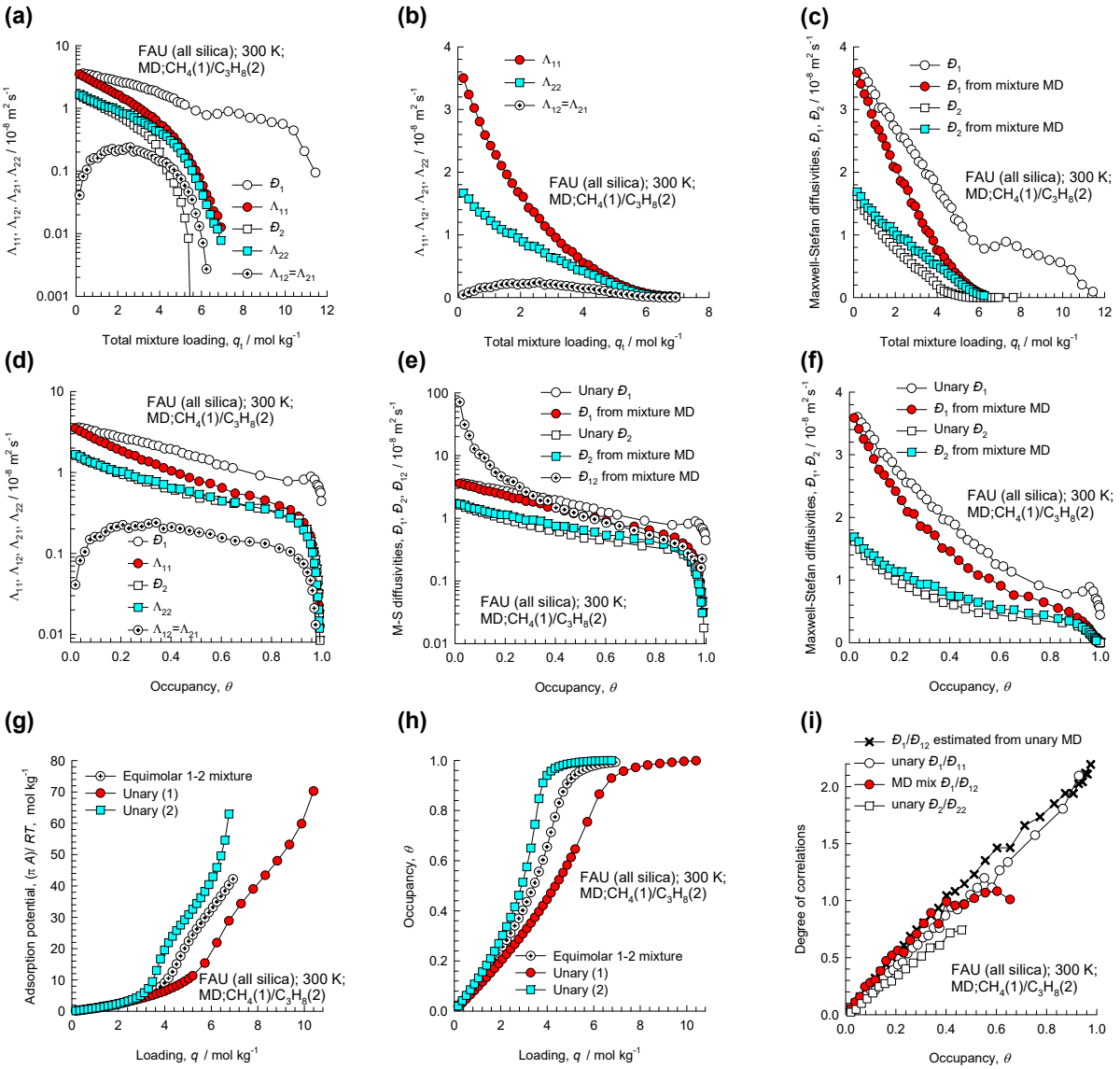

Figure S9-23. MD simulated values of $\Lambda_{11}, \Lambda_{12}, \Lambda_{22}$, along with the backed-out M-S diffusivities, $Đ_1, Đ_2, Đ_{12}$ for equimolar (q_1=q_2) binary $CH_4(1)/C_3H_8(2)$ mixtures in FAU all-silica zeolite at 300 K plotted as a function of (a, b, c) the total mixture loading $q_t = q_1+q_2$, and (d, e, f) occupancy θ. (g, h) The adsorption potential, and the occupancy plotted as function of the molar loading. (i) degree of correlations.

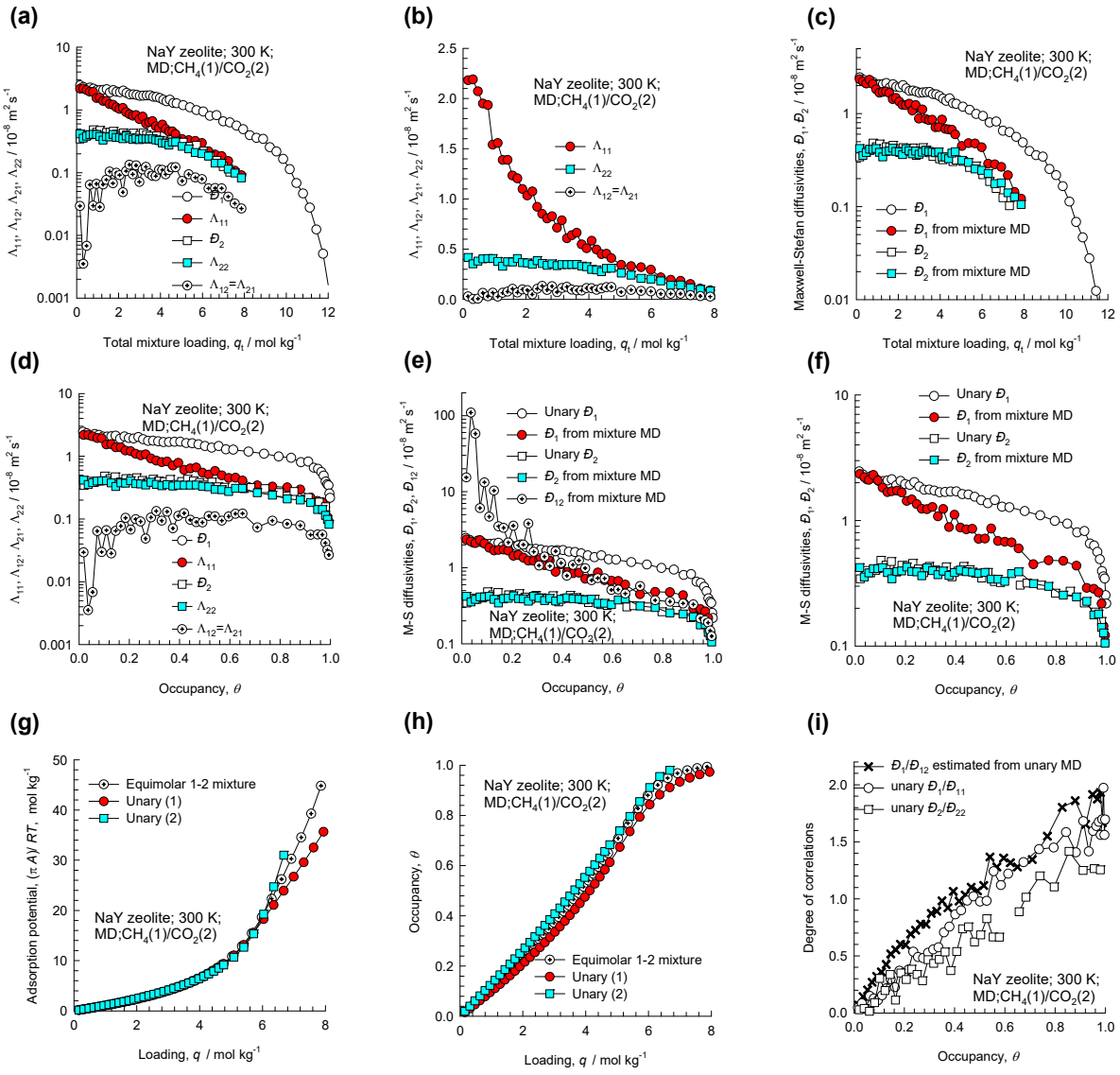

Figure S9-24. MD simulated values of $\Lambda_{11}, \Lambda_{12}, \Lambda_{22}$, along with the backed-out M-S diffusivities, $Đ_1, Đ_2, Đ_{12}$ for equimolar (q_1=q_2) binary $CH_4(1)/CO_2(2)$ mixtures in NaY zeolite (48 Al) at 300 K plotted as a function of (a, b, c) the total mixture loading $q_t = q_1+q_2$, and (d, e, f) occupancy θ. (g, h) The adsorption potential, and the occupancy plotted as function of the molar loading. (i) degree of correlations.

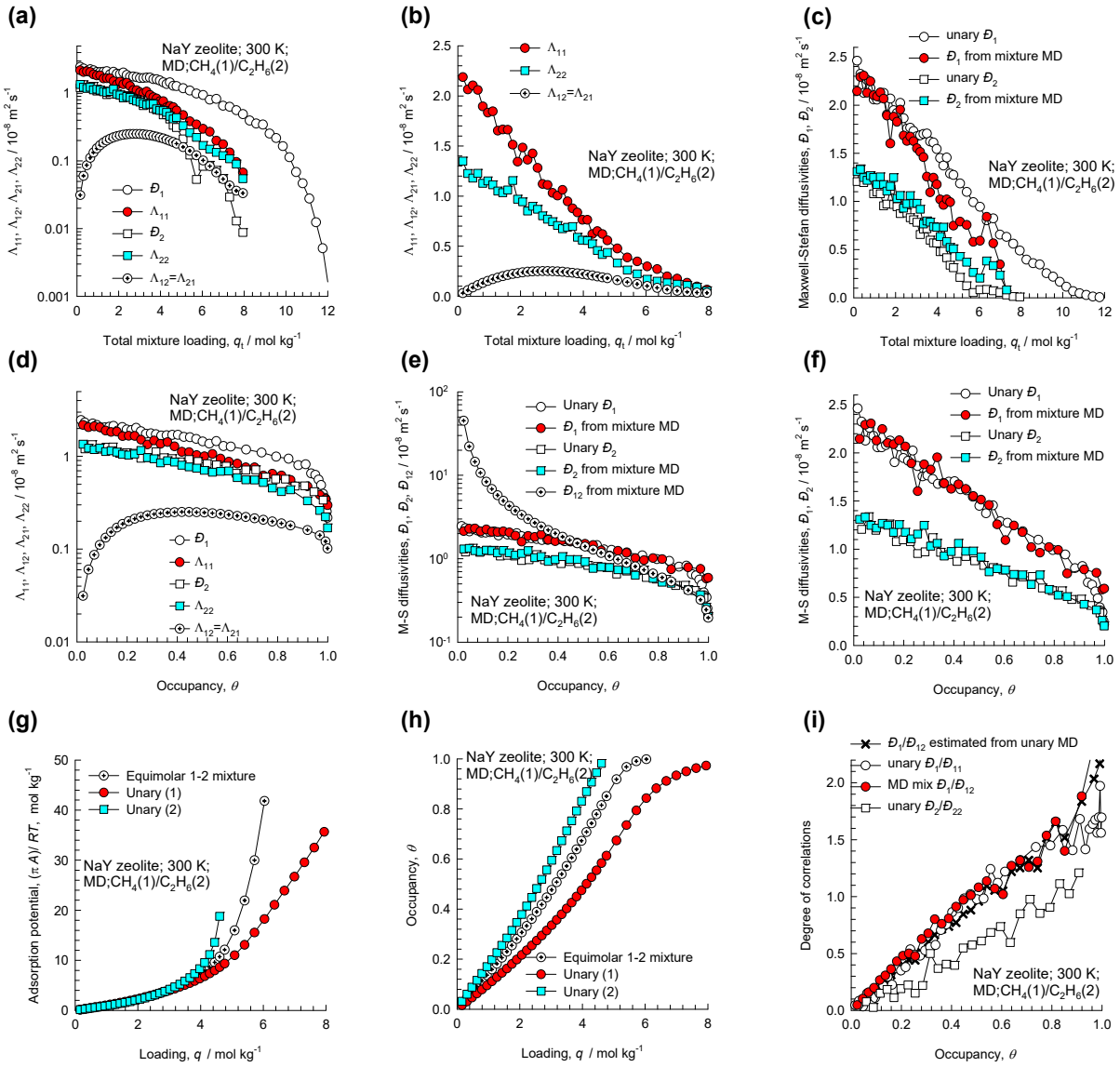

Figure S9-25. MD simulated values of $\Lambda_{11}, \Lambda_{12}, \Lambda_{22}$, along with the backed-out M-S diffusivities, $Đ_1, Đ_2, Đ_{12}$ for equimolar (q_1=q_2) binary $CH_4(1)/C_2H_6(2)$ mixtures in NaY zeolite (48 Al) at 300 K plotted as a function of (a, b, c) the total mixture loading $q_t = q_1+q_2$, and (d, e, f) occupancy θ. (g, h) The adsorption potential, and the occupancy plotted as function of the molar loading. (i) degree of correlations.

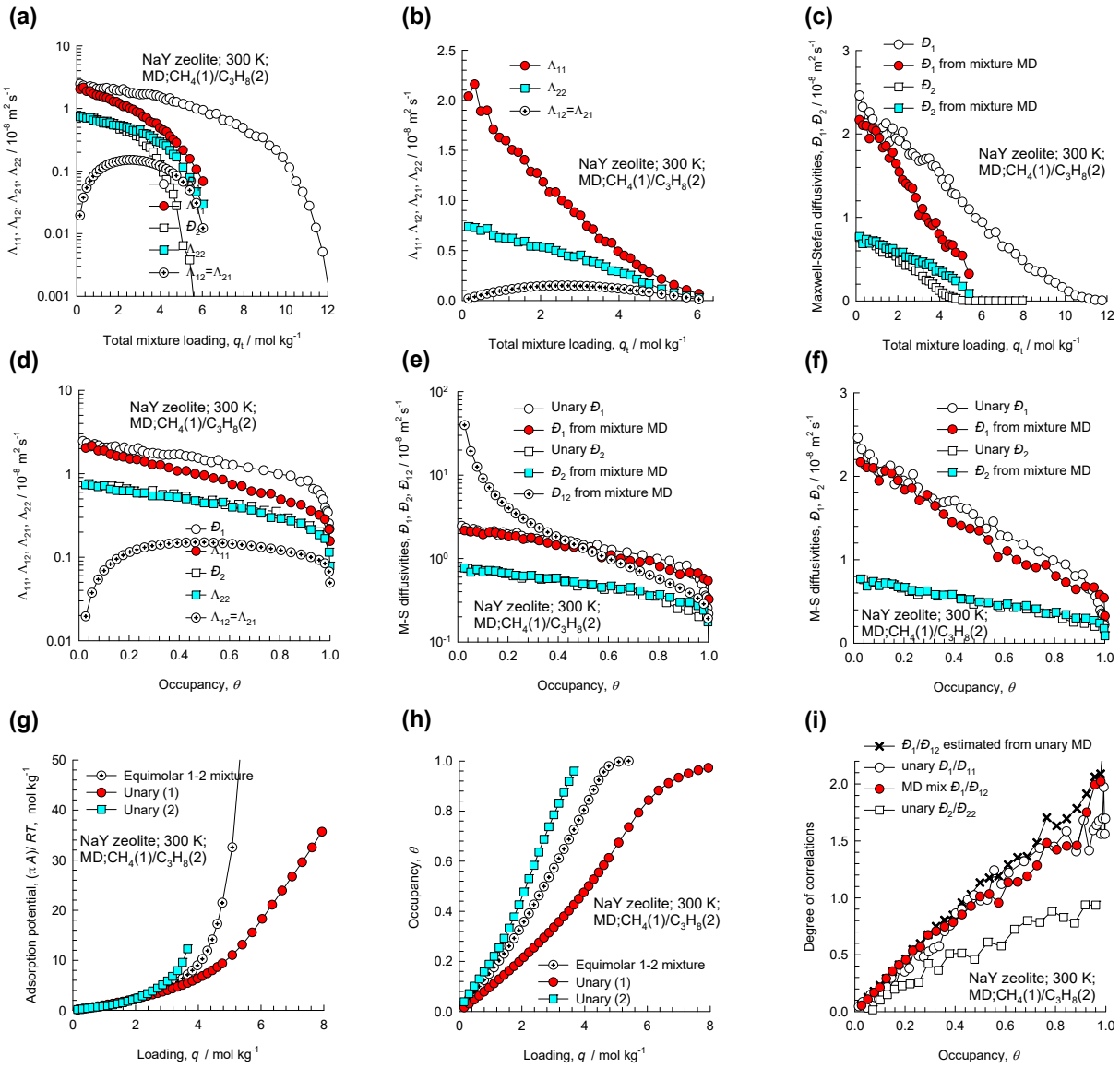

Figure S9-26. MD simulated values of $\Lambda_{11}, \Lambda_{12}, \Lambda_{22}$, along with the backed-out M-S diffusivities, $Đ_1, Đ_2, Đ_{12}$ for equimolar (q_1=q_2) binary $CH_4(1)/C_3H_8(2)$ mixtures in NaY zeolite (48 Al) at 300 K plotted as a function of (a, b, c) the total mixture loading $q_t = q_1+q_2$, and (d, e, f) occupancy θ. (g, h) The adsorption potential, and the occupancy plotted as function of the molar loading. (i) degree of correlations.

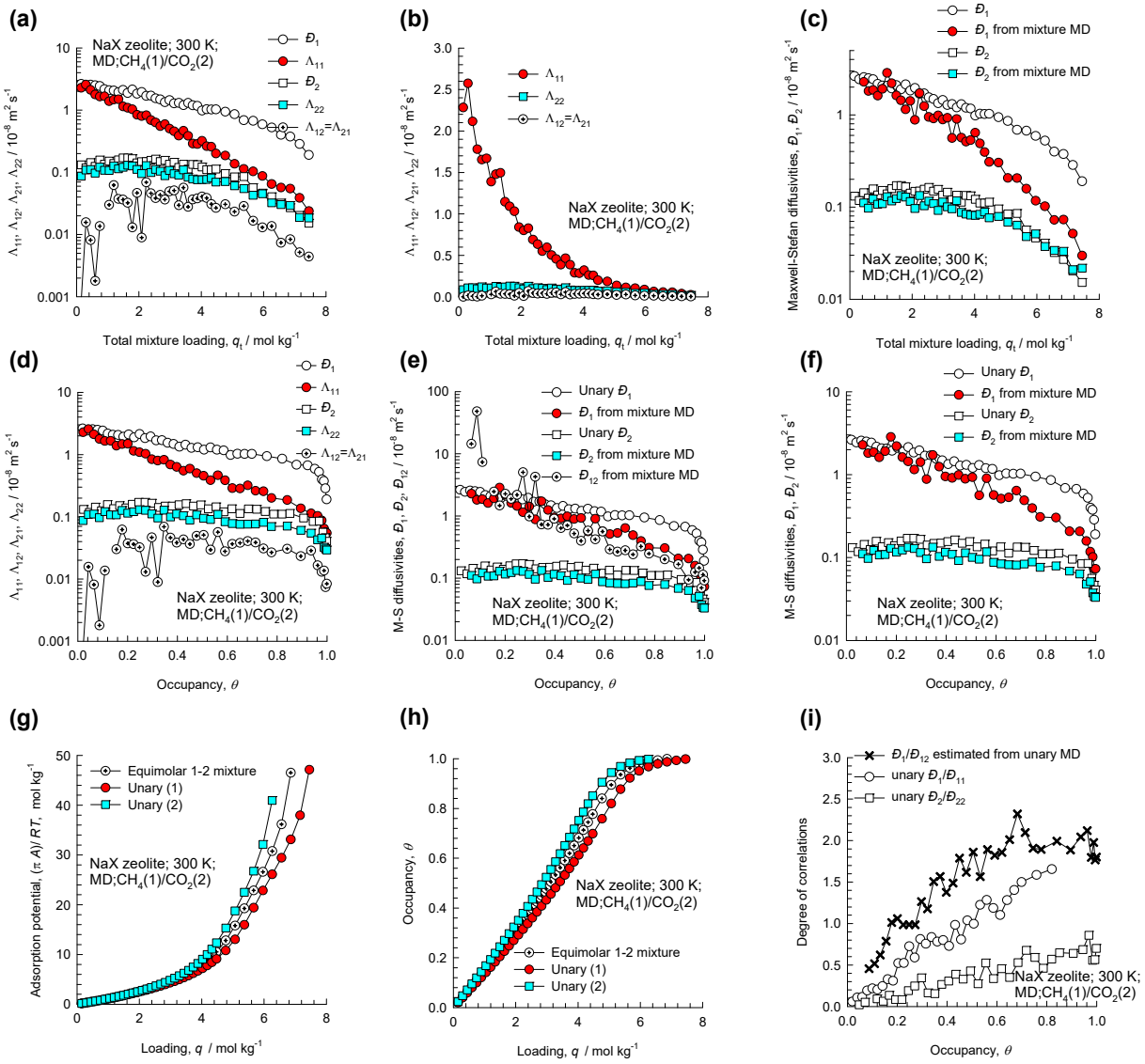

Figure S9-27. MD simulated values of $\Lambda_{11},\Lambda_{12},\Lambda_{22}$, along with the backed-out M-S diffusivities, $Đ_1,Đ_2,Đ_{12}$ for equimolar (q_1=q_2) binary CH_4(1)/CO_2(2) mixtures in NaX zeolite (86 Al) at 300 K plotted as a function of (a, b, c) the total mixture loading q_t= q_1+q_2, and (d, e, f) occupancy θ. (g, h) The adsorption potential, and the occupancy plotted as function of the molar loading. (i) degree of correlations.

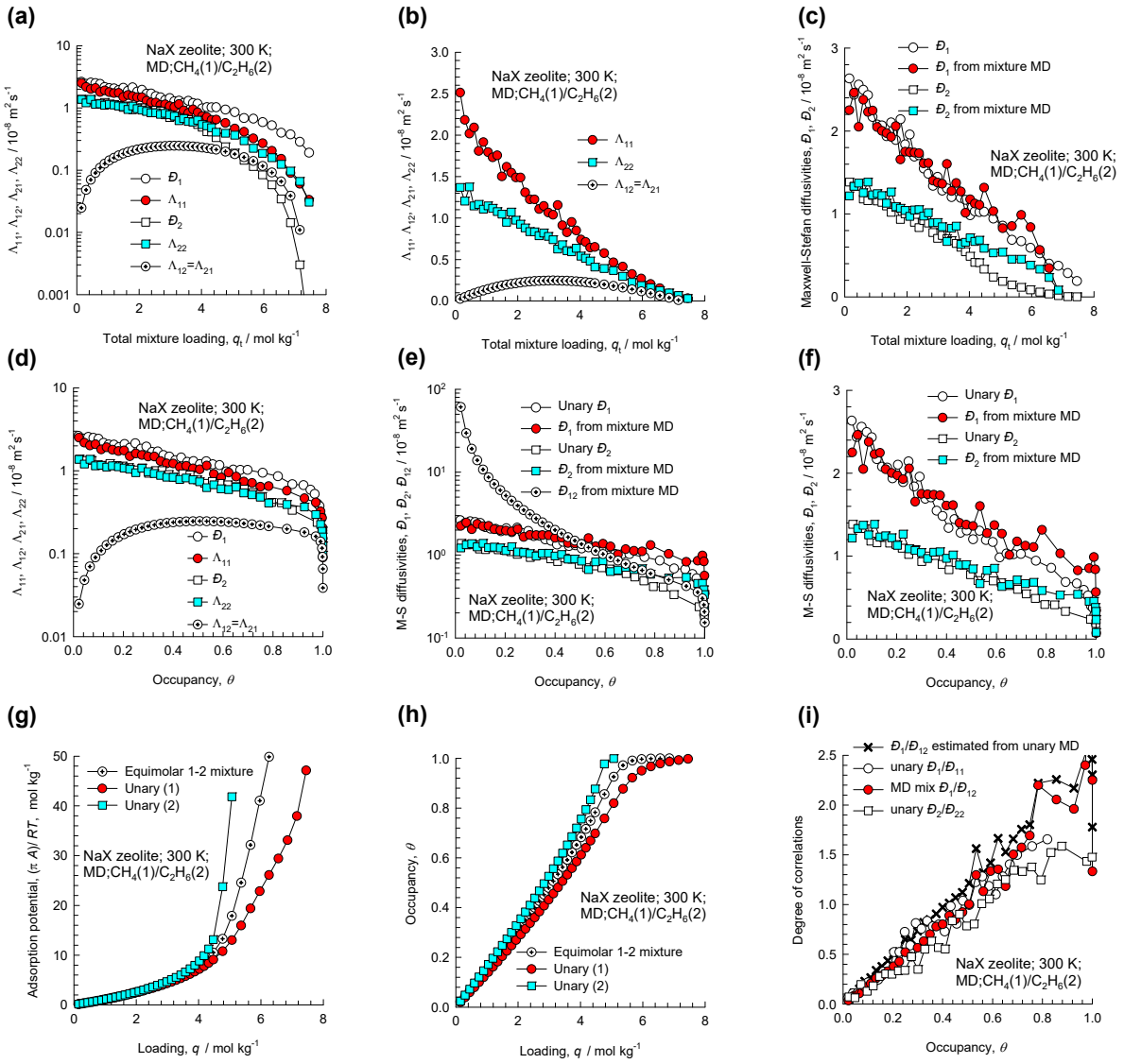

Figure S9-28. MD simulated values of $\Lambda_{11}, \Lambda_{12}, \Lambda_{22}$, along with the backed-out M-S diffusivities, $Đ_1, Đ_2, Đ_{12}$ for equimolar (q_1=q_2) binary $CH_4(1)/C_2H_6(2)$ mixtures in NaX zeolite (86 Al) at 300 K plotted as a function of (a, b, c) the total mixture loading $q_t = q_1+q_2$, and (d, e, f) occupancy θ. (g, h) The adsorption potential, and the occupancy plotted as function of the molar loading. (i) degree of correlations.

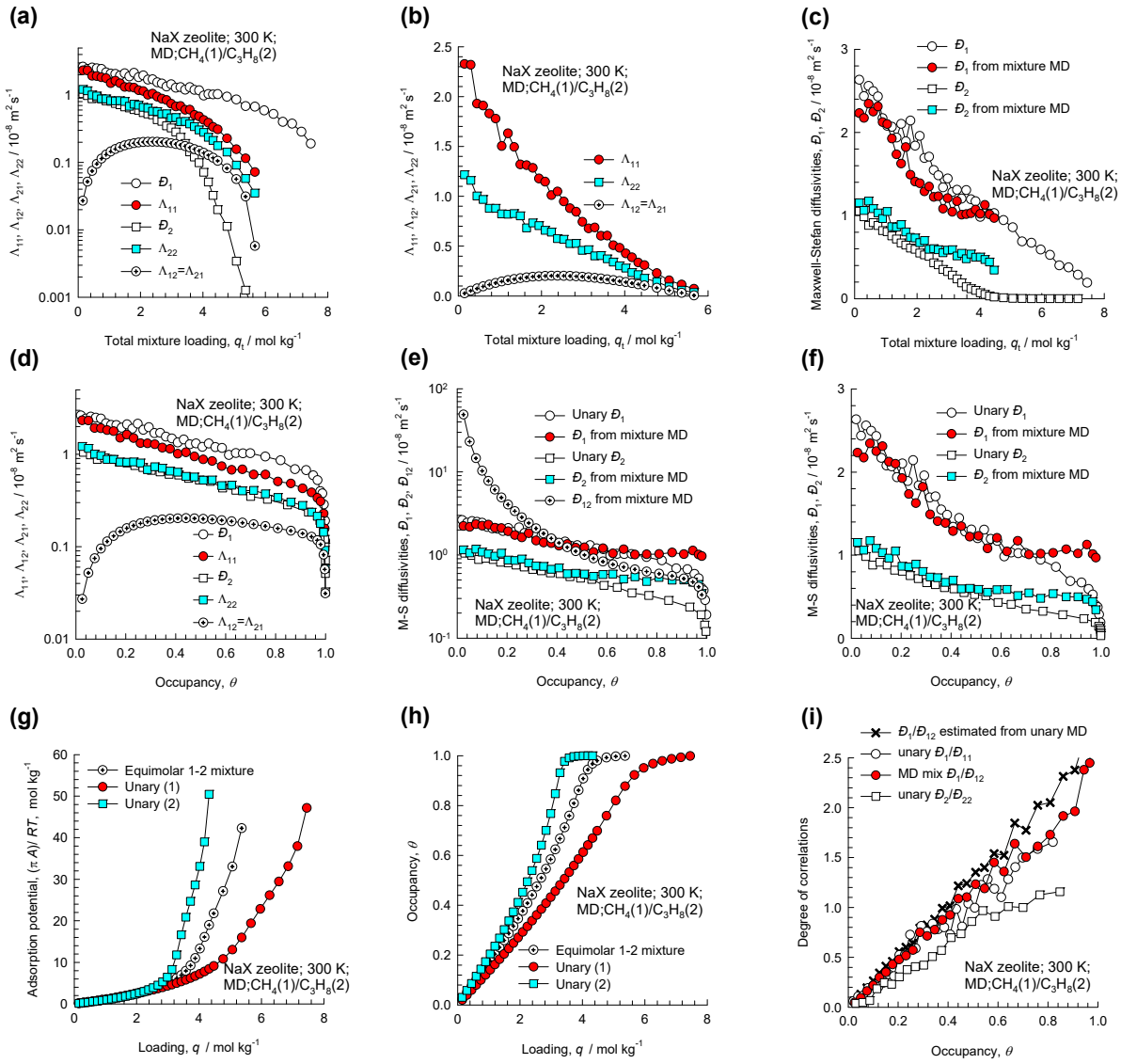

Figure S9-29. MD simulated values of $\Lambda_{11}, \Lambda_{12}, \Lambda_{22}$, along with the backed-out M-S diffusivities, $Đ_1, Đ_2, Đ_{12}$ for equimolar (q_1=q_2) binary CH_4(1)/C_3H_8(2) mixtures in NaX zeolite (86 Al) at 300 K plotted as a function of (a, b, c) the total mixture loading q_t= q_1+q_2, and (d, e, f) occupancy θ. (g, h) The adsorption potential, and the occupancy plotted as function of the molar loading. (i) degree of correlations.

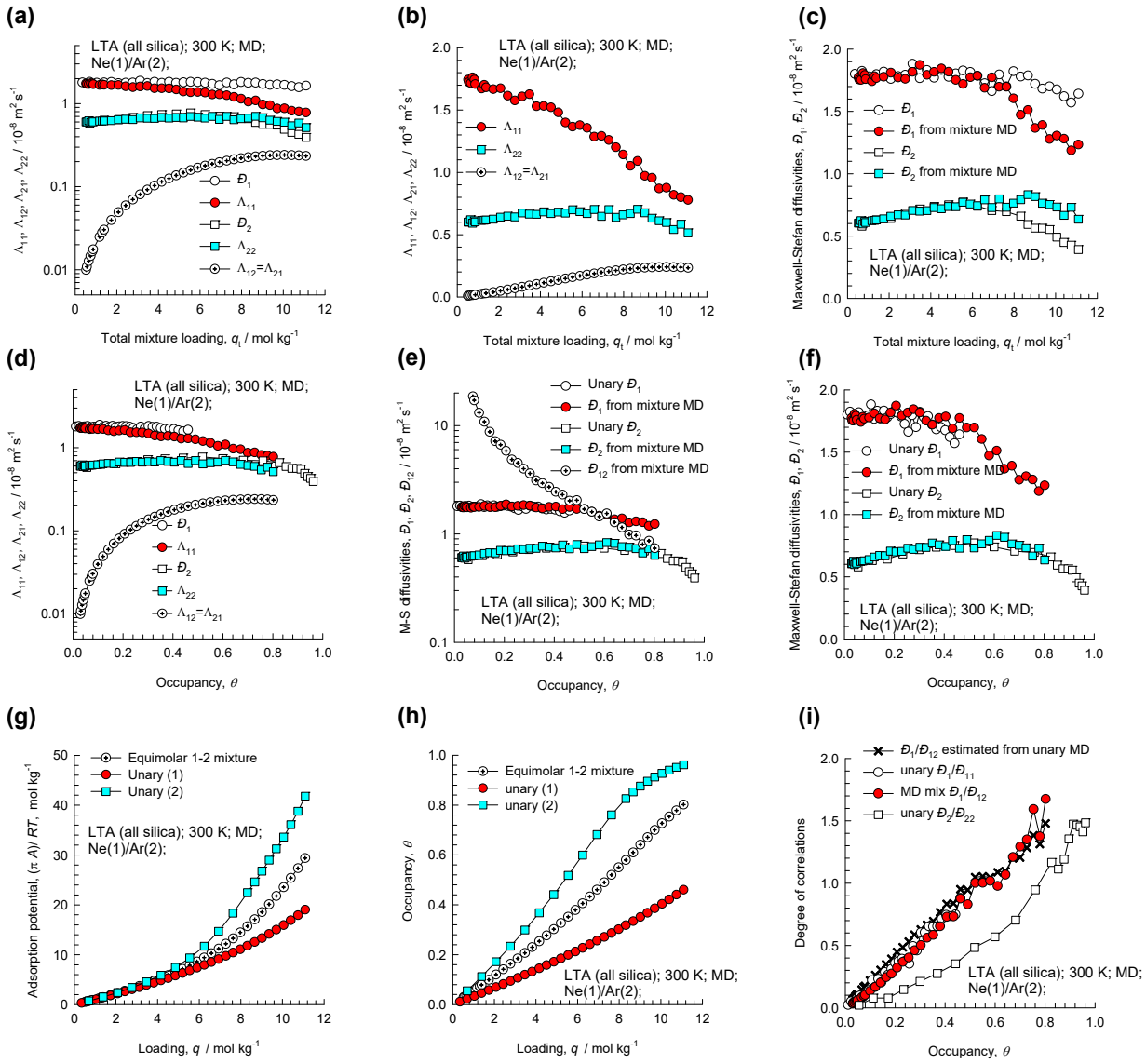

Figure S9-30. MD simulated values of $\Lambda_{11}, \Lambda_{12}, \Lambda_{22}$, along with the backed-out M-S diffusivities, $Đ_1, Đ_2, Đ_{12}$ for equimolar (q_1=q_2) binary Ne(1)/Ar(2) mixtures in LTA all-silica zeolite at 300 K plotted as a function of (a, b, c) the total mixture loading q_t= q_1+q_2, and (d, e, f) occupancy θ. (g, h) The adsorption potential, and the occupancy plotted as function of the molar loading. (i) degree of correlations.

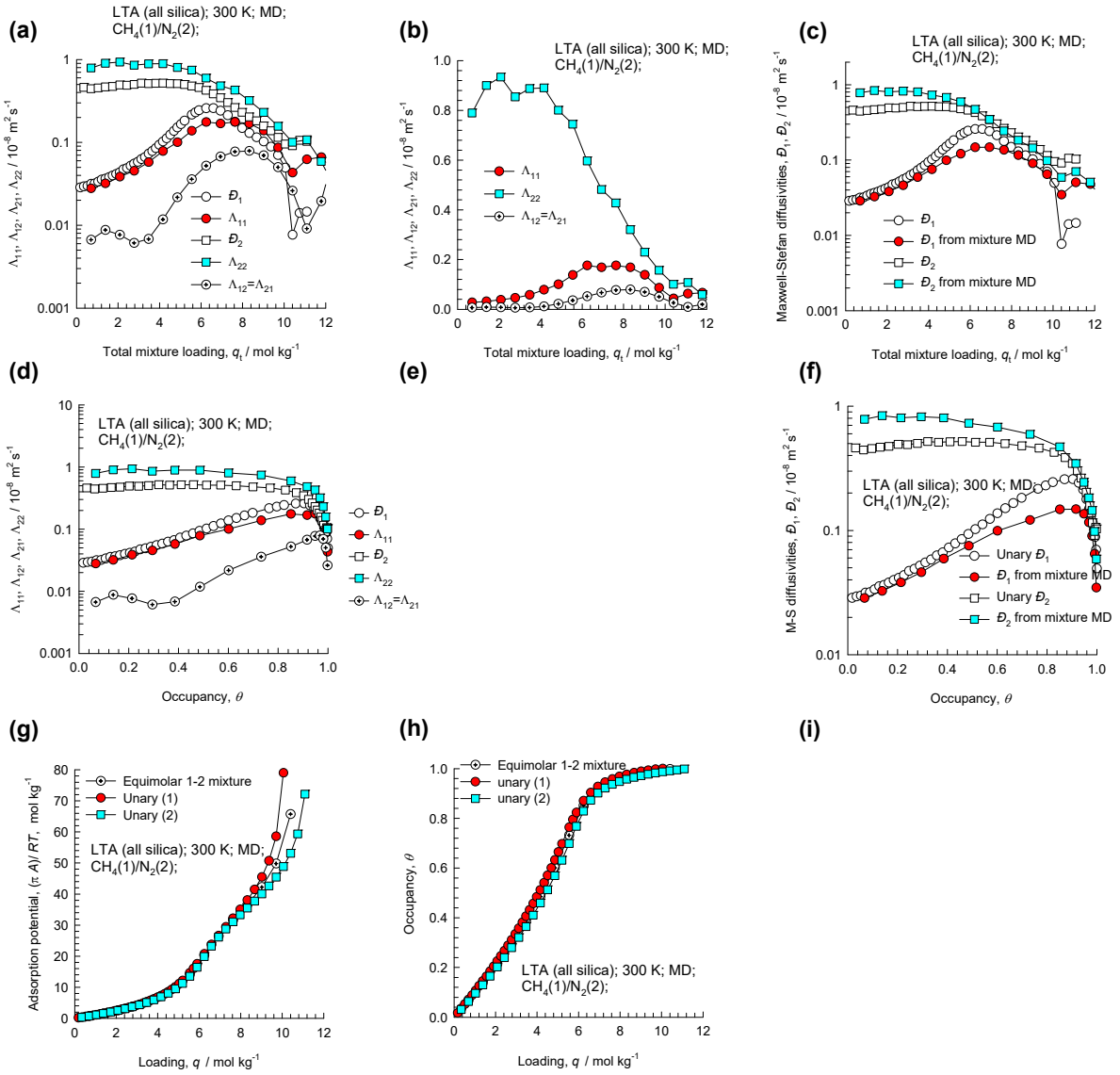

Figure S9-31. MD simulated values of $\Lambda_{11}, \Lambda_{12}, \Lambda_{22}$, along with the backed-out M-S diffusivities, $Đ_1, Đ_2, Đ_{12}$ for equimolar (q_1=q_2) binary $CH_4(1)/N_2(2)$ mixtures in LTA all-silica zeolite at 300 K plotted as a function of (a, b, c) the total mixture loading q_t= q_1+q_2, and (d, e, f) occupancy θ. (g, h) The adsorption potential, and the occupancy plotted as function of the molar loading. It is to be noted there that the correlation effects are of negligible importance for this guest/host combination. Therefore, the Maxwell-Stefan diffusivities reported here are actually the self-diffusivities, $D_{i,self}$, determined from MD using Equation (7-8).

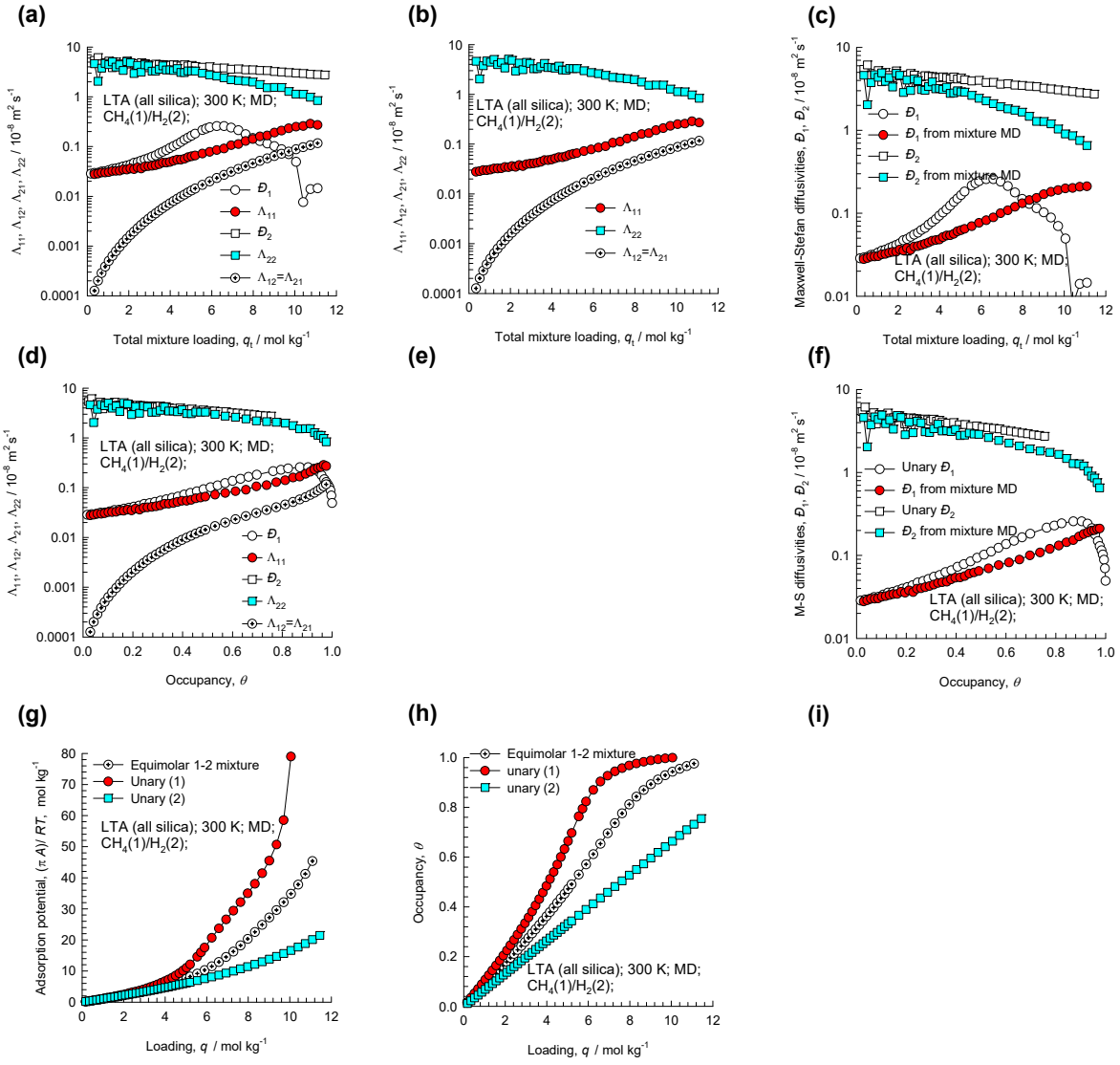

Figure S9-32. MD simulated values of $\Lambda_{11}, \Lambda_{12}, \Lambda_{22}$, along with the backed-out M-S diffusivities, $Đ_1, Đ_2, Đ_{12}$ for equimolar (q_1=q_2) binary $CH_4(1)/H_2(2)$ mixtures in LTA all-silica zeolite at 300 K plotted as a function of (a, b, c) the total mixture loading $q_t = q_1+q_2$, and (d, e, f) occupancy θ. (g, h) The adsorption potential, and the occupancy plotted as function of the molar loading. It is to be noted there that the correlation effects are of negligible importance for this guest/host combination. Therefore, the Maxwell-Stefan diffusivities reported here are actually the self-diffusivities, $D_{i,self}$, determined from MD using Equation (7-8).

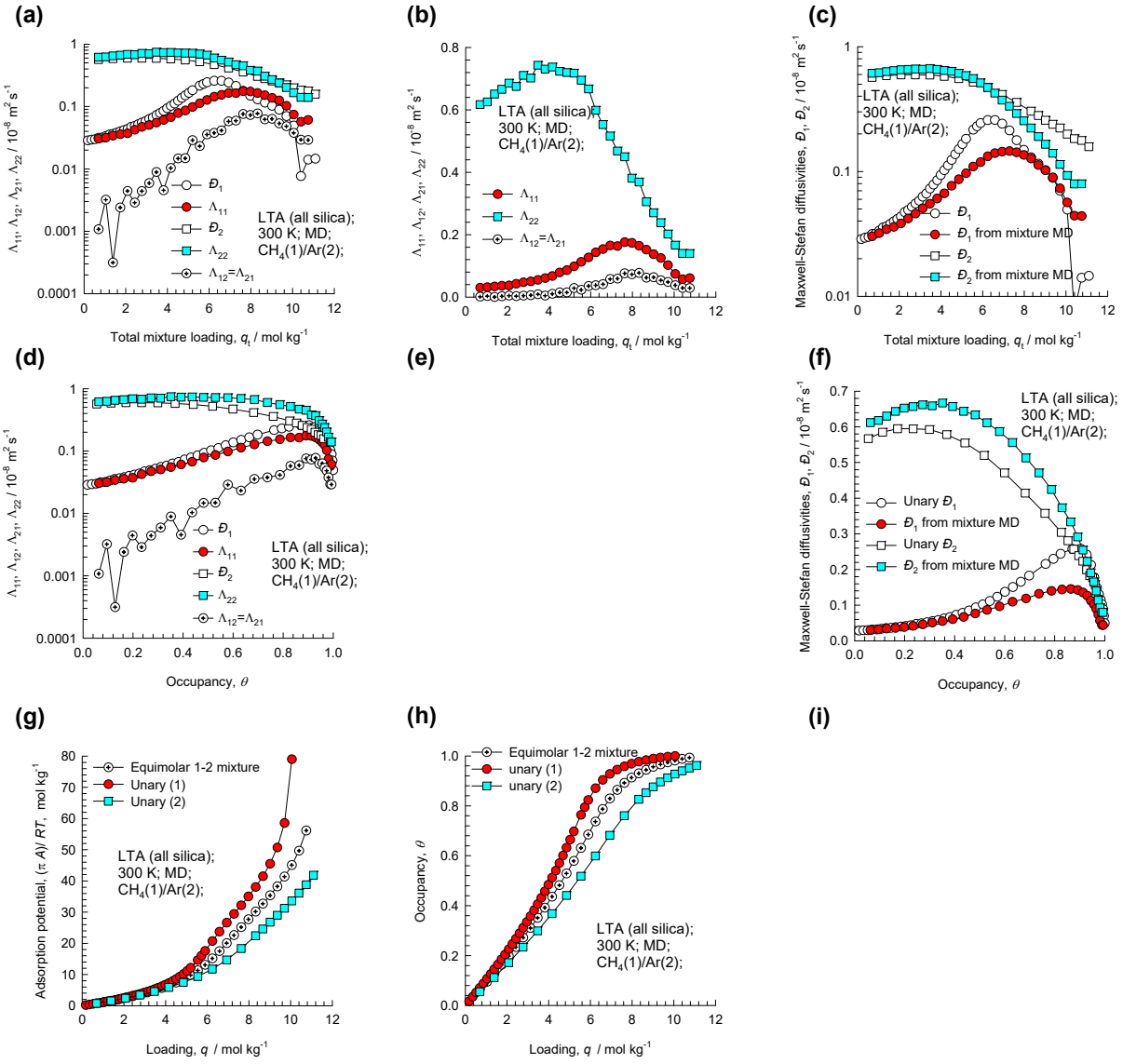

Figure S9-33. MD simulated values of $\Lambda_{11}, \Lambda_{12}, \Lambda_{22}$, along with the backed-out M-S diffusivities, $Đ_1, Đ_2, Đ_{12}$ for equimolar (q_1=q_2) binary CH4(1)/Ar(2) mixtures in LTA all-silica zeolite at 300 K plotted as a function of (a, b, c) the total mixture loading q_t= q_1+q_2, and (d, e, f) occupancy θ. (g, h) The adsorption potential, and the occupancy plotted as function of the molar loading. It is to be noted there that the correlation effects are of negligible importance for this guest/host combination. Therefore, the Maxwell-Stefan diffusivities reported here are actually the self-diffusivities, $D_{i,self}$, determined from MD using Equation (7-8).

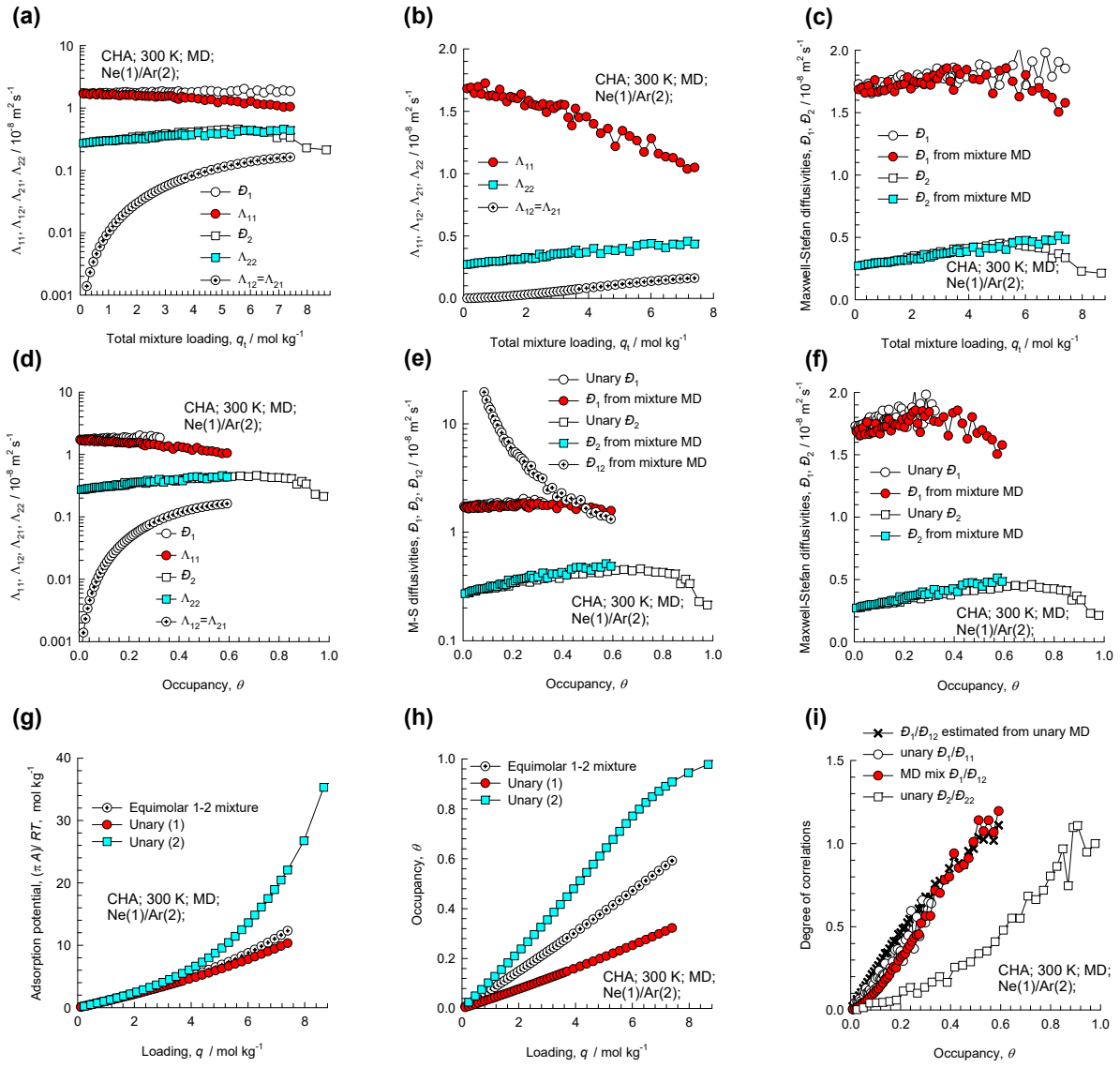

Figure S9-34. MD simulated values of $\Lambda_{11},\Lambda_{12},\Lambda_{22}$, along with the backed-out M-S diffusivities, $Đ_1,Đ_2,Đ_{12}$ for equimolar (q_1=q_2) Ne(1)/Ar(2) mixtures in CHA all-silica zeolite at 300 K plotted as a function of (a, b, c) the total mixture loading q_t= q_1+q_2, and (d, e, f) occupancy θ. (g, h) The adsorption potential, and the occupancy plotted as function of the molar loading. (i) degree of correlations.

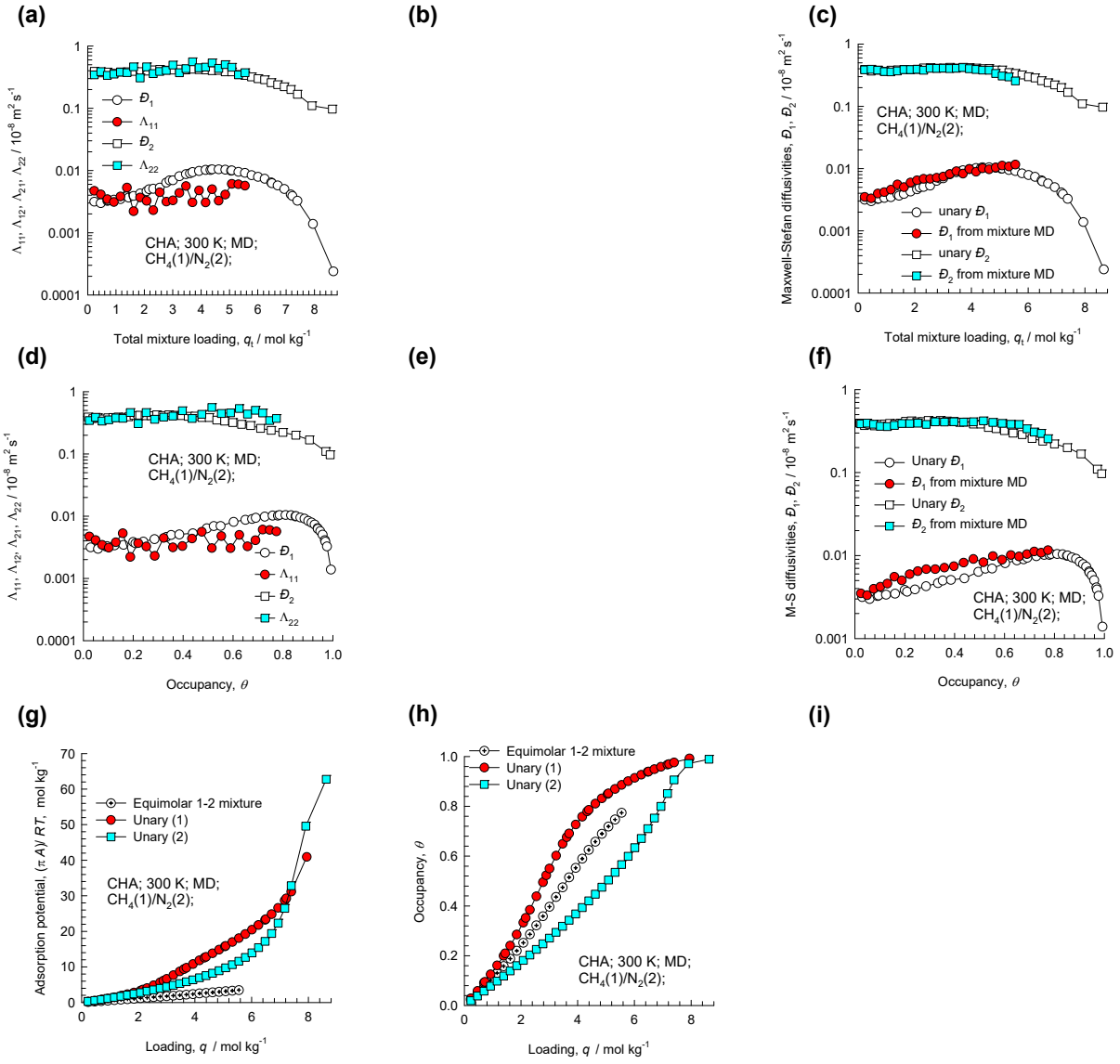

Figure S9-35. MD simulated values of $\Lambda_{11}, \Lambda_{12}, \Lambda_{22}$, along with the backed-out M-S diffusivities, $Đ_1, Đ_2, Đ_{12}$ for equimolar (q_1=q_2) $CH_4(1)/N_2(2)$ mixtures in CHA all-silica zeolite at 300 K plotted as a function of (a, b, c) the total mixture loading $q_t = q_1+q_2$, and (d, e, f) occupancy θ. (g, h) The adsorption potential, and the occupancy plotted as function of the molar loading. It is to be noted there that the correlation effects are of negligible importance for this guest/host combination. Therefore, the Maxwell-Stefan diffusivities reported here are actually the self-diffusivities, $D_{i,self}$, determined from MD using Equation (7-8).

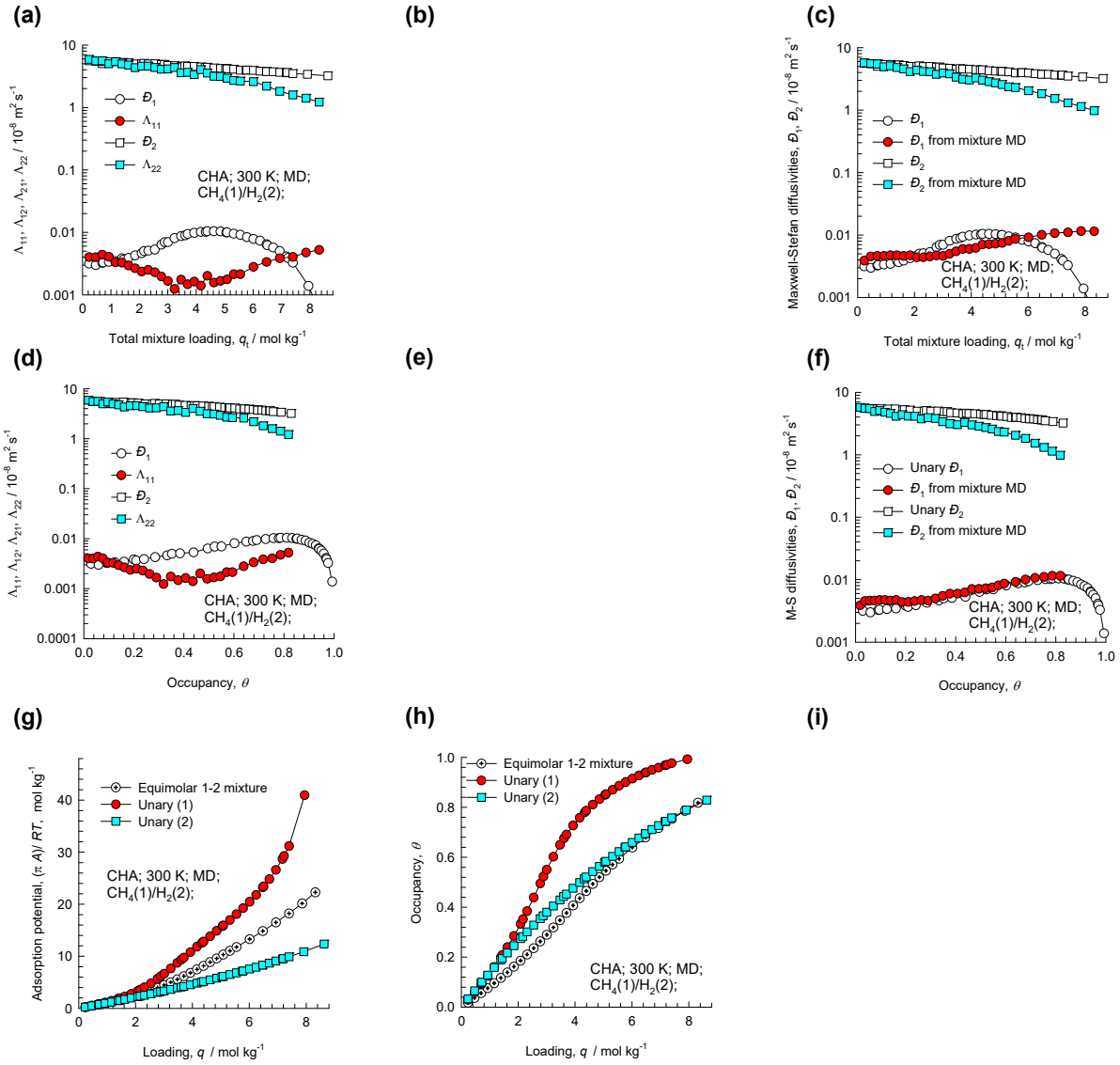

Figure S9-36. MD simulated values of $\Lambda_{11}, \Lambda_{12}, \Lambda_{22}$, along with the backed-out M-S diffusivities, $Đ_1, Đ_2, Đ_{12}$ for equimolar (q_1=q_2) CH_4(1)/H_2(2) mixtures in CHA all-silica zeolite at 300 K plotted as a function of (a, b, c) the total mixture loading $q_t = q_1+q_2$, and (d, e, f) occupancy θ. (g, h) The adsorption potential, and the occupancy plotted as function of the molar loading. It is to be noted there that the correlation effects are of negligible importance for this guest/host combination. Therefore, the Maxwell-Stefan diffusivities reported here are actually the self-diffusivities, $D_{i,self}$, determined from MD using Equation (7-8).

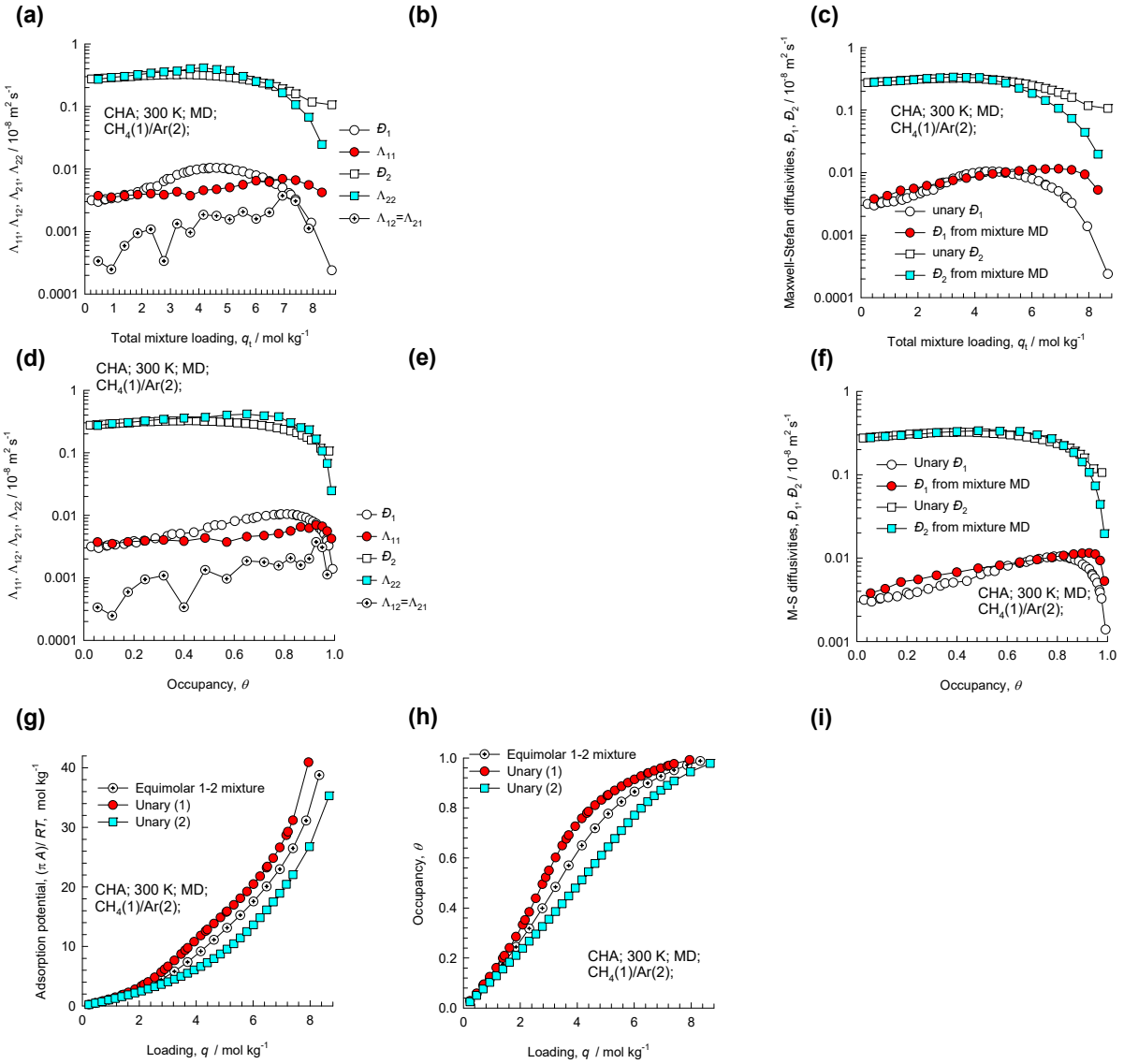

Figure S9-37. MD simulated values of $\Lambda_{11}, \Lambda_{12}, \Lambda_{22}$, along with the backed-out M-S diffusivities, $Đ_1, Đ_2, Đ_{12}$ for equimolar (q_1=q_2) CH_4(1)/Ar(2) mixtures in CHA all-silica zeolite at 300 K plotted as a function of (a, b, c) the total mixture loading $q_t = q_1+q_2$, and (d, e, f) occupancy θ. (g, h) The adsorption potential, and the occupancy plotted as function of the molar loading. It is to be noted there that the correlation effects are of negligible importance for this guest/host combination. Therefore, the Maxwell-Stefan diffusivities reported here are actually the self-diffusivities, $D_{i,self}$, determined from MD using Equation (7-8).

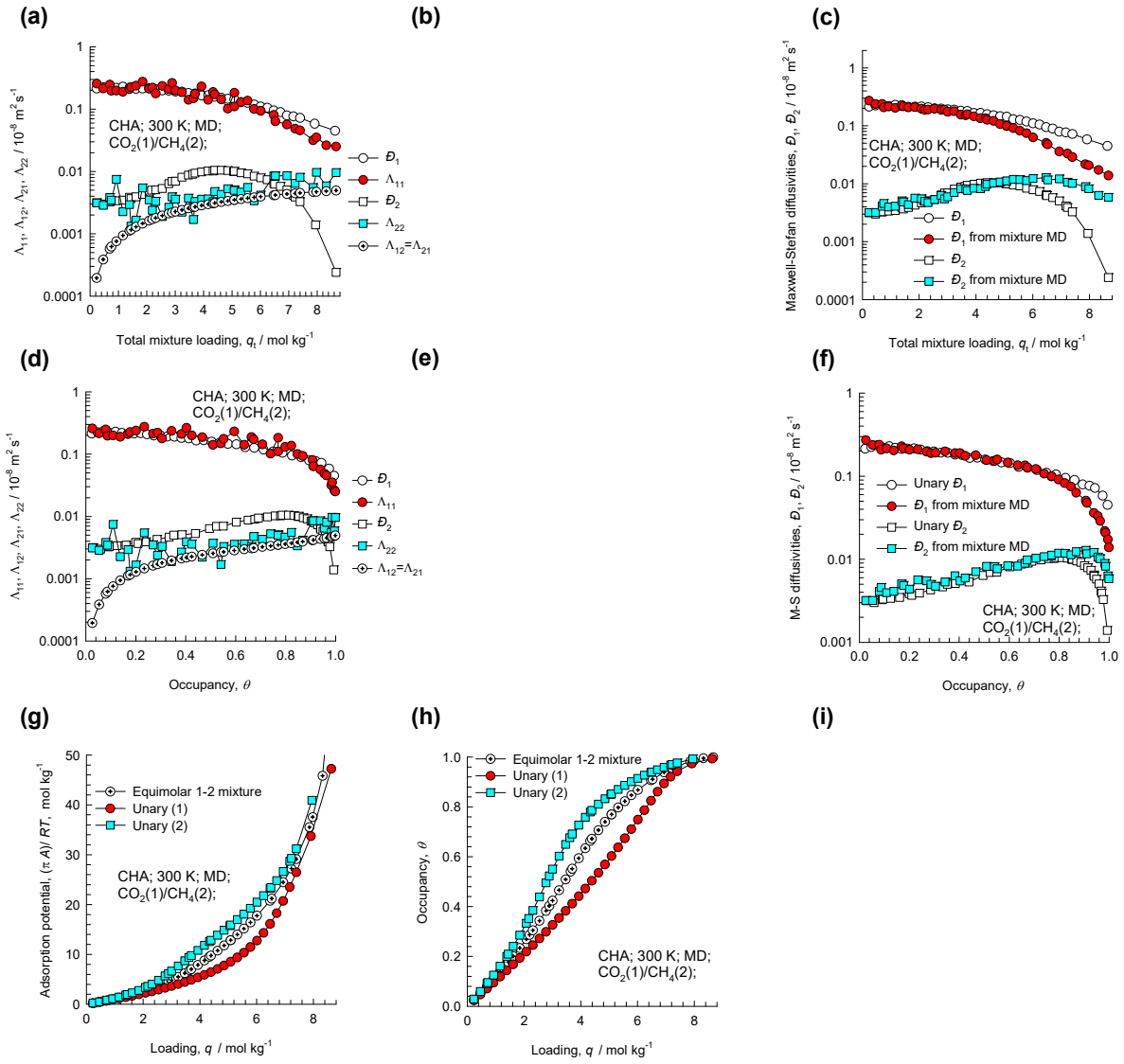

Figure S9-38. MD simulated values of $\Lambda_{11}, \Lambda_{12}, \Lambda_{22}$, along with the backed-out M-S diffusivities, $Đ_1, Đ_2, Đ_{12}$ for equimolar (q_1=q_2) CO_2(1)/CH_4(2) mixtures in CHA all-silica zeolite at 300 K plotted as a function of (a, b, c) the total mixture loading $q_t = q_1+q_2$, and (d, e, f) occupancy θ. (g, h) The adsorption potential, and the occupancy plotted as function of the molar loading. It is to be noted there that the correlation effects are of negligible importance for this guest/host combination. Therefore, the Maxwell-Stefan diffusivities reported here are actually the self-diffusivities, $D_{i,self}$, determined from MD using Equation (7-8).

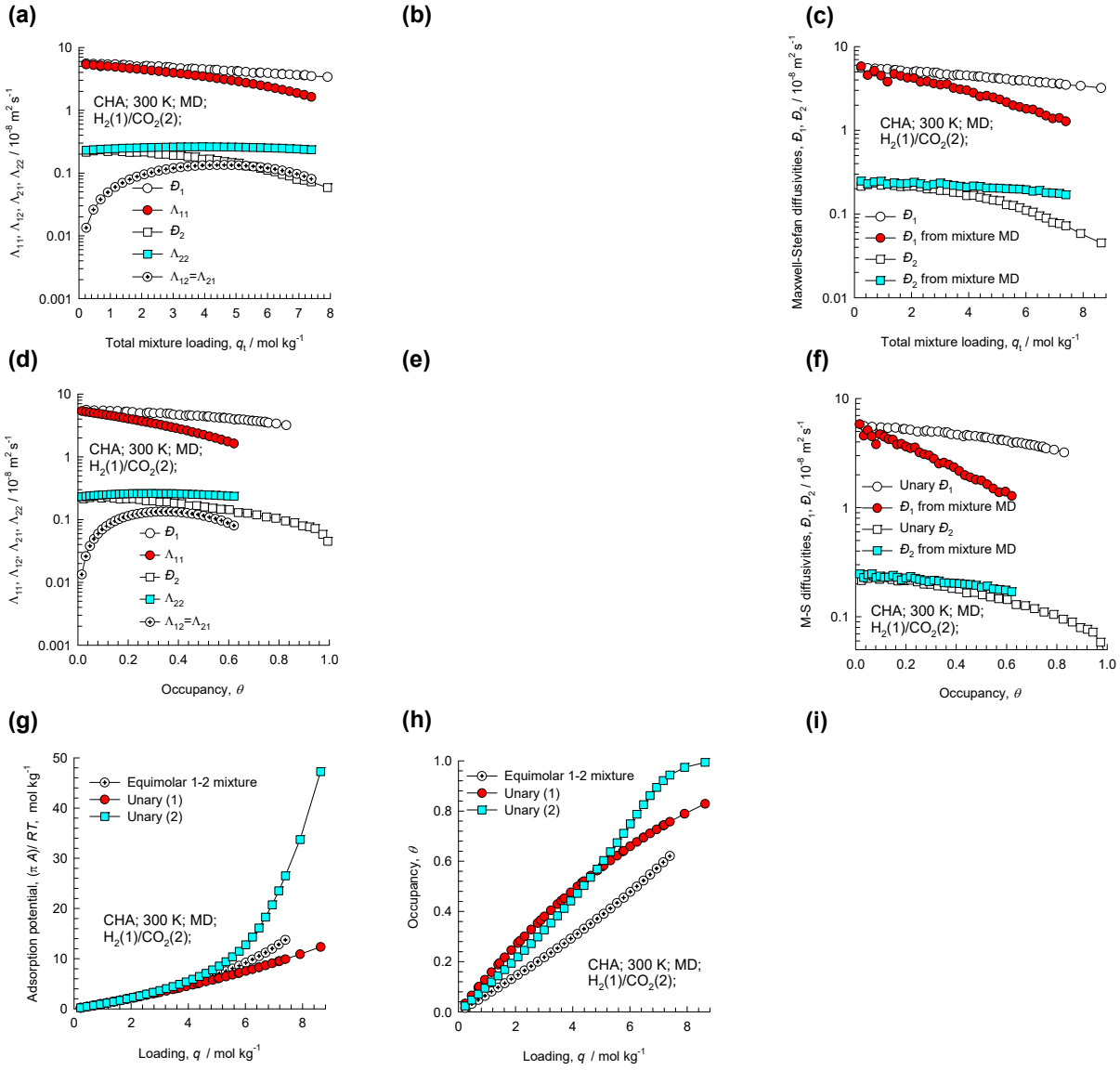

Figure S9-39. MD simulated values of $\Lambda_{11},\Lambda_{12},\Lambda_{22}$, along with the backed-out M-S diffusivities, $Đ_1,Đ_2,Đ_{12}$ for equimolar (q_1=q_2) CO_2(1)/H_2(2) mixtures in CHA all-silica zeolite at 300 K plotted as a function of (a, b, c) the total mixture loading q_t= q_1+q_2, and (d, e, f) occupancy θ. (g, h) The adsorption potential, and the occupancy plotted as function of the molar loading. It is to be noted there that the correlation effects are of negligible importance for this guest/host combination. Therefore, the Maxwell-Stefan diffusivities reported here are actually the self-diffusivities, $D_{i,self}$, determined from MD using Equation (7-8).

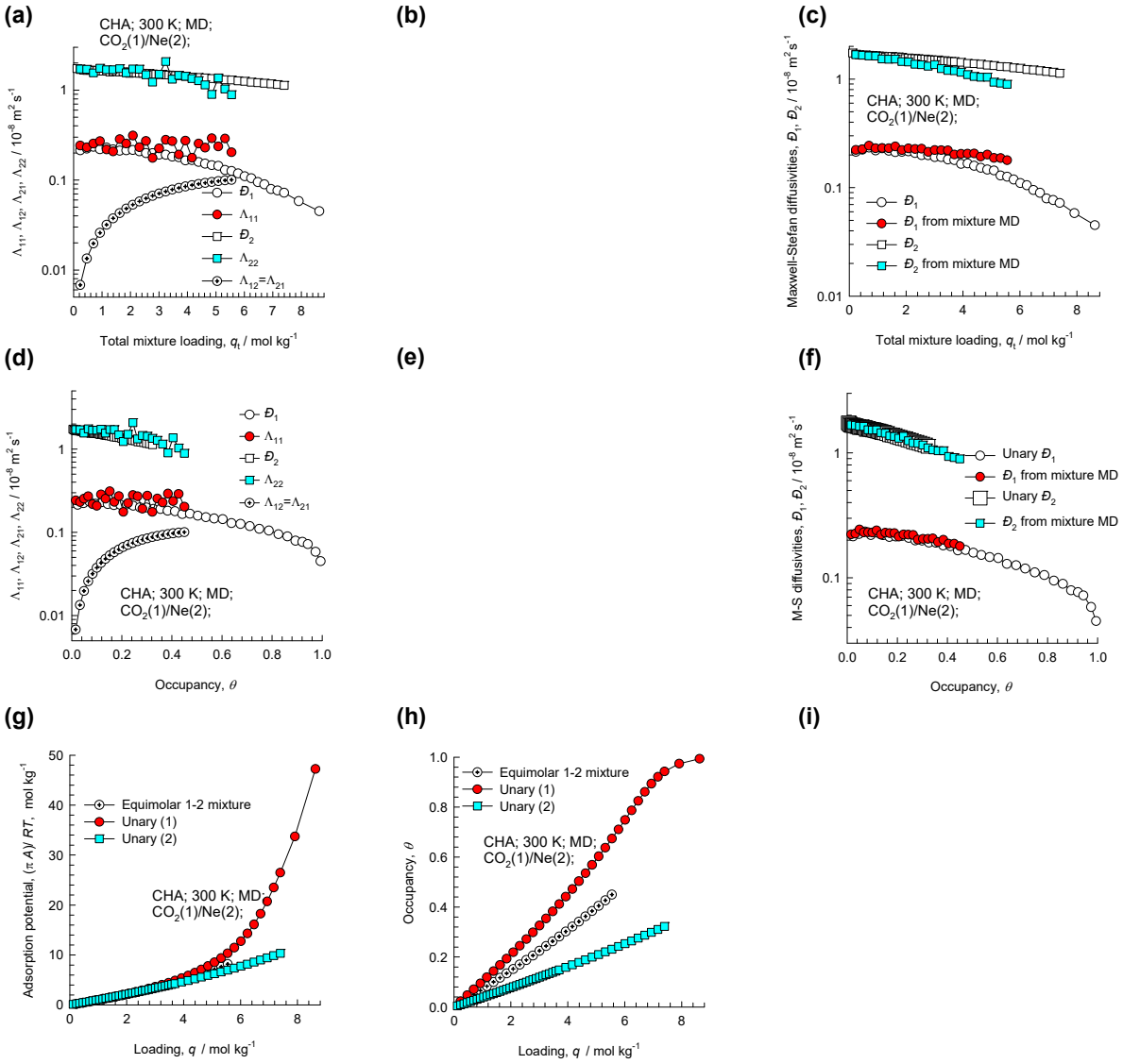

Figure S9-40. MD simulated values of $\Lambda_{11}, \Lambda_{12}, \Lambda_{22}$, along with the backed-out M-S diffusivities, $Đ_1, Đ_2, Đ_{12}$ for equimolar (q_1=q_2) CO_2(1)/Ne(2) mixtures in CHA all-silica zeolite at 300 K plotted as a function of (a, b, c) the total mixture loading $q_t = q_1+q_2$, and (d, e, f) occupancy θ. (g, h) The adsorption potential, and the occupancy plotted as function of the molar loading. It is to be noted there that the correlation effects are of negligible importance for this guest/host combination. Therefore, the Maxwell-Stefan diffusivities reported here are actually the self-diffusivities, $Đ_{i,self}$, determined from MD using Equation (7-8).

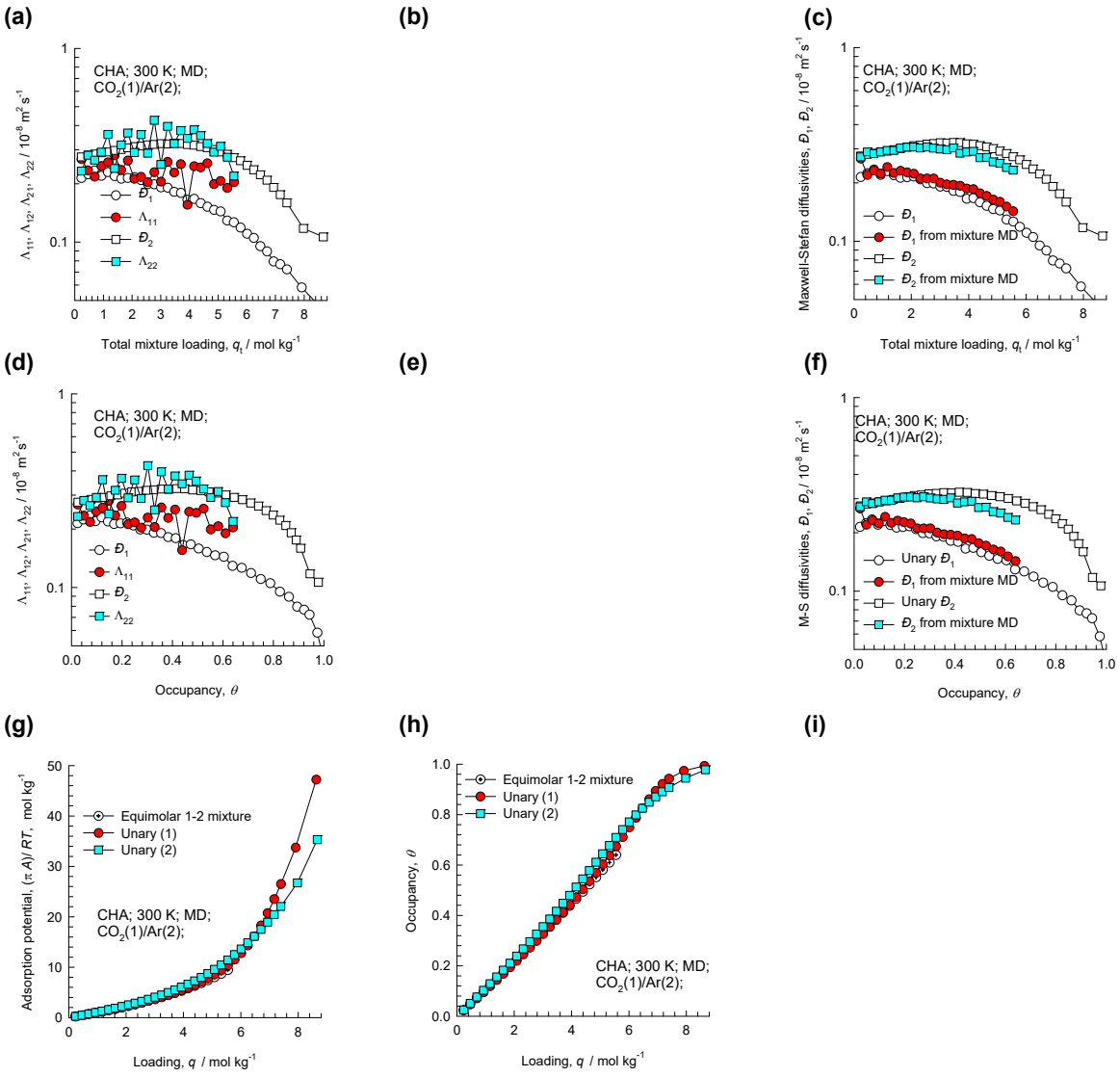

Figure S9-41. MD simulated values of $\Lambda_{11}, \Lambda_{12}, \Lambda_{22}$, along with the backed-out M-S diffusivities, $Đ_1, Đ_2, Đ_{12}$ for equimolar (q_1=q_2) CO_2(1)/Ar(2) mixtures in CHA all-silica zeolite at 300 K plotted as a function of (a, b, c) the total mixture loading $q_t = q_1+q_2$, and (d, e, f) occupancy θ. (g, h) The adsorption potential, and the occupancy plotted as function of the molar loading. It is to be noted there that the correlation effects are of negligible importance for this guest/host combination. Therefore, the Maxwell-Stefan diffusivities reported here are actually the self-diffusivities, $D_{i,self}$, determined from MD using Equation (7-8).

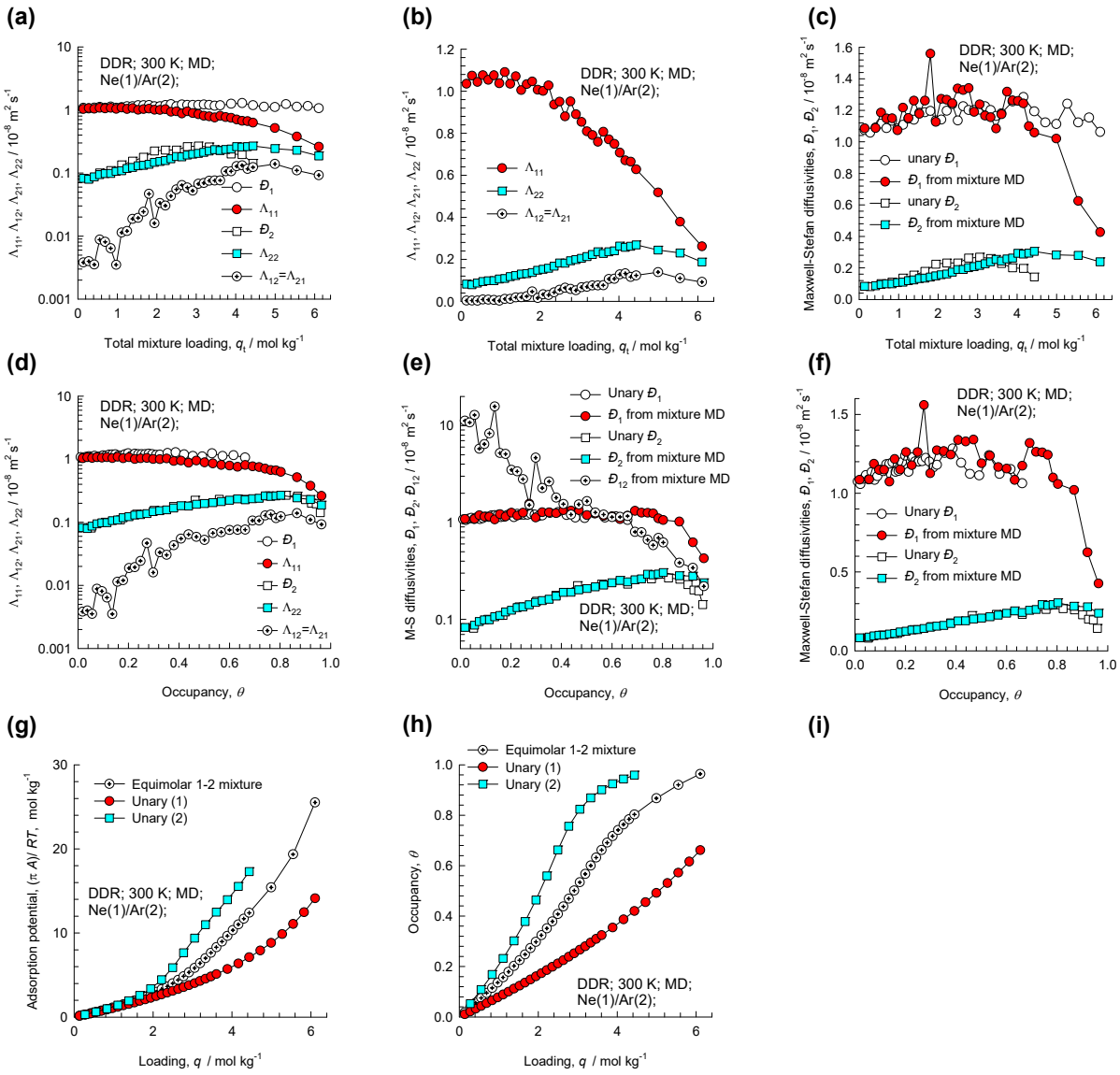

Figure S9-42. MD simulated values of $\Lambda_{11}, \Lambda_{12}, \Lambda_{22}$, along with the backed-out M-S diffusivities, $Đ_1, Đ_2, Đ_{12}$ for equimolar (q_1=q_2) binary Ne(1)/Ar(2) mixtures in DDR all-silica zeolite at 300 K plotted as a function of (a, b, c) the total mixture loading q_t= q_1+q_2, and (d, e, f) occupancy θ. (g, h) The adsorption potential, and the occupancy plotted as function of the molar loading.

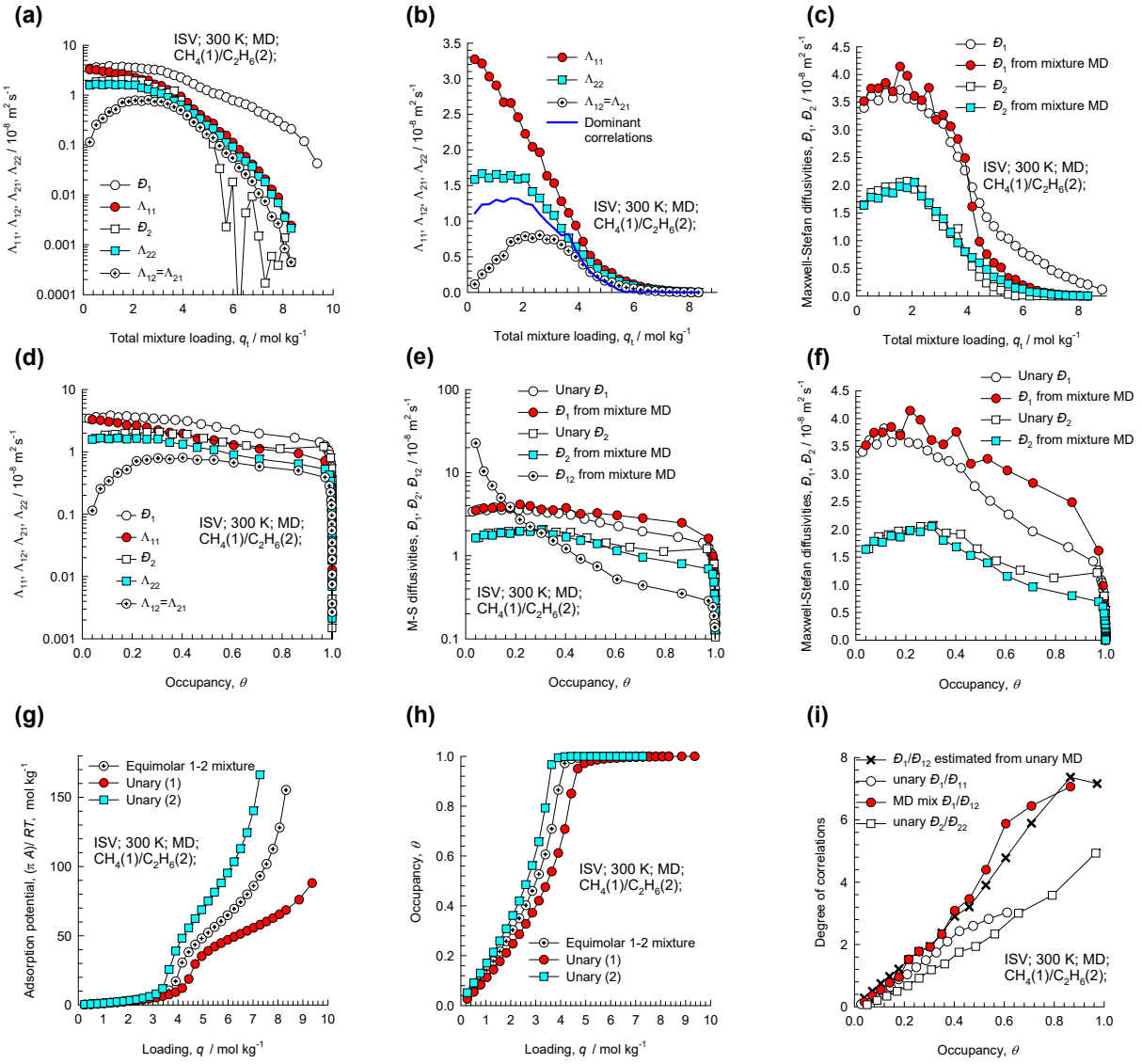

Figure S9-43. MD simulated values of $\Lambda_{11}, \Lambda_{12}, \Lambda_{22}$, along with the backed-out M-S diffusivities, $Đ_1, Đ_2, Đ_{12}$ for equimolar (q_1=q_2) binary $CH_4(1)/C_2H_6(2)$ mixtures in ISV zeolite at 300 K plotted as a function of (a, b, c) the total mixture loading $q_t = q_1+q_2$, and (d, e, f) occupancy θ. (g, h) The adsorption potential, and the occupancy plotted as function of the molar loading. (i) degree of correlations.

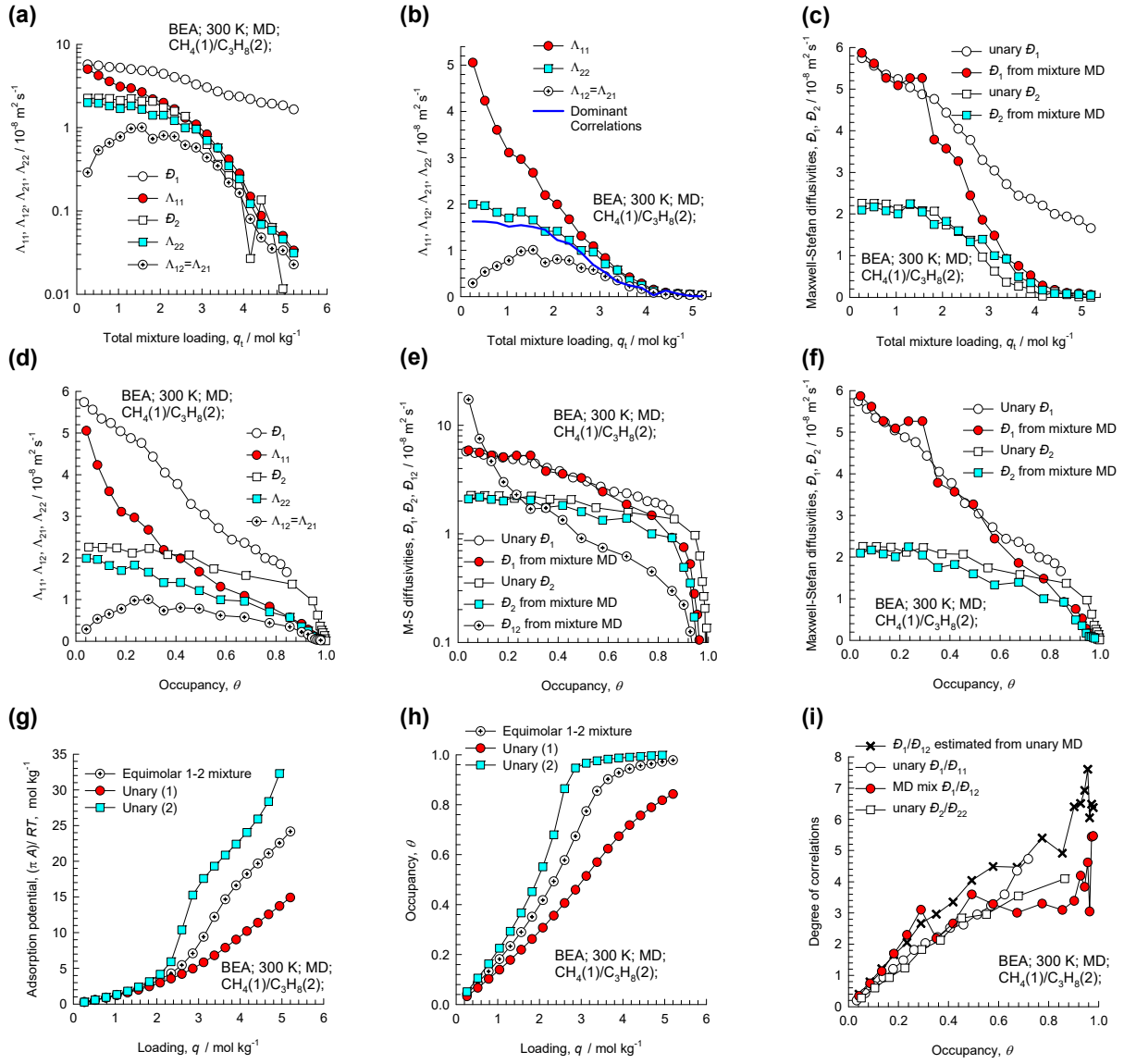

Figure S9-44. MD simulated values of $\Lambda_{11},\Lambda_{12},\Lambda_{22}$, along with the backed-out M-S diffusivities, $Đ_1,Đ_2,Đ_{12}$ for equimolar (q_1=q_2) binary $CH_4(1)/C_3H_8(2)$ mixtures in BEA zeolite at 300 K plotted as a function of (a, b, c) the total mixture loading q_t= q_1+q_2, and (d, e, f) occupancy θ. (g, h) The adsorption potential, and the occupancy plotted as function of the molar loading. (i) degree of correlations.

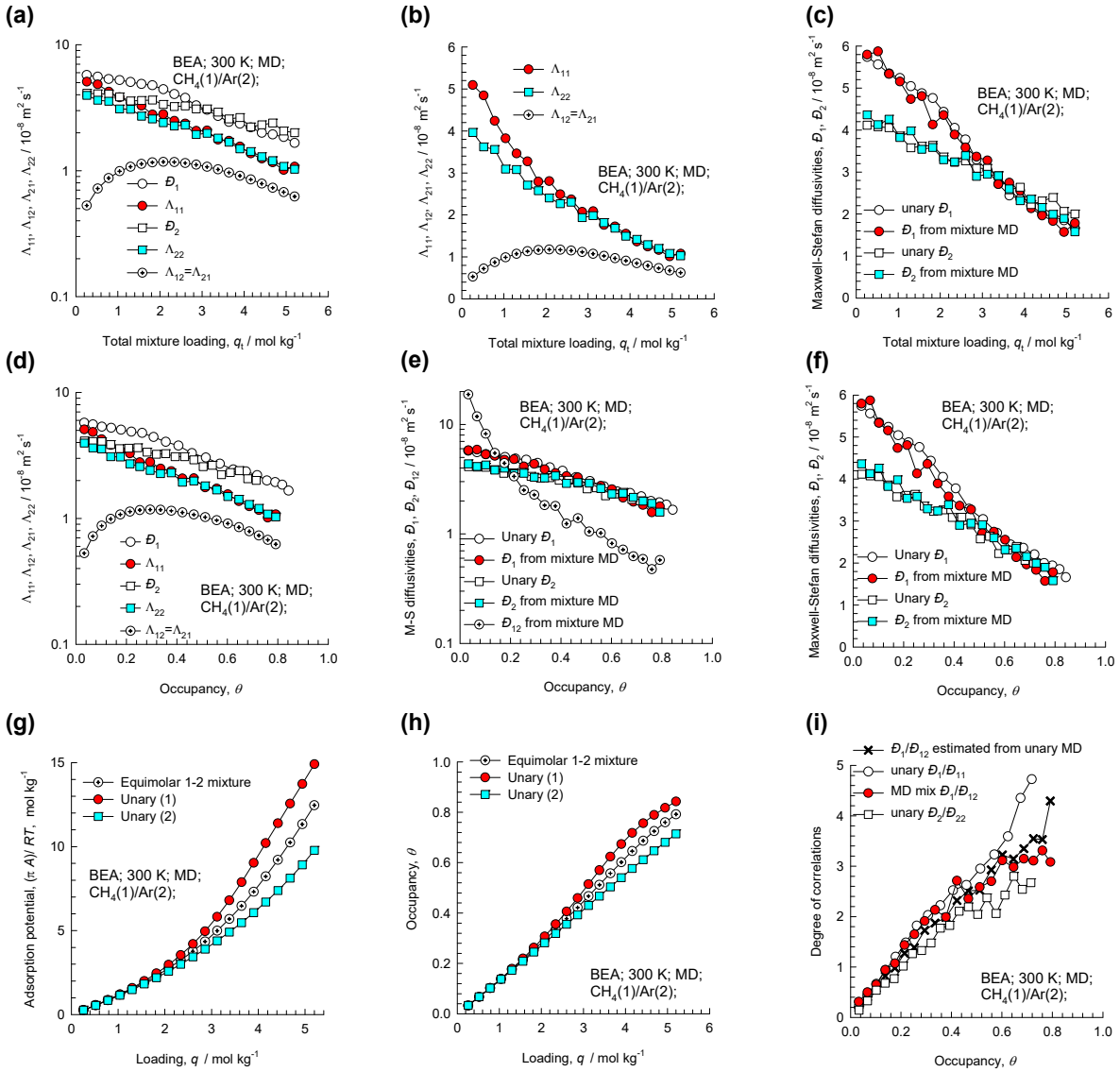

Figure S9-45. MD simulated values of $\Lambda_{11}, \Lambda_{12}, \Lambda_{22}$, along with the backed-out M-S diffusivities, $Đ_1, Đ_2, Đ_{12}$ for equimolar (q_1=q_2) binary CH4(1)/Ar(2) mixtures in BEA zeolite at 300 K plotted as a function of (a, b, c) the total mixture loading $q_t = q_1+q_2$, and (d, e, f) occupancy θ. (g, h) The adsorption potential, and the occupancy plotted as function of the molar loading. (i) degree of correlations.

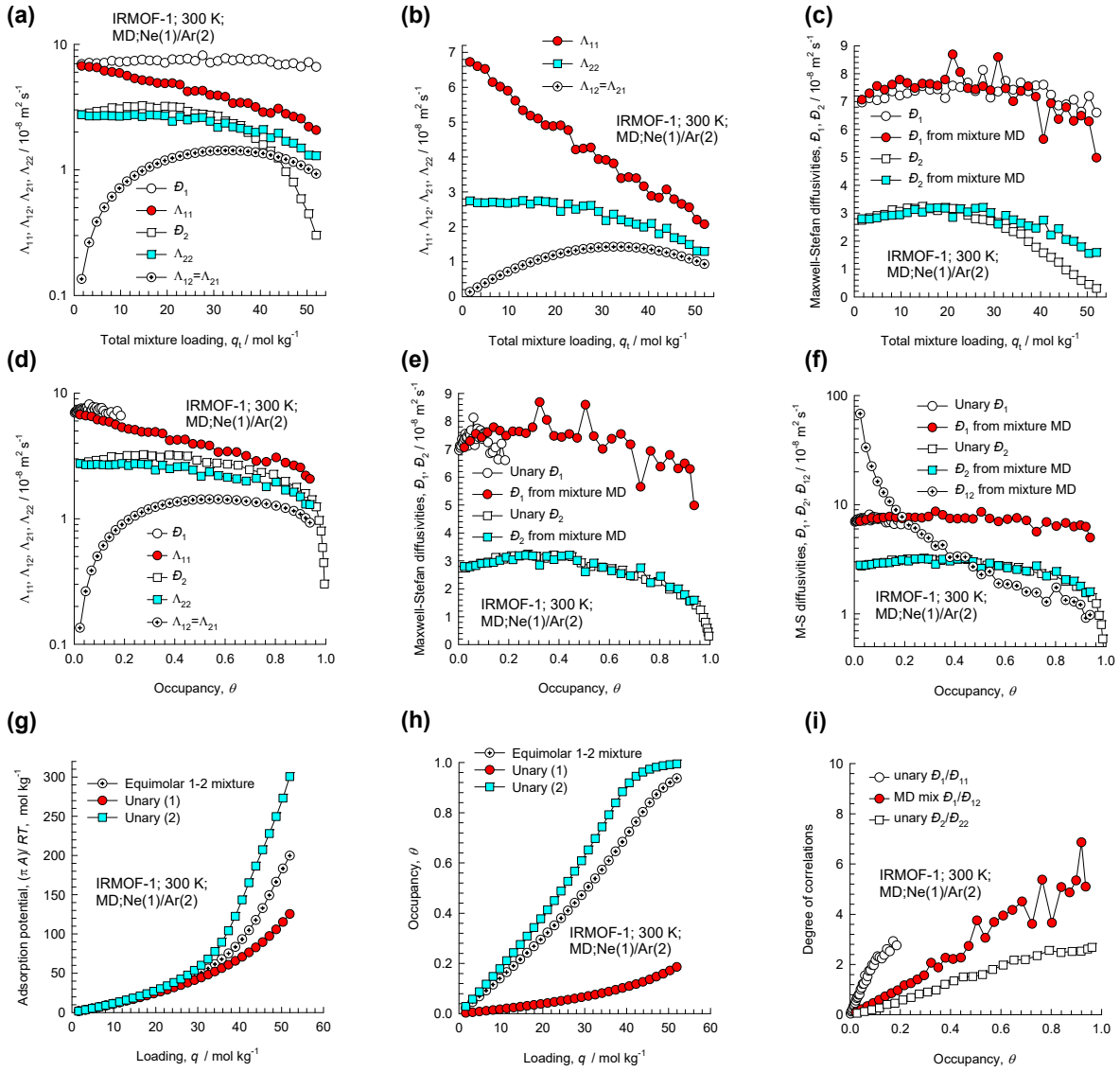

Figure S9-46. MD simulated values of $\Lambda_{11},\Lambda_{12},\Lambda_{22}$, along with the backed-out M-S diffusivities, $Đ_1,Đ_2,Đ_{12}$ for equimolar (q_1=q_2) binary Ne(1)/Ar(2) mixtures in IRMOF-1 at 300 K plotted as a function of (a, b, c) the total mixture loading q_t= q_1+q_2, and (d, e, f) occupancy θ. (g, h) The adsorption potential, and the occupancy plotted as function of the molar loading. (i) degree of correlations.

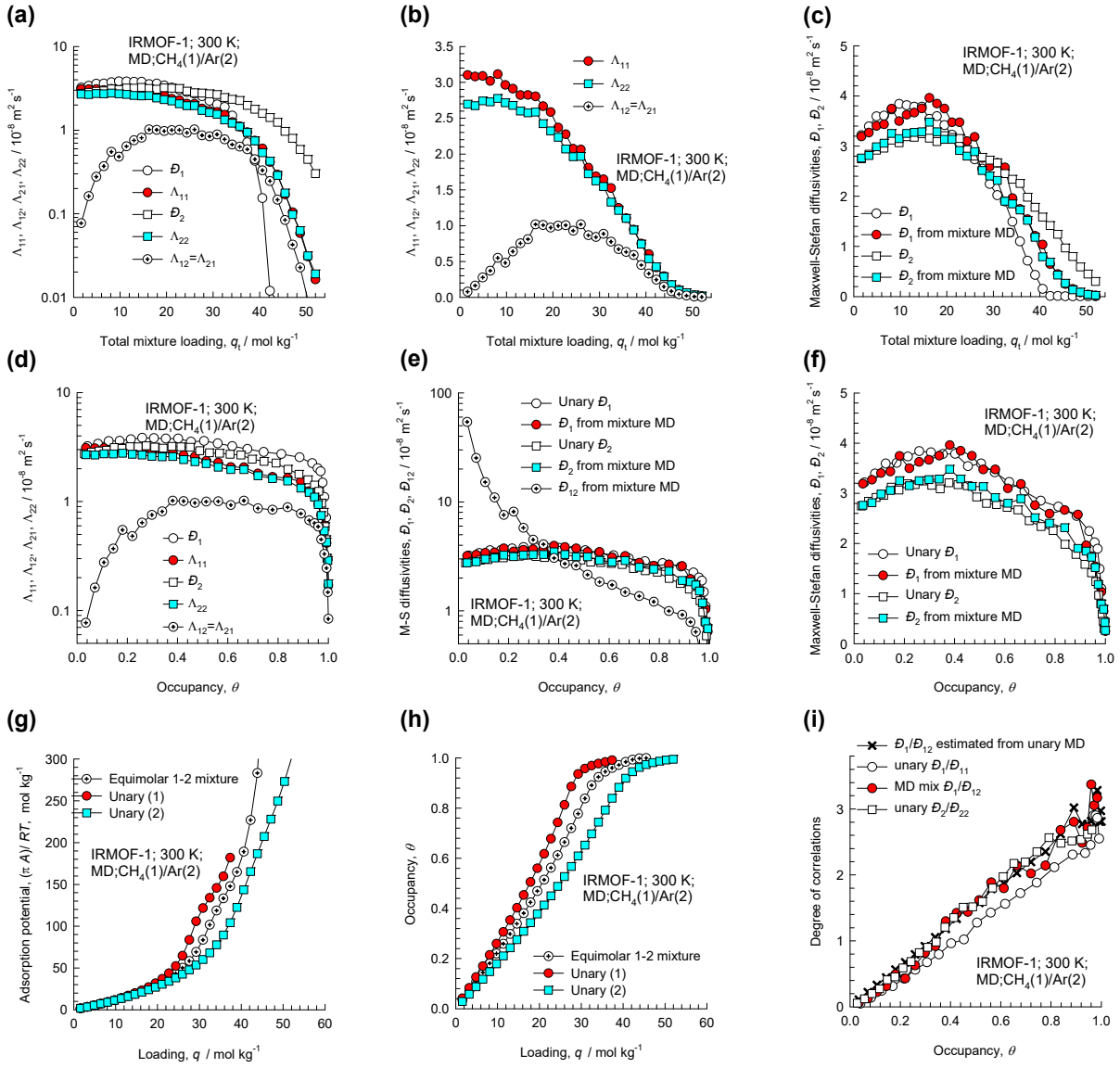

Figure S9-47. MD simulated values of $\Lambda_{11},\Lambda_{12},\Lambda_{22}$, along with the backed-out M-S diffusivities, $Đ_1,Đ_2,Đ_{12}$ for equimolar (q_1=q_2) binary CH_4(1)/Ar(2) mixtures in IRMOF-1 at 300 K plotted as a function of (a, b, c) the total mixture loading q_t= q_1+q_2, and (d, e, f) occupancy θ. (g, h) The adsorption potential, and the occupancy plotted as function of the molar loading. (i) degree of correlations.

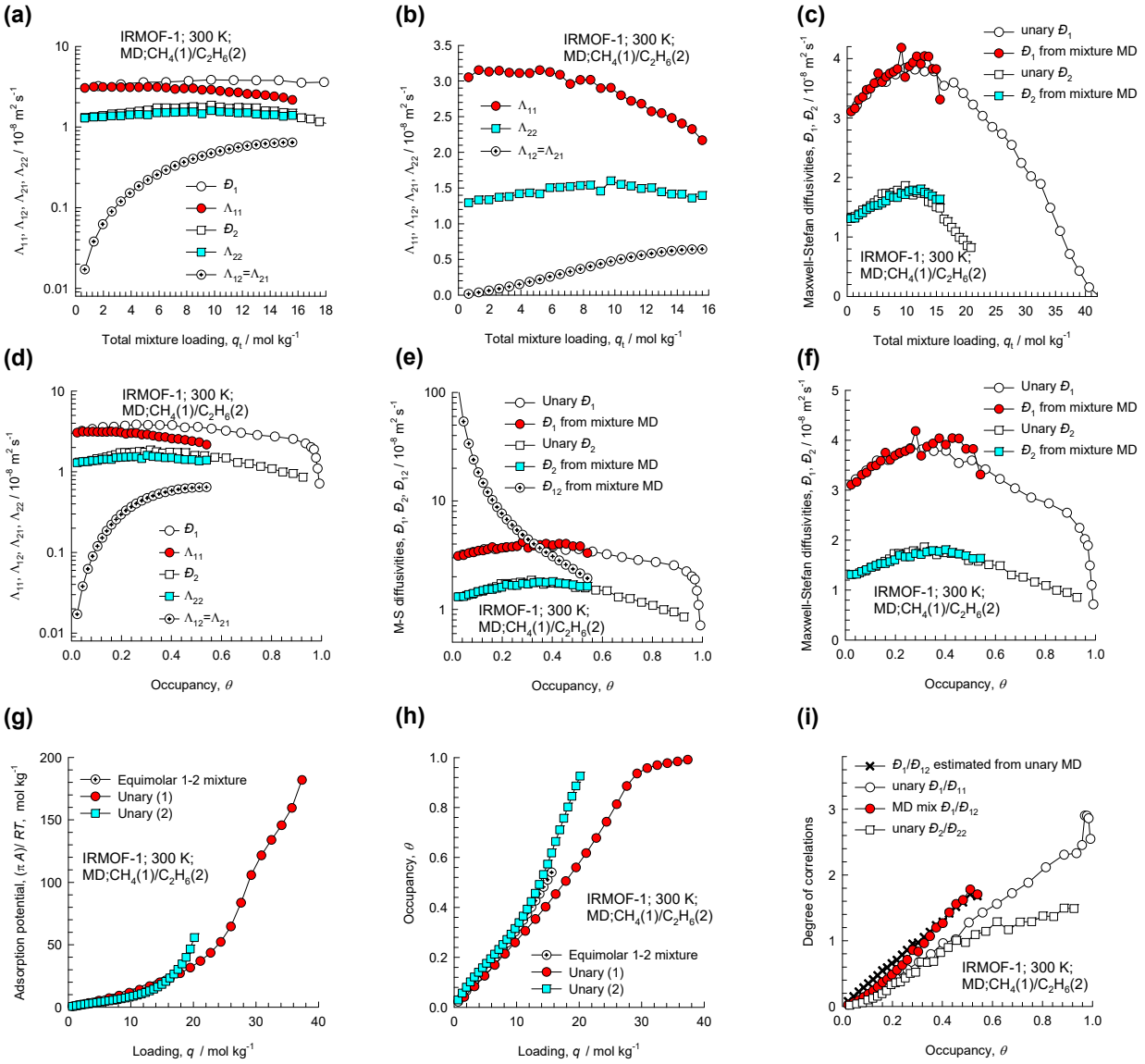

Figure S9-48. MD simulated values of $\Lambda_{11}, \Lambda_{12}, \Lambda_{22}$, along with the backed-out M-S diffusivities, $Đ_1, Đ_2, Đ_{12}$ for equimolar (q_1=q_2) binary $CH_4(1)/C_2H_6(2)$ mixtures in IRMOF-1 at 300 K plotted as a function of (a, b, c) the total mixture loading $q_t = q_1+q_2$, and (d, e, f) occupancy θ. (g, h) The adsorption potential, and the occupancy plotted as function of the molar loading. (i) degree of correlations.

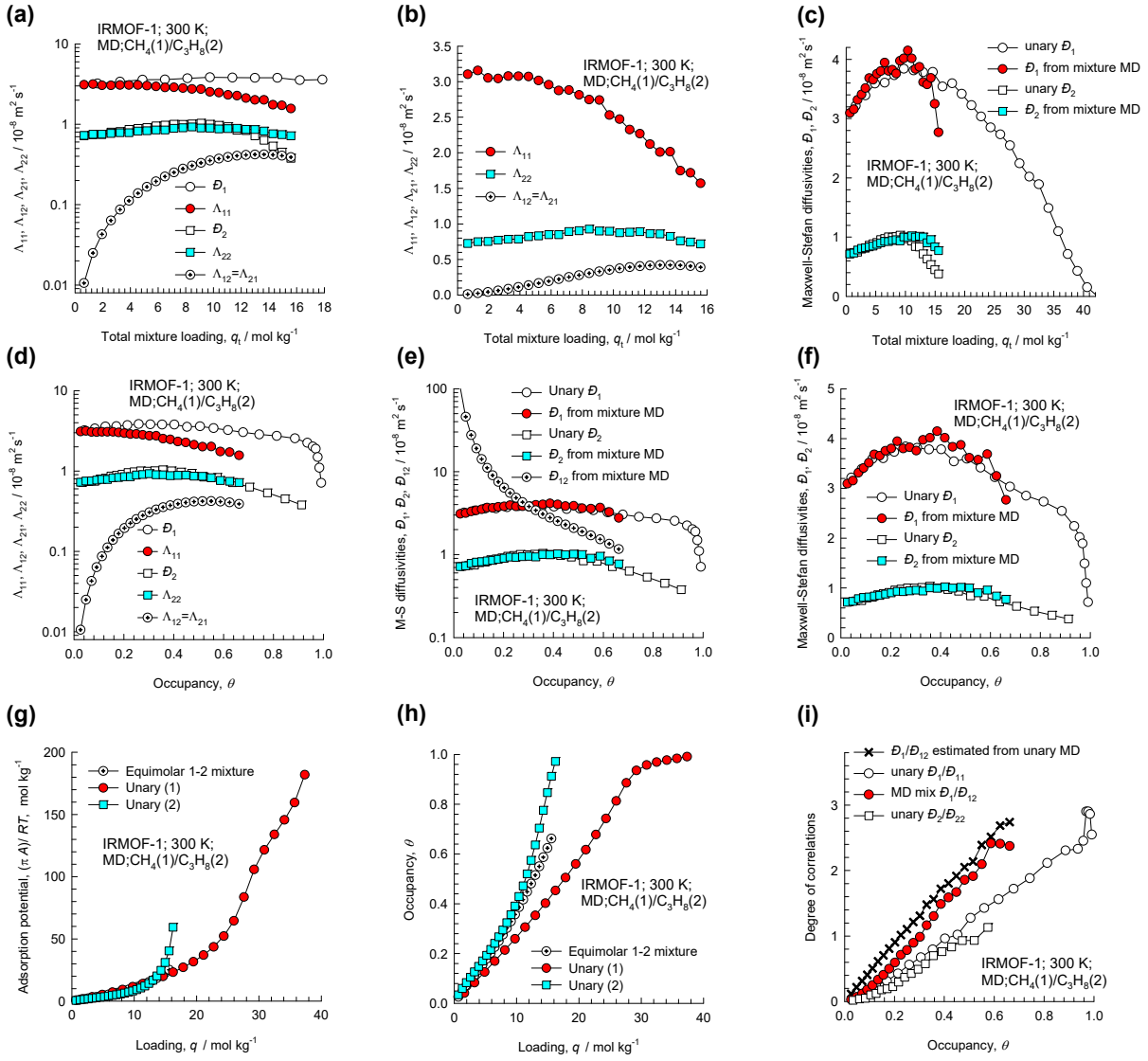

Figure S9-49. MD simulated values of $\Lambda_{11},\Lambda_{12},\Lambda_{22}$, along with the backed-out M-S diffusivities, $Đ_1,Đ_2,Đ_{12}$ for equimolar (q_1=q_2) binary CH_4(1)/C_3H_8(2) mixtures in IRMOF-1 at 300 K plotted as a function of (a, b, c) the total mixture loading q_t= q_1+q_2, and (d, e, f) occupancy θ. (g, h) The adsorption potential, and the occupancy plotted as function of the molar loading. (i) degree of correlations.

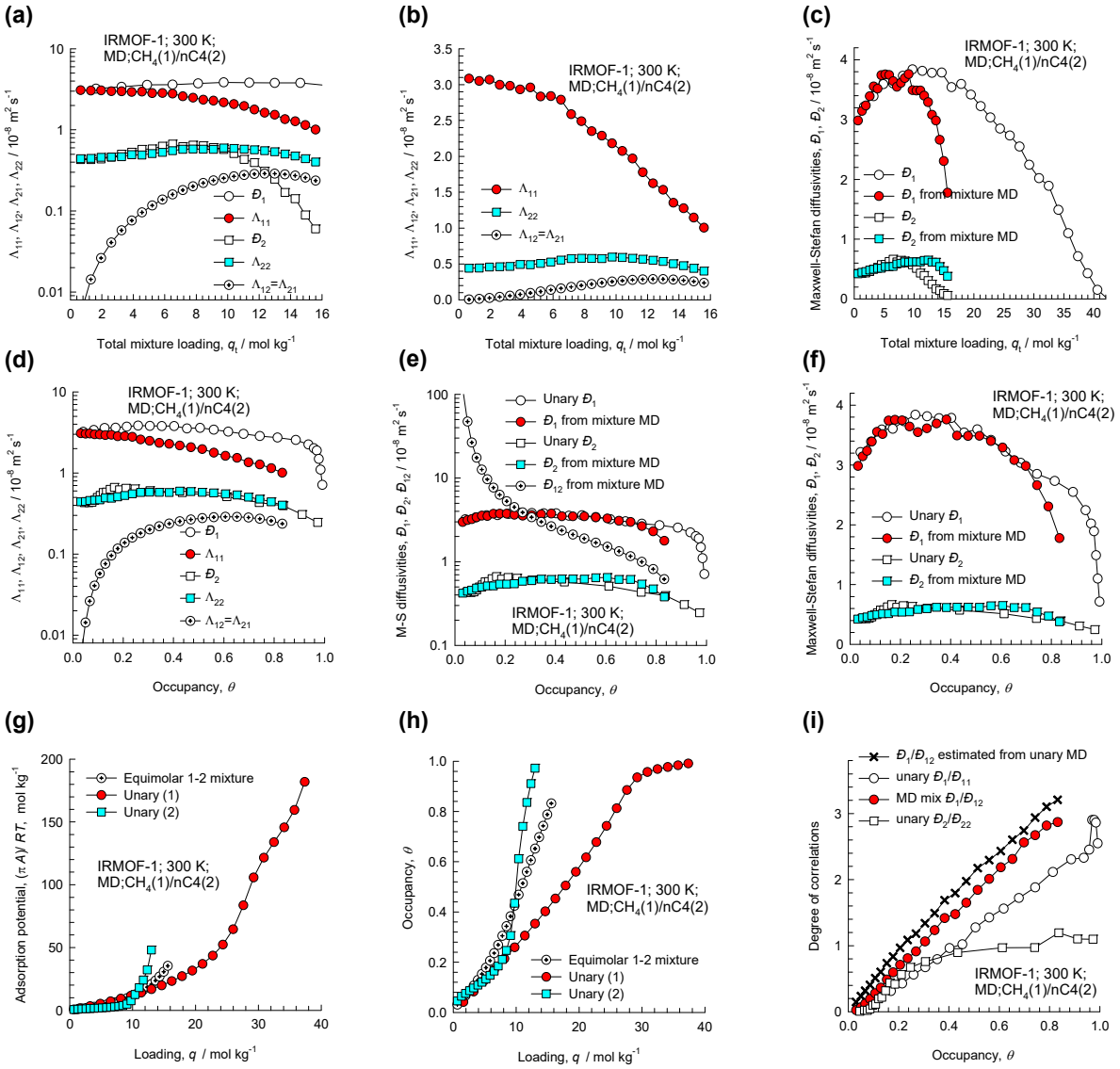

Figure S9-50. MD simulated values of $\Lambda_{11}, \Lambda_{12}, \Lambda_{22}$, along with the backed-out M-S diffusivities, $Đ_1, Đ_2, Đ_{12}$ for equimolar (q_1=q_2) binary CH_4(1)/nC_4H_{10}(2) mixtures in IRMOF-1 at 300 K plotted as a function of (a, b, c) the total mixture loading q_t= q_1+q_2, and (d, e, f) occupancy θ. (g, h) The adsorption potential, and the occupancy plotted as function of the molar loading. (i) degree of correlations.

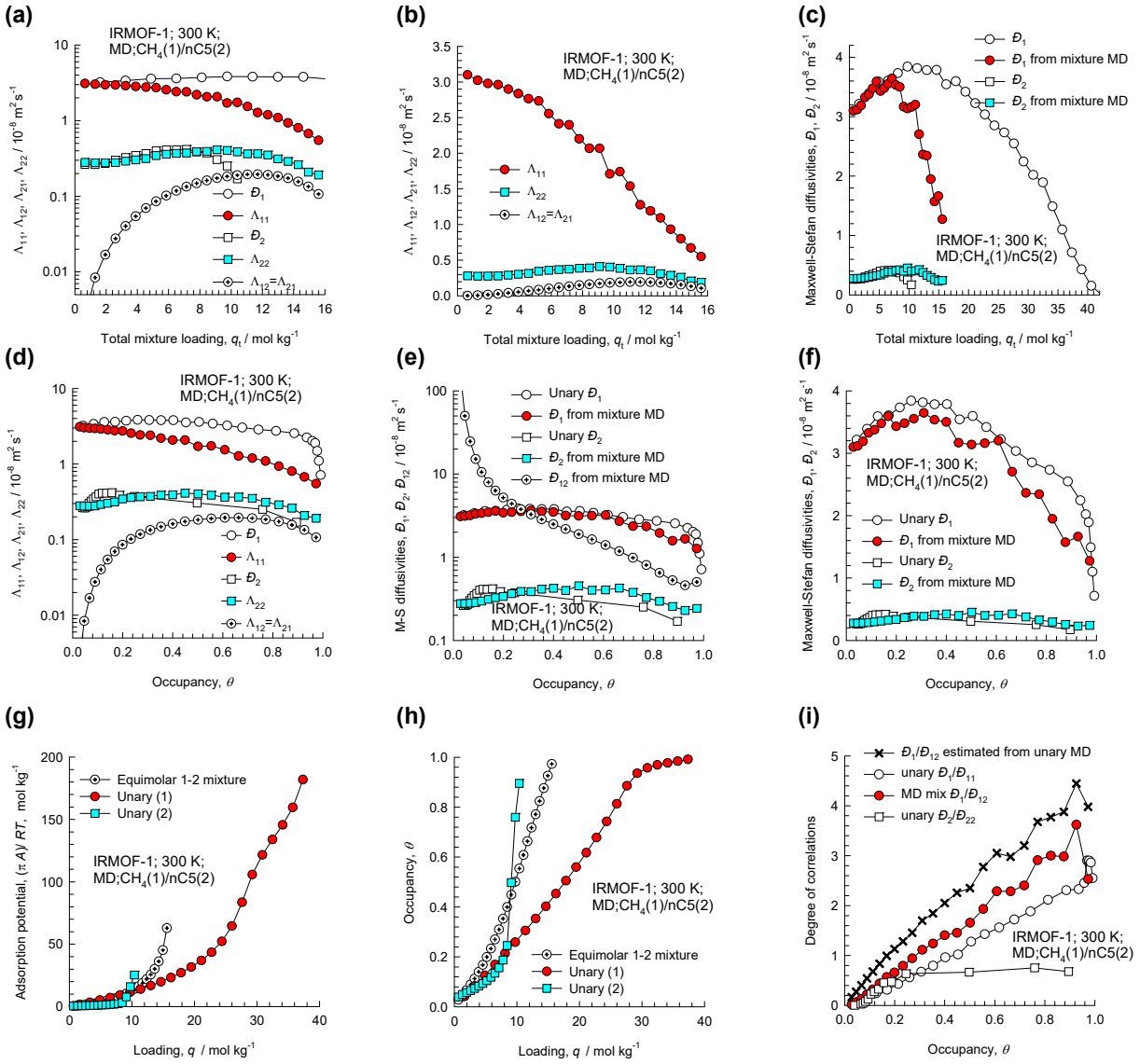

Figure S9-51. MD simulated values of $\Lambda_{11},\Lambda_{12},\Lambda_{22}$, along with the backed-out M-S diffusivities, $Đ_1,Đ_2,Đ_{12}$ for equimolar (q_1=q_2) binary CH_4(1)/nC_5H_{12}(2) mixtures in IRMOF-1 at 300 K plotted as a function of (a, b, c) the total mixture loading q_t= q_1+q_2, and (d, e, f) occupancy θ. (g, h) The adsorption potential, and the occupancy plotted as function of the molar loading. (i) degree of correlations.

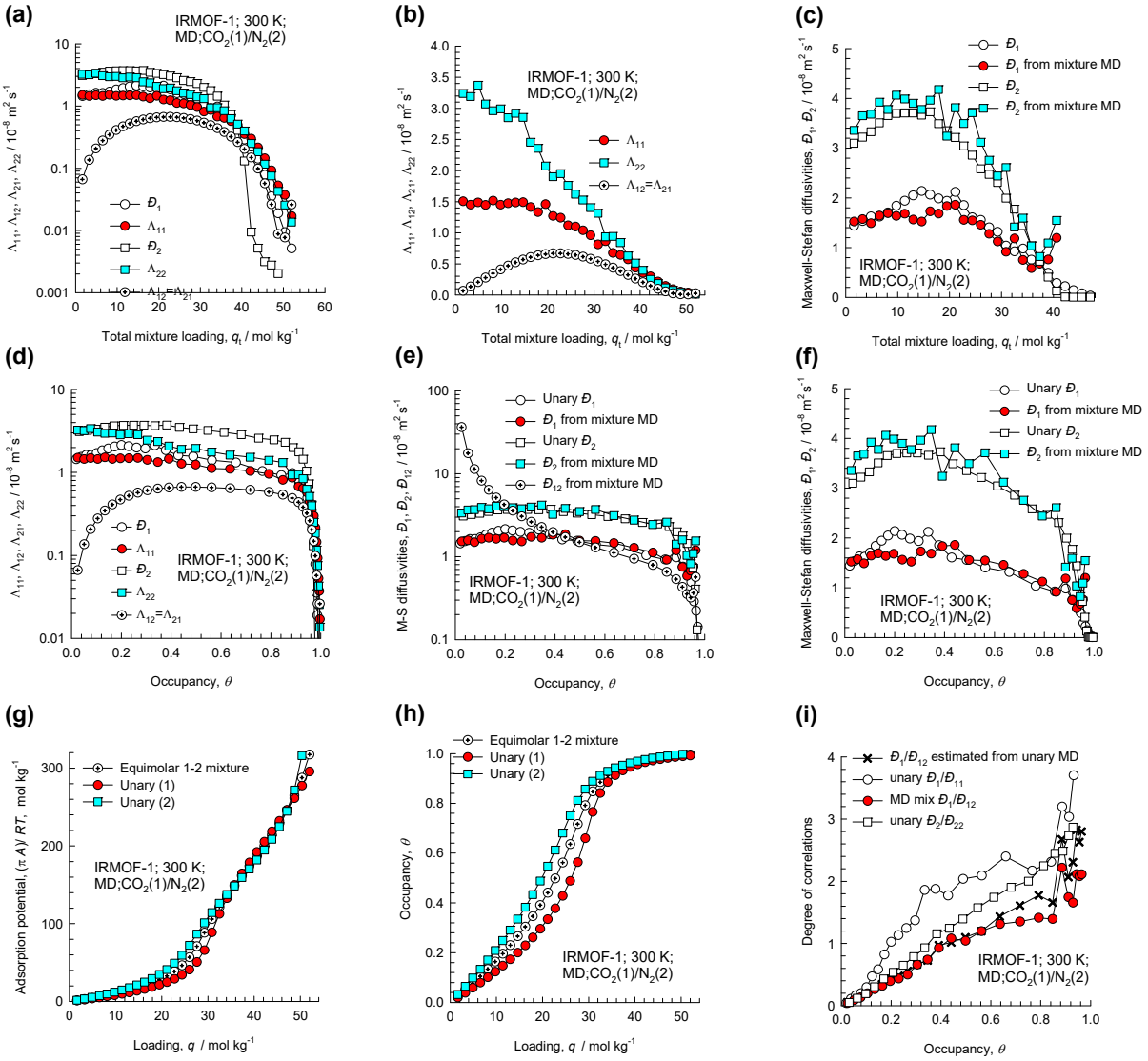

Figure S9-52. MD simulated values of $\Lambda_{11}, \Lambda_{12}, \Lambda_{22}$, along with the backed-out M-S diffusivities, $Đ_1, Đ_2, Đ_{12}$ for equimolar (q_1=q_2) binary CO_2(1)/N_2(2) mixtures in IRMOF-1 at 300 K plotted as a function of (a, b, c) the total mixture loading $q_t = q_1+q_2$, and (d, e, f) occupancy θ. (g, h) The adsorption potential, and the occupancy plotted as function of the molar loading. (i) degree of correlations.

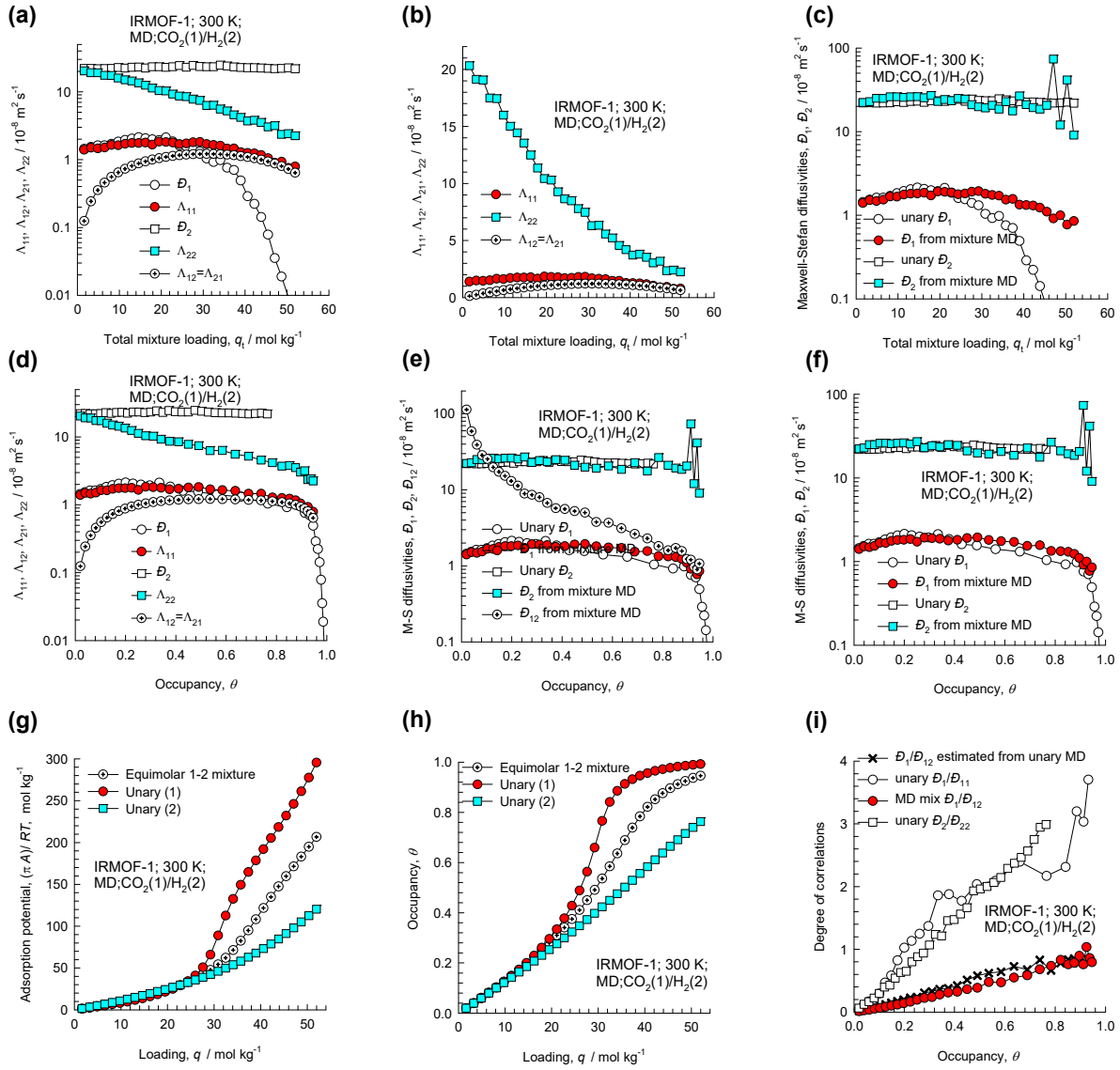

Figure S9-53. MD simulated values of $\Lambda_{11}, \Lambda_{12}, \Lambda_{22}$, along with the backed-out M-S diffusivities, $Đ_1, Đ_2, Đ_{12}$ for equimolar (q_1=q_2) binary CO_2(1)/H_2(2) mixtures in IRMOF-1 at 300 K plotted as a function of (a, b, c) the total mixture loading q_t= q_1+q_2, and (d, e, f) occupancy θ. (g, h) The adsorption potential, and the occupancy plotted as function of the molar loading. (i) degree of correlations.

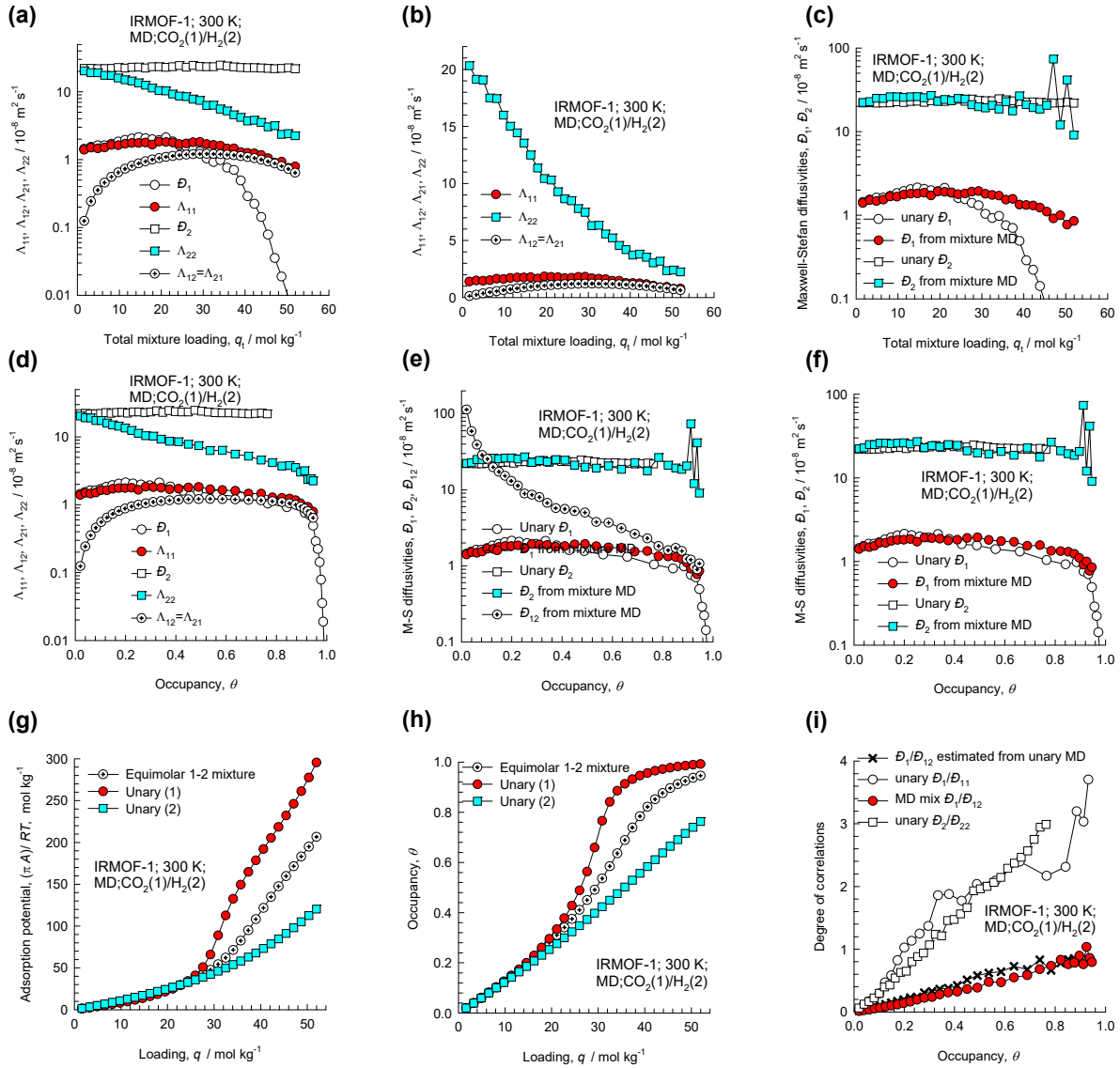

Figure S9-54. MD simulated values of $\Lambda_{11}, \Lambda_{12}, \Lambda_{22}$, along with the backed-out M-S diffusivities, $Đ_1, Đ_2, Đ_{12}$ for equimolar (q_1=q_2) binary CH_4(1)/CO_2(2) mixtures in IRMOF-1 at 300 K plotted as a function of (a, b, c) the total mixture loading $q_t = q_1+q_2$, and (d, e, f) occupancy θ. (g, h) The adsorption potential, and the occupancy plotted as function of the molar loading. (i) degree of correlations.

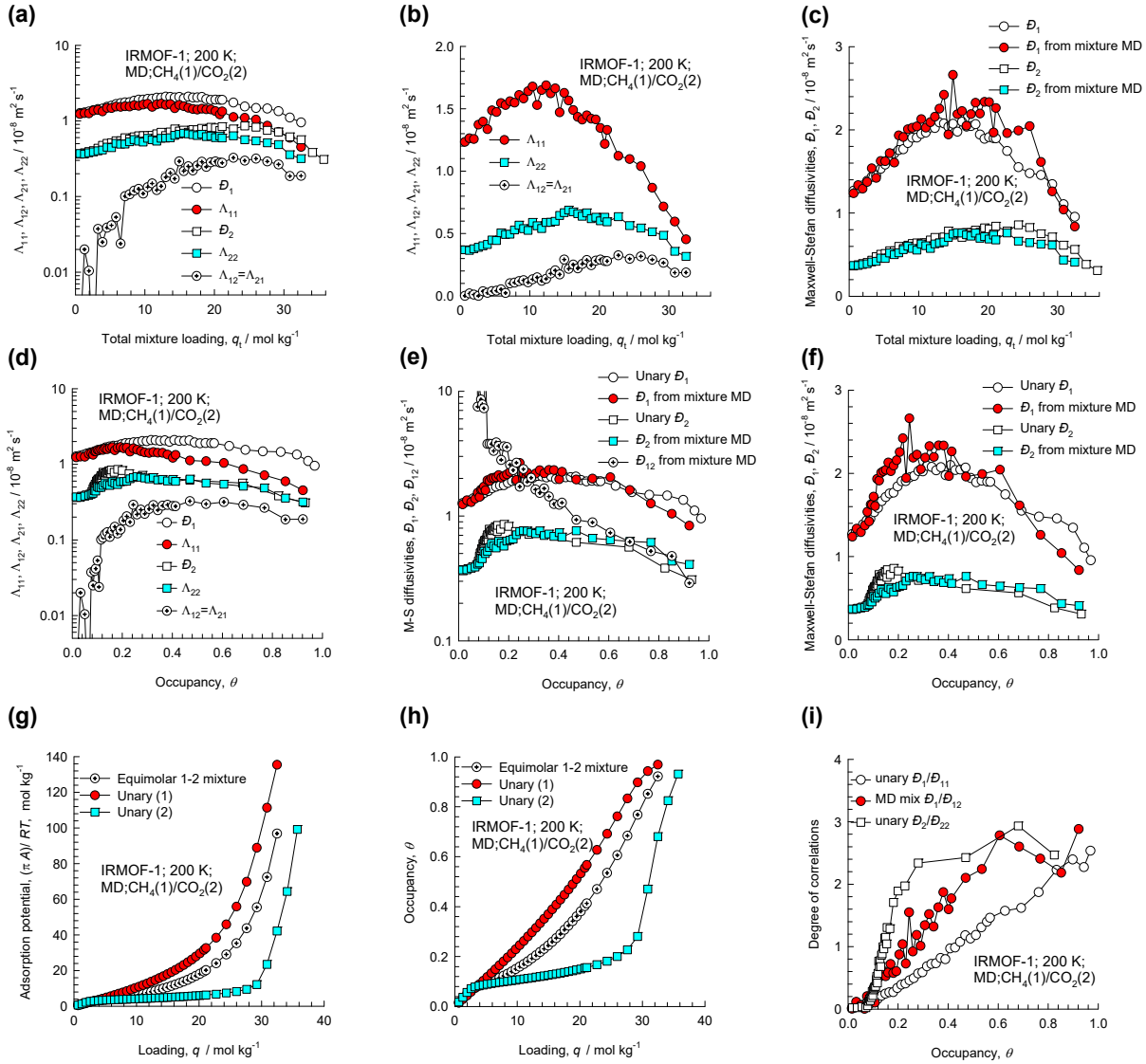

Figure S9-55. MD simulated values of $\Lambda_{11}, \Lambda_{12}, \Lambda_{22}$, along with the backed-out M-S diffusivities, $Đ_1, Đ_2, Đ_{12}$ for equimolar (q_1=q_2) binary CH_4(1)/CO_2(2) mixtures in IRMOF-1 at 200 K plotted as a function of (a, b, c) the total mixture loading q_t= q_1+q_2, and (d, e, f) occupancy θ. (g, h) The adsorption potential, and the occupancy plotted as function of the molar loading. (i) degree of correlations.

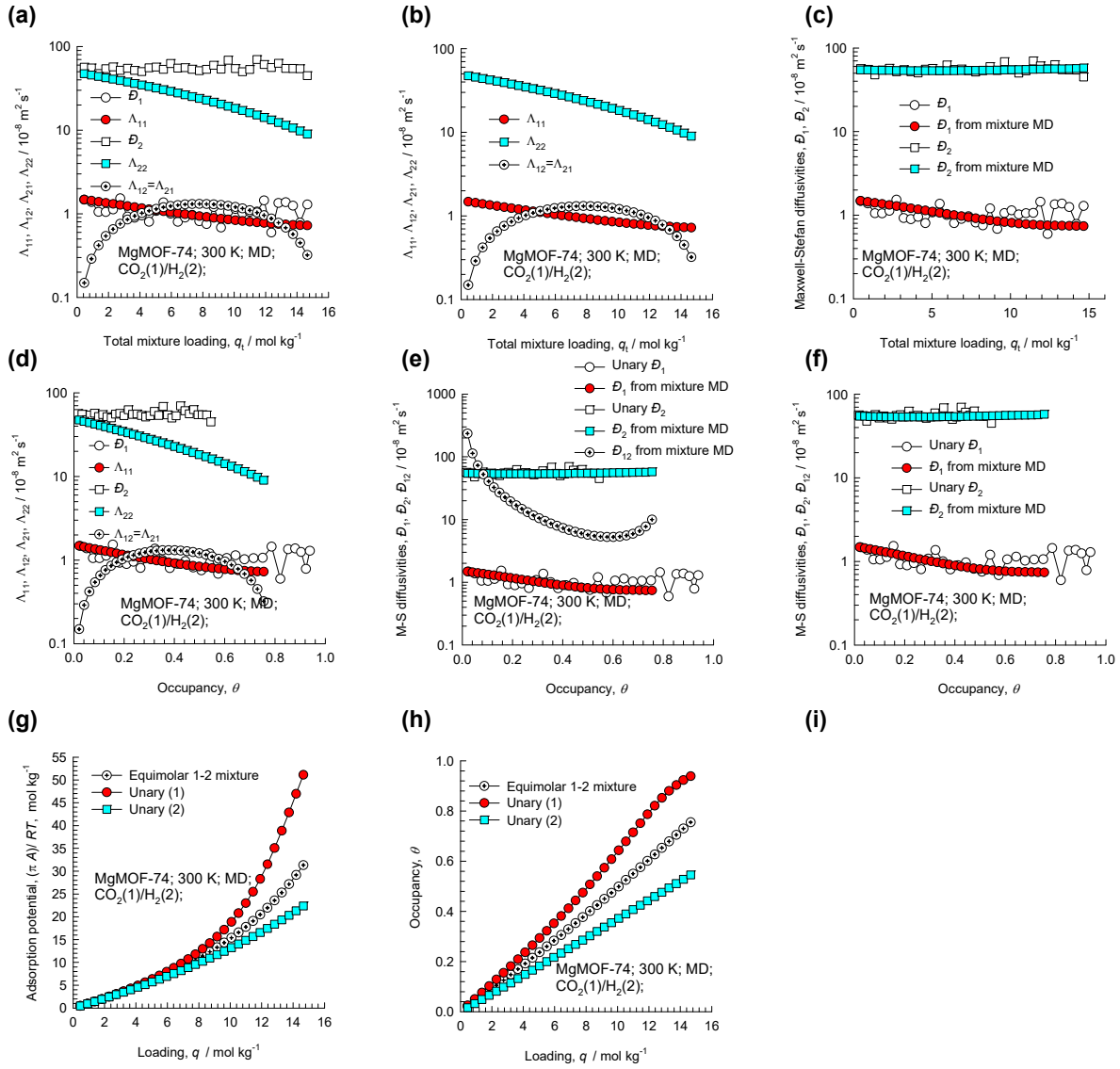

Figure S9-56. MD simulated values of $\Lambda_{11}, \Lambda_{12}, \Lambda_{22}$, along with the backed-out M-S diffusivities, $Đ_1, Đ_2, Đ_{12}$ for equimolar (q_1=q_2) binary CO_2(1)/H_2(2) mixtures in MgMOF-74 at 300 K plotted as a function of (a, b, c) the total mixture loading $q_t = q_1+q_2$, and (d, e, f) occupancy θ. (g, h) The adsorption potential, and the occupancy plotted as function of the molar loading.

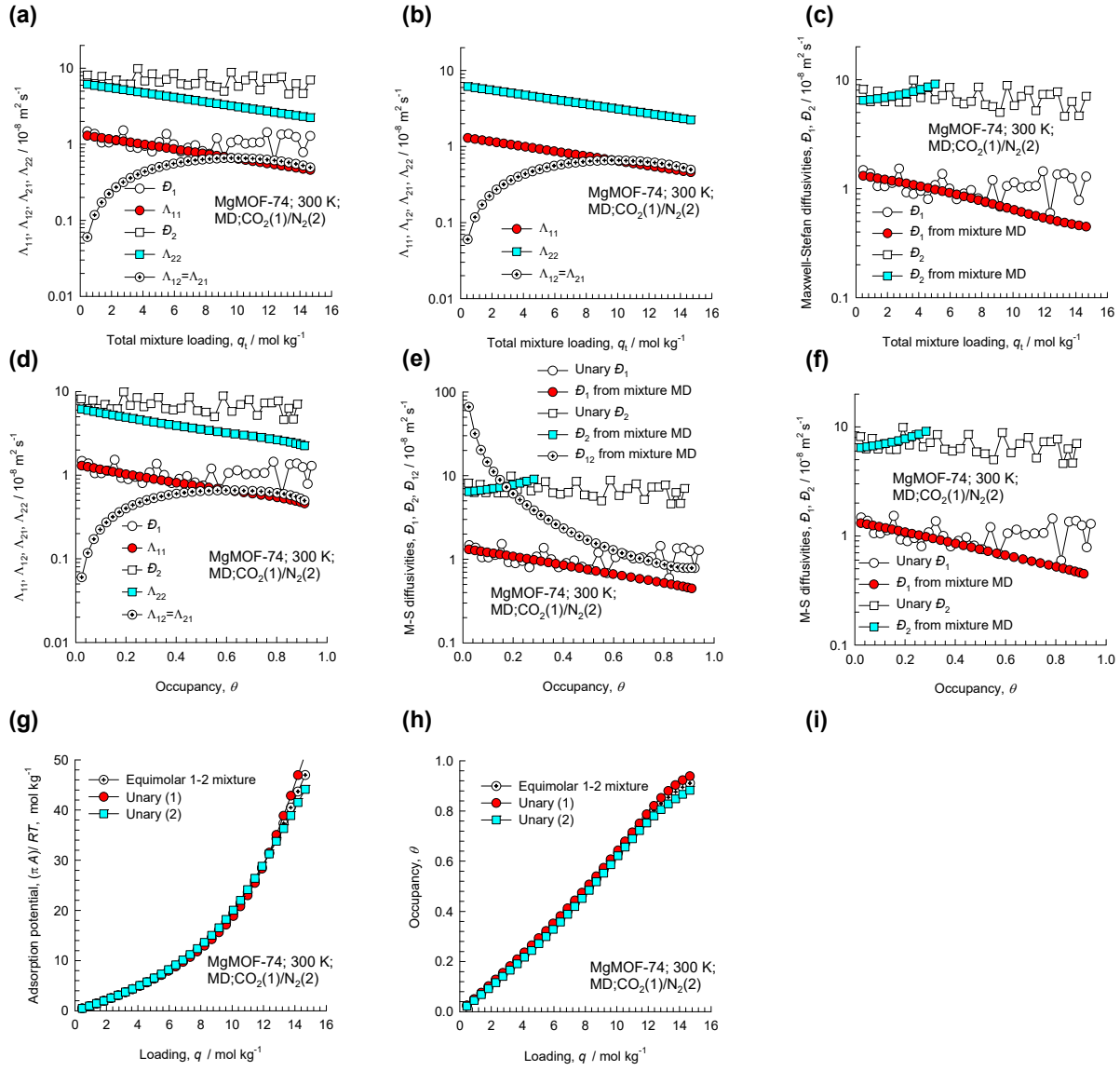

Figure S9-57. MD simulated values of $\Lambda_{11},\Lambda_{12},\Lambda_{22}$, along with the backed-out M-S diffusivities, $Đ_1,Đ_2,Đ_{12}$ for equimolar (q_1=q_2) binary CO_2(1)/N_2(2) mixtures in MgMOF-74 at 300 K plotted as a function of (a, b, c) the total mixture loading q_t= q_1+q_2, and (d, e, f) occupancy θ. (g, h) The adsorption potential, and the occupancy plotted as function of the molar loading.

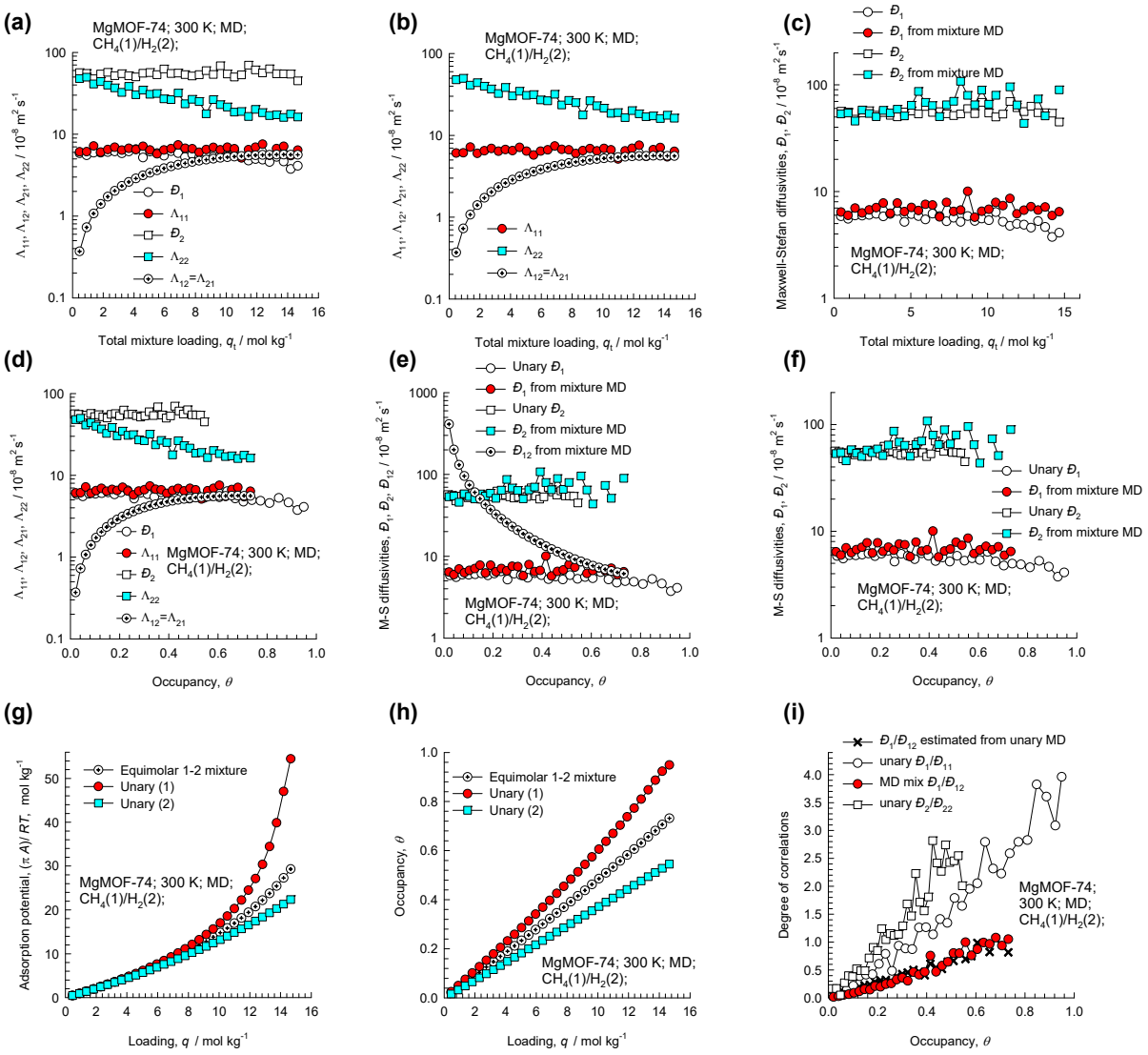

Figure S9-58. MD simulated values of $\Lambda_{11},\Lambda_{12},\Lambda_{22}$, along with the backed-out M-S diffusivities, $Đ_1,Đ_2,Đ_{12}$ for equimolar (q_1=q_2) binary CH$_4$(1)/H$_2$(2) mixtures in MgMOF-74 at 300 K plotted as a function of (a, b, c) the total mixture loading q_t= q_1+q_2, and (d, e, f) occupancy θ. (g, h) The adsorption potential, and the occupancy plotted as function of the molar loading. (i) degree of correlations.

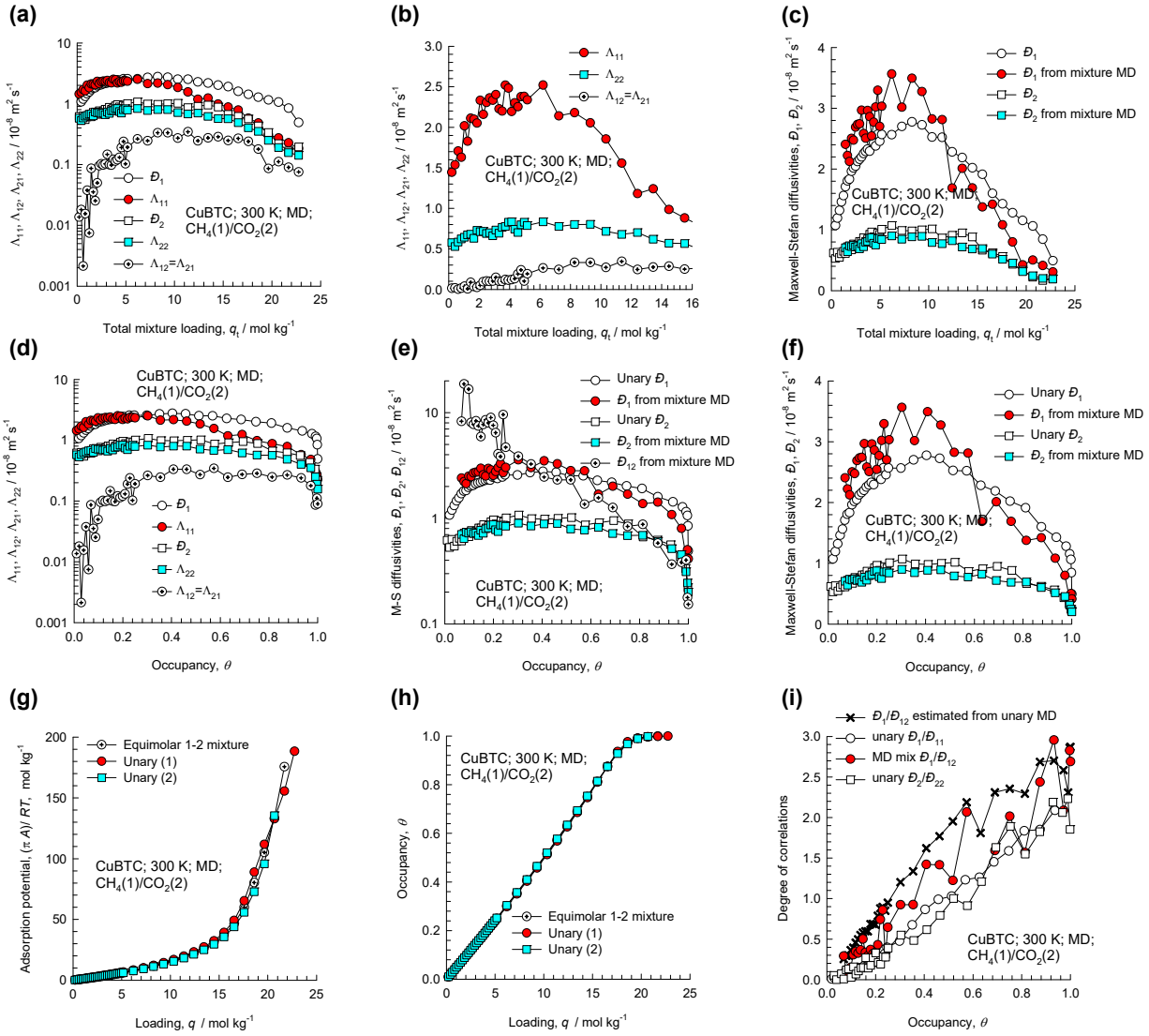

Figure S9-59. MD simulated values of $\Lambda_{11},\Lambda_{12},\Lambda_{22}$, along with the backed-out M-S diffusivities, $Đ_1,Đ_2,Đ_{12}$ for equimolar (q_1=q_2) binary $CH_4(1)/CO_2(2)$ mixtures in CuBTC at 300 K plotted as a function of (a, b, c) the total mixture loading q_t= q_1+q_2, and (d, e, f) occupancy θ. (g, h) The adsorption potential, and the occupancy plotted as function of the molar loading. (i) degree of correlations.

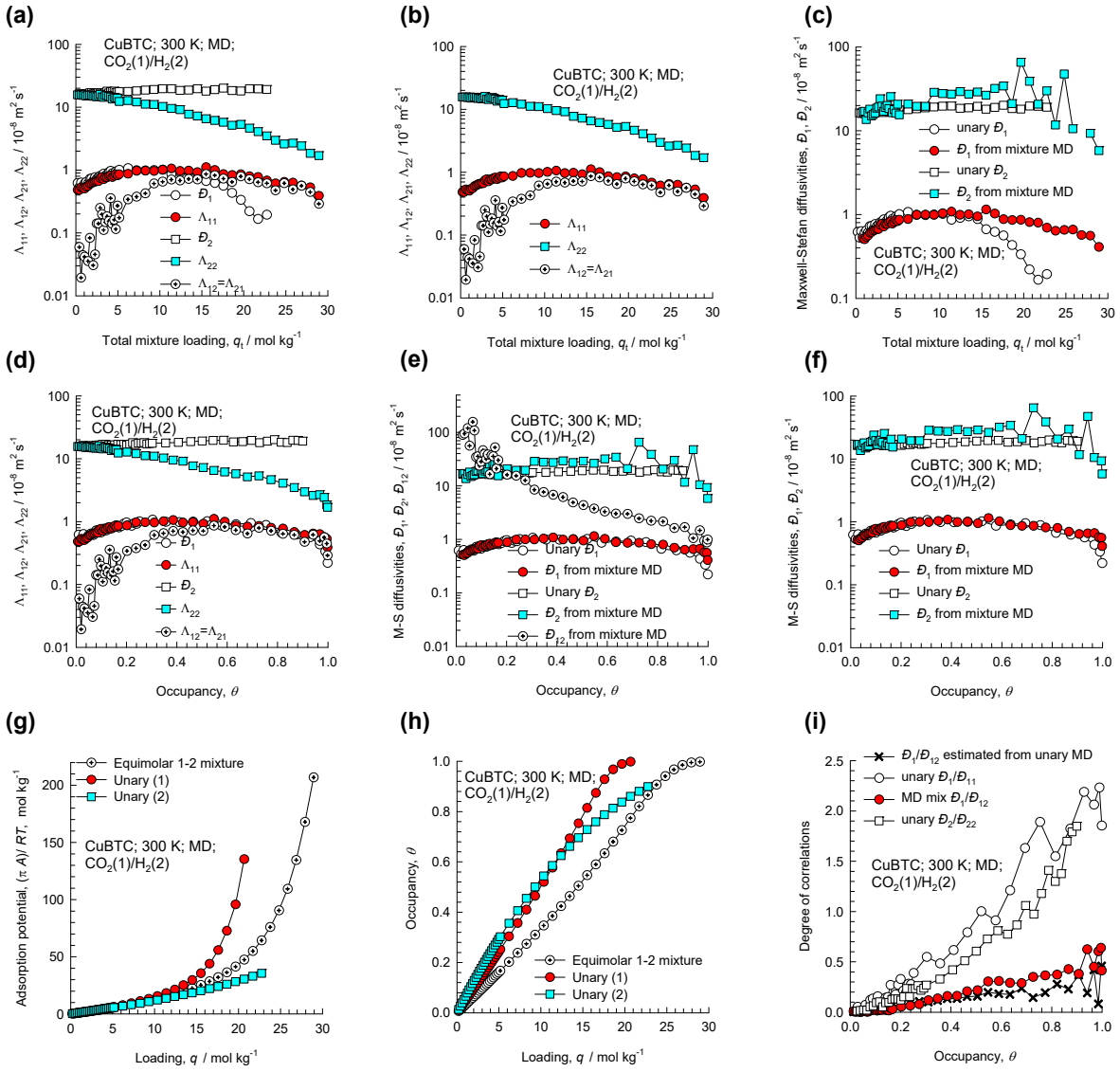

Figure S9-60. MD simulated values of $\Lambda_{11}, \Lambda_{12}, \Lambda_{22}$, along with the backed-out M-S diffusivities, $Đ_1, Đ_2, Đ_{12}$ for equimolar (q_1=q_2) binary $CO_2(1)/H_2(2)$ mixtures in CuBTC at 300 K plotted as a function of (a, b, c) the total mixture loading $q_t = q_1+q_2$, and (d, e, f) occupancy θ. (g, h) The adsorption potential, and the occupancy plotted as function of the molar loading. (i) degree of correlations.

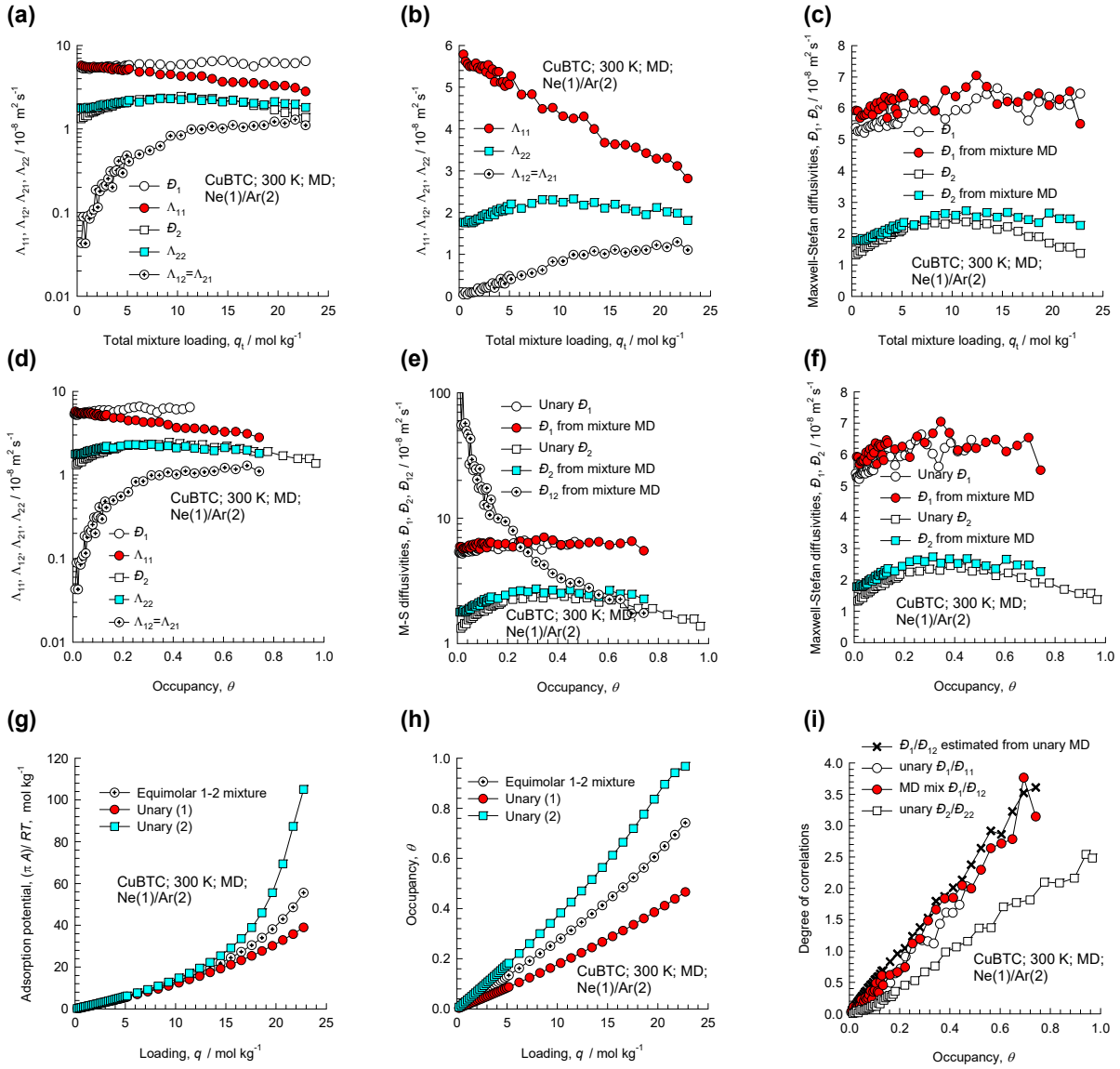

Figure S9-61. MD simulated values of $\Lambda_{11},\Lambda_{12},\Lambda_{22}$, along with the backed-out M-S diffusivities, $Đ_1,Đ_2,Đ_{12}$ for equimolar (q_1=q_2) binary Ne(1)/Ar(2) mixtures in CuBTC at 300 K plotted as a function of (a, b, c) the total mixture loading q_t= q_1+q_2, and (d, e, f) occupancy θ. (g, h) The adsorption potential, and the occupancy plotted as function of the molar loading. (i) degree of correlations.

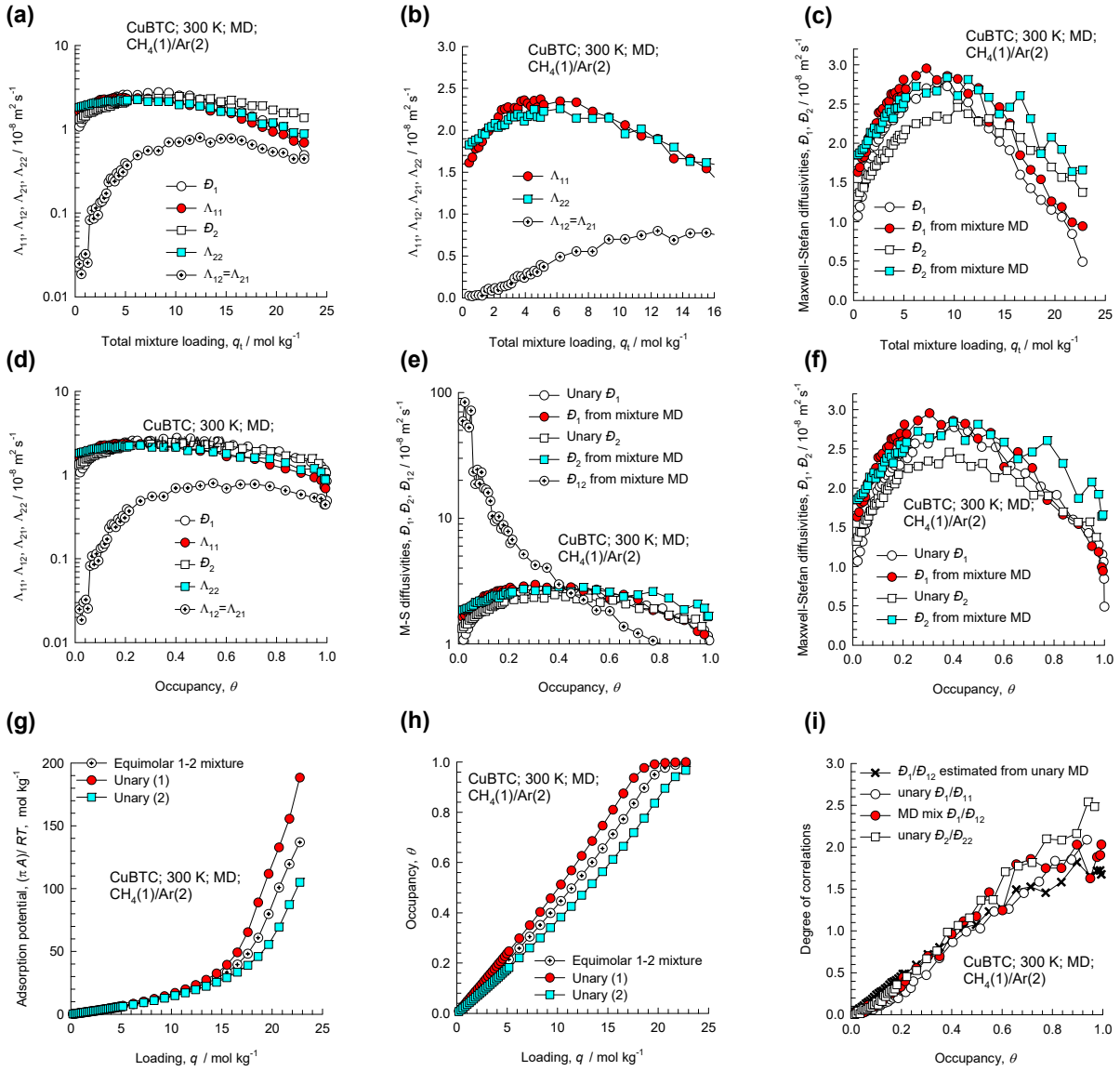

Figure S9-62. MD simulated values of $\Lambda_{11},\Lambda_{12},\Lambda_{22}$, along with the backed-out M-S diffusivities, $Đ_1,Đ_2,Đ_{12}$ for equimolar (q_1=q_2) binary CH$_4$(1)/Ar(2) mixtures in CuBTC at 300 K plotted as a function of (a, b, c) the total mixture loading q_t= q_1+q_2, and (d, e, f) occupancy θ. (g, h) The adsorption potential, and the occupancy plotted as function of the molar loading. (i) degree of correlations.

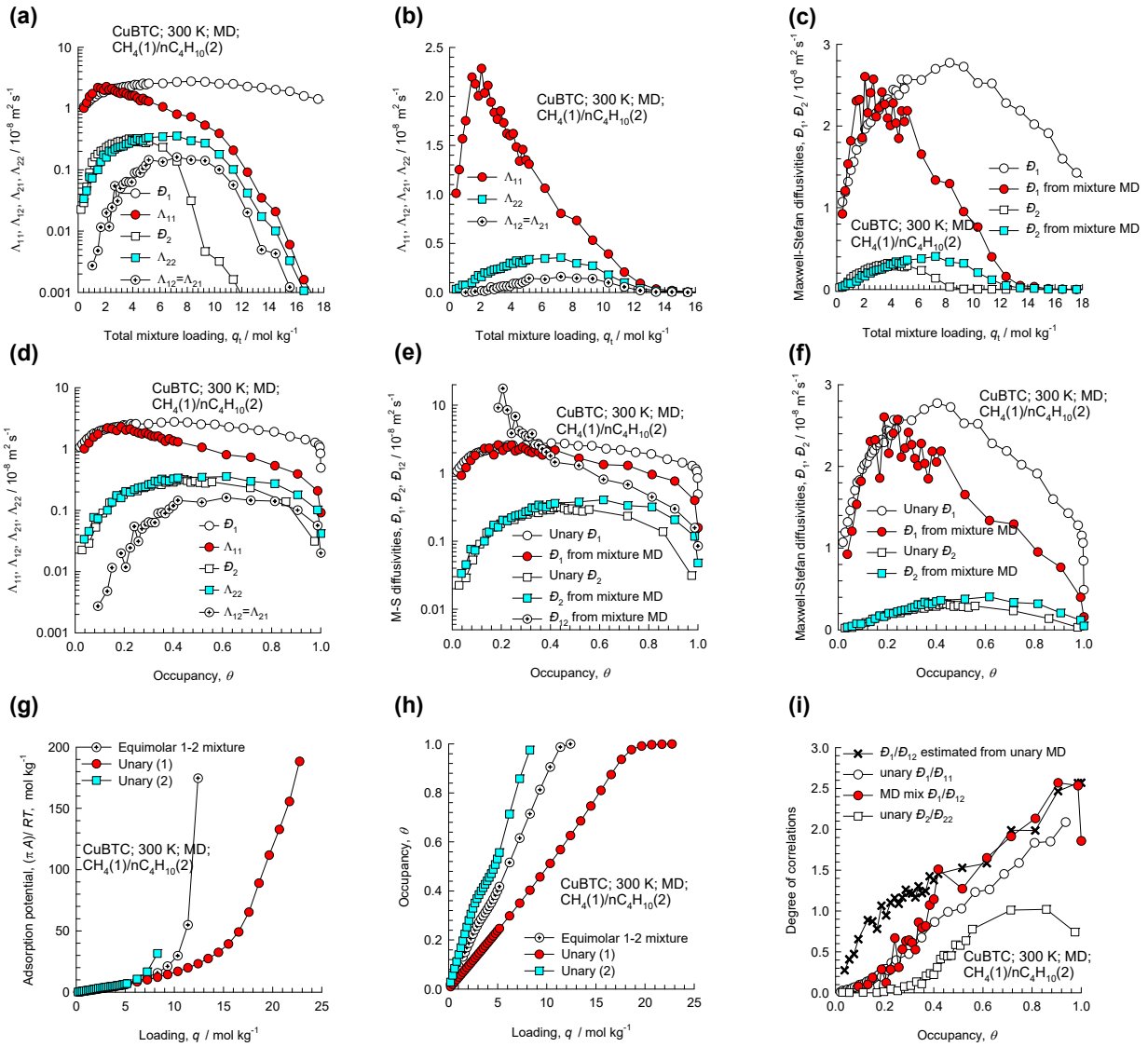

Figure S9-63. MD simulated values of $\Lambda_{11},\Lambda_{12},\Lambda_{22}$, along with the backed-out M-S diffusivities, $Đ_1,Đ_2,Đ_{12}$ for equimolar (q_1=q_2) binary $CH_4(1)/nC_4H_{10}(2)$ mixtures in CuBTC at 300 K plotted as a function of (a, b, c) the total mixture loading q_t= q_1+q_2, and (d, e, f) occupancy θ. (g, h) The adsorption potential, and the occupancy plotted as function of the molar loading. (i) degree of correlations.

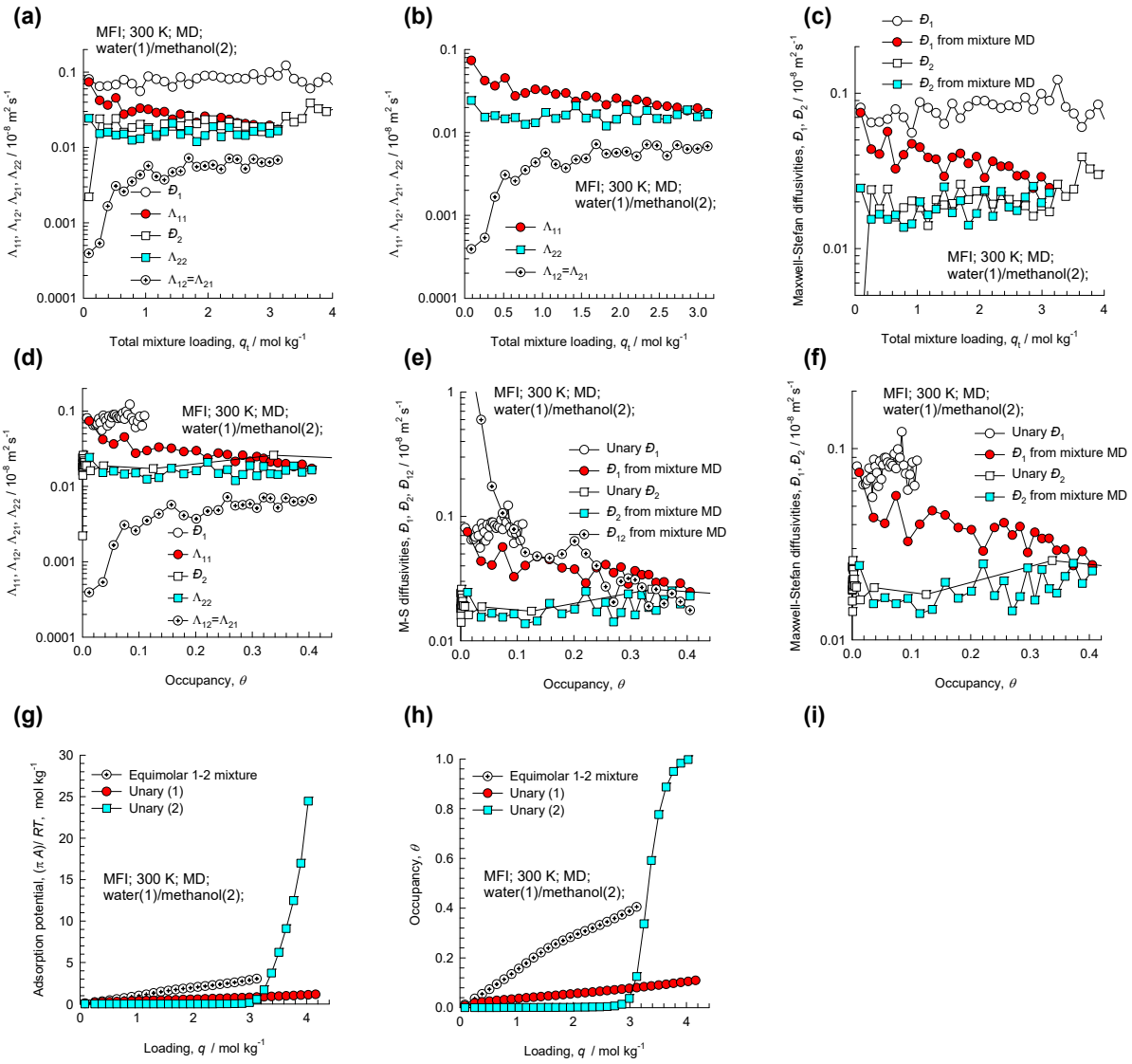

Figure S9-64. MD simulated values of $\Lambda_{11}, \Lambda_{12}, \Lambda_{22}$, along with the backed-out M-S diffusivities, $Đ_1, Đ_2, Đ_{12}$ for equimolar (q_1=q_2) binary water(1)/methanol(2) mixtures in MFI zeolite at 300 K plotted as a function of (a, b, c) the total mixture loading q_t= q_1+q_2, and (d, e, f) occupancy θ. (g, h) The adsorption potential, and the occupancy plotted as function of the molar loading.

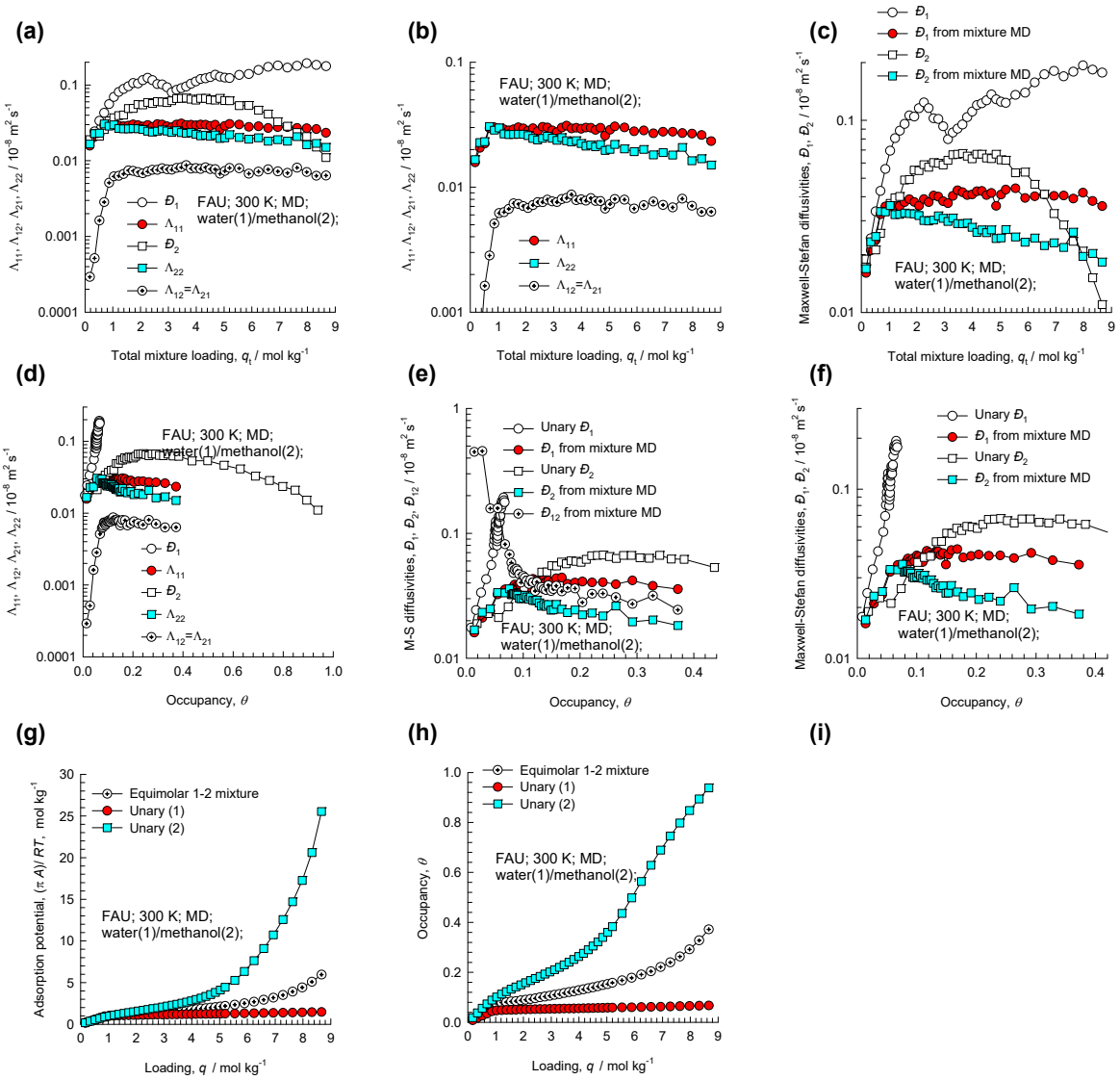

Figure S9-65. MD simulated values of $\Lambda_{11}, \Lambda_{12}, \Lambda_{22}$, along with the backed-out M-S diffusivities, $Đ_1, Đ_2, Đ_{12}$ for equimolar (q_1=q_2) binary water(1)/methanol(2) mixtures in FAU all-silica zeolite at 300 K plotted as a function of (a, b, c) the total mixture loading q_t= q_1+q_2, and (d, e, f) occupancy θ. (g, h) The adsorption potential, and the occupancy plotted as function of the molar loading.

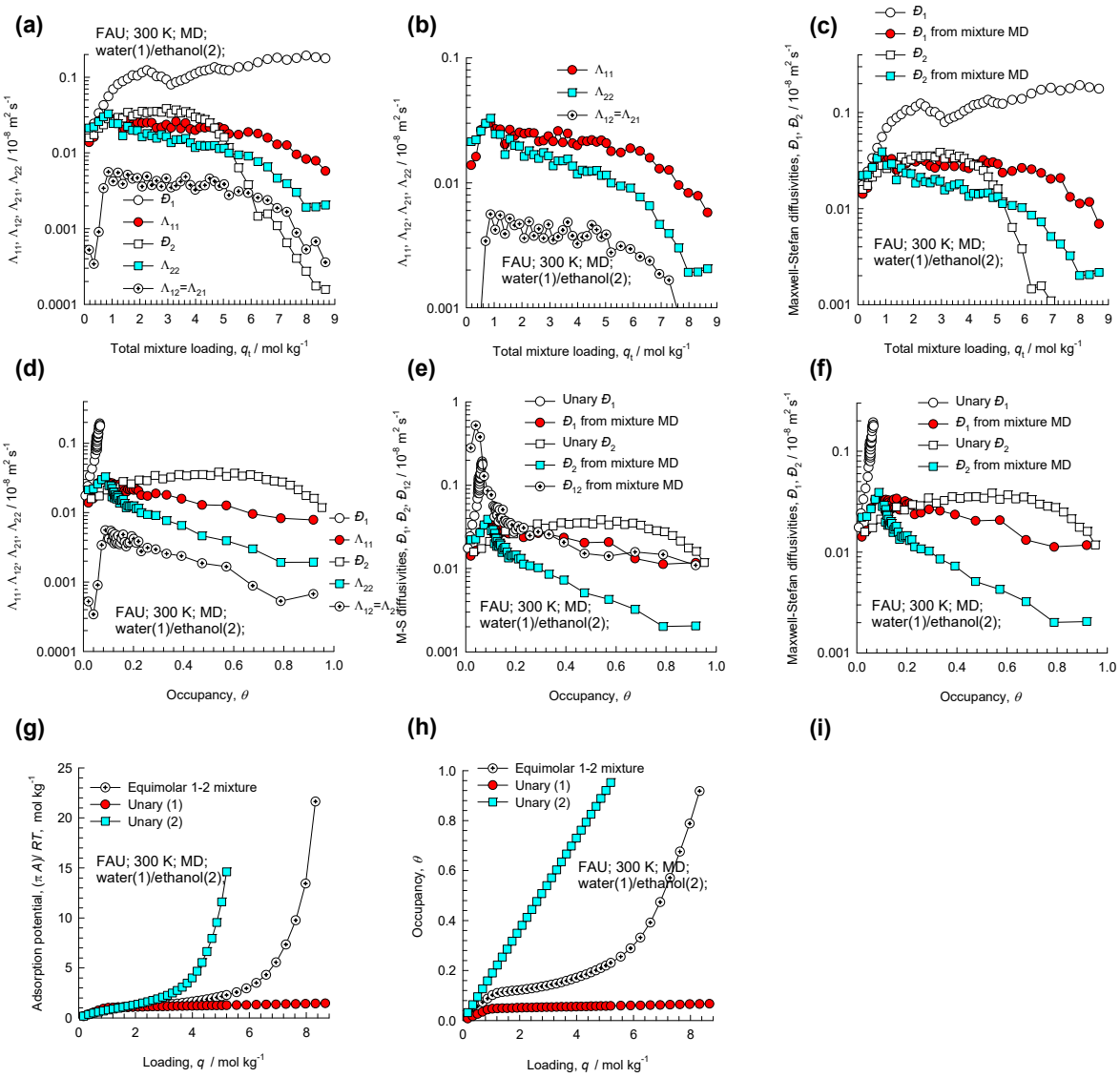

Figure S9-66. MD simulated values of $\Lambda_{11},\Lambda_{12},\Lambda_{22}$, along with the backed-out M-S diffusivities, $Đ_1,Đ_2,Đ_{12}$ for equimolar (q_1=q_2) binary water(1)/ethanol(2) mixtures in FAU all-silica zeolite at 300 K plotted as a function of (a, b, c) the total mixture loading q_t= q_1+q_2, and (d, e, f) occupancy θ. (g, h) The adsorption potential, and the occupancy plotted as function of the molar loading.

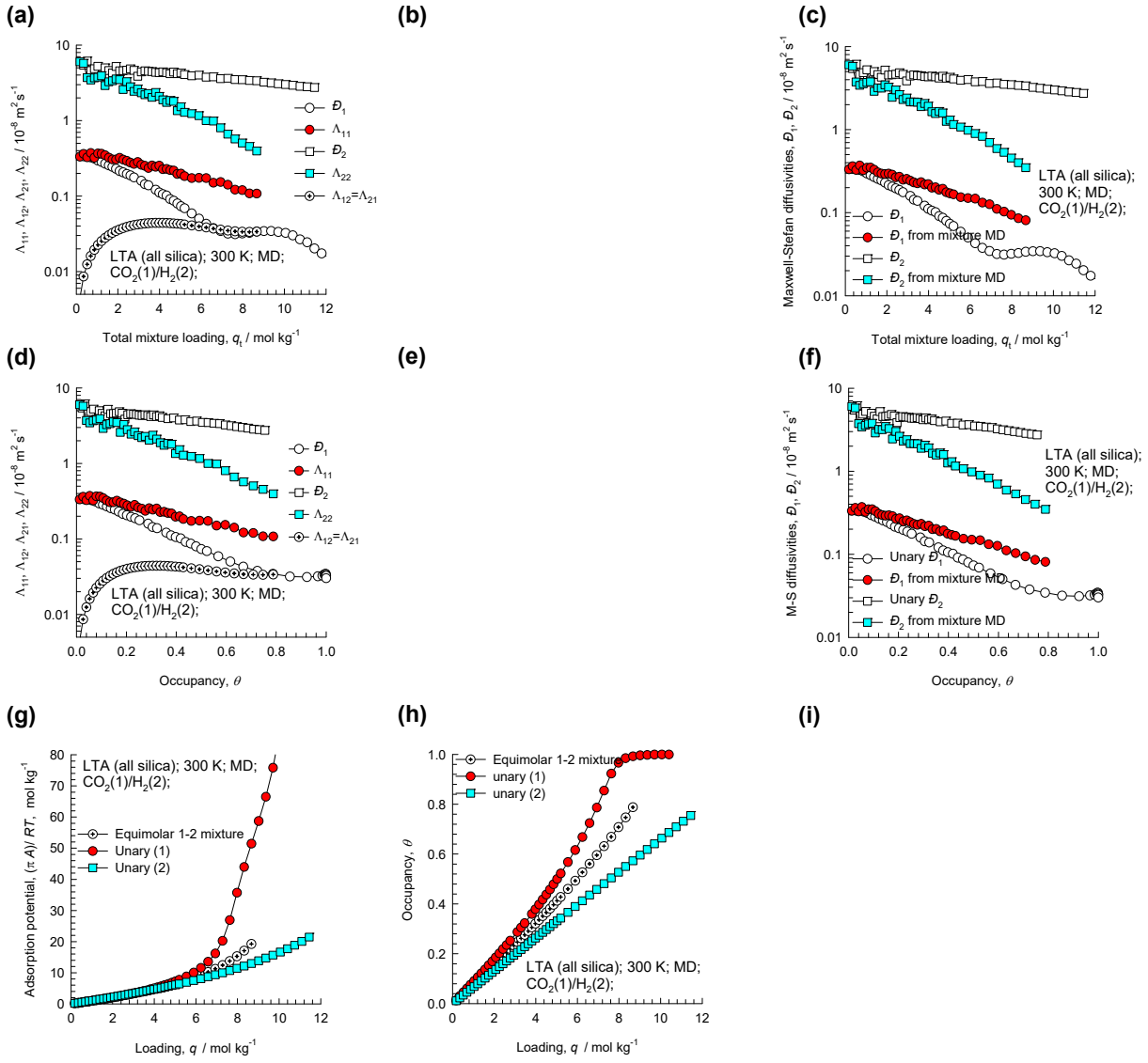

Figure S9-67. MD simulated values of $\Lambda_{11}, \Lambda_{12}, \Lambda_{22}$, along with the backed-out M-S diffusivities, $Đ_1, Đ_2, Đ_{12}$ for equimolar (q_1=q_2) binary CO_2(1)/H_2(2) mixtures in LTA all-silica zeolite at 300 K plotted as a function of (a, b, c) the total mixture loading q_t= q_1+q_2, and (d, e, f) occupancy θ. (g, h) The adsorption potential, and the occupancy plotted as function of the molar loading. It is to be noted there that the correlation effects are of negligible importance for this guest/host combination. Therefore, the Maxwell-Stefan diffusivities reported here are actually the self-diffusivities, $D_{i,self}$, determined from MD using Equation (7-8).

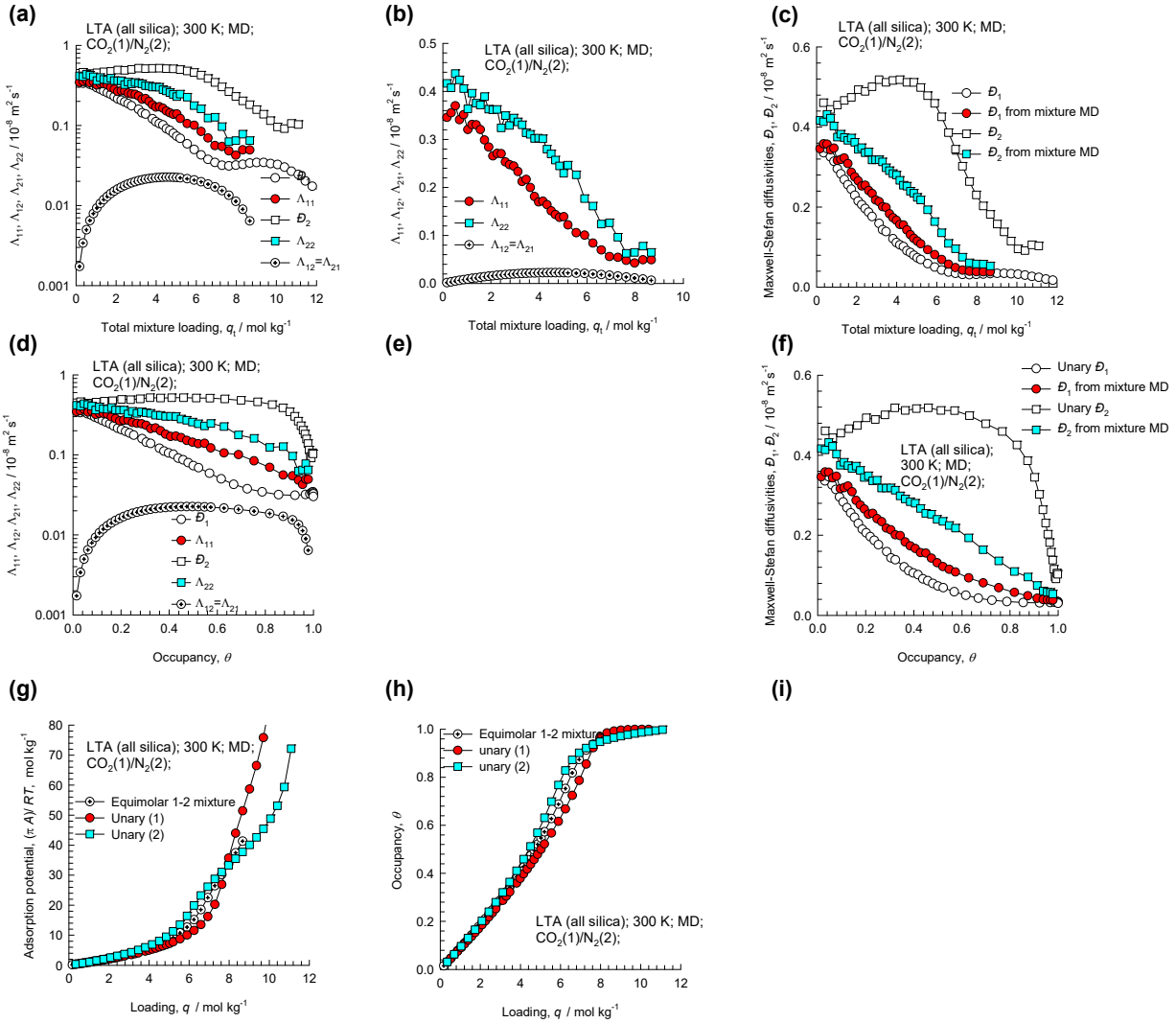

Figure S9-68. MD simulated values of $\Lambda_{11}, \Lambda_{12}, \Lambda_{22}$, along with the backed-out M-S diffusivities, $Đ_1, Đ_2, Đ_{12}$ for equimolar (q_1=q_2) binary CO_2(1)/N_2(2) mixtures in LTA all-silica zeolite at 300 K plotted as a function of (a, b, c) the total mixture loading q_t= q_1+q_2, and (d, e, f) occupancy θ. (g, h) The adsorption potential, and the occupancy plotted as function of the molar loading. It is to be noted there that the correlation effects are of negligible importance for this guest/host combination. Therefore, the Maxwell-Stefan diffusivities reported here are actually the self-diffusivities, $D_{i,self}$, determined from MD using Equation (7-8).

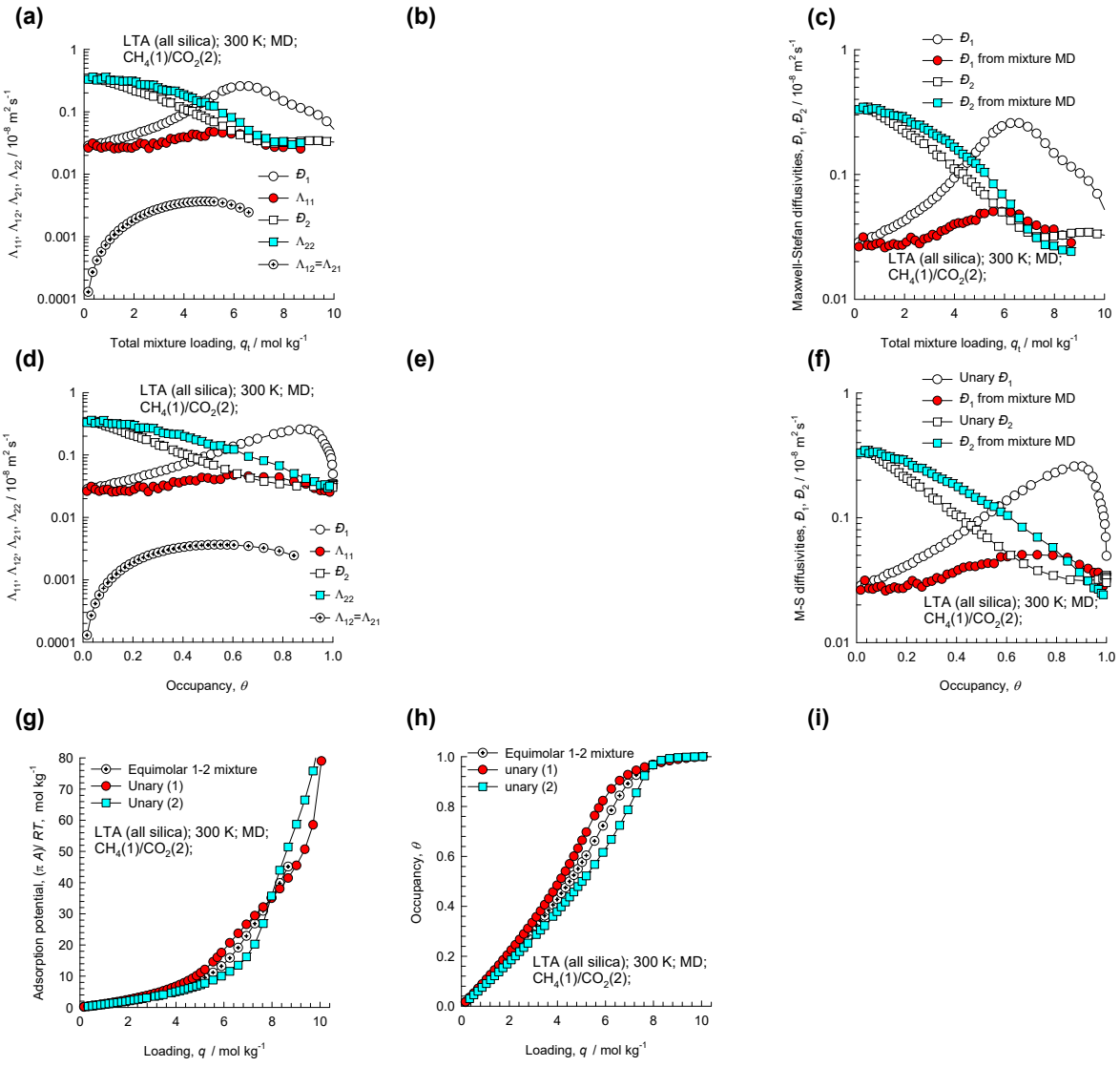

Figure S9-69. MD simulated values of $\Lambda_{11}, \Lambda_{12}, \Lambda_{22}$, along with the backed-out M-S diffusivities, $Đ_1, Đ_2, Đ_{12}$ for equimolar (q_1=q_2) binary $CH_4(1)/CO_2(2)$ mixtures in LTA all-silica zeolite at 300 K plotted as a function of (a, b, c) the total mixture loading $q_t = q_1+q_2$, and (d, e, f) occupancy θ. (g, h) The adsorption potential, and the occupancy plotted as function of the molar loading. It is to be noted there that the correlation effects are of negligible importance for this guest/host combination. Therefore, the Maxwell-Stefan diffusivities reported here are actually the self-diffusivities, $D_{i,self}$, determined from MD using Equation (7-8).

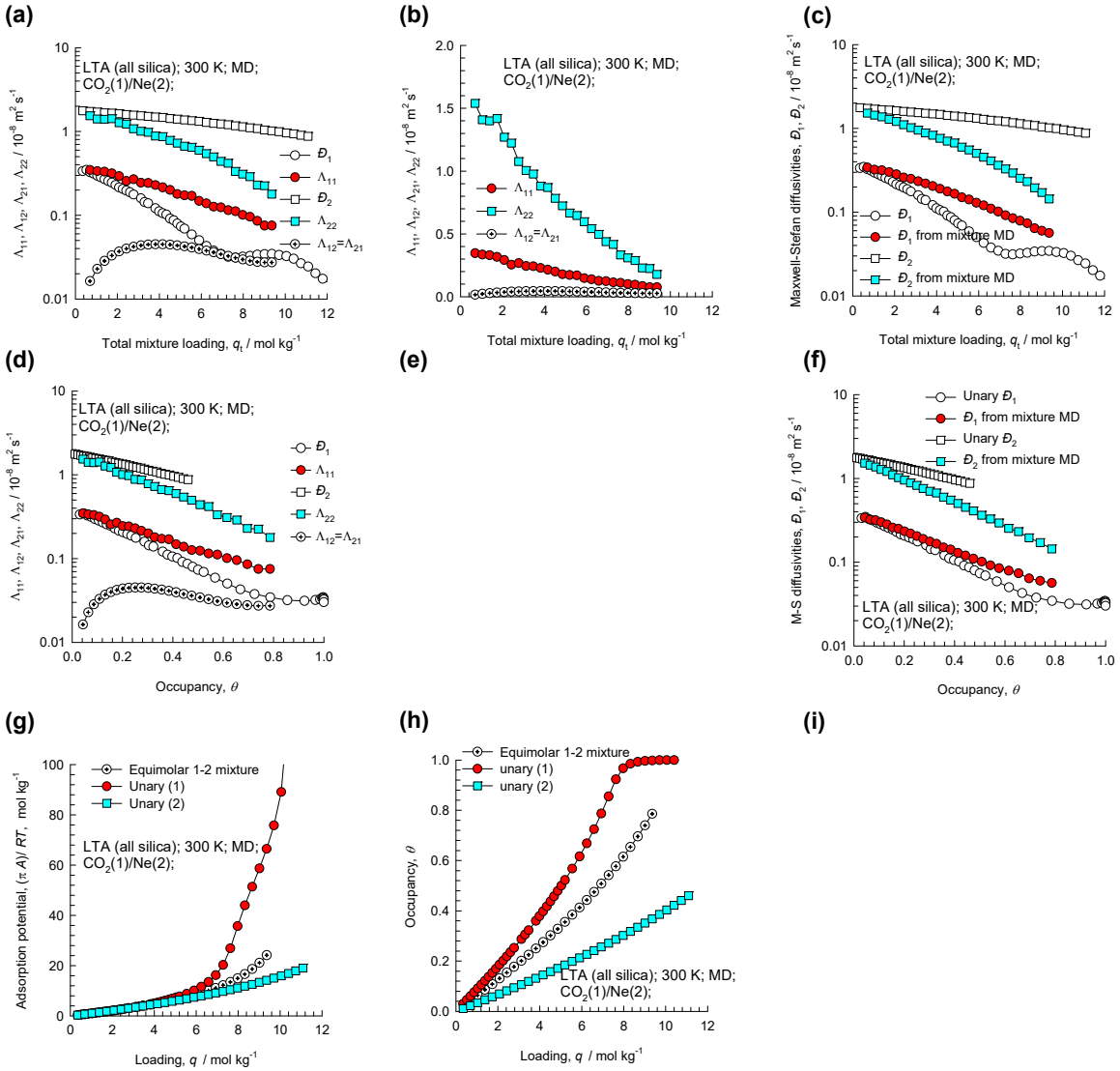

Figure S9-70. MD simulated values of $\Lambda_{11}, \Lambda_{12}, \Lambda_{22}$, along with the backed-out M-S diffusivities, $Đ_1, Đ_2, Đ_{12}$ for equimolar (q_1=q_2) binary CO_2(1)/Ne(2) mixtures in LTA all-silica zeolite at 300 K plotted as a function of (a, b, c) the total mixture loading $q_t = q_1+q_2$, and (d, e, f) occupancy θ. (g, h) The adsorption potential, and the occupancy plotted as function of the molar loading. It is to be noted there that the correlation effects are of negligible importance for this guest/host combination. Therefore, the Maxwell-Stefan diffusivities reported here are actually the self-diffusivities, $D_{i,self}$, determined from MD using Equation (7-8).

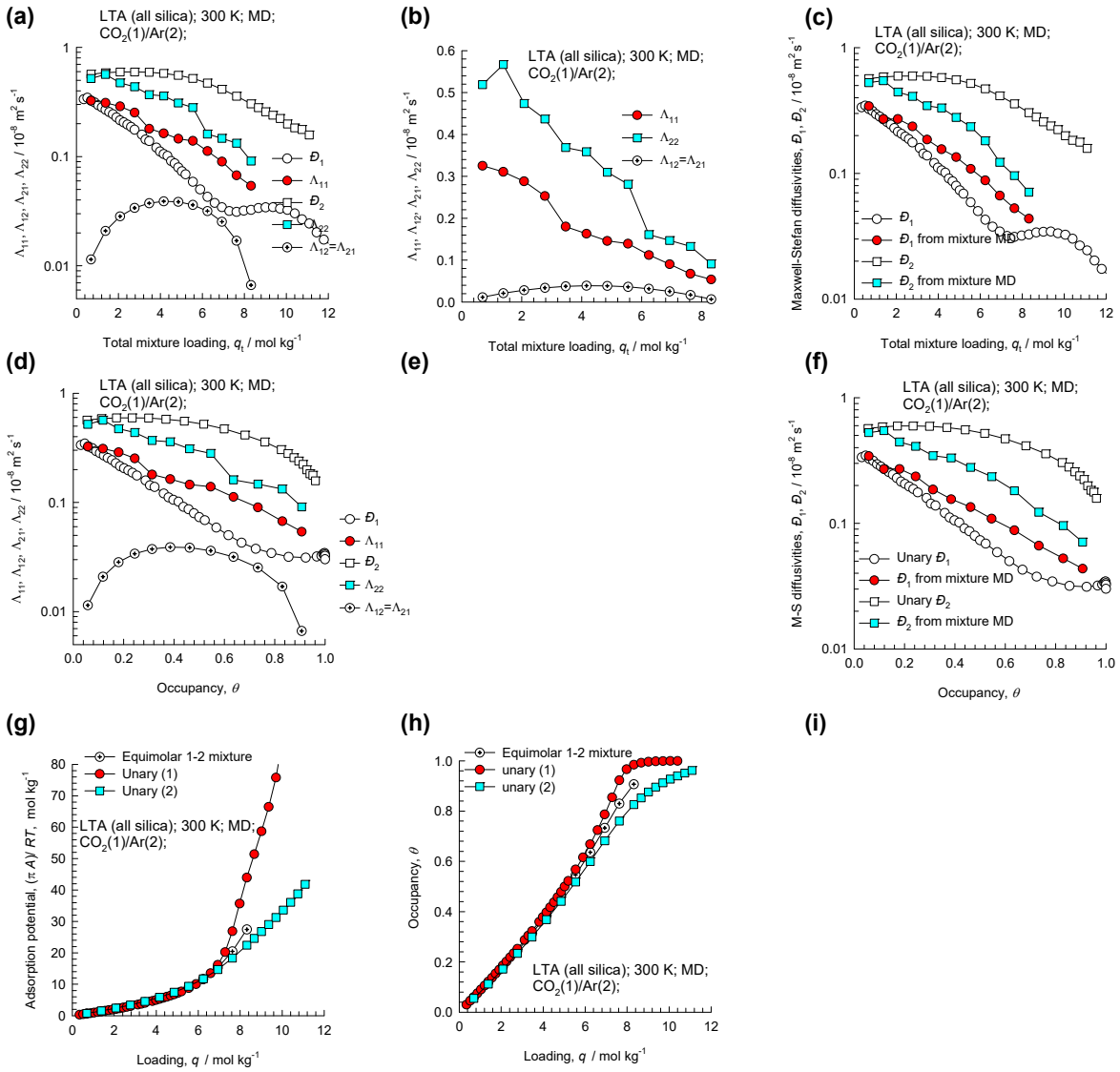

Figure S9-71. MD simulated values of $\Lambda_{11},\Lambda_{12},\Lambda_{22}$, along with the backed-out M-S diffusivities, $Đ_1,Đ_2,Đ_{12}$ for equimolar (q_1=q_2) binary CO_2(1)/Ar(2) mixtures in LTA all-silica zeolite at 300 K plotted as a function of (a, b, c) the total mixture loading q_t= q_1+q_2, and (d, e, f) occupancy θ. (g, h) The adsorption potential, and the occupancy plotted as function of the molar loading. It is to be noted there that the correlation effects are of negligible importance for this guest/host combination. Therefore, the Maxwell-Stefan diffusivities reported here are actually the self-diffusivities, $D_{i,self}$, determined from MD using Equation (7-8).

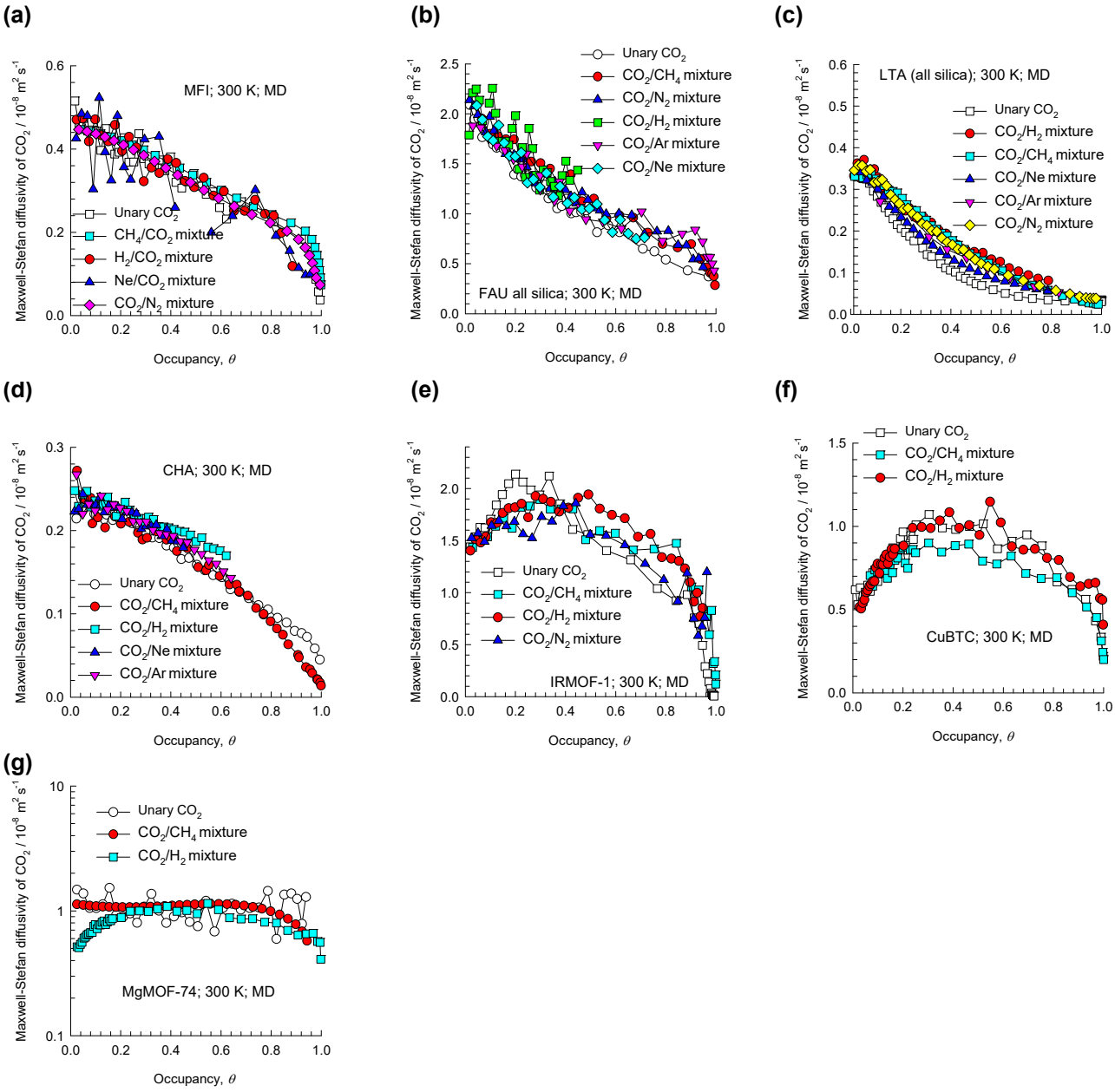

Figure S9-72. Maxwell-Stefan diffusivity, $Đ_i$, of CO_2 determined MD simulation data for diffusion of a variety of equimolar ($q_1 = q_2$) binary mixtures of CO_2 and different partner species in (a) MFI, (b) FAU (all silica), (c) LTA, (d) CHA, (e) IRMOF-1, (f) CuBTC, and (g) MgMOF-74. The x- axes represent the fractional occupancy θ. Also shown in open symbols are the MD simulations of $Đ_i$, for unary CO_2 diffusion. The plotted data are based on combining the information contained in Figure S9-1 to Figure S9-71.

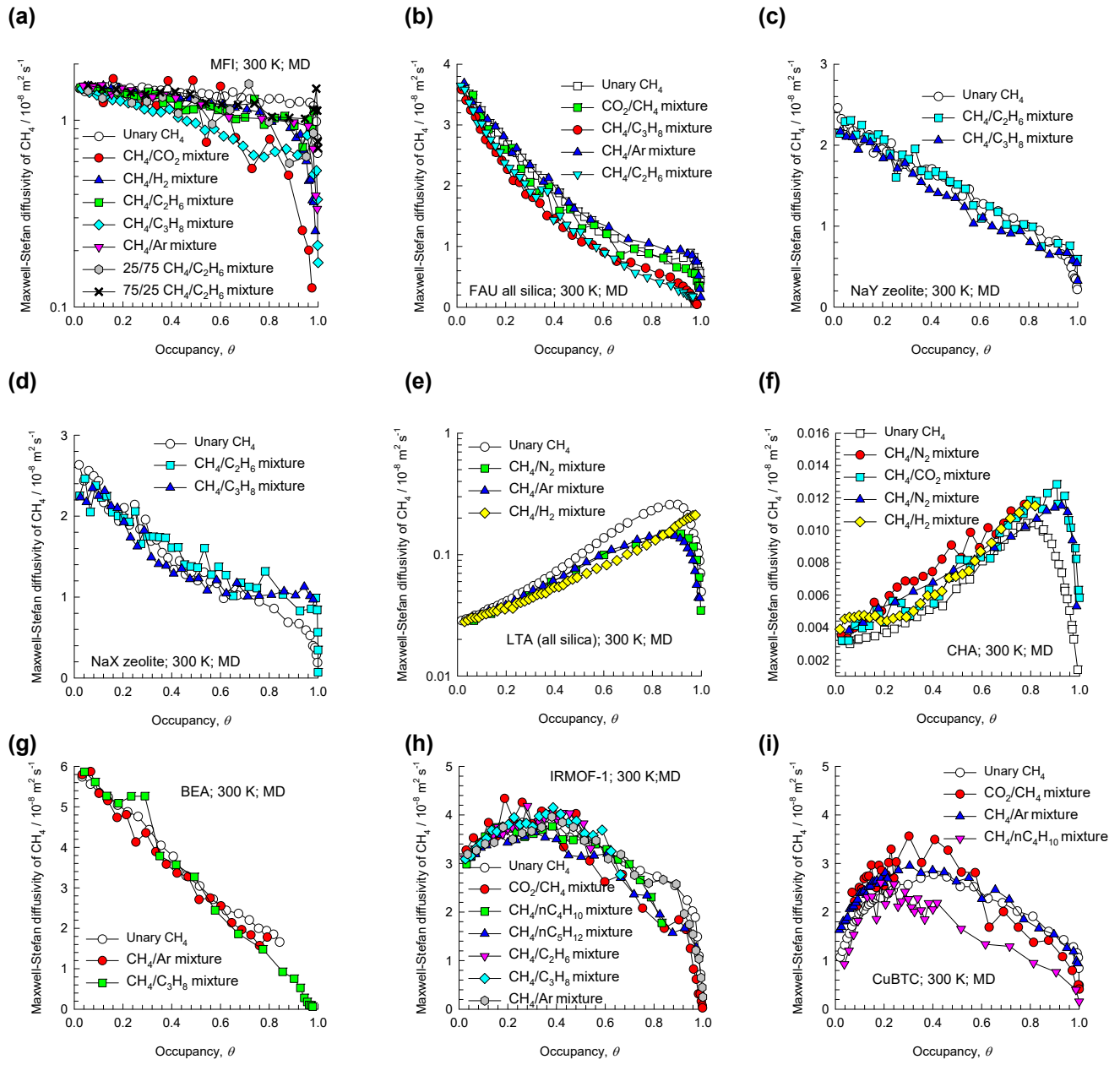

Figure S9-73. Maxwell-Stefan diffusivity, $Đ_i$, of CH_4 determined MD simulation data for diffusion of a variety of equimolar ($q_1 = q_2$) binary mixtures of CH_4 and different partner species in (a) MFI, (b) FAU (all silica), (c) NaY (48 Al), (d) NaX (86 Al), (e) LTA, (f) CHA, (g) BEA, (h) IRMOF-1, and (i) CuBTC. The *x*- axes represent the fractional occupancy θ. Also shown in open symbols are the MD simulations of $Đ_i$, for unary CH_4 diffusion. The plotted data are based on combining the information contained in Figure S9-1 to Figure S9-71.

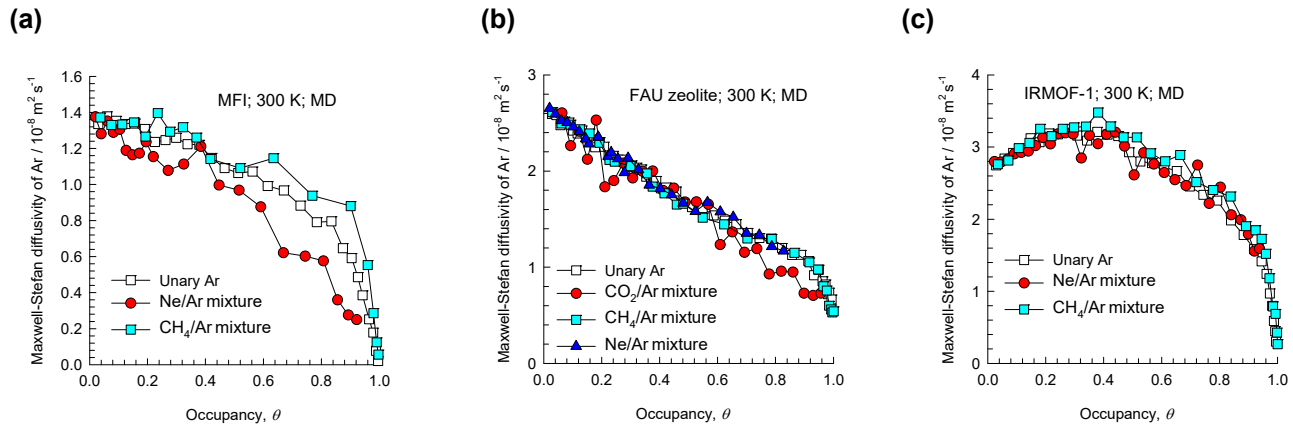

Figure S9-74. Maxwell-Stefan diffusivity, $Đ_i$, of Ar determined MD simulation data for diffusion of a variety of equimolar ($q_1 = q_2$) binary mixtures of Ar and different partner species in (a) MFI, (b) FAU-Si, and (c) IRMOF-1. The x- axes represent the fractional occupancy θ. Also shown in open symbols are the MD simulations of $Đ_i$, for unary Ar diffusion. The plotted data are based on combining the information contained in Figure S9-1 to Figure S9-71.

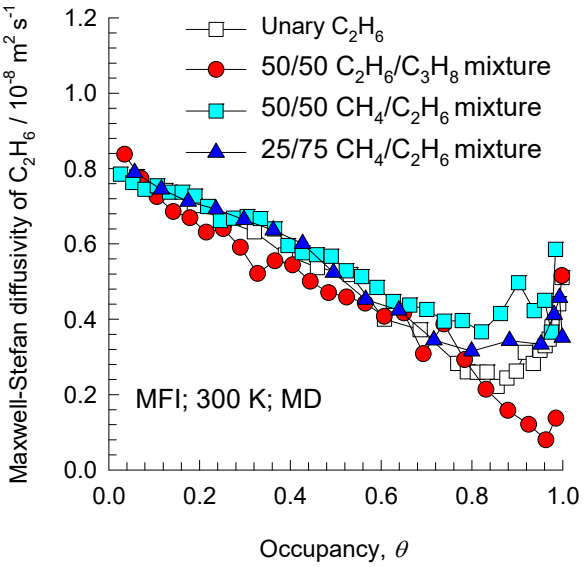

Figure S9-75. Maxwell-Stefan diffusivity, $Đ_i$, of C_2H_6 determined MD simulation data for diffusion of three binary mixtures of C_2H_6 in MFI at 300 K. The *x*- axes represent the fractional occupancy θ. Also shown in open symbols are the MD simulations of $Đ_i$, for unary C_2H_6 diffusion. The plotted data are based on combining the information contained in Figure S9-1 to Figure S9-71.

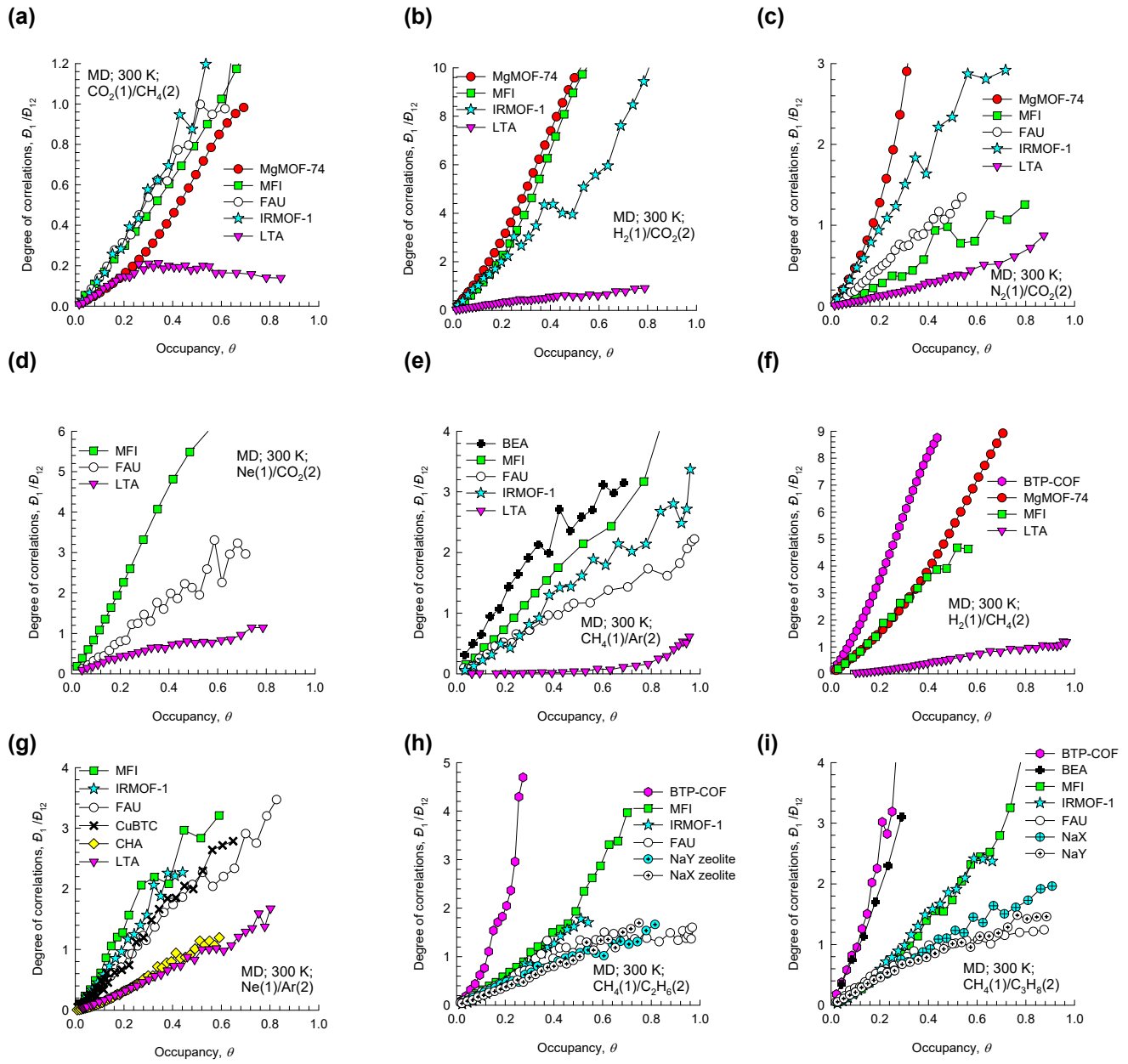

Figure S9-76. MD simulation data for the degree of correlations, $Đ_1/Đ_{12}$, for diffusion of equimolar ($q_1 = q_2$) binary mixtures (a) CO_2/CH_4, (b) H_2/CO_2, (c) N_2/CO_2, (d) Ne/CO_2, (e) CH_4/Ar (f) H_2/CH_4, (g) Ne/Ar, (h) CH_4/C_2H_6, and (i) CH_4/C_3H_8 at 300 K in a variety of host materials. The *x*- axes represent the fractional occupancy θ.

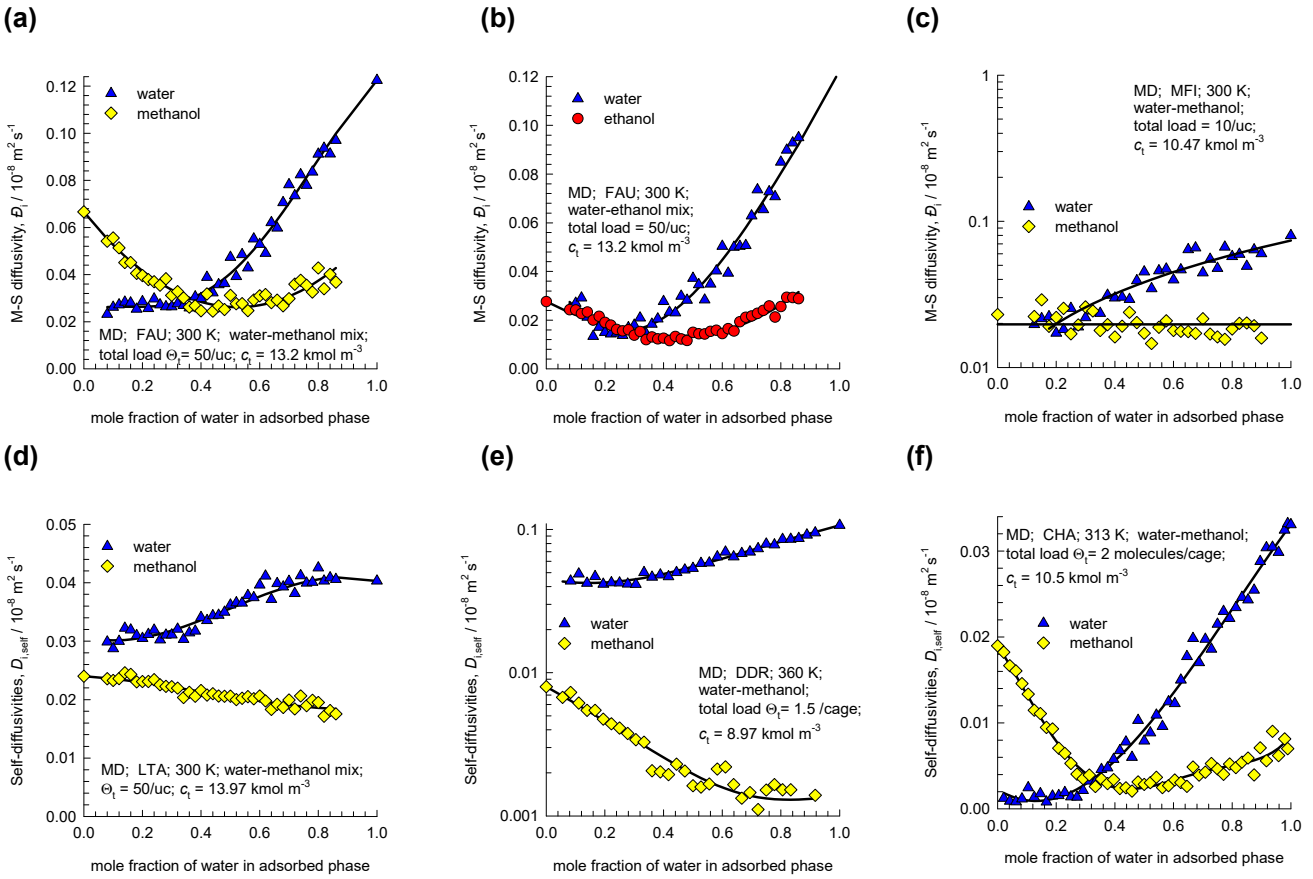

Figure S9-77. Maxwell-Stefan diffusivities, $Đ_i$, in water/methanol, and water/ethanol mixtures of varying composition in (a, b) FAU, (c) MFI, (d) LTA, (e) DDR, and (f) CHA zeolites. The data are compiled from MD simulation results published in the literature.[93, 99, 101] In all cases the MD simulations were carried out under conditions in which the total concentration within the pores, c_t, is held constant; the values c_t are specified in each case and are based on the accessible pore volume in the various zeolites. In some cases the corresponding loadings per unit cell, Θ_t, are also specified. For CHA, DDR, and LTA the plotted diffusivities are the self-diffusivities, $D_{i,self}$, that are more accurate to determine and provide good approximations of the M-S diffusivities, i.e. $D_{i,self} \approx Đ_i$. The MD data are culled from our previous publications.[93, 97-99, 101, 103]

10 Estimation of the Degree of Correlations for Mixture Diffusion

The objective in this chapter is to develop a procedure for estimation of the degree of correlations for binary mixture diffusion, that are quantified by the metrics $Đ_1/Đ_{12}$, and $Đ_2/Đ_{12}$ using data (MD or experimental) on the data for *unary* diffusivities (both $D_{i,self}$ and M-S $Đ_i$) of each constituent partner. The development of the estimation procedure relies on the estimation procedure for the M-S diffusivity for binary fluid phase mixtures; as is first discussed below.

10.1 M-S diffusivities for diffusion in fluid phase mixtures

The use of equation (6-14) and pore concentrations c_i in terms of the accessible pore volume are particularly convenient for estimation of the exchange coefficients $Đ_{ij}$. To appreciate this, let us consider the limiting case of *n*-component mixture diffusion in the absence of any interactions with the pore walls. In this case, we have $\varepsilon = 1$, and equation (6-14) degenerates to the Maxwell-Stefan equation for describing bulk *fluid phase* mixture diffusion[40]

$$-\frac{c_i}{RT}\frac{d\mu_i}{dz} = \sum_{\substack{j=1 \\ j\neq i}}^{n} \frac{x_j N_i - x_i N_j}{Đ_{ij,fl}}; \qquad i = 1,2,...n; \quad \text{bulk fluid mixture} \tag{10-1}$$

where $Đ_{ij,fl}$ represents the M-S diffusivity for the binary pair *i-j* in the *n*-component fluid mixture. For bulk fluid phase mixtures, the chemical potential gradients satisfy the Gibbs-Duhem relationship

$$\sum_{i=1}^{n} x_i d\mu_i = 0 \tag{10-2}$$

and so only *n*-1 of the equations (10-1) are independent. For a binary fluid phase mixture, equations (10-1) simplify to yield just one independent equation

$$-\frac{c_1}{RT}\frac{d\mu_1}{dz} = -c_t\left(1+\frac{\partial \ln \gamma_1}{\partial \ln x_1}\right)\frac{dx_1}{dz} = -c_t\Gamma\frac{dx_1}{dz} = \frac{x_2 N_1 - x_1 N_2}{Đ_{12,fl}} \tag{10-3}$$

where $c_t = \sum_{i=1}^{n} c_i$ is the total molar concentration of the mixture. Equation (10-3) can be recast into the form

$$N_1 - x_1\left(N_1 + N_2\right) = -\frac{c_1}{RT}Đ_{12,fl}\frac{d\mu_1}{dz} = -c_t Đ_{12,fl}\Gamma\frac{dx_1}{dz} \tag{10-4}$$

The Fick diffusivity for binary fluid mixtures is related to the corresponding M-S diffusivity

$$D_{12,fl} = Đ_{12,fl}\Gamma \tag{10-5}$$

It is to be noted that for binary fluid mixtures, the Fick and M-S diffusivities are defined in terms of fluxes defined with respect to the molar average velocity of the mixture $u = \sum_{i=1}^{n} x_i u_i$.

For highly non-ideal liquid mixtures, because of the strong composition dependence of the thermodynamic factor $\Gamma = \left(1 + \frac{\partial \ln \gamma_1}{\partial \ln x_1}\right)$, we should expect the Fick diffusivity to also exhibit a corresponding strong composition dependence; this is indeed borne out by experimental data of Clark and Rowley[41] for the system methanol (1) – *n*-hexane for which we note that the Fick diffusivity tends to approach zero in the region of the phase transition point near $x_1 \approx 0.5$; see Figure S10-1(a). The Maxwell-Stefan diffusivity, calculated from the experimental Fick diffusivity data using equation (10-5) shows a relatively mild dependence on mixture composition. The experimental data of Clark and Rowley [41] are in reasonably good agreement with the MD simulations of Krishna and van Baten;[42] see Figure S10-1(b).

For a fluid phase mixture, the Vignes[43, 44] interpolation formula is commonly used in practice for estimation of the $Đ_{12,\mathrm{fl}}$

$$Đ_{12,fl} = \left(Đ_{11,fl}\right)^{x_1}\left(Đ_{22,fl}\right)^{x_2} \tag{10-6}$$

where the $Đ_{\mathrm{ii,fl}}$ represent the self-exchange coefficients, or self-diffusivities, for *unary* fluid phase diffusion. The Vignes relation (10-6) implies that the logarithm of $Đ_{12,\mathrm{fl}}$ should be linear in the mole fraction x_1. From the data in Figure S10-1 we see that the Vignes interpolation formula holds

reasonably well. The factoring-out of the influence of mixture thermodynamics, is the root cause of the well-behaved characteristics of the M-S diffusivity $Đ_{12,fl}$.

Further validation of the Vignes interpolation formula (10-6) is demonstrated in Figure S10-2 for nine different equimolar fluid mixtures. Reliable procedures for estimation of $Đ_{12,fl}$ from molecular properties of the individual species are available in the literature; for further information regarding the estimation of the Maxwell-Stefan diffusivity for gaseous and liquid mixtures, the reader is referred to Taylor and Krishna[45] and Wesselingh and Krishna.[46] The dashed lines in Figure S10-2 show the estimations of $Đ_{12,fl}$ using the method of Fuller, Schettler and Giddings (FSG) [47], developed for *ideal gas* mixtures. We note that for concentrations $c_t < 6$ kmol m^{-3}, the MD simulated $Đ_{12,fl}$ values are in excellent agreement with the FSG estimations. For concentrations $c_t > 6$ kmol m^{-3}, the $Đ_{12,fl}$ values reflect those in dense condensed fluids, for which some estimation procedures are also available in the literature. [48]

The estimations of $Đ_{12,fl}$ provide a good starting point for estimation of the corresponding $Đ_{12}$ in nanoporous materials.

10.2 Relating $Đ_{12}$ in *meso*-porous materials to fluid phase $Đ_{12,fl}$

In the absence of pore walls, i.e. in *fluid phase* mixtures, the molecule-molecule interactions are quantified by the M-S diffusivity $Đ_{12,fl}$. As illustration, Figure S10-3 presents MD simulation data on $Đ_{12,fl}$ for eight different equimolar binary mixtures a function of the total molar concentration c_t; these simulations were carried out with the methodology described in the literature.[105] MD simulations of $Đ_{12}$ in BTP-COF, that consists of one-dimensional (1D) hexagonal shaped channels of 3.4 nm size are in excellent agreement with the values of $Đ_{12,fl}$ over the range of c_t. This conclusion also holds for cylindrical mesopores of 2 nm, 3 nm, 4 nm, and 5.8 nm. This leads us to conclude that the assumption that molecule-molecule interactions in mesoporous hosts is practically the same as that within the same *fluid phase* mixture at the same total molar concentration, c_t, i.e. $Đ_{12} = Đ_{12,fl}$.

Reliable procedures for estimation of $Đ_{12,fl}$ from molecular properties of the individual species are available in the literature, offering the possibility of *a priori* estimations of correlations. As illustration, the continuous solid lines in Figure S10-3 show the estimations of $Đ_{12,fl}$ using the method of Fuller, Schettler and Giddings (FSG),[106] developed for *ideal gas* mixtures. We note that for concentrations $c_t <$ 6 kmol m^{-3}, the MD simulated $Đ_{12,fl}$ values are in excellent agreement with the FSG estimations. For concentrations $c_t >$ 6 kmol m^{-3}, the $Đ_{12,fl}$ values reflect those in dense condensed fluids, for which some estimation procedures are also available in the literature.[107]

10.3 Relating $Đ_{12}$ in *micro*-porous materials to fluid phase $Đ_{12,fl}$

For micro-porous materials, the exchange coefficient $Đ_{12}$ cannot be directly identified with the corresponding fluid phase diffusivity $Đ_{12,fl}$ because the molecule-molecule interactions are also significantly influenced by molecule-wall interactions. This is underscored by MD data for $Đ_{12}$ for nine binary mixtures in a variety of micro-porous hosts; see Figure S10-4. For every guest/host combination, at any specific c_t, the $Đ_{12}$ is lower than the value of $Đ_{12,fl}$. The extent of lowering can be quantified by defining the fraction F

$$F \equiv Đ_{12} \big/ Đ_{12,fl} \tag{10-7}$$

Every guest/host combination can be characterized by a constant fraction F, that is determined by data fitting. For "open" structures, with large pore volumes, V_p, the values of F are closer to unity. For example, for CH_4/Ar diffusion in IRMOF-1, COF-102, COF-103, and COF-108, the values are F = 0.6, 0.65, 0.65, and 0.8, respectively, increasing with increasing void fractions, ϕ. Remarkably, for IRMOF-1, the fraction F is in the narrow range of 0.6 – 0.7 for every guest mixture investigated.

At the other end of the spectrum, materials with low pore volumes, the values of the fraction F lie significantly below unity. In MFI that has a set of intersecting channels, F lies in the range of 0.1 – 0.15 for all mixtures. For BEA, also with intersecting channels, but with a slightly higher void fraction, we obtain F = 0.2. For materials such as FAU, NaX, NaY, LTA, and MgMOF-74 with intermediate void fractions, the values of F fall in range 0.3 – 0.6.

Figure S10-5 presents a plot of F as a function of the pore volume V_p of different porous host materials for nine different binary mixtures. The correlation is not perfect, suggesting that other aspects such as channel dimensions, and pore connectivity are also determinants of the exchange coefficient $Đ_{12}$.

The similarity in the plots for unary (Figure S8-2) systems, and binary mixtures (Figure S10-5) is noteworthy.

10.4 Estimating $Đ_{12}$ from information on self-exchange coefficients $Đ_{ii}$

The Vignes interpolation formula (10-6), for binary *fluid* mixtures, can be extended to apply to micro-porous materials in the following manner

$$Đ_{12} = \left(Đ_{11}\right)^{x_1}\left(Đ_{22}\right)^{x_2} \tag{10-8}$$

where the $Đ_{ii}$ represent the self-exchange coefficients determined for unary systems, as reported in Figure S8-2.

Comparisons of the predictions of the interpolation formula (10-8) with MD simulations of $Đ_{12}$ for a wide variety of guest/host combinations are provided in Figure S10-6, Figure S10-7, Figure S10-8, Figure S10-9, Figure S10-10, Figure S10-11, and Figure S10-11. Equation (10-8) is seen to be of good accuracy for all guest/host combinations.

10.5 Estimating the degree of correlations for binary mixture diffusion

As noted in Figure S8-5, the degree of correlations, $\frac{Đ_i}{Đ_{ii}}$, for *unary* diffusion of various guest/host combinations is linearly dependent on fractional occupancy, θ, determined from Equation (6-4). Therefore for a binary 1-2 mixture, the degree of correlations, $\frac{Đ_1}{Đ_{12}}$ can be estimated from $\frac{Đ_1}{Đ_{11}}$ and $\frac{Đ_2}{Đ_{22}}$ by invoking the Vignes interpolation formula (10-8), as follows:

$$\frac{Đ_1}{Đ_{12}} = \left(\frac{Đ_1}{Đ_{11}}\right)^{x_1}\left(\frac{Đ_2}{Đ_{22}}\right)^{x_2}\left(\frac{Đ_1}{Đ_2}\right)^{x_2} \tag{10-9}$$

The validation of Equation (10-9) for various mixture/host combinations is included as the ninth item (i) in panel in the following set of Figures.

Figure S9-1: Ne(1)/Ar(2) mixtures in MFI zeolite

Figure S9-2: CH_4(1)/H_2(2) mixtures in MFI zeolite

Figure S9-3: H_2(1)/Ar(2) mixtures in MFI zeolite

Figure S9-4: CH_4(1)/Ar(2) mixtures in MFI zeolite

Figure S9-5: C_2H_6(1)/C_3H_8(2) mixtures in MFI zeolite

Figure S9-6: equimolar (q_1=q_2) binary CH_4(1)/C_2H_6(2) mixtures in MFI zeolite

Figure S9-7: 25/75 (q_1/q_2=25/75) binary CH_4(1)/C_2H_6(2) mixtures in MFI zeolite

Figure S9-8: 75/25 (q_1/q_2=75/25) binary CH_4(1)/C_2H_4(2) mixtures in MFI zeolite

Figure S9-9: CH_4(1)/C_3H_8(2) mixtures in MFI zeolite

Figure S9-10: CO_2(1)/N_2(2) mixtures in MFI zeolite

Figure S9-11: CO_2(1)/H_2(2) mixtures in MFI zeolite

Figure S9-12: CH_4(1)/CO_2(2) mixtures in MFI zeolite

Figure S9-13: CO_2(1)/Ne(2) mixtures in MFI zeolite

Figure S9-14: Ne(1)/Ar(2) mixtures in FAU all-silica zeolite

Figure S9-15: CO_2(1)/CH_4(2) mixtures in FAU all-silica zeolite

Figure S9-16: CO_2(1)/N_2(2) mixtures in FAU all-silica zeolite

Figure S9-17: CO_2(1)/Ar(2) mixtures in FAU all-silica zeolite

Figure S9-18: CO_2(1)/Ne(2) mixtures in FAU all-silica zeolite

Figure S9-19: CO_2(1)/H_2(2) mixtures in FAU all-silica zeolite

Figure S9-20: CH_4(1)/H_2(2) mixtures in FAU all-silica zeolite

Figure S9-21: CH_4(1)/Ar(2) mixtures in FAU all-silica zeolite

Figure S9-22: CH_4(1)/C_2H_6(2) mixtures in FAU all-silica zeolite

Figure S9-23: CH_4(1)/C_3H_8(2) mixtures in FAU all-silica zeolite

Figure S9-24: CH_4(1)/CO_2(2) mixtures in NaY zeolite (48 Al)

Figure S9-63: $CH_4(1)/nC_4H_{10}(2)$ mixtures in CuBTC

In the above set of Figures, the MD simulated data for $\frac{Đ_1}{Đ_{12}}$, indicated by the red circles, are to be compared with the estimations of Equation (10-9), indicated by the crosses. In these estimations: (a) the ratio of the M-S diffusivities $\left(\frac{Đ_1}{Đ_2}\right)$ is calculated on the basis of the backed-out M-S diffusivities for binary mixture diffusion, and (b) the $\left(\frac{Đ_1}{Đ_{11}}\right)$ and $\left(\frac{Đ_2}{Đ_{22}}\right)$ are determined from the corresponding *unary* diffusion data (on self, and M-S diffusivities) at the same occupancy θ as in the mixture.

These comparisons show that Equation (10-9) provides good estimates of $\frac{Đ_1}{Đ_{12}}$ in the various guest/host combinations.

10.6 List of Figures for Estimation of the Degree of Correlations for Mixture Diffusion

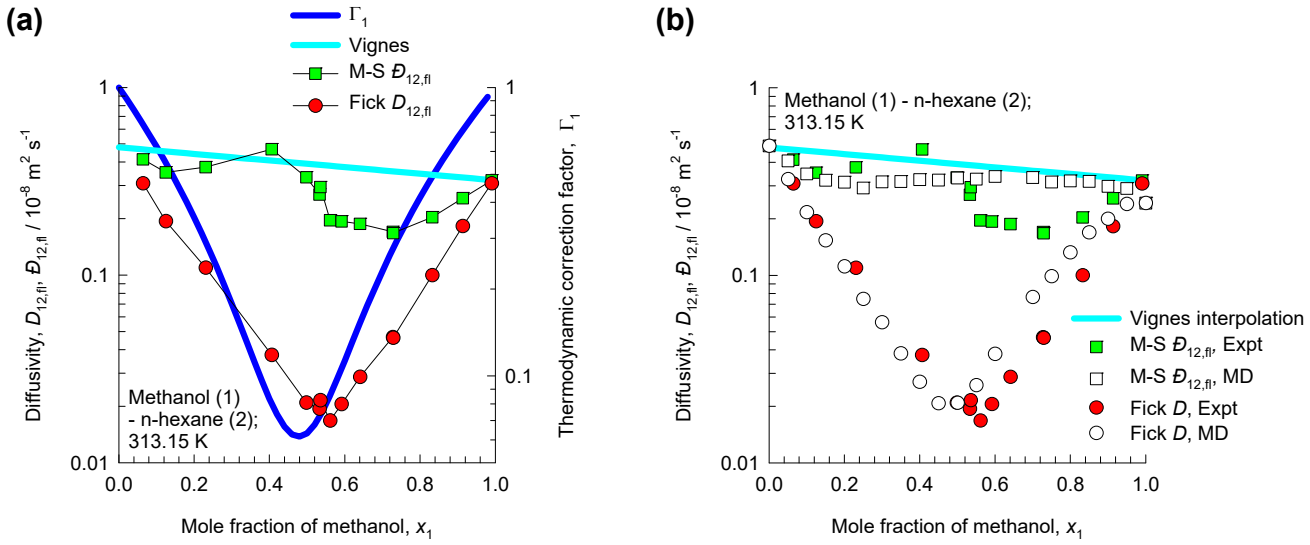

Figure S10-1. (a) Experimental data of Clark and Rowley [108] for the Fick diffusivities, $D_{12,fl}$, and Maxwell-Stefan diffusivities, $Đ_{12,fl}$,, for methanol – *n*-hexane mixtures at 313.15 K (b) Comparison of the experimental data of Clark and Rowley[108] with the MD simulations of Krishna and van Baten.[109] Also shown are the calculations using the Vignes interpolation formula (10-6).

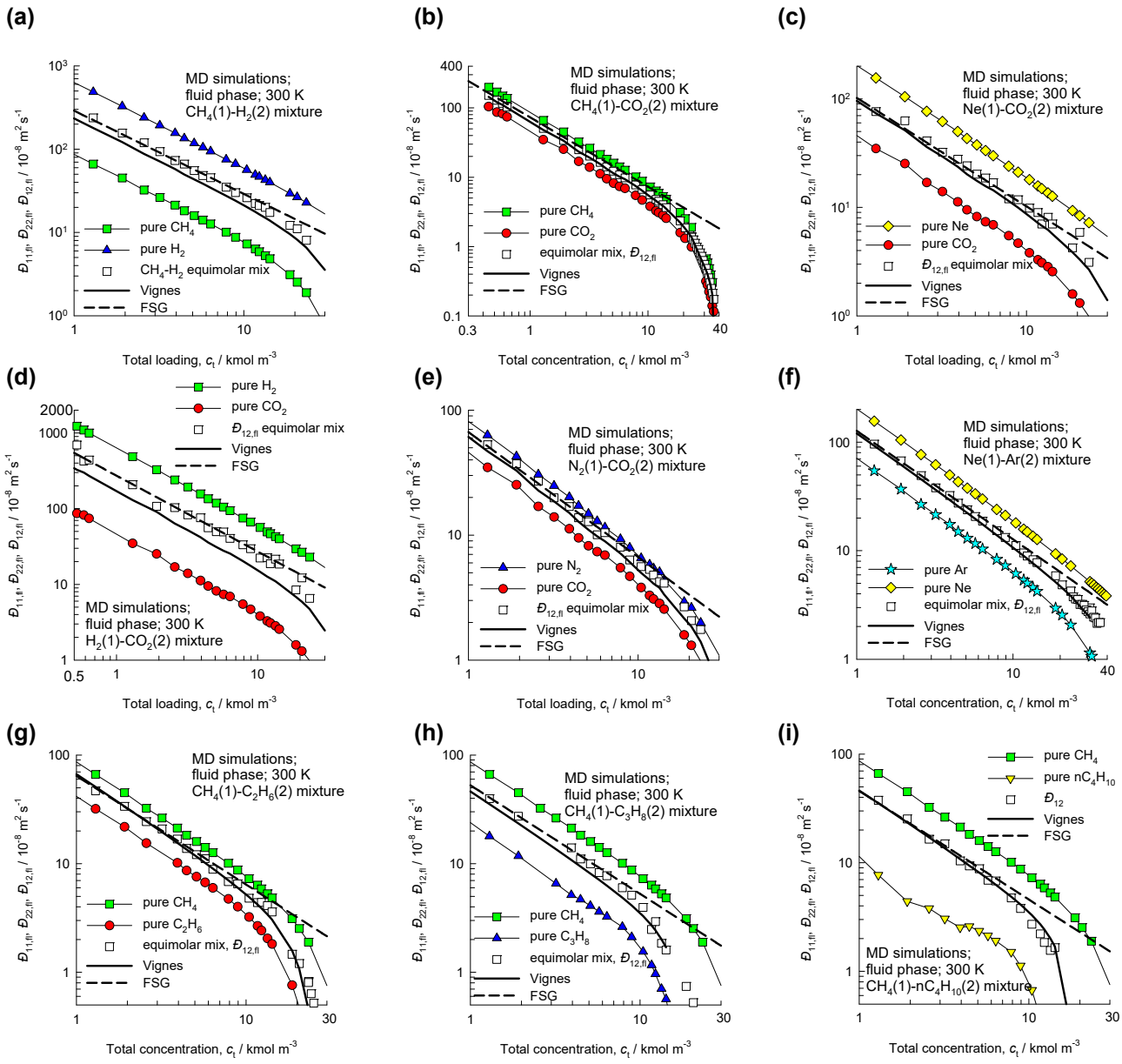

Figure S10-2. MD simulations of self-diffusivities, $Đ_{ii,fl}$, along with the $Đ_{12,fl}$ for diffusion in nine equimolar binary fluid mixtures as a function of the total fluids concentration, c_t. The calculations of $Đ_{12,fl}$ following the Vignes interpolation formula (10-6) are shown by the continuous solid lines. The calculation of $Đ_{12,fl}$ using correlation of Fuller, Schettler and Giddings (FSG),[106] developed for *binary gas* mixtures, is indicated by the dashed lines. The MD data are culled from our previous publications.[7, 10, 13, 14, 16, 62, 63, 77, 80-83]

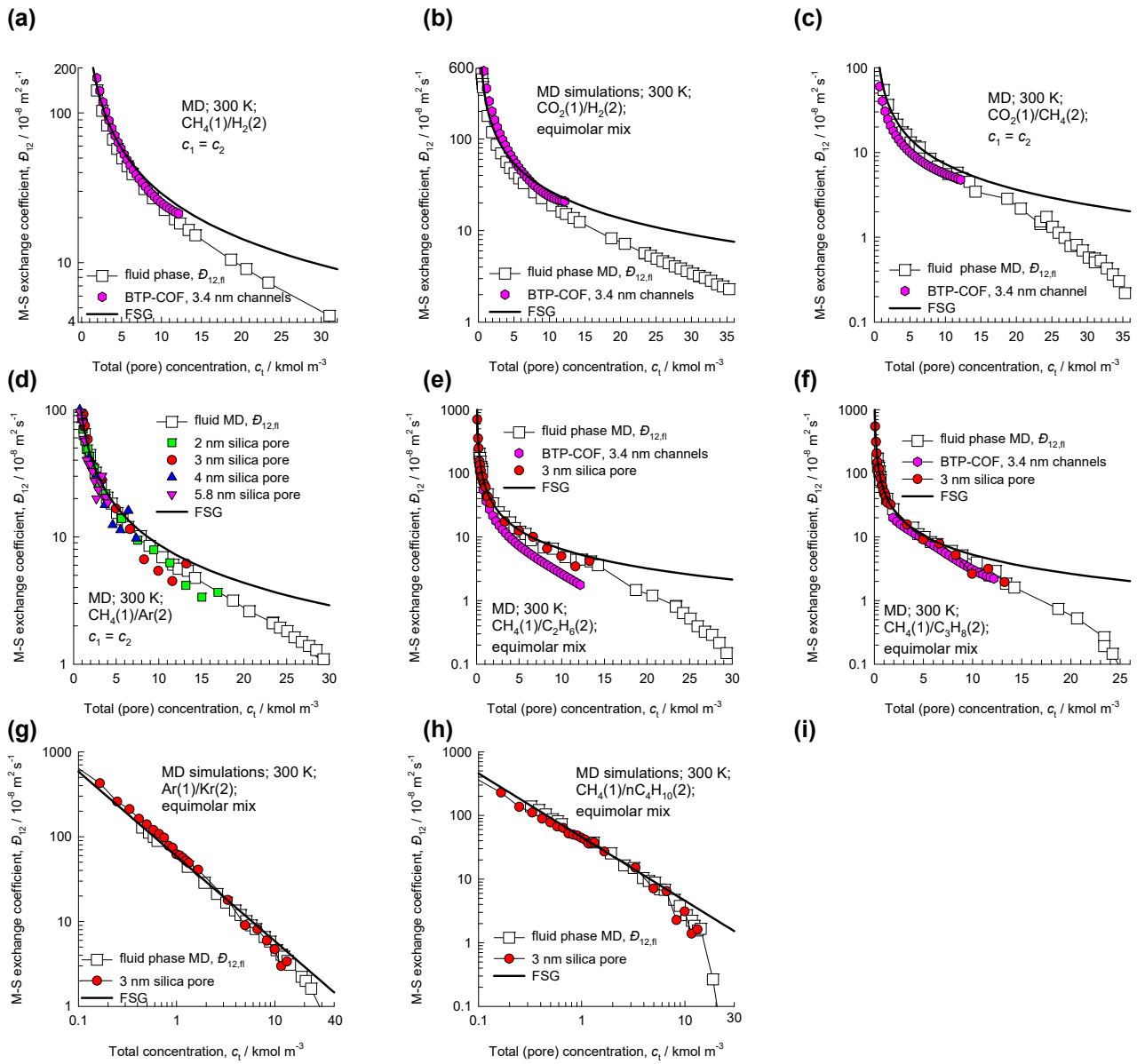

Figure S10-3. The MD simulations for fluid phase diffusivity $Đ_{12,fl}$ (square symbols) for equimolar ($c_1 = c_2$) binary (a) H_2/CH_4, (b) CO_2/H_2, (c) CH_4/CO_2, (d) CH_4/Ar, (e) CH_4/C_2H_6, (f) CH_4/C_3H_8, (g) Ar/Kr, and (h) CH_4/nC_4H_{10} mixtures as a function of the total fluid phase molar concentration c_t. The calculation of $Đ_{12,fl}$ using the FSG correlation,[106] is indicated by the continuous solid line. Also indicated are MD data for the exchange coefficients $Đ_{12}$ in cylindrical silica mesopores (of diameters 3 nm, 4 nm, and 5.8 nm), and BTP-COF (with 3.4 nm size 1D hexagonal-shaped channels).

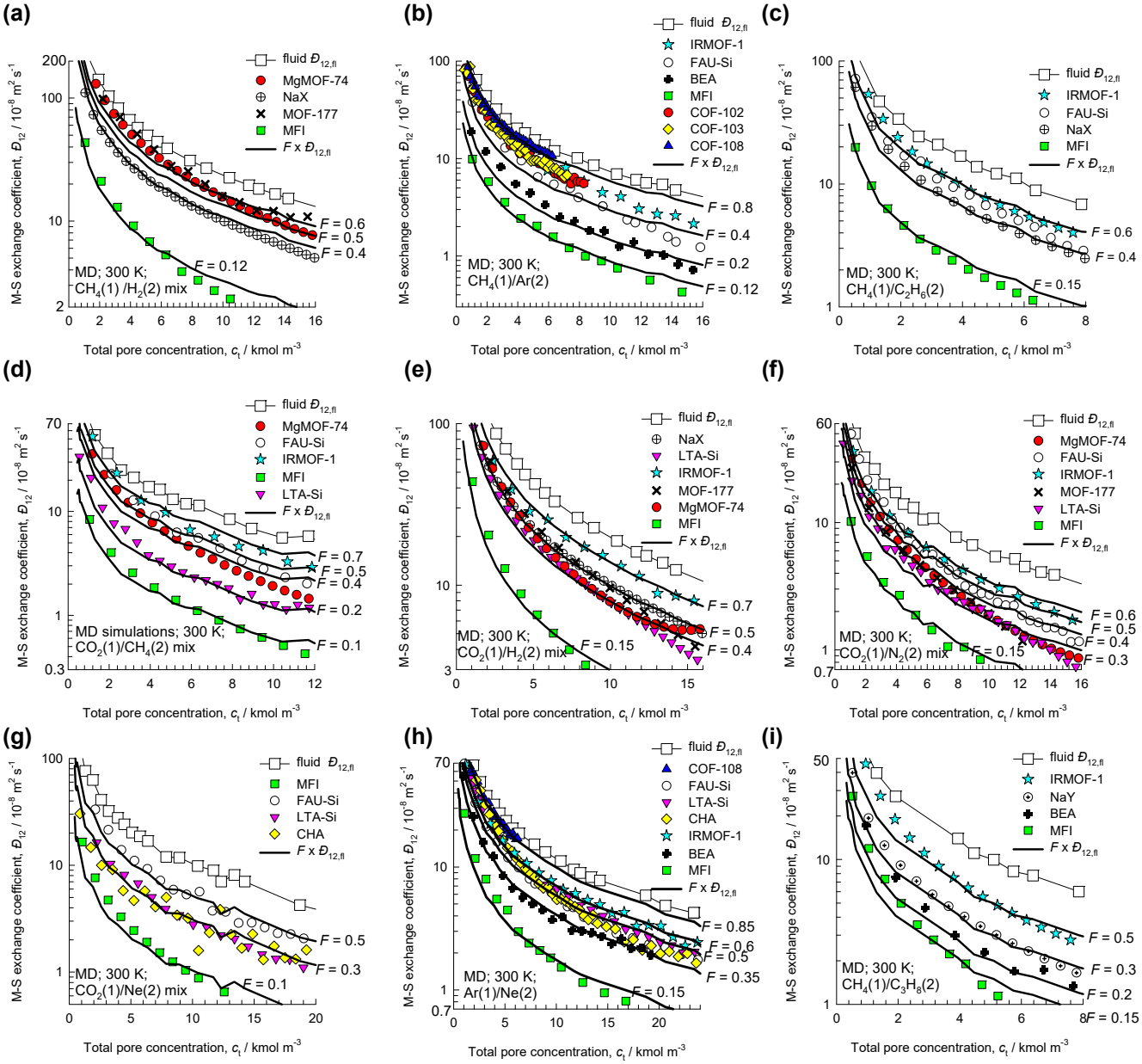

Figure S10-4. The M-S binary exchange coefficients $Đ_{12}$, for diffusion of equimolar ($c_1 = c_2$) binary (a) H_2/CH_4, (b) CH_4/Ar, (c) CH_4/C_2H_6, (d) CH_4/CO_2, (e) H_2/CO_2, (f) CO_2/N_2, (g) CO_2/Ne, (h) Ar/Ne, and (i) CH_4/C_3H_8 mixtures at 300 K in a variety of host materials as a function of the total pore concentration, c_t. The $Đ_{12,fl}$ for binary *fluid phase* mixture diffusion, obtained from independent MD simulations, are also presented in square symbols, along with continuous solid lines that represent the fraction F times $Đ_{12,fl}$.

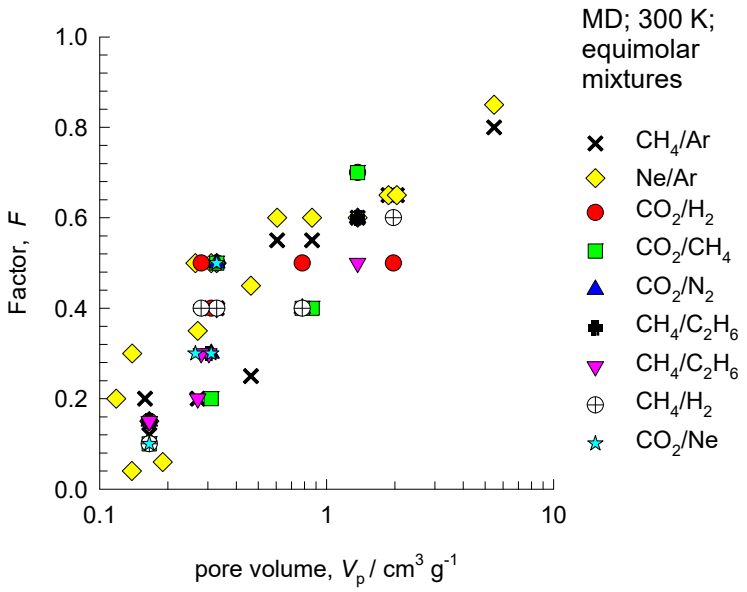

Figure S10-5. Fraction F determined from MD simulations of the exchange coefficient for binary mixtures, expressed as a function of the pore volume of the micro-porous host structures, V_p.

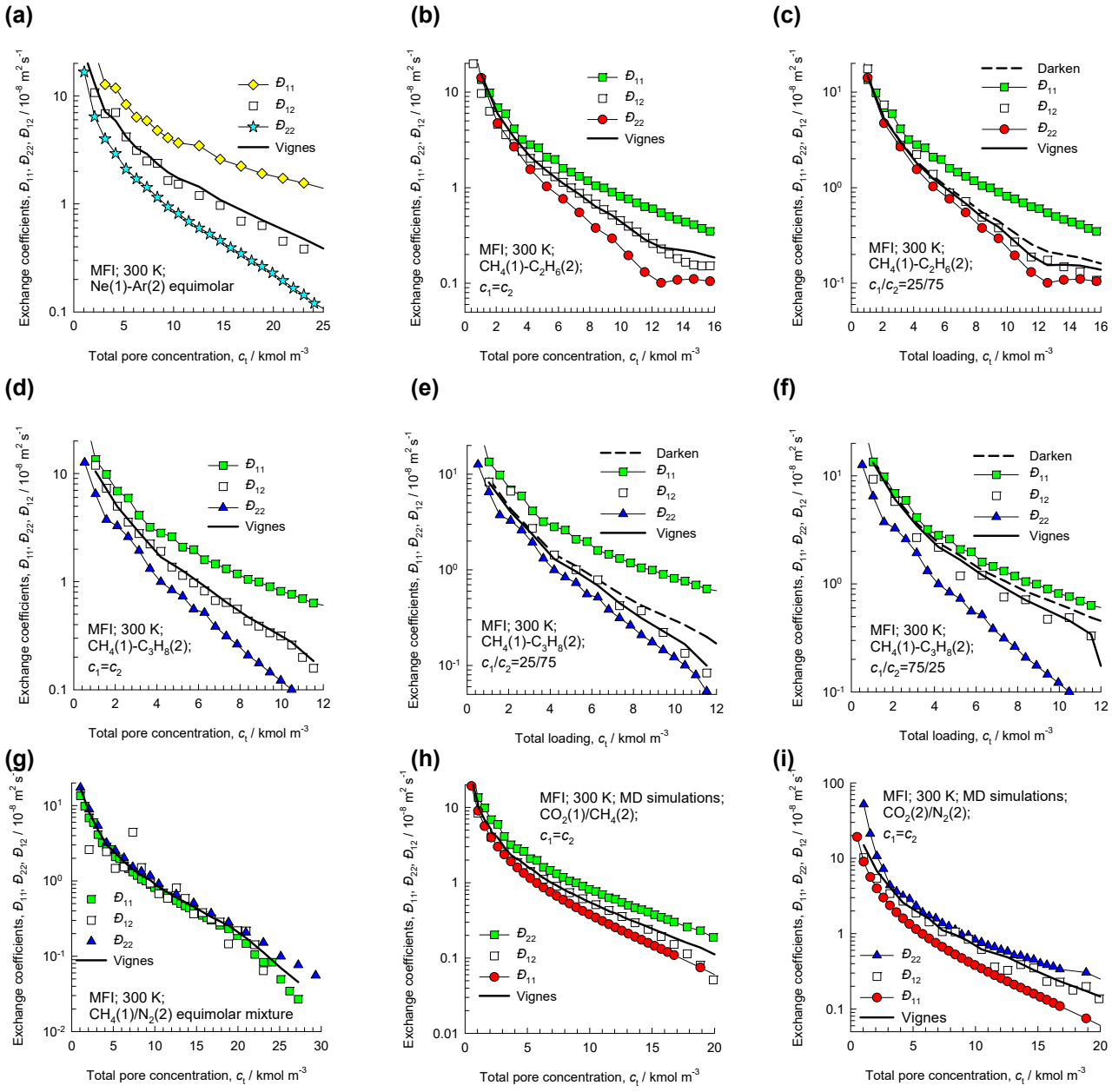

Figure S10-6. Test of the Vignes interpolation formula interpolation formula (10-8) for diffusion of nine different binary mixtures in MFI zeolite at 300 K. The MD data are culled from our previous publications.[7, 10, 13, 14, 16, 62, 63, 77, 80-83]

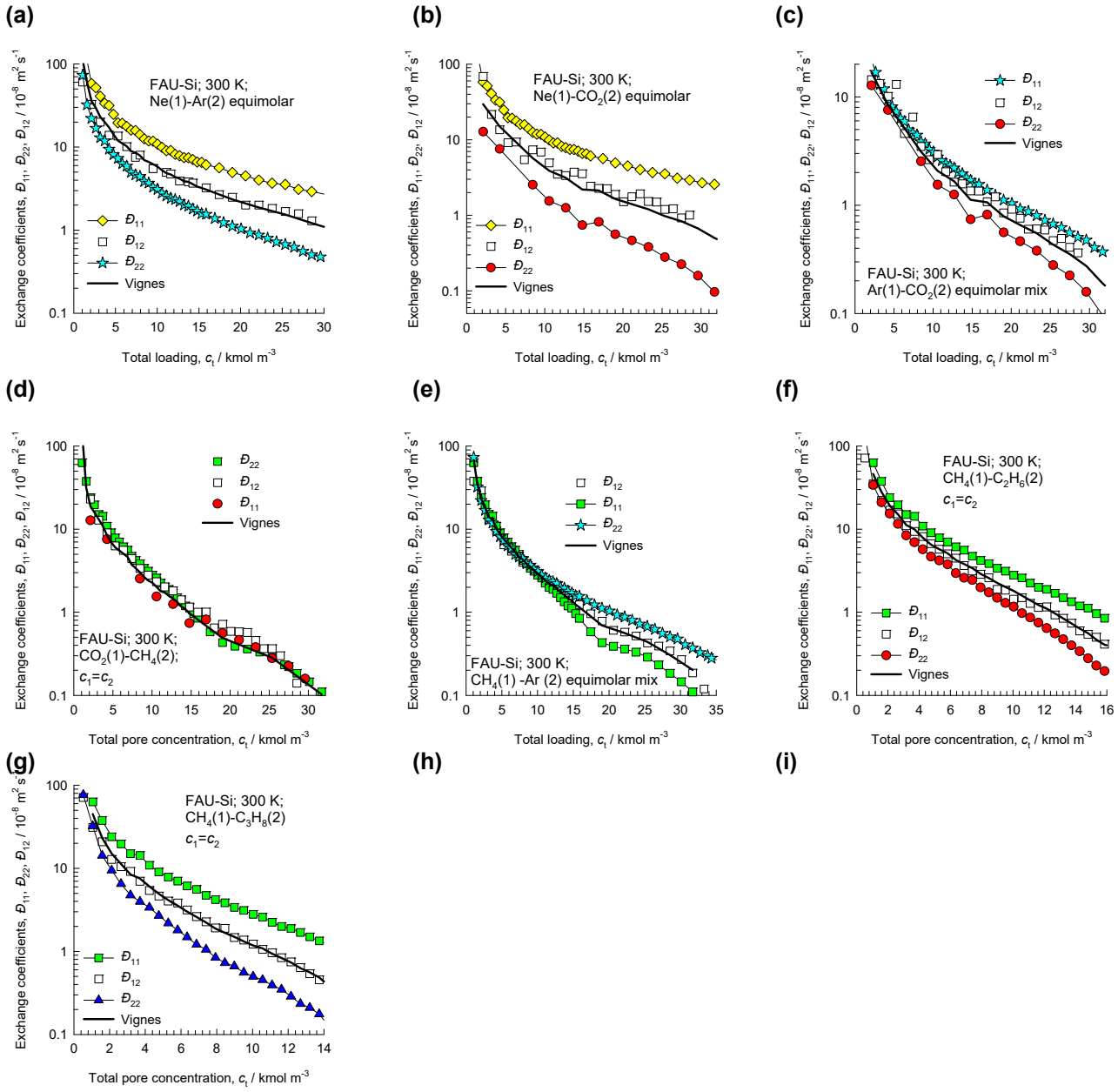

Figure S10-7. Test of the Vignes interpolation formula interpolation formula (10-8) for diffusion of seven different binary mixtures in FAU all-silica zeolite at 300 K. The MD data are culled from our previous publications.[7, 10, 13, 14, 16, 62, 63, 77, 80-83]

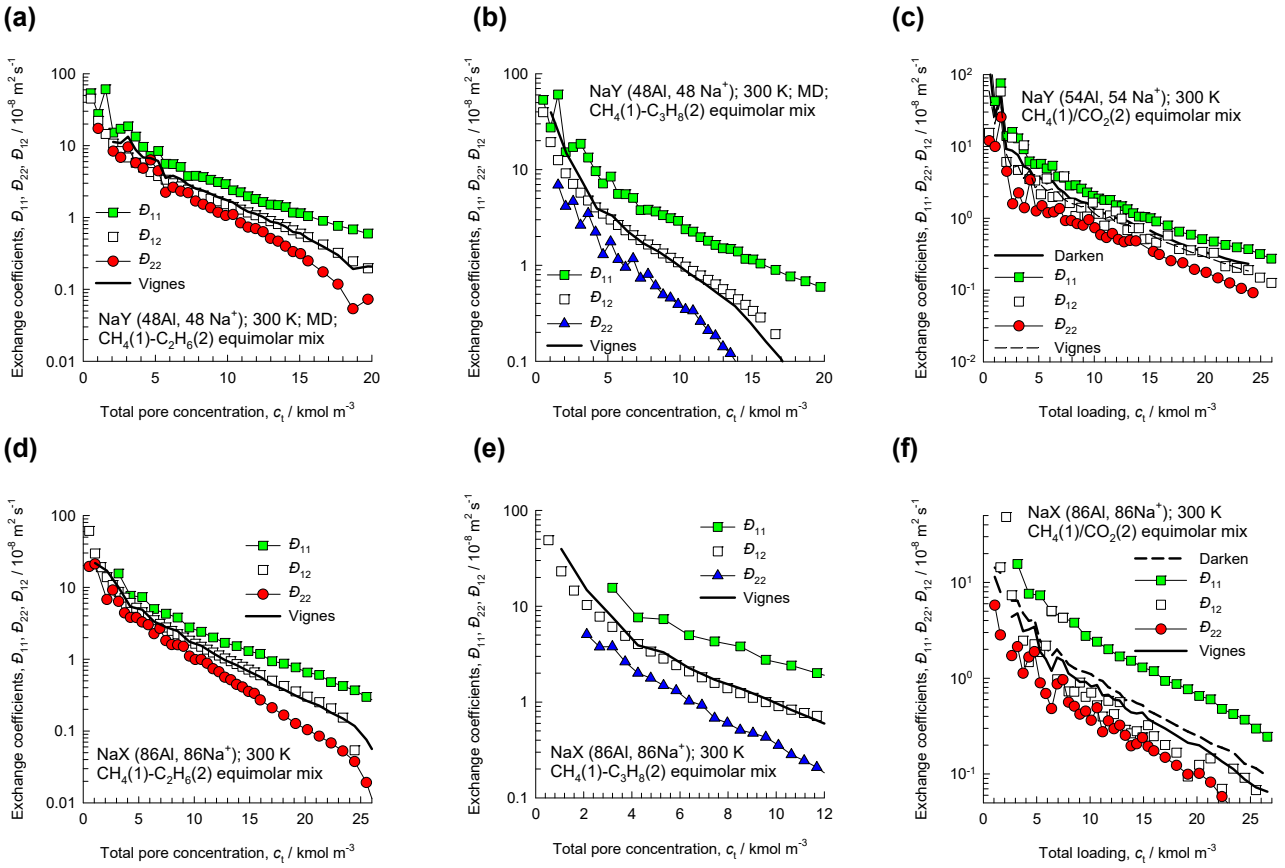

Figure S10-8. Test of the Vignes interpolation formula interpolation formula (10-8) for diffusion of three different binary mixtures in NaY, and NaX zeolites at 300 K. The MD data are culled from our previous publications.[7, 10, 13, 14, 16, 62, 63, 77, 80-83]

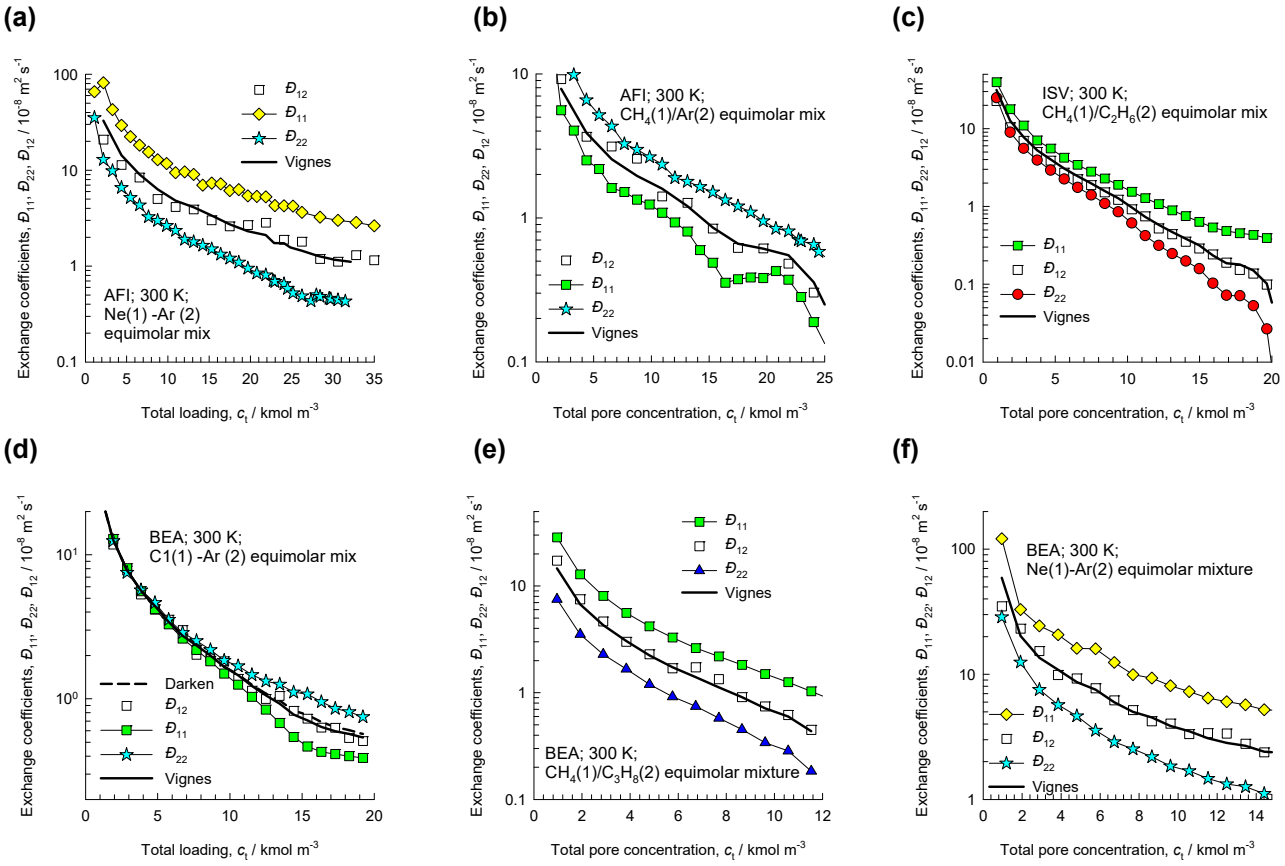

Figure S10-9. Test of the Vignes interpolation formula interpolation formula (10-8) for diffusion of a variety of equimolar binary mixtures in AFI, ISV, and BEA zeolites at 300 K. The MD data are culled from our previous publications.[7, 10, 13, 14, 16, 62, 63, 77, 80-83]

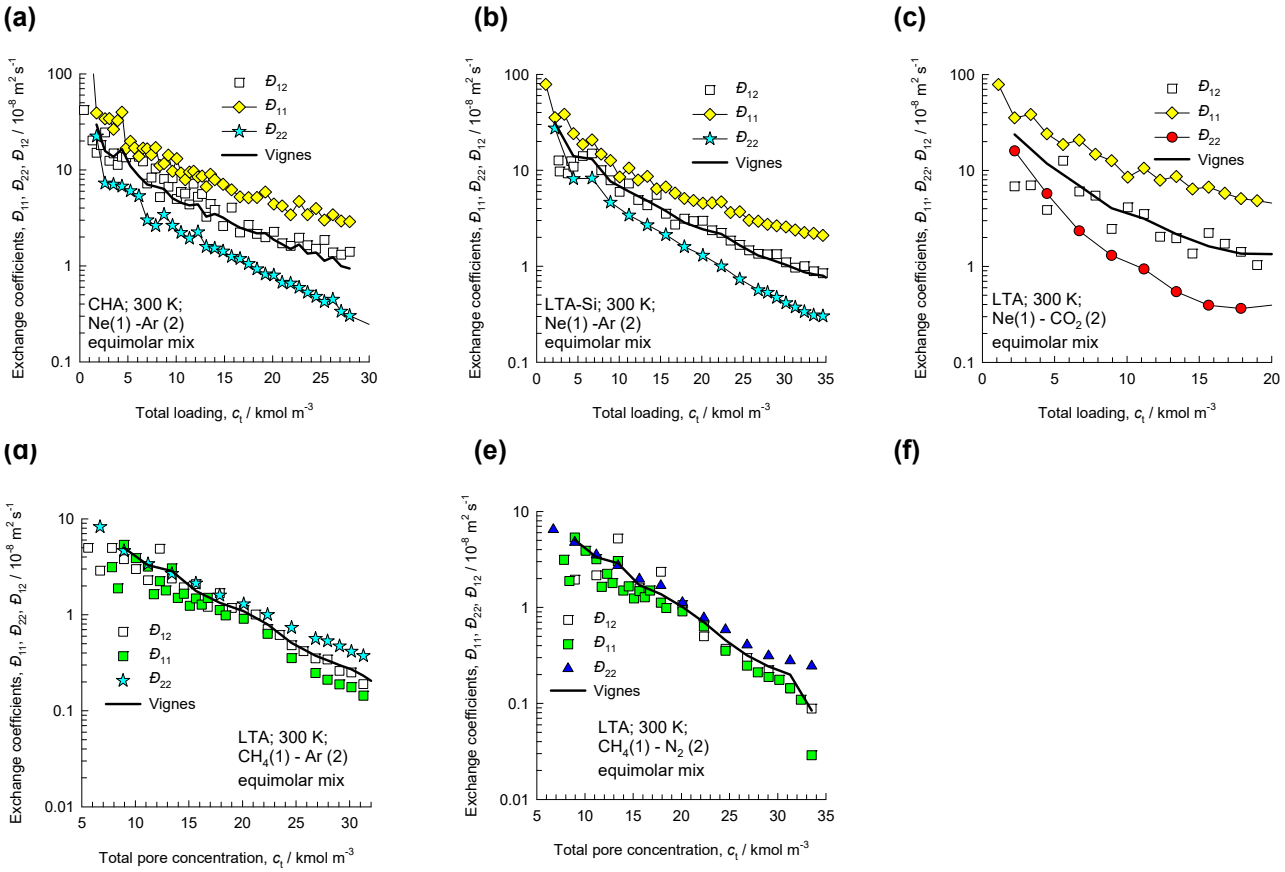

Figure S10-10. Test of the Vignes interpolation formula interpolation formula (10-8) for diffusion of a variety of equimolar binary mixtures in CHA and LTA all-silica zeolites at 300 K. The MD data are culled from our previous publications.[7, 10, 13, 14, 16, 62, 63, 77, 80-83]

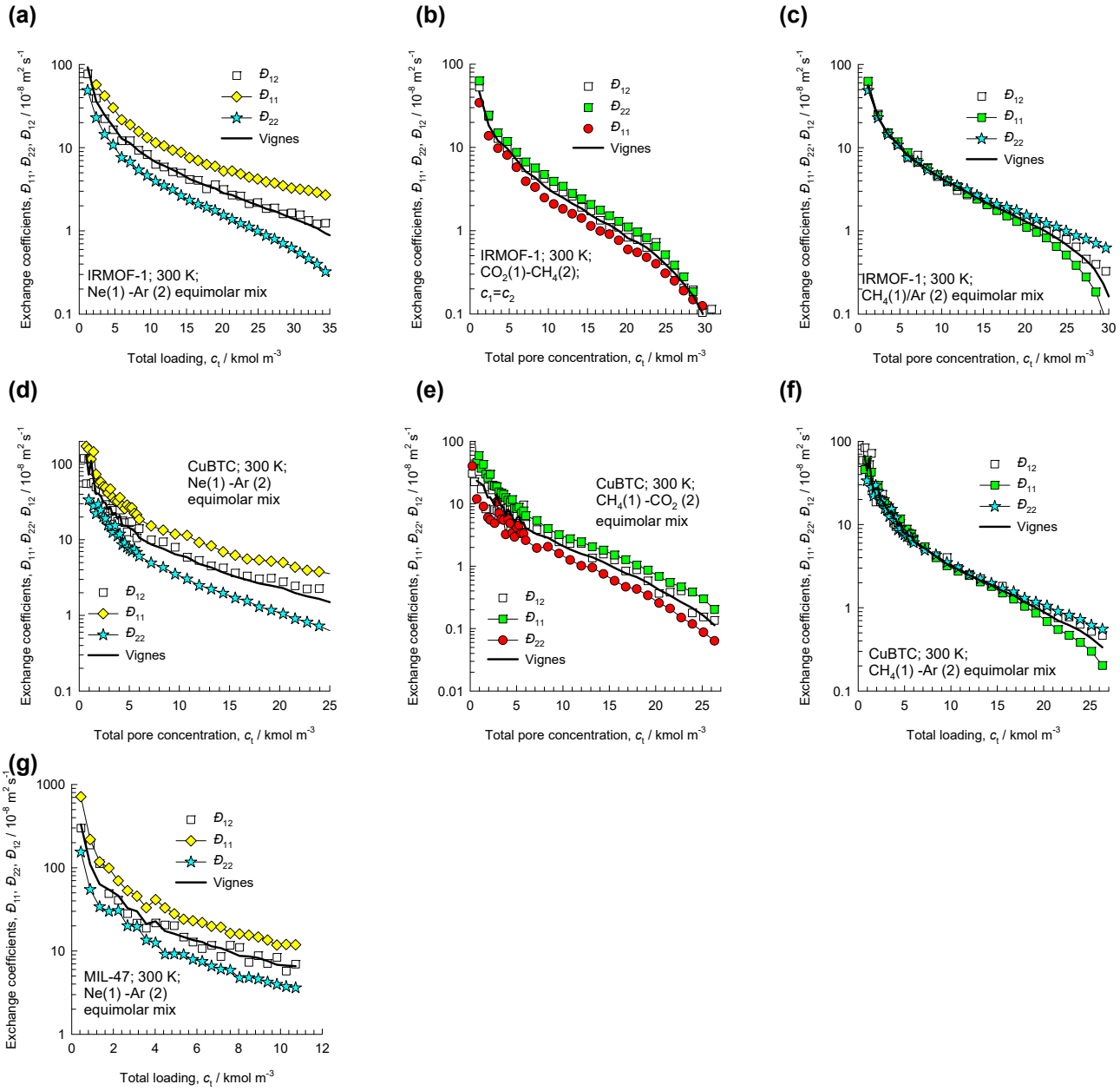

Figure S10-11. Test of the Vignes interpolation formula interpolation formula (10-8) for diffusion of a variety of equimolar binary mixtures in IRMOF-1, CuBTC, and MIL-47 at 300 K. The MD data are culled from our previous publications.[7, 10, 13, 14, 16, 62, 63, 77, 80-83]

11 Nomenclature

Latin alphabet

A	surface area per kg of framework, $m^2\ kg^{-1}$
b_A	dual-Langmuir-Freundlich constant for species i at adsorption site A, $Pa^{-\nu_i}$
b_B	dual-Langmuir-Freundlich constant for species i at adsorption site B, $Pa^{-\nu_i}$
$[B]$	M-S matrix, $m^{-2}\ s$
c_i	pore concentration of species i, mol m^{-3}
c_t	total pore concentration in mixture, mol m^{-3}
d_p	pore diameter, m
$Đ_i$	Maxwell-Stefan diffusivity for molecule-wall interaction, $m^2\ s^{-1}$
$Đ_i(0)$	M-S diffusivity at zero-loading, $m^2\ s^{-1}$
$Đ_{ij}$	M-S exchange coefficient, $m^2\ s^{-1}$
$Đ_{ii,fl}$	self-diffusivity of species i in fluid phase, $m^2\ s^{-1}$
$Đ_{12}$	M-S exchange coefficient for binary mixture, $m^2\ s^{-1}$
$Đ_{12,fl}$	M-S diffusivity in binary fluid mixture, $m^2\ s^{-1}$
$D_{i,self}$	self-diffusivity of species i, $m^2\ s^{-1}$
f_i	partial fugacity of species i, Pa
f_t	total fugacity of bulk fluid mixture, Pa
F	factor defined by equation (8-2), or (10-7), dimensionless
$[I]$	Identity matrix with elements δ_{ij}, dimensionless
n	number of species in the mixture, dimensionless
N_i	molar flux of species i with respect to framework, mol $m^{-2}\ s^{-1}$

Nomenclature

p_i	partial pressure of species *i* in mixture, Pa
p_t	total system pressure, Pa
P_i^0	sorption pressure, Pa
q_i	component molar loading of species *i*, mol kg^{-1}
$q_{i,sat}$	molar loading of species *i* at saturation, mol kg^{-1}
q_t	total molar loading in mixture, mol kg^{-1}
R	gas constant, 8.314 J mol^{-1} K^{-1}
T	absolute temperature, K
u_i	velocity of motion of adsorbate species *i* with respect to the framework material, m s^{-1}
V_p	accessible pore volume, m^3 kg^{-1}
x_i	mole fraction of species *i* in adsorbed phase, dimensionless
z	distance coordinate, m

Greek alphabet

Γ_{ij}	thermodynamic factors, dimensionless
$[\Gamma]$	matrix of thermodynamic factors, dimensionless
δ_{ij}	Kronecker delta, dimensionless
ε	fractional pore volume of particle, dimensionless
$[\Lambda]$	matrix of Maxwell-Stefan diffusivities, m^2 s^{-1}
μ_i	molar chemical potential of component *i*, J mol^{-1}
π	spreading pressure, N m^{-1}
θ	fractional occupancy, dimensionless
Θ_i	loading of species *i*, molecules per unit cell
$\Theta_{i,sat}$	saturation loading of species *i*, molecules per unit cell
Θ_t	total mixture loading, molecules per unit cage, or per unit cell

Nomenclature

ν	exponent in dual-Langmuir-Freundlich isotherm, dimensionless
ρ	framework density, kg m^{-3}

Subscripts

1	referring to component 1
2	referring to component 2
i	referring to component *i*
t	referring to total mixture
sat	referring to saturation conditions
V	vacancy

12 References

(1) Kärger, J.; Ruthven, D. M.; Theodorou, D. N. *Diffusion in Nanoporous Materials*. Wiley - VCH: Weinheim, 2012.

(2) Krishna, R.; van Baten, J. M. In Silico Screening of Zeolite Membranes for CO_2 Capture. *J. Membr. Sci.* **2010**, *360*, 323-333.

(3) Krishna, R.; van Baten, J. M. In silico screening of metal-organic frameworks in separation applications. *Phys. Chem. Chem. Phys.* **2011**, *13*, 10593-10616.

(4) Thomas, A. Functional Materials: From Hard to Soft Porous Frameworks. *Angew. Chem. Int. Ed.* **2010**, *49*, 8328 – 8344.

(5) Baerlocher, C.; Meier, W. M.; Olson, D. H. *Atlas of Zeolite Framework Types*. 5th Edition, Elsevier: Amsterdam, 2002.

(6) Baerlocher, C.; McCusker, L. B. Database of Zeolite Structures. http://www.iza-structure.org/databases/, International Zeolite Association, 10 January 2002.

(7) Krishna, R. Diffusion in Porous Crystalline Materials. *Chem. Soc. Rev.* **2012**, *41*, 3099-3118.

(8) Krishna, R. The Maxwell-Stefan Description of Mixture Diffusion in Nanoporous Crystalline Materials. *Microporous Mesoporous Mater.* **2014**, *185*, 30-50.

(9) Krishna, R. Describing the Diffusion of Guest Molecules inside Porous Structures. *J. Phys. Chem. C* **2009**, *113*, 19756-19781.

(10) Krishna, R.; van Baten, J. M. Investigating the Relative Influences of Molecular Dimensions and Binding Energies on Diffusivities of Guest Species Inside Nanoporous Crystalline Materials *J. Phys. Chem. C* **2012**, *116*, 23556-23568.

(11) Krishna, R.; van Baten, J. M. Investigating the Influence of Diffusional Coupling on Mixture Permeation across Porous Membranes *J. Membr. Sci.* **2013**, *430*, 113-128.

(12) Krishna, R.; van Baten, J. M. Influence of Adsorption Thermodynamics on Guest Diffusivities in Nanoporous Crystalline Materials. *Phys. Chem. Chem. Phys.* **2013**, *15*, 7994-8016.

(13) Krishna, R.; van Baten, J. M. Insights into diffusion of gases in zeolites gained from molecular dynamics simulations. *Microporous Mesoporous Mater.* **2008**, *109*, 91-108.

(14) Krishna, R.; van Baten, J. M. Diffusion of alkane mixtures in MFI zeolite. *Microporous Mesoporous Mater.* **2008**, *107*, 296-298.

(15) Krishna, R.; van Baten, J. M. Describing Mixture Diffusion in Microporous Materials under Conditions of Pore Saturation. *J. Phys. Chem. C* **2010**, *114*, 11557-11563.

(16) Krishna, R.; van Baten, J. M. Diffusion of alkane mixtures in zeolites. Validating the Maxwell-Stefan formulation using MD simulations. *J. Phys. Chem. B* **2005**, *109*, 6386-6396.

(17) Ryckaert, J. P.; Bellemans, A. Molecular dynamics of liquid alkanes. *Faraday Discuss. Chem. Soc.* **1978**, *66*, 95-106.

(18) Dubbeldam, D.; Calero, S.; Vlugt, T. J. H.; Krishna, R.; Maesen, T. L. M.; Smit, B. United Atom Forcefield for Alkanes in Nanoporous Materials. *J. Phys. Chem. B* **2004**, *108*, 12301-12313.

(19) Skoulidas, A. I.; Sholl, D. S. Transport diffusivities of CH_4, CF_4, He, Ne, Ar, Xe, and SF_6 in silicalite from atomistic simulations. *J. Phys. Chem. B* **2002**, *106*, 5058-5067.

(20) Talu, O.; Myers, A. L. Reference Potentials for Adsorption of Helium, Argon, Methane and Krypton in High-Silica Zeolites. *Colloids Surf., A* **2001**, *187-188*, 83-93.

(21) Makrodimitris, K.; Papadopoulos, G. K.; Theodorou, D. N. Prediction of permeation properties of CO_2 and N_2 through silicalite via molecular simulations. *J. Phys. Chem. B* **2001**, *105*, 777-788.

(22) García-Pérez, E.; Parra, J. B.; Ania, C. O.; García-Sánchez, A.; Van Baten, J. M.; Krishna, R.; Dubbeldam, D.; Calero, S. A computational study of CO_2, N_2 and CH_4 adsorption in zeolites. *Adsorption* **2007**, *13*, 469-476.

(23) García-Sánchez, A.; Ania, C. O.; Parra, J. B.; Dubbeldam, D.; Vlugt, T. J. H.; Krishna, R.; Calero, S. Development of a Transferable Force Field for Carbon Dioxide Adsorption in Zeolites. *J. Phys. Chem. C* **2009**, *113*, 8814-8820.

(24) Dubbeldam, D.; Walton, K. S.; Ellis, D. E.; Snurr, R. Q. Exceptional Negative Thermal Expansion in Isoreticular Metal–Organic Frameworks. *Angew. Chem. Int. Ed.* **2007**, *46*, 4496-4499.

(25) Dubbeldam, D.; Frost, H.; Walton, K. S.; Snurr, R. Q. Molecular simulation of adsorption sites of light gases in the metal-organic framework IRMOF-1. *Fluid Phase Equilib.* **2007**, *261*, 152-161.

(26) Chui, S. S. Y.; Lo, S. M. F.; Charmant, J. P. H.; Orpen, A. G.; Williams, I. D. A Chemically Functionalizable Nanoporous Material $[Cu_3(TMA)_2(H2O)_3]_n$. *Science* **1999**, *283*, 1148-1150.

(27) Yang, Q.; Zhong, C. Electrostatic-Field-Induced Enhancement of Gas Mixture Separation in Metal-Organic Frameworks: A Computational Study. *ChemPhysChem* **2006**, *7*, 1417-1421.

(28) Bárcia, P. S.; Zapata, F.; Silva, J. A. C.; Rodrigues, A. E.; Chen, B. Kinetic Separation of Hexane Isomers by Fixed-Bed Adsorption with a Microporous Metal-Organic Framework. *J. Phys. Chem. B* **2008**, *111*, 6101-6103.

(29) Lee, J. Y.; Olson, D. H.; Pan, L.; Emge, T. J.; Li, J. Microporous Metal–Organic Frameworks with High Gas Sorption and Separation Capacity. *Adv. Funct. Mater.* **2007**, *17*, 1255-1262.

(30) Alaerts, L.; Kirschhock, C. E. A.; Maes, M.; van der Veen, M.; Finsy, V.; Depla, A.; Martens, J. A.; Baron, G. V.; Jacobs, P. A.; Denayer, J. F. M.; De Vos, D. Selective Adsorption and Separation of Xylene Isomers and Ethylbenzene with the Microporous Vanadium(IV) Terephthalate MIL-47. *Angew. Chem. Int. Ed.* **2007**, *46*, 4293-4297.

(31) Finsy, V.; Verelst, H.; Alaerts, L.; De Vos, D.; Jacobs, P. A.; Baron, G. V.; Denayer, J. F. M. Pore-Filling-Dependent Selectivity Effects in the Vapor-Phase Separation of Xylene Isomers on the Metal-Organic Framework MIL-47. *J. Am. Chem. Soc.* **2008**, *130*, 7110-7118.

(32) Barthelet, K.; Marrot, J.; Riou, D.; Férey, G. A Breathing Hybrid Organic - Inorganic Solid with Very Large Pores and High Magnetic Characteristics. *Angew. Chem. Int. Ed.* **2007**, *41*, 281-284.

(33) Coombes, D. S.; Corà, F.; Mellot-Draznieks, C.; Bell, R. G. Sorption-Induced Breathing in the Flexible Metal Organic Framework CrMIL-53: Force-Field Simulations and Electronic Structure Analysis. *J. Phys. Chem. C* **2009**, *113*, 544-552.

(34) Banerjee, R.; Phan, A.; Wang, B.; Knobler, C.; Furukawa, H.; O'Keeffe, M.; Yaghi, O. M. High-Throughput Synthesis of Zeolitic Imidazolate Frameworks and Application to CO_2 Capture. *Science* **2008**, *319*, 939-943.

(35) Britt, D.; Furukawa, H.; Wang, B.; Glover, T. G.; Yaghi, O. M. Highly efficient separation of carbon dioxide by a metal-organic framework replete with open metal sites. *Proc. Natl. Acad. Sci. U.S.A.* **2009**, *106*, 20637-20640.

(36) Rosi, N. L.; Kim, J.; Eddaoudi, M.; Chen, B.; O'Keeffe, M.; Yaghi, O. M. Rod Packings and Metal-Organic Frameworks Constructed from Rod-Shaped Secondary Building Units. *J. Am. Chem. Soc.* **2005**, *127*, 1504-1518.

(37) Dietzel, P. D. C.; Panella, B.; Hirscher, M.; Blom, R.; Fjellvåg, H. Hydrogen adsorption in a nickel based coordination polymer with open metal sites in the cylindrical cavities of the desolvated framework. *Chem. Commun.* **2006**, 959-961.

(38) Dietzel, P. D. C.; Besikiotis, V.; Blom, R. Application of metal–organic frameworks with coordinatively unsaturated metal sites in storage and separation of methane and carbon dioxide. *J. Mater. Chem.* **2009**, *19*, 7362-7370.

(39) Caskey, S. R.; Wong-Foy, A. G.; Matzger, A. J. Dramatic Tuning of Carbon Dioxide Uptake via Metal Substitution in a Coordination Polymer with Cylindrical Pores. *J. Am. Chem. Soc.* **2008**, *130*, 10870-10871.

(40) Yazaydın, A. Ö.; Snurr, R. Q.; Park, T. H.; Koh, K.; Liu, J.; LeVan, M. D.; Benin, A. I.; Jakubczak, P.; Lanuza, M.; Galloway, D. B.; Low, J. J.; Willis, R. R. Screening of Metal-Organic Frameworks for Carbon Dioxide Capture from Flue Gas using a Combined Experimental and Modeling Approach. *J. Am. Chem. Soc.* **2009**, *131*, 18198-18199.

(41) Bloch, E. D.; Murray, L.; Queen, W. L.; Chavan, S. M.; Maximoff, S. N.; Bigi, J. P.; Krishna, R.; Peterson, V. K.; Grandjean, F.; Long, G. J.; Smit, B.; Bordiga, S.; Brown, C. M.; Long, J. R. Selective Binding of O_2 over N_2 in a Redox-Active Metal-Organic Framework with Open Iron(II) Coordination Sites. *J. Am. Chem. Soc.* **2011**, *133*, 14814-14822.

(42) Chae, H. K.; Siberio-Pérez, D. Y.; Kim, J.; Go, Y. B.; Eddaoudi, M.; Matzger, A. J.; O'Keeffe, M.; Yaghi, O. M. A route to high surface area, porosity and inclusion of large molecules in crystals. *Nature* **2004**, *427*, 523-527.

(43) Rappé, A. K.; Casewit, C. J.; Colwel, K. S.; Goddard, W. A.; Skiff, W. M. UFF, A Full Periodic Table Force Field for Molecular Mechanics and Molecular Dynamics Simulations. *J. Am. Chem. Soc.* **1992**, *114*, 10024-10035.

(44) Mayo, S. L.; Olafson, B. D.; Goddard, W. A. DREIDING: A Generic Force Field for Molecular Simulations. *J. Phys. Chem.* **1990**, *94*, 8897-8909.

(45) Martín-Calvo, A.; García-Pérez, E.; Calero, S. Molecular simulations for adsorption and separation of natural gas in IRMOF-1 and Cu-BTC metal-organic frameworks. *Phys. Chem. Chem. Phys.* **2008**, *10*, 7085-7091.

(46) Walton, K. S.; Millward, A. R.; Dubbeldam, D.; Frost, H.; Low, J. J.; Yaghi, O. M.; Snurr, R. Q. Understanding Inflections and Steps in Carbon Dioxide Adsorption Isotherms in Metal-Organic Frameworks. *J. Am. Chem. Soc.* **2008**, *130*, 406-407.

(47) Rosenbach, N.; Jobic, H.; Ghoufi, A.; Salles, F.; Maurin, G.; Bourrelly, S.; Llewellyn, P. L.; Devic, T.; Serre, C.; Férey, G. Quasi-Elastic Neutron Scattering and Molecular Dynamics Study of Methane Diffusion in Metal Organic Frameworks MIL-47(V) and MIL-53(Cr). *Angew. Chem. Int. Ed.* **2008**, *47*, 6611-6615.

(48) Salles, F.; Ghoufi, A.; Maurin, G.; Bell, R. G.; Mellot-Draznieks, C.; Férey, G. Molecular Dynamics Simulations of Breathing MOFs: Structural Transformations of MIL-53(Cr) upon Thermal Activation and CO2 Adsorption. *Angew. Chem. Int. Ed.* **2008**, *47*, 8487-8491.

(49) Yang, Q.; Zhong, C. Understanding Hydrogen Adsorption in Metal-Organic Frameworks with Open Metal Sites: A Computational Study. *J. Phys. Chem. B* **2006**, *110*, 655-658.

(50) Jorgensen, W. L.; Maxwell, D. S.; Tirado-Rives, J. Development and Testing of the OPLS All-Atom Force Field on Conformational Energetics and Properties of Organic Liquids. *J. Am. Chem. Soc.* **1996**, *118*, 11225-11236.

(51) Zhou, M.; Wang, Q.; Zhang, L.; Liu, Y. C.; Kang, Y. Adsorption Sites of Hydrogen in Zeolitic Imidazolate Frameworks. *J. Phys. Chem. B* **2009**, *113*, 11049-11053.

(52) Xu, Q.; Zhong, C. A General Approach for Estimating Framework Charges in Metal-Organic Frameworks. *J. Phys. Chem. C* **2010**, *114*, 5035-5042.

(53) Myers, A. L.; Monson, P. A. Adsorption in Porous Materials at High Pressure: Theory and Experiment. *Langmuir* **2002**, *18*, 10261-10273.

(54) Babarao, R.; Hu, Z.; Jiang, J.; Chempath, S.; Sandler, S. I. Storage and separation of CO_2 and CH_4 in silicalite, C_{168} schwarzite, and IRMOF-1: A comparative study from Monte Carlo simulation. *Langmuir* **2007**, *23*, 659-666.

(55) Babarao, R.; Jiang, J. Exceptionally high CO_2 storage in covalent-organic frameworks: Atomistic simulation study. *Energy Environ. Sci.* **2008**, *1*, 139-143.

(56) Frenkel, D.; Smit, B. *Understanding Molecular Simulations: From Algorithms to Applications*. 2nd Edition, Academic Press: San Diego, 2002.

(57) Talu, O.; Myers, A. L. Molecular Simulation of Adsorption: Gibbs Dividing Surface and Comparison with Experiment. *A.I.Ch.E.J.* **2001**, *47*, 1160-1168.

(58) Düren, T.; Millange, F.; Férey, G.; Walton, K. S.; Snurr, R. Q. Calculating Geometric Surface Areas as a Characterization Tool for Metal-Organic Frameworks. *J. Phys. Chem. C* **2007**, *111*, 15350-15356.

(59) Foster, M. D.; Rivin, I.; Treacy, M. M. J.; Friedrichs, O. D. A geometric solution to the largest-free-sphere problem in zeolite frameworks. *Microporous Mesoporous Mater.* **2006**, *90*, 32-38.

(60) Smith, W.; Forester, T. R.; Todorov, I. T. The DL_POLY Molecular Simulation Package. http://www.cse.clrc.ac.uk/msi/software/DL_POLY/index.shtml, Warrington, England, March 2006.

(61) SARA Computing & Networking Services. https://subtrac.sara.nl/userdoc/wiki/lisa/description, Amsterdam, 16 January 2008.

(62) Krishna, R.; van Baten, J. M. Unified Maxwell-Stefan Description of Binary Mixture Diffusion in Micro- and Meso- Porous Materials. *Chem. Eng. Sci.* **2009**, *64*, 3159-3178.

(63) Krishna, R.; van Baten, J. M. Onsager coefficients for binary mixture diffusion in nanopores. *Chem. Eng. Sci.* **2008**, *63*, 3120-3140.

(64) van Baten, J. M.; Krishna, R. Entropy effects in adsorption and diffusion of alkane isomers in mordenite: An investigation using CBMC and MD simulations. *Microporous Mesoporous Mater.* **2005**, *84*, 179-191.

(65) Krishna, R.; van Baten, J. M. Describing binary mixture diffusion in carbon nanotubes with the Maxwell-Stefan equations. An investigation using molecular dynamics simulations. *Ind. Eng. Chem. Res.* **2006**, *45*, 2084-2093.

(66) Myers, A. L.; Prausnitz, J. M. Thermodynamics of Mixed Gas Adsorption. *A.I.Ch.E.J.* **1965**, *11*, 121-130.

(67) Ruthven, D. M. *Principles of Adsorption and Adsorption Processes*. John Wiley: New York, 1984.

(68) Siperstein, F. R.; Myers, A. L. Mixed-Gas Adsorption. *A.I.Ch.E.J.* **2001**, *47*, 1141-1159.

(69) PTC MathCad 15.0. http://www.ptc.com/, PTC Corporate Headquarters, Needham, 3 November 2015.

(70) Babbitt, J. D. On the Differential Equations of Diffusion. *Canad. J. Res.* **1950**, *28 A*, 449-474.

(71) Babbitt, J. D. A Unified Picture of Diffusion. *Canad. J. Phys.* **1951**, *29*, 427-436.

(72) Krishna, R. Uphill Diffusion in Multicomponent Mixtures. *Chem. Soc. Rev.* **2015**, *44*, 2812-2836.

(73) Skoulidas, A. I.; Sholl, D. S.; Krishna, R. Correlation effects in diffusion of CH_4/CF_4 mixtures in MFI zeolite. A study linking MD simulations with the Maxwell-Stefan formulation. *Langmuir* **2003**, *19*, 7977-7988.

(74) Chempath, S.; Krishna, R.; Snurr, R. Q. Nonequilibrium MD simulations of difusion of binary mixtures containing short n-alkanes in faujasite. *J. Phys. Chem. B* **2004**, *108*, 13481-13491.

(75) Hansen, N.; Keil, F. J. Multiscale modeling of reaction and diffusion in zeolites: from the molecular level to the reactor. *Soft Mater.* **2012**, *10*, 179-201.

(76) Krishna, R.; van Baten, J. M. An Investigation of the Characteristics of Maxwell-Stefan Diffusivities of Binary Mixtures in Silica Nanopores. *Chem. Eng. Sci.* **2009**, *64*, 870-882.

(77) Krishna, R.; van Baten, J. M. Maxwell-Stefan modeling of slowing-down effects in mixed gas permeation across porous membranes. *J. Membr. Sci.* **2011**, *383*, 289-300.

(78) Krishna, R. Using the Maxwell-Stefan formulation for Highlighting the Influence of Interspecies (1-2) Friction on Binary Mixture Permeation across Microporous and Polymeric Membranes. *J. Membr. Sci.* **2017**, *540*, 261-276.

(79) Krishna, R. Tracing the Origins of Transient Overshoots for Binary Mixture Diffusion in Microporous Crystalline Materials. *Phys. Chem. Chem. Phys.* **2016**, *18*, 15482-15495.

(80) Krishna, R. Adsorptive separation of $CO_2/CH_4/CO$ gas mixtures at high pressures. *Microporous Mesoporous Mater.* **2012**, *156*, 217-223.

(81) Krishna, R.; van Baten, J. M. Investigating the potential of MgMOF-74 membranes for CO_2 capture. *J. Membr. Sci.* **2011**, *377*, 249-260.

(82) Krishna, R.; van Baten, J. M. Investigating the Validity of the Knudsen Prescription for Diffusivities in a Mesoporous Covalent Organic Framework. *Ind. Eng. Chem. Res.* **2011**, *50*, 7083-7087.

(83) Krishna, R.; van Baten, J. M. Investigating the Validity of the Bosanquet Formula for Estimation of Diffusivities in Mesopores. *Chem. Eng. Sci.* **2012**, *69*, 684-688.

(84) Krishna, R.; Baur, R. Modelling Issues in Zeolite Based Separation Processes. *Sep. Purif. Technol.* **2003**, *33*, 213-254.

(85) Krishna, R. The Maxwell-Stefan Description of Mixture Permeation across Nanoporous Graphene Membranes. *Chem. Eng. Res. Des.* **2018**, *133*, 316-325. https://doi.org/10.1016/j.cherd.2018.03.033.

(86) Reed, D. A.; Ehrlich, G. Surface diffusion, atomic jump rates and thermodynamics. *Surf. Sci.* **1981**, *102*, 588-609.

(87) Krishna, R.; Paschek, D.; Baur, R. Modelling the occupancy dependence of diffusivities in zeolites. *Microporous Mesoporous Mater.* **2004**, *76*, 233-246.

(88) Krishna, R.; van Baten, J. M. A molecular dynamics investigation of a variety of influences of temperature on diffusion in zeolites. *Microporous Mesoporous Mater.* **2009**, *125*, 126-134.

(89) Vlugt, T. J. H.; Krishna, R.; Smit, B. Molecular Simulations of Adsorption Isotherms for Linear and Branched Alkanes and Their Mixtures in Silicalite. *J. Phys. Chem. B* **1999**, *103*, 1102-1118.

(90) Chmelik, C.; Heinke, L.; Kärger, J.; Shah, D. B.; Schmidt, W.; van Baten, J. M.; Krishna, R. Inflection in the Loading Dependence of the Maxwell-Stefan Diffusivity of Iso-butane in MFI Zeolite. *Chem. Phys. Lett.* **2008**, *459*, 141-145.

(91) Krishna, R.; van Baten, J. M. Letter to the Editor. *A.I.Ch.E.J.* **2010**, *56*, 3288-3289.

(92) Pollard, W. G.; Present, R. D. On gaseous self-diffusion in long capillary tubes. *Phys. Rev.* **1948**, *73*, 762-774.

(93) Krishna, R.; van Baten, J. M. Hydrogen Bonding Effects in Adsorption of Water-alcohol Mixtures in Zeolites and the Consequences for the Characteristics of the Maxwell-Stefan Diffusivities. *Langmuir* **2010**, *26*, 10854-10867.

(94) Krishna, R.; van Baten, J. M. Segregation effects in adsorption of CO_2 containing mixtures and their consequences for separation selectivities in cage-type zeolites. *Sep. Purif. Technol.* **2008**, *61*, 414-423.

(95) Krishna, R.; van Baten, J. M. Influence of segregated adsorption on mixture diffusion in DDR zeolite. *Chem. Phys. Lett.* **2007**, *446*, 344-349.

(96) Krishna, R.; Paschek, D. Self-diffusivities in multicomponent mixtures in zeolites. *Phys. Chem. Chem. Phys.* **2002**, *4*, 1891-1898.

(97) Krishna, R.; van Baten, J. M. Investigating cluster formation in adsorption of CO_2, CH_4, and Ar in zeolites and metal organic frameworks at sub-critical temperatures. *Langmuir* **2010**, *26*, 3981-3992.

(98) Krishna, R.; van Baten, J. M. Highlighting a variety of unusual characteristics of adsorption and diffusion in microporous materials induced by clustering of guest molecules. *Langmuir* **2010**, *26*, 8450-8463.

(99) Krishna, R.; van Baten, J. M. Mutual slowing-down effects in mixture diffusion in zeolites. *J. Phys. Chem. C* **2010**, *114*, 13154-13156.

(100) Caro, J.; Bülow, M.; Richter-Mendau, J.; Kärger, J.; Hunger, M.; Freude, D. Nuclear Magnetic Resonance Self-diffusion Studies of Methanol-Water Mixtures in Pentasil-type Zeolites. *J. Chem. Soc., Faraday Trans.* **1987**, *83*, 1843-1849.

(101) Krishna, R.; van Baten, J. M. Highlighting Pitfalls in the Maxwell-Stefan Modeling of Water-Alcohol Mixture Permeation across Pervaporation Membranes. *J. Membr. Sci.* **2010**, *360*, 476-482.

References

(102) Krishna, R.; van Baten, J. M. A Molecular Dynamics Investigation of the Unusual Concentration Dependencies of Fick Diffusivities in Silica Mesopores. *Microporous Mesoporous Mater.* **2011**, *138*, 228-234.

(103) Krishna, R.; van Baten, J. M. A rationalization of the Type IV loading dependence in the Kärger-Pfeifer classification of self-diffusivities. *Microporous Mesoporous Mater.* **2011**, *142*, 745-748.

(104) Chmelik, C.; Kärger, J.; Wiebcke, M.; Caro, J.; van Baten, J. M.; Krishna, R. Adsorption and Diffusion of Alkanes in CuBTC Crystals Investigated Using Infrared Microscopy and Molecular Simulations. *Microporous Mesoporous Mater.* **2009**, *117*, 22-32.

(105) Krishna, R.; van Baten, J. M. The Darken relation for multicomponent diffusion in liquid mixtures of linear alkanes. An investigation using Molecular Dynamics (MD) simulations. *Ind. Eng. Chem. Res.* **2005**, *44*, 6939-6947.

(106) Fuller, E. N.; Schettler, P. D.; Giddings, J. C. A New Method for Prediction of Binary Gas-phase Diffusion Coefficients. *Ind. Eng. Chem.* **1966**, *58*, 19-27.

(107) Poling, B. E.; Prausnitz, J. M.; O'Connell, J. P. *The Properties of Gases and Liquids*. 5th Edition, McGraw-Hill: New York, 2001.

(108) Clark, W. M.; Rowley, R. L. The mutual diffusion coefficient of methanol - n-hexane near the consolute point. *A.I.Ch.E.J.* **1986**, *32*, 1125-1131.

(109) Krishna, R.; van Baten, J. M. MD simulations of diffusivities in methanol – n-hexane mixtures near the liquid-liquid phase splitting region. *Chem Eng Technol* **2006**, *29*, 516-519.